

DISS. ETH NO. 23350

# Study of $\nu$ and $\bar{\nu}$ flavor oscillations at the T2K experiment and impact on the $\delta_{CP}$ phase determination within the 3- $\nu$ paradigm

A thesis submitted to attain the degree of

**DOCTOR OF SCIENCES of ETH ZURICH**

(Dr. sc. ETH Zurich)

presented by

**Davide Sgalaberna**

Laurea Magistrale in Fisica, Università di Bologna

born on 15.04.1986

citizen of Italy

accepted on recommendation of

Prof. Dr. André Rubbia, examiner

Prof. Dr. Günther Dissertori, co-examiner

2016



# Contents

<b>1</b>	<b>Introduction to neutrino physics</b>	<b>13</b>
1.1	Historical introduction to neutrinos . . . . .	13
1.2	Theory of neutrino oscillations . . . . .	14
1.2.1	Matter effects . . . . .	17
1.2.2	Approximated oscillation probabilities . . . . .	18
1.3	Neutrino oscillation experiments . . . . .	19
1.3.1	Solar neutrino oscillation parameters . . . . .	20
1.3.2	Atmospheric neutrino oscillation parameters . . . . .	21
1.3.3	Measurement of $\theta_{13}$ and search for CP violation . . . . .	22
1.4	Status of three-neutrino oscillation parameters . . . . .	23
1.5	Hints of light sterile neutrinos . . . . .	23
1.6	Sterile neutrino oscillations . . . . .	27
1.7	Motivations of the thesis work . . . . .	28
<b>2</b>	<b>The T2K experiment</b>	<b>29</b>
2.1	The beam line . . . . .	30
2.1.1	Primary beamline . . . . .	30
2.1.2	Secondary beamline . . . . .	31
2.1.3	Off-axis beam . . . . .	32
2.2	The near detector . . . . .	32
2.2.1	INGRID . . . . .	33
2.2.2	ND280 . . . . .	33
2.3	The far detector: Super-Kamiokande . . . . .	37
2.4	Summary of the data taking . . . . .	39
2.5	The neutrino flux prediction . . . . .	39
2.5.1	The simulation chain . . . . .	39
2.6	Auxiliary hadron production experiment and flux tuning . . . . .	41
2.6.1	MC reweighting procedure with external data . . . . .	43
2.6.2	Uncertainty on the flux prediction . . . . .	45
2.7	Neutrino cross sections at T2K . . . . .	46
2.7.1	Impact of neutrino cross-sections on the energy reconstruction . . . . .	50
<b>3</b>	<b>Hadron production measurements with the auxiliary NA61/SHINE experiment</b>	<b>51</b>
3.1	The NA61 experimental setup . . . . .	51
3.1.1	CERN accelerator chain . . . . .	52
3.1.2	Beam line and trigger system . . . . .	53

3.1.3	Tracking system and ToF . . . . .	55
3.2	Collected data . . . . .	56
3.3	Hadron production cross section measurement . . . . .	57
3.3.1	The interaction trigger cross section . . . . .	59
3.3.2	Event selection . . . . .	60
3.3.3	Interaction probability after the event selection . . . . .	61
3.3.4	Systematic uncertainties on trigger cross section . . . . .	63
3.3.5	Inelastic and production cross section . . . . .	67
3.3.6	Final result of inelastic and production cross section . . . . .	69
3.4	Normalization of the measured hadron multiplicities with 2009 run data . . . . .	69
<b>4</b>	<b>Search for short baseline <math>\nu_e</math> disappearance at T2K</b>	<b>73</b>
4.1	Overview of the analysis . . . . .	73
4.2	Analysis templates . . . . .	75
4.3	The event selection . . . . .	75
4.3.1	The electron neutrino selection . . . . .	76
4.3.2	The control sample selection . . . . .	77
4.4	The systematic uncertainties . . . . .	78
4.4.1	Detector systematic uncertainties . . . . .	78
4.4.2	Flux systematic uncertainties . . . . .	79
4.4.3	Cross section systematic uncertainties . . . . .	80
4.4.4	Final state interactions . . . . .	81
4.4.5	Constraining the systematic uncertainties with the near detector . . . . .	82
4.4.6	Summary of systematic uncertainties . . . . .	83
4.5	Analysis method . . . . .	85
4.6	Sensitivity study . . . . .	86
4.7	Oscillation results . . . . .	86
4.7.1	P-value . . . . .	87
4.7.2	Confidence intervals . . . . .	88
4.8	Summary . . . . .	90
<b>5</b>	<b>Framework for oscillation analyses at Super-K</b>	<b>91</b>
5.1	Analysis templates . . . . .	91
5.2	Fit method . . . . .	92
5.3	Event selection . . . . .	93
5.3.1	Electron-like samples . . . . .	94
5.3.2	Muon-like samples . . . . .	96
5.4	Systematic uncertainties . . . . .	96
5.4.1	Uncertainty on the oscillation parameters . . . . .	97
5.4.2	Flux systematic uncertainties . . . . .	99
5.4.3	Cross section systematic uncertainties . . . . .	99
5.4.4	Detector systematic uncertainties . . . . .	101
5.4.5	Final State and secondary interaction uncertainty and photo-nuclear effect	103
5.4.6	Near detector measurement . . . . .	103
5.4.7	Summary of systematic uncertainties . . . . .	104

<b>6</b>	<b>Search for <math>\bar{\nu}_\mu \rightarrow \bar{\nu}_e</math> appearance at Super-K</b>	<b>107</b>
6.1	Sensitivity study . . . . .	108
6.2	Result of run 5-6 data set analysis . . . . .	109
<b>7</b>	<b>Neutrino and antineutrino joint analysis at Super-K</b>	<b>113</b>
7.1	Sensitivity study . . . . .	115
7.2	Results of run 1-6 data analysis . . . . .	116
7.3	Discussion of the results and future sensitivities . . . . .	116
	<b>Appendices</b>	<b>129</b>
<b>A</b>	<b>Theory of neutrinos</b>	<b>131</b>
A.1	Neutrinos in the Standard Model . . . . .	131
A.2	Neutrinos masses . . . . .	133
A.3	Leptogenesis . . . . .	137
A.4	Light sterile neutrinos . . . . .	139
<b>B</b>	<b>Flux and cross section systematic uncertainties used in the analysis at Super-K</b>	<b>141</b>
<b>C</b>	<b>Statistical methods</b>	<b>145</b>
C.1	Discussion of marginalization and profiling and best-fit spectra . . . . .	145
C.2	Methods for confidence intervals . . . . .	147
C.2.1	Feldman-Cousins method . . . . .	148
C.3	P-value and method for $\bar{\nu}_\mu \rightarrow \bar{\nu}_e$ appearance analysis . . . . .	149
<b>D</b>	<b>Templates of joint fit analysis</b>	<b>151</b>
<b>E</b>	<b>Comparison of data with expected MC for electron-like T2K run 1-6 data sample</b>	<b>157</b>



# Abstract

T2K (Tokai-to-Kamioka) is a long baseline neutrino oscillation experiment in Japan which goal is to precisely measure the parameters  $\theta_{23}$ ,  $\Delta m_{32}^2$  and  $\theta_{13}$  of the PMNS matrix in the context of the 3-neutrinos paradigm and to search for a hint of CP violation in the leptonic sector. The only way to search for CP violation is looking for differences between  $\bar{\nu}_\mu \rightarrow \bar{\nu}_e$  and  $\nu_\mu \rightarrow \nu_e$  oscillations. Furthermore T2K aims to observe for the first time  $\bar{\nu}_e$  appearance in a  $\bar{\nu}_\mu$  beam, which is predicted by the theory but never observed so far.

A muon neutrino beam is produced at the J-PARC Main Ring (MR) accelerator that provides a 31 GeV/c proton beam interacting on a 90 cm long graphite target. The collisions produce hadrons, mainly charged pions and kaons, that further decay into  $\nu_\mu$  with a contamination of  $\nu_e$  below 1%. In order to produce a  $\bar{\nu}_\mu$  beam the polarity of the magnet is inverted and  $\bar{\mu}$ 's are focused instead of  $\mu$ 's. The neutrino beam is first detected by the near detector complex (ND280) located about 280 m downstream of the hadron production target, where neutrinos have not enough time to oscillate, then by the far detector Super-Kamiokande (Super-K), a 50 kt water Cherenkov detector located at a distance of about 295 km from the neutrino production point. The direction of the neutrino beamline is  $2.5^\circ$  off the axis between the target and the far detector. This configuration produces a narrow-band neutrino beam with a peak energy of about 0.6 GeV at the far detector, which is exactly on the first  $\nu_\mu \rightarrow \nu_e$  oscillation maximum.  $\nu_\mu$  ( $\bar{\nu}_\mu$ ) disappearance and  $\nu_e$  ( $\bar{\nu}_e$ ) appearance can be probed by comparing the neutrino flux prediction, based on the measurement at ND280, to the observed flux at Super-K.

T2K is collecting both neutrino and antineutrino data and for the first time is attempting to look for CP violation in the leptonic sector by directly comparing neutrino and antineutrino oscillations. Furthermore T2K has a very good sensitivity to  $\nu_\mu$  disappearance and can provide the best measurements of  $\theta_{23}$  and  $\Delta m_{32}^2$ .

In order to perform precision measurements of the oscillation parameters, the reduction of the systematic uncertainties is critical. The largest source of uncertainty comes from the poor knowledge on the neutrino flux prediction, dominated by the uncertainty on the production of the parent hadrons that further decay into neutrinos. The flux estimation is based on hadron production models that provide flux predictions with discrepancies up to about 30%. In order to reach the goals of T2K, the hadron production is measured with the NA61/SHINE (SHINE = SPS Heavy Ion and Neutrino Experiment), a multi-purpose fixed target experiment at the CERN SPS. Interactions of incoming 31 GeV/c protons on carbon are measured with a 2 cm thin target, 4% of the nuclear interaction length, in order to study the primary interactions and measure the total hadron production cross section, and a 90 cm long target ( $1.9\lambda_L$ ), a replica of the one used in T2K, needed to reproduce the same configuration and measure both the secondary and tertiary hadron re-interactions. Spectra of the produced  $\pi$ ,  $K$ ,  $p$ ,  $\lambda^0$  as well as the total hadron production cross section were measured. In 2007 a low statistic pilot run has been

conducted with the thin and the replica target in order to test the analysis method. The measured spectra were used to tune the T2K neutrino flux prediction. The detector underwent many updates in 2008 and new data were collected in 2009, increasing the statistics approximately by a factor 10. This allowed to drastically reduce the uncertainty on the T2K neutrino flux prediction.

In the context of 3-neutrino oscillations, the near detector is used to measure the un-oscillated neutrino flux, reducing both the flux and cross section systematic uncertainties. However searches for new physics can be performed as well. There exist several experimental anomalies that could be explained as short baseline neutrino oscillations. There are different scenarios of new physics that could justify these unexpected observations, like the existence of sterile neutrinos that can be accommodated in an extended version of the 3-neutrino framework. Sterile neutrinos do not interact via the electroweak force and cannot be directly detected. If they have a mass of the order of  $1\text{eV}^2/c^2$ , they could undergo oscillations with standard neutrinos ( $\nu_e$ ,  $\nu_\mu$  and  $\nu_\tau$ ), detectable by short baseline detectors like ND280 by looking for a deficit or an excess of neutrinos with respect to the prediction.

This thesis is focused on the search for short baseline neutrino oscillations, consistent with the existence of sterile neutrinos, at the near detector as well as the measurement of long baseline 3-flavor oscillations at the far detector, with a particular emphasis to the search for  $\bar{\nu}_\mu \rightarrow \bar{\nu}_e$  appearance and CP violation in the leptonic sector. The goal is to test the validity of the 3-neutrino framework and precisely measure the oscillation parameters as well as search for the first hint of CP violation.

I started my Ph.D. working in the NA61/SHINE experiment and I measured the total hadron production cross section of proton-carbon interactions at the T2K energy, with the high statistics 2009 run data. This measurement is not only indispensable for T2K but is also of great interest on its own right, since it can be compared to analogue measurements from other experiments helping in the understanding of the theoretical models of particle interactions.

Then I joined the ND280 electron neutrino working group at T2K and I performed the search for short baseline electron neutrino disappearance in the context of an extended framework with one additional sterile neutrino. The analysis result, for which a paper has been written [136], is presented.

Finally I worked in the oscillation analysis working group at the far detector. My first work was to search for standard  $\bar{\nu}_e$  appearance in a  $\bar{\nu}_\mu$  beam, not yet observed so far. This measurement is very interesting because it is the first step toward the search for CP violation which can be studied by looking for differences between  $\nu_\mu \rightarrow \nu_e$  and  $\bar{\nu}_\mu \rightarrow \bar{\nu}_e$  oscillations. Finally I performed the first search for CP violation where both neutrino and antineutrino data were simultaneously analyzed.

The first chapter of the thesis provides an introduction to the theory of neutrino physics, in particular neutrino oscillations. A review of the most important discoveries and experiments about neutrinos is given as well. In the second chapter the T2K experiment is described as well as the requirements for a precise knowledge of the neutrino beam. In the first part of the third chapter the NA61/SHINE experimental setup is described, while in the second part the measurement of the hadron production cross section is shown. The result of the search for short baseline  $\nu_e$  disappearance at the T2K near detector is shown in the fourth chapter, while in the last three chapters the 3-flavor neutrino oscillation analyses performed at the far detector are presented.



# Sommario

T2K (Tokai-to-Kamioka) è un esperimento situato in Giappone che studia le oscillazioni di neutrini a grande distanza, con l'obiettivo di misurare con precisione i parametri  $\theta_{23}$ ,  $\Delta m_{32}^2$  e  $\theta_{13}$  della matrice PMNS nel contesto del paradigma dei 3 neutrini e cercare un primo segnale di violazione di CP nel settore leptónico.

L'unico modo per osservare la violazione di CP è trovare differenze tra le oscillazioni  $\bar{\nu}_\mu \rightarrow \bar{\nu}_e$  e  $\nu_\mu \rightarrow \nu_e$ . Inoltre T2K punta ad osservare per la prima volta l'apparizione di  $\bar{\nu}_e$  in un fascio di  $\bar{\nu}_\mu$ , predetto dalla teoria ma mai osservato finora.

Un fascio di neutrini muonici viene prodotto dall'acceleratore circolare principale a J-PARC che fornisce un fascio di protoni di 31 GeV/c, che interagiscono in una targhetta di grafite lunga 90 cm. Le collisioni producono adroni, in gran parte pioni e kaoni carichi che in seguito decadono in  $\nu_\mu$  con una contaminazione di  $\nu_e$  minore dell' 1%. Un fascio di  $\bar{\nu}_\mu$  viene prodotto invertendo la polarità del magnete, in modo da focalizzare i  $\bar{\mu}$  piuttosto che i  $\mu$ . Il fascio di neutrini viene rivelato prima dal rivelatore vicino (ND280), che si trova a circa 280 m di distanza dalla targhetta di produzione degli adroni, dove i neutrini non hanno abbastanza tempo per oscillare, poi dal rivelatore lontano, Super-Kamiokande (Super-K), composto da 50 kt di acqua che sfrutta la tecnologia Cherenkov ed è situato a circa 295 km dal punto di produzione dei neutrini. Il fascio di neutrini viene prodotto in una "beamline" la cui direzione è di  $2.5^\circ$  rispetto l'asse che congiunge la targhetta ed il rivelatore lontano. Questa configurazione produce un fascio di neutrini con uno spettro di energia molto stretto ed un picco a circa 0.6 GeV al rivelatore lontano, esattamente sul primo massimo di oscillazione di  $\nu_\mu \rightarrow \nu_e$ . La sparizione di  $\nu_\mu$  ( $\bar{\nu}_\mu$ ) e l'apparizione di  $\nu_e$  ( $\bar{\nu}_e$ ) può essere provata confrontando il flusso di neutrini predetto, in base alle misure eseguite al rivelatore vicino, e quello osservato a Super-K.

T2K sta accumulando dati sia di neutrini che antineutrini e per la prima volta sta tentando di osservare la violazione di CP nel settore leptónico confrontando direttamente oscillazioni di neutrini e antineutrini. Inoltre T2K ha un'ottima sensitività alla sparizione di  $\nu_\mu$  e può fornire le migliori misure di  $\theta_{23}$  e  $\Delta m_{32}^2$ .

Per poter ottenere una misura precisa dei parametri di oscillazione, la riduzione delle incertezze sistematiche è fondamentale. La maggior fonte di incertezza viene dalla cattiva conoscenza nella predizione del flusso di neutrini, dominata dall'incertezza nella produzione degli adroni "genitori" che decadono in neutrini. La stima del flusso si basa su modelli di produzione di adroni che fornisce discrepanze nella predizione del flusso fino al 30%. Per raggiungere i goal prefissati di T2K, la produzione di adroni viene misurata da NA61/SHINE (SHINE = SPS Heavy Ion and Neutrino Experiment) un esperimento a targhetta fissa all'SPS del CERN. Le interazioni di protoni di 31 GeV/c su carbonio sono misurate con una targhetta sottile di 2 cm, 4% della lunghezza di interazione nucleare, per poter studiare le interazioni primarie e misurare la sezione totale di produzione adronica, e una targhetta lunga 90 cm ( $1.9\lambda_L$ ), una replica di

quella usata a T2K, che serve per poter riprodurre la stessa configurazione. e misurare le rein-terazioni secondarie e terziarie. Gli spettri di  $\pi$ ,  $K$ ,  $p$ ,  $\lambda^0$  e la sezione d'urto totale adronica vengono misurate. Nel 2007 è fu preso un “run” di dati pilota di bassa statistica sia con la targhetta sottile e lunga usato per testare il metodo di analisi. Gli spettri misurati furono usati per calibrare il flusso di neutrini di T2K predetto. Il rivelatore è stato sottoposto a diverse modifiche nel 2008 e nuovi dati sono stati presi nel 2009, incrementando la statistica di circa un fattore 10. Questo ha permesso di ridurre drasticamente l'incertezza sulla predizione del flusso di neutrini a T2K.

Nel contesto delle oscillazioni dei 3 neutrini, il rivelatore vicino viene usato per misurare il flusso di neutrini non oscillato, riducendo sia le incertezze sistematiche sul flusso che sulla sezione d'urto. Comunque pure ricerche di nuova fisica possono essere fatte. Esistono alcune anomalie sperimentali che potrebbero essere spiegate assumendo oscillazioni di neutrini a piccola distanza. Ci sono diversi scenari di nuova fisica che potrebbero spiegare queste osservazioni inaspettate, come l'esistenza di neutrini sterili che possono essere introdotte in una versione estesa della struttura dei 3 neutrini. I neutrini sterili non interagiscono mediante la forza elettrodebole e quindi non possono essere rivelati direttamente. Nel caso avessero una massa di circa  $1 \text{ eV}^2/c^2$  potrebbero oscillare con i neutrini standard ( $\nu_e$ ,  $\nu_\mu$  e  $\nu_\tau$ ), che possono essere osservati mediante rivelatori situati a piccola distanza, come ND280, cercando un disavanzo o un eccesso di neutrini rispetto alla predizione.

Questa tesi è focalizzata sia sulla ricerca di oscillazioni di neutrini a piccola distanza al rivelatore vicino, consistente con l'esistenza di neutrini sterili, che sulla misura a grande distanza di oscillazioni tra i 3 sapori al rivelatore lontano, con una particolare enfasi alla ricerca dell'apparizione  $\bar{\nu}_\mu \rightarrow \bar{\nu}_e$  e della violazione di CP nel settore leptonico. L'obiettivo è testare la validità della struttura a 3 neutrini, misurare con precisione i parametri di oscillazione e ricercare per la prima volta la violazione di CP.

Ho iniziato il Ph.D lavorando nell'esperimento NA61/SHINE misurando la sezione d'urto totale di produzione adronica in interazioni tra protoni e carbonio all'energia di T2K con il “run” di dati di alta statistica del 2009. Questa misura è di grande interesse non solo perché importante per T2K, ma anche perché può essere confrontata con altre misure analoghe di altri esperimenti fornendo un'aiuto alla comprensione dei modelli teorici di interazioni di particelle.

In seguito ho aderito al gruppo di lavoro del neutrino elettronico di ND280 a T2K ed ho portato a termine l'analisi di ricerca della sparizione del neutrino elettronico a piccola distanza nel contesto della struttura di neutrini estesa con l'aggiunta di un neutrino sterile. Il risultato dell'analisi, per cui un articolo è stato pubblicato [136], viene presentato.

Infine ho lavorato nel gruppo di analisi di oscillazioni al rivelatore lontano. Il mio primo lavoro è stato lo studio di apparizione standard di  $\bar{\nu}_e$  in un fascio di  $\bar{\nu}_\mu$ , mai osservata finora. Questa misura è molto interessante in quanto si tratta del primo passo verso la ricerca di violazione di CP, che può essere studiata cercando differenze nelle oscillazioni  $\nu_\mu \rightarrow \nu_e$  e  $\bar{\nu}_\mu \rightarrow \bar{\nu}_e$ . Poi ho portato a termine la prima analisi di ricerca di violazione di CP dove sia i dati di neutrini che di antineutrini vengono analizzati simultaneamente.

Il primo capitolo della tesi fornisce una introduzione alla teoria della fisica del neutrino, in particolare le oscillazioni di neutrini. Viene anche fornita una rassegna delle più importanti scoperte e degli esperimenti sui neutrini. Nel secondo capitolo viene descritto l'esperimento T2K e tutti i requisiti per una conoscenza precisa del fascio di neutrini. Nella prima parte

del terzo capitolo viene descritto l'esperimento NA61/SHINE, mentre nella seconda parte viene presentata la misura della sezione d'urto totale di produzione adronica. Il risultato della ricerca di scomparsa di  $\nu_e$  a piccola distanza al rivelatore vicino di T2K viene mostrato nel quarto capitolo, mentre negli ultimi tre capitoli le analisi di oscillazione di neutrini a 3 sapori prodotte al rivelatore lontano viene presentata.

## Acknowledgements

First of all I would like to thank to Prof. André Rubbia, who gave me the opportunity to join his research group and work in a very exciting physics experiment with very well prepared people.

Secondly I would like to thank Dr. Silvestro Di Luise, who gave me many advices and suggestions. It was a pleasure to have the opportunity to work with him and learn a lot of new things. I also want to thank to him for his friendship.

Another great thank is to Dr. Khoi Nguyen, my officemate for about four years, Cosimo Cantini and Shuoxing Wu for their great friendship.

I want to thank to all the colleagues, in particular Dipanwita Banerjee, Adamo Gendotti, Dr. Lukas Epprecht, Dr. Sosuke Horikawa, Dr. Devis Lussi, Dr. Alessandro Curioni, Dr. Ursina Degunda, Dr. Katalin Nikolics, Dr. Sebastien Murphy, Dr. Christian Regenfus, Dr. Filippo Resnati, Thierry Viant and many others for their help and friendship.

An enormous thank is to Rosa Baechli and Rita Vonesch, who helped me taking care of all the administrative formalities.

I am very grateful to Dr. Claudio Giganti and Dr. Marco Zito with whom I started to work in T2K. They taught me how to move in such a big collaboration and their advices were very important for the data analyses I did as well as when I had to present my first results at the T2K collaboration.

I would like to thank to Javier Caravaca with whom I worked during the first part of the Ph.D.

I am deeply thankful to Costas Andreopoulos, Steve Dennis, Raj Shah and all the people I worked with in the VALOR neutrino oscillation analysis group for their many helps on the oscillation analyses at the T2K far detector. It was a great opportunity to join their analysis group and work with very well prepared people from whom I could steal some of their expertise.

Many thanks also to Ichikawa-san and Mark Hartz for their many suggestions, comments and for the coordination of the neutrino oscillation analyses at T2K.

I want to thank Marek Gazdzicki, Alexander Korzenev, Boris Popov, Peter Seyboth, Laura Zambelli and all the people who helped and guided me in the work I did within the NA61/SHINE experiment. I am very happy to have been part of this collaboration.

I am very grateful to Dr. Lorenzo Magaletti, Prof. Vincenzo Berardi, Sara Bolognesi, Stefania Bordini, Francesco Gizzarelli, Ciro Riccio and all the people with whom I spent most of my time during my permanence in Japan for collaboration meetings.

A very special thank is to my daughter, my wife and my parents for their strong support. I am very lucky to have them as part of my life.

# Chapter 1

## Introduction to neutrino physics

Neutrinos are very light particles which interact very weakly and are very elusive. They are introduced in the Standard Model, the theory that describes the strong, electromagnetic, and weak interactions of elementary particles, as fermions (particles with spin  $\frac{1}{2}$ ) which interact via the weak force, exchanging a  $W^\pm$  or a  $Z^0$  boson, but do not carry electric charge. There are three neutrino electroweak fields  $\nu_e$ ,  $\nu_\mu$ ,  $\nu_\tau$  and each of them couples with the corresponding charged lepton field ( $e^-$ ,  $\mu^-$  and  $\tau^-$ ) in the charged weak current. They are expected to be mass-less. However we know that at least two out of three neutrinos have a tiny mass, since the phenomenon of the oscillations has been observed. More details on the way neutrinos are described by the Standard Model are shown in app. A.1. Theories proposed to explain the small neutrino masses are shown in app. A.2.

### 1.1 Historical introduction to neutrinos

Between the end of the 19<sup>th</sup> and the first part of the 20<sup>th</sup> century several radioactive processes were discovered. The  $\beta$  decay ( $n \rightarrow p + e^- + \bar{\nu}_e$ ), where  $n$ ,  $p$ ,  $e^-$  and  $\bar{\nu}_e$  are respectively the neutron, proton, electron and electron antineutrino, showed a strange feature. It was demonstrated by Chadwick that the spectrum of the electron was continuous in energy and not discrete as expected, like for  $\alpha$ - and  $\gamma$ - rays [1]. This new discovery created some confusion in the physics community at the point that some scientists, like Niels Bohr, proposed that the energy conservation was a purely statistical problem. The solution was found by Wolfgang Pauli in 1930 when, in a famous letter [2], he postulated a new neutral weakly interacting particle, with spin  $\frac{1}{2}$  and a very small mass, to preserve the energy and momentum conservation in the  $\beta$  decay. He called it “*neutron*”. In 1924 Chadwick discovered the neutron, as we know now, and Fermi renamed the new Pauli particle as neutrino, because of the small mass. Later he concluded that this particle could be also massless. In 1934 Fermi formulated the first theory of weak interactions. He described the  $\beta$ -decay as a point-like reaction with a weak coupling strength. A few decades later Glashow, Weinberg and Salam unified the electromagnetic and weak forces in the electroweak theory. The weak theory is not point-like, though it is still a very good approximation at low energy, but is mediated by the charged  $W^\pm$  and neutral  $Z^0$  bosons. In 1937 Ettore Majorana proposed that neutrinos and antineutrinos might be the same entity [3]. The main issue of neutrino experiments is that these particles are very difficult to detect and some physicist argued that neutrinos would have never been detected. However in 1956 Clyde Cowan and Frederic Reines detected for the first time this very elusive particle at the Savannah river nuclear power plant [4]. The experiment was based on the idea of Bruno Pontecorvo to

exploit the huge amount of antineutrinos produced by the nuclear fission in the reactor power plants via the inverse beta decay. In 1956 Lee and Yang discovered that weak interactions do not conserve parity, i.e. the weak force is not invariant under a mirror reflection of the physics system [5]. In 1958 Maurice Goldhaber measured the neutrino helicity to be consistent with a single state, as formulated by Lee and Yang: all neutrinos are left-handed and all anti-neutrinos are right-handed [6]. In 1962 Leon Lederman, Melvin Schwartz and Jack Steinberger showed the existence of muon neutrinos using for the first time an accelerator to produce a neutrino beam [7]. In the meanwhile in 1968, V. N. Gribov and B. Pontecorvo proposed that, if neutrinos are massive, oscillations can occur among the two types of neutrinos known at the time, the electron and the muon neutrino, [8]. Finally in 1998 the Super-Kamiokande experiment measured for the first time neutrino oscillations by observing a deficit of the atmospheric  $\nu_\mu$ , which are produced by cosmic rays interacting on the Earth's atmosphere and has oscillated into  $\nu_\tau$ . This was the confirmation that neutrinos have mass. Though many experiments indirectly evidenced the existence of a third neutrino, only in 2000 the DONUT experiment at Fermilab directly detected the  $\nu_\tau$  [11], completing the framework of the three standard neutrinos ( $\nu_e$ ,  $\nu_\mu$  and  $\nu_\tau$ ).

Another anomaly, not understood since the late 60's, was the deficit of flux of neutrinos produced in the core of the Sun, which was observed by the Kamiokande [12], SAGE [13] and GALLEX [14] experiments. Finally in 2001 the SNO experiments confirmed that the anomaly was due oscillations of the solar neutrinos [15].

A few years earlier the LEP experiment at CERN precisely measured the Z boson decay width, strictly consistent with three active neutrinos [16]. However this does not preclude the existence of other neutrinos, which would not undergo the electroweak force. These are the so-called sterile neutrinos ( $\nu_s$ ), in general introduced in an extended framework as right-handed. In the 1990s with the LSND experiment [17] and a few years ago with the MiniBooNE experiment [18], possible hints of the existence of sterile neutrinos have been observed by detecting an excess of  $\nu_e$  events compatible with short baseline  $\nu_e$  appearance due to sterile neutrino oscillations with a mass of the order of  $1 \text{ eV}^2/c^4$ . Instead other experimental data show a deficit of  $\bar{\nu}_e$  (reactor [19] and gallium [20] anomalies) and are compatible with  $\nu_e \rightarrow \nu_s$  disappearance. Anyway since  $\nu_\mu \rightarrow \nu_s$  has not been observed yet it is difficult to accommodate all these observations in a common theoretical framework.

In the last few years very important discoveries have been done in the context of the 3-neutrinos framework.  $\nu_\mu \rightarrow \nu_\tau$  oscillations were observed for the first time by the OPERA experiment at Gran Sasso [21]. The Daya Bay experiment measured the non-zero  $\theta_{13}$  with a  $5\sigma$  significance [22] and T2K observed  $\nu_\mu \rightarrow \nu_e$  appearance with a significance of  $7.5\sigma$  [23].

## 1.2 Theory of neutrino oscillations

The indication of a non null neutrino mass for at least two of the three active neutrinos is given by the fact that neutrinos have been experimentally observed to oscillate between different flavor eigenstates. An active neutrino with flavor  $\alpha$  and momentum  $\vec{p}$ , created in a charged-current weak interaction process from a charged lepton  $l_\alpha^-$  or together with a charged antilepton  $l_\alpha^+$ , is described by the flavor eigenstate as a linear combination of the mass eigenstates:

$$|\nu_\alpha\rangle = \sum_k U_{\alpha k} |\nu_k\rangle \quad (\alpha = e, \mu, \tau) \quad (1.1)$$

where  $k = 1, 2, 3$  if we consider only the three active neutrinos.  $U_{\alpha k}$  is an element of the  $3 \times 3$  unitary matrix which is called Pontecorvo-Maki-Nakagawa-Sakata (PMNS) matrix [9].

The massive neutrinos  $|\nu_\alpha\rangle$  are eigenstates of the Hamiltonian

$$H|\nu_k\rangle = E_k|\nu_k\rangle \quad (1.2)$$

with energy eigenvalues  $\sqrt{\vec{p}^2 + E_k^2}$  in vacuum. If we consider the Schroedinger equation

$$i \frac{d}{dt} |\nu_k\rangle = e^{-iE_k t} |\nu_k\rangle \quad (1.3)$$

we obtain that the massive neutrino state evolves in time as a plane wave. The flavor state at the time  $t$  can be written as:

$$|\nu_\alpha(t)\rangle = \sum_k U_{\alpha k}^* e^{-iE_k t} |\nu_k\rangle \quad (1.4)$$

Substituting eq. 1.1 in eq. 1.4 we get

$$|\nu_\alpha(t)\rangle = \sum_{\alpha=e,\mu,\tau} \left( \sum_k U_{\alpha k}^* e^{-iE_k t} U_{\beta k} \right) |\nu_\beta\rangle \quad (1.5)$$

i.e. the superposition of massive neutrino states  $|\nu_k\rangle$  becomes a superposition of different flavor states at  $t > 0$  if the mixing matrix  $U$  is not diagonal.

The transition probability  $\nu_\alpha \rightarrow \nu_\beta$  as a function of the time is

$$P_{\nu_\alpha \rightarrow \nu_\beta}(t) \equiv |\langle \nu_\beta | \nu_\alpha(t) \rangle|^2 = \sum_k U_{\alpha k}^* U_{\beta k} U_{\alpha j} U_{\beta j}^* e^{-i(E_k - E_j)t} \quad (1.6)$$

Since the neutrinos are very light they can be considered in the ultra-relativistic limit and the approximation  $E_k - E_j \simeq \frac{\Delta m_{kj}^2}{2E}$  can be done, where  $\Delta m_{kj}^2 = m_k^2 - m_j^2$  and  $E = |\vec{p}|$  are obtained neglecting the neutrino mass. Since in the experiments the distance between the neutrino source and the detector  $L$  is measured but not the neutrino time of propagation, in the ultra-relativistic limit the approximation  $t = L$  holds, leading to

$$P_{\nu_\alpha \rightarrow \nu_\beta}(L, E) = \sum_{k,j} U_{\alpha k}^* U_{\beta k} U_{\alpha j} U_{\beta j}^* e^{-i \frac{\Delta m_{kj}^2 L}{2E}} \quad (1.7)$$

The oscillation phase is determined by the mass squared difference  $\Delta m_{kj}^2$  between different neutrino mass eigenstates. If neutrinos oscillates  $\Delta m_{kj}^2$  must be larger than zero because the time propagation of the three mass eigenstates are different from each other. The oscillation amplitude is determined only by the mixing matrix  $U$ . The product  $U_{\alpha k}^* U_{\beta k} U_{\alpha j} U_{\beta j}^*$  is invariant under a phase rotation and does not depend on the parametrization of the mixing matrix. Exploiting the unitarity of  $U$ ,  $\sum_k U_{\alpha k} U_{\beta k}^* = \delta_{\alpha\beta}$ , the oscillation probability of active neutrinos traveling in vacuum can be written as

$$\begin{aligned}
P_{\nu_\alpha \rightarrow \nu_\beta}(L, E) = & \delta_{\alpha\beta} - 4 \sum_{k>j} \text{Re} [U_{\alpha k}^* U_{\beta k} U_{\alpha j} U_{\beta j}^*] \sin^2 \left( \frac{\Delta m_{kj}^2 L}{4E} \right) \\
& + 2 \sum_{k>j} \text{Im} [U_{\alpha k}^* U_{\beta k} U_{\alpha j} U_{\beta j}^*] \sin \left( \frac{\Delta m_{kj}^2 L}{2E} \right)
\end{aligned} \tag{1.8}$$

for neutrinos and

$$\begin{aligned}
P_{\nu_\alpha \rightarrow \nu_\beta}(L, E) = & \delta_{\alpha\beta} - 4 \sum_{k>j} \text{Re} [U_{\alpha k}^* U_{\beta k} U_{\alpha j} U_{\beta j}^*] \sin^2 \left( \frac{\Delta m_{kj}^2 L}{4E} \right) \\
& - 2 \sum_{k>j} \text{Im} [U_{\alpha k}^* U_{\beta k} U_{\alpha j} U_{\beta j}^*] \sin \left( \frac{\Delta m_{kj}^2 L}{2E} \right)
\end{aligned} \tag{1.9}$$

for antineutrinos, obtained by replacing  $U$  with  $U^*$ .

The PMNS mixing matrix is

$$\begin{aligned}
U = & \begin{pmatrix} 1 & 0 & 0 \\ 0 & c_{23} & s_{23} \\ 0 & -s_{23} & c_{23} \end{pmatrix} \begin{pmatrix} c_{13} & 0 & s_{13}e^{-i\delta_{CP}} \\ 0 & 1 & 0 \\ -s_{13}e^{i\delta_{CP}} & 0 & c_{13} \end{pmatrix} \begin{pmatrix} c_{12} & s_{12} & 0 \\ -s_{12} & c_{12} & 0 \\ 0 & 0 & 1 \end{pmatrix} \begin{pmatrix} 1 & 0 & 0 \\ 0 & e^{i\lambda_2} & 0 \\ 0 & 0 & e^{i\lambda_3} \end{pmatrix} \\
= & \begin{pmatrix} c_{12}c_{13} & s_{12}c_{13} & s_{13}e^{-i\delta_{CP}} \\ -s_{12}c_{23} - c_{12}s_{23}s_{13}e^{i\delta_{CP}} & c_{12}c_{23} - s_{12}s_{23}s_{13}e^{i\delta_{CP}} & s_{23}c_{13} \\ s_{12}s_{23} - c_{12}c_{23}s_{13}e^{i\delta_{CP}} & -c_{12}s_{23} - s_{12}c_{23}s_{13}e^{i\delta_{CP}} & c_{23}c_{13} \end{pmatrix}
\end{aligned} \tag{1.10}$$

where  $s_{ij} \equiv \sin \theta_{ij}$  and  $c_{ij} \equiv \cos \theta_{ij}$ ,  $\theta_{ij}$  are the three mixing angles and  $\delta_{CP}$  is the CP violating phase.  $\lambda_i$  are the Majorana phases, physically relevant only if neutrinos are Majorana, but in any case they do not have any effect on the oscillation probability. Hence the neutrino oscillation probability between the three active states is determined by six parameters: the mixing angles  $\theta_{12}$ ,  $\theta_{13}$ ,  $\theta_{23}$ , the mass squared differences  $\Delta m_{21}^2 = m_2^2 - m_1^2$ ,  $\Delta m_{32}^2 = m_3^2 - m_2^2$  and the CP violating phase  $\delta_{CP}$ .  $L$  is the neutrino travelled distance and  $E$  is the neutrino energy. Depending on the *mass hierarchy*, i.e. the neutrino mass ordering,  $m_3 > m_2 > m_1$  is denoted by  $\Delta m_{32}^2$  and is called *normal mass hierarchy*, while the case  $m_2 > m_1 > m_3$  is denoted by  $\Delta m_{13}^2$  and is called *inverted mass hierarchy*. It has been observed that  $m_2^2 > m_1^2$ . The mass squared difference defines the value of  $\frac{L}{E}$  at which neutrino oscillations occur as well as the frequency of the oscillations.

If only two of the three active neutrinos are considered, for example  $\nu_\mu \rightarrow \nu_e$ , the oscillation probability becomes

$$P(\nu_\mu \rightarrow \nu_e) = \sin^2 2\theta \sin^2 \left( \frac{\Delta m^2 L}{4E} \right) \tag{1.11}$$

where  $\sin^2 2\theta$  defines the oscillation amplitude and  $\Delta m^2 = m_2^2 - m_1^2$ . If  $\alpha \neq \beta$  the transition  $\nu_\alpha \rightarrow \nu_\beta$  is called neutrino *appearance*, since neutrinos of a different flavor from the produced ones are observed. While if  $\alpha = \beta$  the transition probability describes the disappearance of neutrinos, given by

$$P(\nu_\mu \rightarrow \nu_\mu) = 1 - \sin^2 2\theta \sin^2 \left( \frac{\Delta m^2 L}{4E} \right) \tag{1.12}$$



which is called *survival* probability because the number of neutrinos that did not disappear is observed.

CPT transformations are invariant and the following equality is satisfied:

$$P(\nu_\alpha \rightarrow \nu_\beta) = P(\bar{\nu}_\beta \rightarrow \bar{\nu}_\alpha) \quad (1.13)$$

As it can be seen by comparing eq. 1.8 and eq. 1.9 the neutrino and antineutrino oscillations differ by a sign in the second term, the imaginary part of the formula. As a consequence, if  $\delta_{CP} \neq 0$  we get

$$P(\nu_\alpha \rightarrow \nu_\beta) \neq P(\bar{\nu}_\alpha \rightarrow \bar{\nu}_\beta) \quad (1.14)$$

that means CP is violated. Looking to eq. 1.10 it is clear that, in order to have effects of CP violation, all the three mixing angles must be non-zero.

### 1.2.1 Matter effects

Neutrinos propagating in matter are affected by a potential due to the coherent forward elastic scattering with the particles in the medium (electrons and nucleons). This potential is equivalent to an index of refraction and modifies the oscillation probability [28].

Since neutrinos interact in matter with  $e, p$  or  $n$ , they can have coherent forward elastic scattering through neutral current interactions (e.g.  $\nu_X + n \rightarrow \nu_X + n$ ), relevant for all the neutrino flavors, and charged current interactions ( $\nu_e + e^- \rightarrow \nu_e + e^-$ ) relevant only for  $\nu_e$ . Since neutral current gives a phase common to all flavors the electron neutrinos have an additional potential, responsible for the *matter effect*. It is interesting to note that neutrinos in matter are affected also by incoherent scatterings with the particles in the medium. However, it has an extremely small effect and can be neglected in neutrino oscillation experiments.

We can include matter effects in the neutrino oscillations starting from the Shroedinger equation, expanding the Hamiltonian in vacuum  $H$ :

$$i \frac{d}{dt} |\nu_\alpha\rangle = (H + V) |\nu_\alpha\rangle \quad (1.15)$$

where

$$H = \frac{1}{2E} U \begin{pmatrix} 0 & 0 & 0 \\ 0 & \Delta m_{21}^2 & 0 \\ 0 & 0 & \Delta m_{31}^2 \end{pmatrix} \quad (1.16)$$

and

$$V = \begin{pmatrix} V_{CC} & 0 & 0 \\ 0 & 0 & 0 \\ 0 & 0 & 0 \end{pmatrix} \quad (1.17)$$

$V_{CC}$  is defined as

$$V_{CC} = \pm \sqrt{2} G_F N_e \quad (1.18)$$

where  $G_F$  is the Fermi constant,  $N_e$  is the matter electron density,  $+$  is for neutrinos and  $-$  for antineutrinos.

For simplicity we consider oscillations in the two neutrino approximation eq. 1.11. The mixing angle which defines the transition  $\nu_\alpha \rightarrow \nu_\beta$  is given by

$$\tan 2\theta_M = \frac{\tan 2\theta}{1 - \frac{A_{CC}}{\Delta m^2 \cos 2\theta}} \quad (1.19)$$

and the effective mass squared difference is

$$\Delta m_M^2 = \sqrt{(\Delta m^2 \cos 2\theta - A_{CC})^2 + (\Delta m^2 \sin 2\theta)^2} \quad (1.20)$$

where  $A_{CC} \equiv 2 E V_{CC}$  and is positive in normal matter.

The interesting phenomenon called Mikheev-Smirnov-Wolfenstein effect (MSW) [29, 30] admits a resonance when

$$A_{CC}^R = \Delta m^2 \cos 2\theta \quad (1.21)$$

for which the effective mixing is maximal, i.e.  $\theta$  is equal to  $\pi/4$ , making possible a total transition between the two flavors if the resonance region is wide enough.

An analogue result can be obtained for antineutrino oscillations  $\bar{\nu}_\alpha \rightarrow \bar{\nu}_\beta$  by changing  $N_e$  with  $(-N_e)$ . However the presence of matter can enhance either the  $\nu_\alpha \rightarrow \nu_\beta$  or  $\bar{\nu}_\alpha \rightarrow \bar{\nu}_\beta$  oscillations but not both. For instance if  $\Delta m^2 \cos 2\theta < 0$  only  $\bar{\nu}_\alpha \rightarrow \bar{\nu}_\beta$  oscillations are enhanced, while  $\nu_\alpha \rightarrow \nu_\beta$  oscillations are suppressed. This difference between neutrinos and antineutrinos is a consequence of the fact that the matter in the Sun or in the Earth contains  $e^-$ ,  $p$  and  $n$ , but does not contain their antiparticles. Therefore the oscillations in matter are neither CP- nor CPT- invariant. It is also clear that if neutrino oscillations are strongly affected by matter effects, it becomes possible to measure the sign of  $\Delta m^2$ , by comparing neutrino and antineutrino oscillations.

### 1.2.2 Approximated oscillation probabilities

The oscillation probability depends on the neutrino travelled distance  $L$  and true energy  $E$ . Thus the effect of oscillations can be different from experiment to experiment.

In the limit  $|\Delta m_{32}^2| \gg |\Delta m_{21}^2|$  the  $\nu_\mu \rightarrow \nu_\mu$  survival probability can be written as

$$P(\nu_\mu \rightarrow \nu_\mu) \simeq 1 - (\sin^2 2\theta_{23} \cos^4 \theta_{13} + \sin^2 \theta_{23} \sin^2 2\theta_{13}) \sin^2 \left( \frac{\Delta m_{32}^2 L}{4E} \right) \quad (1.22)$$

Since  $\theta_{13} < 10^\circ$  (see sec. 1.4), the leading term corresponds to  $\sin^2 2\theta_{23} \cos^4 \theta_{13}$  and has the degenerate solutions

$$\sin^2 \theta_{23} = \left[ 1 \pm \sqrt{1 - \sin^2 2\theta_{23}} \right] / 2$$

in the first and second octant, respectively  $\theta_{23} > \pi/4$  and  $\theta_{23} < \pi/4$ . At the first order the 2-flavors approximation of eq. 1.12 works.

The maximal mixing occurs when

$$\sin^2 \theta_{23}^{Max} = \frac{1}{2 \cos^2 \theta_{13}} \quad (1.23)$$

For a non-zero value of  $\theta_{13}$ ,  $\sin^2 \theta_{23}^{Max}$  is no longer equal to 0.5, but strongly depends on the value of  $\theta_{13}$ .

Below the approximated oscillation probabilities of the  $\nu_\mu \rightarrow \nu_e$  transition is shown with the first and second leading terms

$$P(\nu_\mu \rightarrow \nu_e) \simeq \sin^2 \theta_{23} \sin^2 \theta_{13} \sin^2 \left( \frac{\Delta m_{31}^2 L}{4E} \right) - \frac{\sin 2\theta_{12} \sin 2\theta_{23}}{2 \sin \theta_{13}} \sin \left( \frac{\Delta m_{21}^2 L}{4E} \right) \sin^2 2\theta_{13} \sin \left( \frac{\Delta m_{31}^2 L}{4E} \right) \sin \delta_{CP} \quad (1.24)$$

The measurement of  $P(\nu_\mu \rightarrow \nu_e)$  oscillations is of particular interest because it is sensitive to both  $\theta_{13}$  and  $\delta_{CP}$ . Since the probability depends on  $\sin^2 \theta_{23}$  the appearance channel is also sensitive to the determination of the  $\theta_{23}$  octant.

The electron neutrino appearance probability also includes sub-leading terms which depend on CP and terms that describe matter interactions [31]:

$$P(\nu_\mu \rightarrow \nu_e) = \frac{1}{(A-1)^2} \sin^2 2\theta_{13} \sin^2 \theta_{23} \sin^2 [(A-1)\Delta] \pm \frac{\alpha}{A(1-A)} \cos \theta_{13} \sin 2\theta_{12} \sin 2\theta_{23} \sin 2\theta_{13} \times \sin \delta_{CP} \sin \Delta \sin A\Delta \sin [(1-A)\Delta] + \frac{\alpha}{A(1-A)} \cos \theta_{13} \sin 2\theta_{12} \sin 2\theta_{23} \sin 2\theta_{13} \times \cos \delta_{CP} \cos \Delta \sin A\Delta \sin [(1-A)\Delta] + \frac{\alpha^2}{A^2} \cos^2 \theta_{23} \sin^2 2\theta_{12} \sin^2 A\Delta \quad (1.25)$$

where  $\alpha = \frac{\Delta m_{21}^2}{\Delta m_{32}^2} \ll 1$ ,  $\Delta = \frac{\Delta m_{32}^2 L}{4E}$  and  $A = 2\sqrt{2}G_F N_e \frac{E}{\Delta m_{32}^2}$

In the three-neutrino paradigm CP violation can only occur when all the three mixing angles, including  $\theta_{13}$ , have non-zero values. The second term has a negative sign for neutrinos and a positive sign for antineutrinos and violates CP, which suggests the possibility of observing CP violation by measuring the difference in the appearance probabilities for electron neutrinos and antineutrinos.  $\delta_{CP}$  appears only in the second and third order terms and, in order to have a non negligible effect, needs  $\theta_{13}$  to be non-zero in order to produce  $\nu_\mu \rightarrow \nu_e$  events, but small because the effect of  $\delta_{CP}$  is approximately proportional to the factor  $\frac{1}{\sin^2 \theta_{13}}$  in the second term, as shown in eq. 1.24.

The  $A$  dependence in the oscillation probability arises from matter effects and, as already shown in sec. 1.2.1, introduces a dependence on the sign of the mass-squared splitting  $\Delta m_{32}^2$  ( $\Delta m_{13}^2$ ). In order to measure the mass hierarchy a neutrino oscillation experiments with a baseline of hundreds or thousands kilometers is required. Indeed the size of the matter effect is proportional to the distance travelled by the neutrino. An experiment such as T2K, with a baseline of 295 km has not a very good sensitivity to the mass hierarchy, since the matter effects account for only about the 10% of the oscillation probability.

### 1.3 Neutrino oscillation experiments

The goal of neutrino oscillation experiments is to measure the parameters of the PMNS matrix (eq. 1.10) and confirm whether it is unitary or not. All the mixing angles and the mass squared

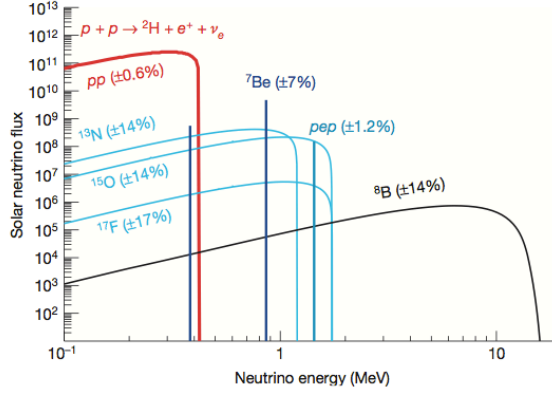


Figure 1.1: Solar neutrino energy spectrum. The flux (vertical scale) is given in  $\text{cm}^{-2}\text{s}^{-1}\text{MeV}^{-1}$  for continuum sources and in  $\text{cm}^{-2}\text{s}^{-1}$  for mono-energetic ones. The quoted uncertainties are from the SSM [57].

differences have been measured. Only the parameter  $\delta_{CP}$  is not measured yet. The discovery of non-zero  $\delta_{CP}$  could be interpreted as a hint of *leptogenesis* as the cause of the matter/antimatter asymmetry. For more details see app. A.3.

In this section all the achievements obtained by the past and current neutrino oscillation experiments will be presented. The oscillation parameters are usually sub-divided into different groups, *solar* ( $\theta_{12}$  and  $\Delta m_{21}^2$ ) and *atmospheric* ( $\theta_{23}$  and  $\Delta m_{32}^2$ ). The first parameters affect oscillations of neutrinos coming from the Sun, while experiments that detect neutrinos produced in the atmosphere are sensitive to the latter parameters. The parameter  $\theta_{13}$  can be measured by accelerator and reactor experiments, while only accelerator experiments that measure  $\bar{\nu}_\mu \rightarrow \bar{\nu}_e$  and  $\nu_\mu \rightarrow \nu_e$  oscillations can measure  $\delta_{CP}$ .

### 1.3.1 Solar neutrino oscillation parameters

Experiments that measure oscillations by observing neutrinos produced in the Sun and that travelled toward the Earth are called *solar neutrino* experiments. Electron neutrinos are produced from nuclear fusion in the nucleus of the Sun mainly by the *pp* reaction

$$p + p \rightarrow {}^2\text{H} + e^+ + \nu_e \quad (1.26)$$

about 99.76% of the times. These neutrinos are not easy to detect because at a very low energy below 420 KeV a detector with a very good energy resolution is needed. They have been directly detected for the first time by the Borexino experiment [48] in 2014.

At higher energy, from 3 to 10 MeV, the dominant nuclear reaction, called  ${}^8\text{B}$  process, is

$${}^8\text{B} \rightarrow {}^8\text{Be}^* + e^+ + \nu_e \quad (1.27)$$

Since neutrinos interact weakly, they can travel uninhibited through the interior of the Sun, and act as probes of the stellar core when measured on the Earth.

Several solar neutrino experiments [49, 50, 51, 52, 53, 54, 55] observed a significant deficit of  $\nu_e$  from the Sun, about 1/3 of the flux predicted by the Standard Solar Model (SSM) [56, 57, 58]. A possible explanation of the so-called “solar neutrino problem” was the phenomenon of neutrino

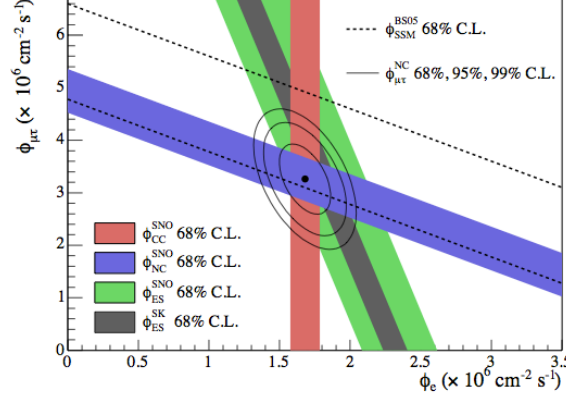


Figure 1.2: Flux of  $\nu_\mu$  and  $\nu_\tau$  versus flux of  $\nu_e$  measured at SNO [59]. CC, NC and ES flux measurements are indicated by the filled bands. The total  $^8\text{B}$  solar neutrino flux predicted by the SSM [58] is represented by the band enclosed by the dashed lines. The total neutrino flux measured with NC interactions is shown as the solid purple band parallel to the model prediction, while the red and green bands correspond respectively to the measured CC and ES interactions. The narrow grey band parallel to the SNO ES result corresponds to the Super-Kamiokande result [60]. The fluxes were measured to be  $\Phi_e = 1.76^{+0.05}_{-0.05}(\text{stat.})^{+0.09}_{-0.09}(\text{syst.})$  and  $\Phi_{\mu\tau} = 3.41^{+0.45}_{-0.45}(\text{stat.})^{+0.48}_{-0.48}(\text{syst.})$ .

oscillations when matter effects are taken into account. The direct proof was given by the Sudbury Neutrino Observatory experiment (SNO), that used heavy water ( $D_2O$ ) to detect the following reactions

$$CC : \nu_e + d \rightarrow p + p + e^- \quad (1.28)$$

$$NC : \nu_\alpha + d \rightarrow p + n + \nu_\alpha \quad (1.29)$$

$$ES : \nu_\alpha + e^- \rightarrow \nu_\alpha + e^- \quad (1.30)$$

The Charged Current (CC) and Elastic Scattering (ES) interactions involve only  $\nu_e$  and were sensitive to neutrino oscillations, while the NC interaction involves all the three flavors and was used to measure the total neutrino flux, because not sensitive to oscillations. A clear deficit of CC interactions, i.e.  $\nu_e$ , was observed, while the rate of NC interactions was in agreement with the prediction of the SSM. A confirmation of neutrino oscillations was given with a significance of  $5.5\sigma$  [59]. In fig. 1.2 the experimental result is shown.

Experiments probing the solar oscillations are affected by a very large  $L/E$ , about 15000 km/GeV, and sensitive to the solar parameters  $\theta_{12}$  and  $\Delta m_{21}^2$ . These parameters are also measured by KamLAND, a reactor experiment with a long baseline of about 1000 km that detects MeV  $\bar{\nu}_e$  produced by the nuclear fission in the nuclear reactors [61].

### 1.3.2 Atmospheric neutrino oscillation parameters

Atmospheric neutrinos are produced by primary cosmic rays, mainly composed of protons and only a small component of heavier nuclei, that interact in the atmosphere and produce secondary cosmic rays, mainly pions and kaons at higher energy, which decay into muon neutrinos as

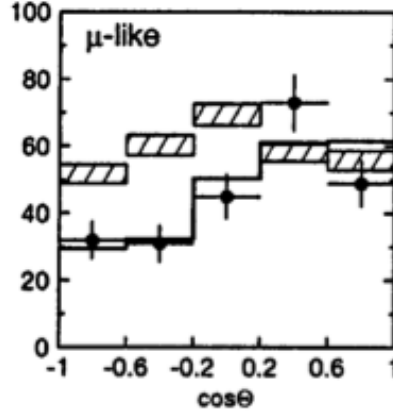


Figure 1.3: Zenith angle distributions of  $\nu_\mu$  candidates with  $p < 2.5$  GeV/c. Downward-going particles have  $\cos \theta > 0$  and upward-going particles have  $\cos \theta < 0$ . The hatched region shows the Monte Carlo expectation for no oscillations normalized to the data live time with statistical errors. The bold line is the best-fit expectation for  $\nu_\mu \rightarrow \nu_\tau$  [10].

following:

$$\pi^+ \rightarrow \mu^+ + \nu_\mu \quad \pi^- \rightarrow \mu^- + \bar{\nu}_\mu \quad (1.31)$$

Then muons can decay into neutrinos as well:

$$\mu^+ \rightarrow e^+ + \nu_e + \bar{\nu}_\mu \quad \mu^- \rightarrow e^- + \bar{\nu}_e + \nu_\mu \quad (1.32)$$

and also  $\nu_e$  are produced. These neutrinos are called *atmospheric* and have energies from about 100 MeV to 100 GeV with a maximum at about 1 GeV. They can be detected through scattering on nuclei in underground laboratories where the muons of secondary cosmic rays are shielded.

Since the cosmic ray flux is isotropic, the resulting neutrino flight length can vary from 10 to  $10^4$  km, corresponding respectively to neutrinos coming from above and below the detector with a certain zenith angle, traveling through the Earth. The oscillation parameters that govern the oscillations of atmospheric neutrinos are  $\theta_{23}$  and  $\Delta m_{32}^2$  and a wide range of  $\Delta m_{32}^2$  from  $10^{-4}$  to  $1 \text{ eV}^2/c^4$  can be scanned. The first evidence of atmospheric neutrino oscillations (and for neutrino oscillations in general) was given by the Super-Kamiokande experiment in 1998, that observed a deficit of upward atmospheric neutrinos with respect to the downward component [10]. As shown in fig. 1.3, differently from up-going neutrinos, the down-going muon neutrinos could not travel enough to oscillate to a different flavor state.

The atmospheric parameters can be also measured by accelerator experiments such as T2K [62] and MINOS [63] that provide respectively the best measurements of  $\theta_{23}$  and  $\Delta m_{32}^2$  by looking for a deficit of events in a  $\nu_\mu$  ( $\bar{\nu}_\mu$ ) beam. The method used to produce a  $\nu_\mu$  ( $\bar{\nu}_\mu$ ) beam with an accelerator will be discussed more in detail in chap. 2.

### 1.3.3 Measurement of $\theta_{13}$ and search for CP violation

The last measured neutrino mixing angle is  $\theta_{13}$ . The T2K collaboration reported in 2011 the observation of a relatively large  $\theta_{13}$  with a significance of  $3\sigma$  [64].

It was measured for the first time with a significance higher than  $5\sigma$  in early 2012 by the Daya Bay experiment [22], a *reactor experiment* with a baseline of about 1 km, which measures disappearance of  $\bar{\nu}_e$  coming from three different reactor cores. Later T2K discovered the  $\nu_\mu \rightarrow \nu_e$  appearance with a  $7.5\sigma$  significance to non-zero  $\theta_{13}$  [23].

The first experiment that started looking for CP violation in the leptonic sector is T2K by observing  $\nu_\mu \rightarrow \nu_e$  appearance. One of the goals of this thesis work is to search for a hint of CP violation by comparing the neutrino and antineutrino oscillations (see sec. 1.2.2).

## 1.4 Status of three-neutrino oscillation parameters

The status of the measurement of the neutrino oscillation parameters of the PMNS matrix in 2012 [32], when this thesis work has started, is shown in this section. One of the goals of this thesis is to improve the knowledge of the PMNS matrix parameters and results shown in fig. 1.4 are taken as reference.

At the time all the oscillation parameter were measured except  $\delta_{CP}$ : though limits at  $1\sigma$  level were provided, none of the possible values was excluded with a significance of  $3\sigma$ . The value of  $\theta_{13}$  is dominated by the measurement of Daya Bay, that measured it with a precision better than  $5\sigma$  (see sec. 1.3.3). Non-maximal  $\theta_{23}$  is favored at the level of  $\sim 2\sigma$  ( $\sim 1.5\sigma$ ) for NH (IH) and the first octant is slightly preferred, though the significance is pretty low. The combination of data from reactor experiments, that constrain  $\theta_{13}$  very well, with accelerator and in particular atmospheric experiments, such as Super-Kamiokande, offers some sensitivity to the CP phase: a statistical significance at the level of  $1.7\sigma$  is found and a preference is given to  $\delta_{CP} = 300^\circ$  ( $-1.05$  rad). The  $\Delta\chi^2$  between the minimum of  $\delta_{CP}$  and the less likely value is  $\sim 2$  for NH and less than 3 for IH. The global fit does not give any significant result for what concern the mass hierarchy. Both neutrino mass orderings (normal and inverted hierarchies) provide a fit of very similar quality to the global data, with  $\Delta\chi^2 \sim 0.5$ . In fig. 1.5 the  $\Delta\chi^2$  distributions for all the oscillation parameters are shown.

The analysis of the T2K data will allow to improve the sensitivity to  $\delta_{CP}$ , since for the first time both neutrino and antineutrino oscillations will be measured. Furthermore an improvement on the measured values of  $\theta_{23}$  and  $\Delta m_{32}^2$  is expected by analyzing the samples of  $\nu_\mu$  and  $\bar{\nu}_\mu$  candidates. The parameters that cannot be improved by the T2K data are  $\theta_{13}$ , since the reactor experiments can collect much more statistics and perform more precise measurements than accelerator experiments, and  $\theta_{12}$  as well as  $\Delta m_{12}^2$ , for which a baseline 10-20 times longer is needed.

## 1.5 Hints of light sterile neutrinos

The number of active neutrino flavors has been measured at LEP with very high precision to be  $2.984 \pm 0.008$  [34] by measuring the  $Z$  production in  $e^+e^-$  collisions as shown in fig. 1.6.

However there exist several anomalies in short-baseline neutrino oscillation experiments that can be interpreted as the existence of right-handed sterile neutrinos, which number could not be measured at LEP. These anomalies are compatible with oscillations from active to sterile neutrinos with a mass squared splitting of the order of  $1 \text{ eV}^2/c^4$ . A comprehensive review of the status of the art of sterile neutrinos can be found in [67, 68].

The first anomaly is the so-called *LSND signal*. A  $\sim 3\sigma$  excess of detected  $\bar{\nu}_e$  and  $\nu_e$  candidates in a  $\nu_\mu / \bar{\nu}_\mu$  beam, that might be explained as a short baseline oscillation due to

	Free Fluxes + RSBL		Huber Fluxes, no RSBL	
	bfp $\pm 1\sigma$	$3\sigma$ range	bfp $\pm 1\sigma$	$3\sigma$ range
$\sin^2 \theta_{12}$	$0.302^{+0.013}_{-0.012}$	$0.267 \rightarrow 0.344$	$0.311^{+0.013}_{-0.013}$	$0.273 \rightarrow 0.354$
$\theta_{12}/^\circ$	$33.36^{+0.81}_{-0.78}$	$31.09 \rightarrow 35.89$	$33.87^{+0.82}_{-0.80}$	$31.52 \rightarrow 36.49$
$\sin^2 \theta_{23}$	$0.413^{+0.037}_{-0.025} \oplus [0.594^{+0.021}_{-0.022}]$	$0.342 \rightarrow 0.667$	$0.416^{+0.036}_{-0.029} \oplus [0.600^{+0.019}_{-0.026}]$	$0.341 \rightarrow 0.670$
$\theta_{23}/^\circ$	$40.0^{+2.1}_{-1.5} \oplus [50.4^{+1.3}_{-1.3}]$	$35.8 \rightarrow 54.8$	$40.1^{+2.1}_{-1.6} \oplus [50.7^{+1.2}_{-1.5}]$	$35.7 \rightarrow 55.0$
$\sin^2 \theta_{13}$	$0.0227^{+0.0023}_{-0.0024}$	$0.0156 \rightarrow 0.0299$	$0.0255^{+0.0024}_{-0.0024}$	$0.0181 \rightarrow 0.0327$
$\theta_{13}/^\circ$	$8.66^{+0.44}_{-0.46}$	$7.19 \rightarrow 9.96$	$9.20^{+0.41}_{-0.45}$	$7.73 \rightarrow 10.42$
$\delta_{CP}/^\circ$	$300^{+66}_{-138}$	$0 \rightarrow 360$	$298^{+59}_{-145}$	$0 \rightarrow 360$
$\frac{\Delta m_{21}^2}{10^{-5} \text{ eV}^2}$	$7.50^{+0.18}_{-0.19}$	$7.00 \rightarrow 8.09$	$7.51^{+0.21}_{-0.15}$	$7.04 \rightarrow 8.12$
$\frac{\Delta m_{31}^2}{10^{-3} \text{ eV}^2} \text{ (N)}$	$+2.473^{+0.070}_{-0.067}$	$+2.276 \rightarrow +2.695$	$[+2.489^{+0.055}_{-0.051}]$	$+2.294 \rightarrow +2.715$
$\frac{\Delta m_{32}^2}{10^{-3} \text{ eV}^2} \text{ (I)}$	$[-2.427^{+0.042}_{-0.065}]$	$-2.649 \rightarrow -2.242$	$-2.468^{+0.073}_{-0.065}$	$-2.678 \rightarrow -2.252$

Figure 1.4: Three-flavour oscillation parameters from the global fit performed on the data sets released until 2012 [32]. For “Free Fluxes + RSBL” reactor fluxes have been left free in the fit and short baseline reactor data (RSBL) with  $L < 100$  m are included; for “Huber Fluxes, no RSBL” the flux prediction from [33] are adopted and RSBL data are not used in the fit. Both the  $\pm 1\sigma$  and  $3\sigma$  ranges are shown.

mixing with the sterile mass states, was seen by both the LSND [69] and the MiniBooNE [70] experiments.

Another anomaly consists of a deficit in the  $\bar{\nu}_e$  flux produced by reactors that has been measured by several short baseline detectors. It is called *reactor anomaly* and could be interpreted as  $\bar{\nu}_e \rightarrow \nu_s$  disappearance (see eq. 1.33). Until late 2010 all the data from reactor neutrino experiments appeared to be fully consistent with the standard three neutrino framework but in 2010 a more reliable re-evaluation of the reactor anti-neutrino flux slightly increased the predicted fluxes [71]. The effect of this analysis was that all these experiments show a deficit of electron neutrinos of about  $3\sigma$  consistent with the parameter values  $\sin^2 2\theta_{ee} \sim 0.15$  and  $\Delta m_{41}^2 \sim 1 \text{ eV}^2$  [72]. Another possible explanation is that the nuclear processes, involved in the production of  $\bar{\nu}_e$  in the reactors, are not well understood and the uncertainties are underestimated [73].

A third anomaly that can be interpreted as a short baseline  $\bar{\nu}_e$  disappearance is the *Gallium anomaly*. It is due to the GALLEX [50] and SAGE [51, 52] experiments that tested the  $\nu_e$  flux of intense artificial  $^{51}\text{Cr}$  and  $^{37}\text{Ar}$  sources at the center of their cylindrical detector, with an average distance of 1.9 m and 0.6 m respectively, by observing  $\nu_e + {}^{71}\text{Ga} \rightarrow {}^{71}\text{Ge} + e^-$  reactions. In both the experiments the ratios of the measured interactions is smaller than the prediction. The deficit has a significance of about  $2.7\sigma$  and is consistent with the reactor anomaly. The global fit of the reactor and gallium anomalies as well as the results from other experimental data set is shown in eq. 1.7.

However, since there is no evidence of short baseline  $\nu_\mu \rightarrow \nu_s$  disappearance [74], the LSND signal and the reactor plus gallium anomalies show a strong tension and at least some of the hints could not be real. This tension does not vanish even considering models with more than one sterile neutrinos [68, 75, 76].



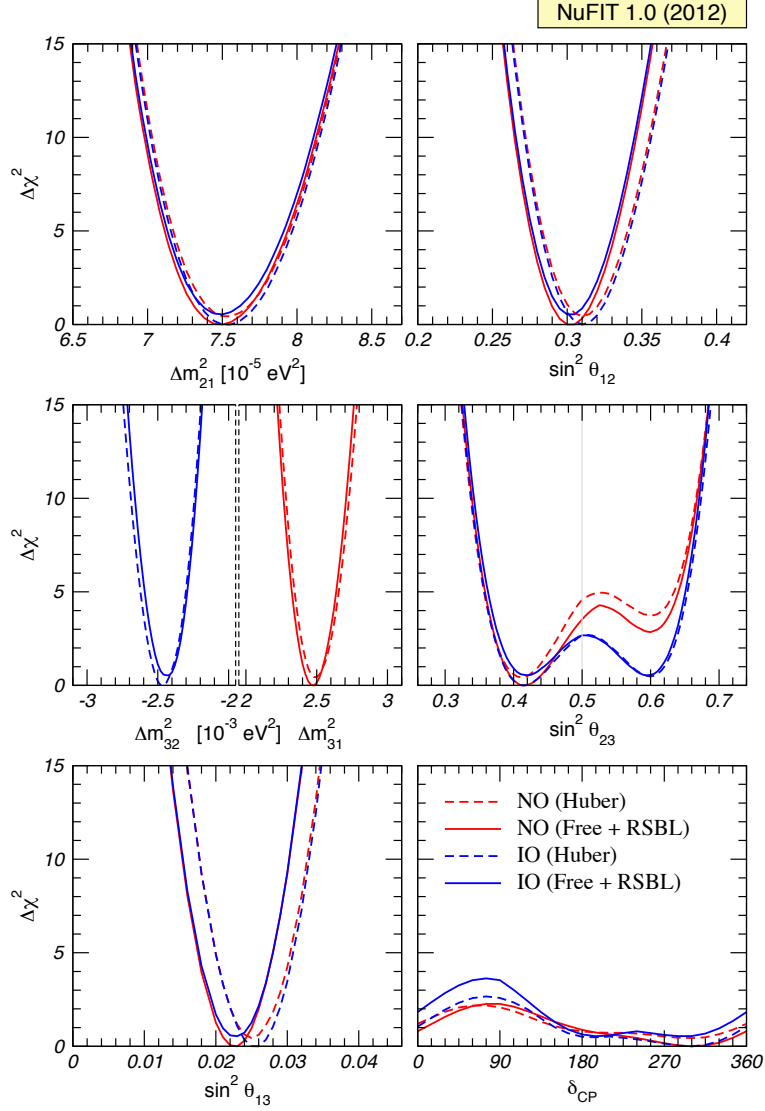


Figure 1.5: Global 3-flavor oscillation analysis on the data sets released until 2012 [32]. The red (blue) curves are for Normal (Inverted) Hierarchy. Results for different assumptions concerning the analysis of data from reactor experiments are shown: for solid curves the normalization of reactor fluxes is left free and data from short-baseline (less than 100 m) reactor experiments are included. For dashed curves short-baseline data are not included but reactor fluxes as predicted in [33] are assumed. As atmospheric mass-squared splitting the notation uses  $\Delta m_{31}^2$  for NH and  $\Delta m_{32}^2$  for IH.

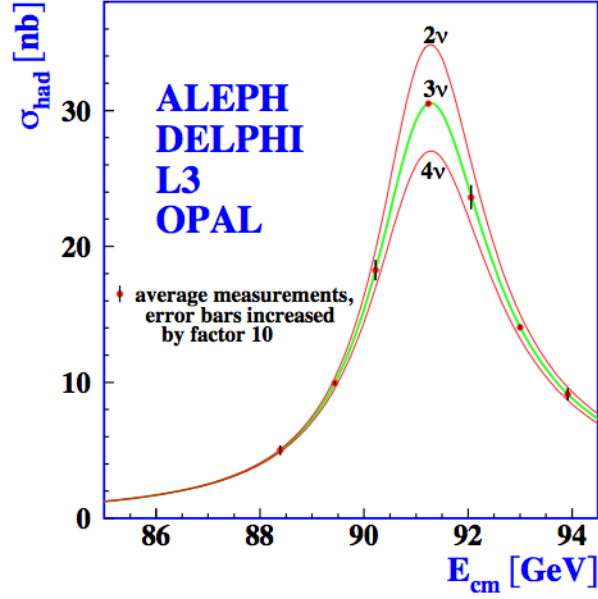


Figure 1.6: Measurements of the hadron production cross-section around the Z resonance [34]. The curves indicate the predicted cross-section for two, three and four neutrino species with SM couplings and negligible mass.

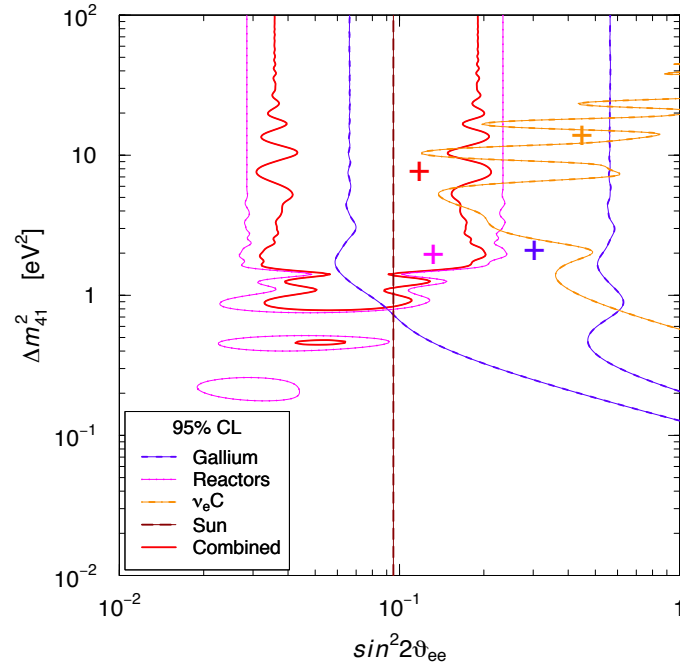


Figure 1.7: Allowed regions of gallium and reactor anomalies and excluded regions by  $\nu_e$ -carbon interaction data and solar neutrino data at 95% confidence level in the  $\sin^2 2\theta_{ee} - \Delta m^2_{41}$  parameters space [72]. Another analogous global fit result can be found in [68].

More details about sterile neutrinos and the theoretical models that could involve are presented in app. A.4.

## 1.6 Sterile neutrino oscillations

Sterile neutrino oscillations can be described by the analogous of eq. 1.8 extended to  $3 + N_S$  flavors, where  $N_S$  is the number of additional sterile neutrinos, that means the  $3 \times 3$  PMNS matrix of eq. 1.10 is not unitary any longer. The neutrino mass eigenstates are  $\nu_1, \dots, \nu_{3+S}$ . We assume that the  $S$  linear combinations of mass states, which are orthogonal to the three flavor states participating in weak interactions, are singlets and have no interaction with Standard Model particles. Oscillation physics is described by a rectangular matrix  $U_{\alpha i}$  with  $\alpha = e, \mu, \tau$  and  $i = 1, \dots, 3+S$ . Besides there are some experimental anomalies that could be associated to sterile neutrinos with a mass of the order of 1 eV. The sterile neutrinos that could be responsible for the mass generation in the see-saw model (see app. A.2 and app. A.4) are too massive and cannot be generated. Since, as shown in sec. 1.5, there are tensions between different experiments and the addition of more than one sterile neutrino does not improve the agreement, the description of the oscillation probability will be limited to one more sterile neutrino, which is the simplest extension of the framework. The eigenstate  $\nu_4$  provides the mass squared difference  $\Delta m_{41}^2 = m_4^2 - m_1^2$  much larger than  $\Delta m_{32}^2$  and  $\Delta m_{12}^2$ . In the 3+1 model the oscillation probability is invariant under CP transformations. This is not true any longer once more than one additional mass eigenstate are taken into account.

In the short-baseline limit of the 3+1 scenario, the only relevant parameter is  $|U_{e4}|$ . and the  $\nu_e$  survival probability takes an effective two flavor form

$$P(\nu_e^{(-)} \rightarrow \nu_e^{(-)}) = 1 - \sin^2 2\theta_{ee} \sin^2 \left( \frac{\Delta m_{41}^2 L}{4E} \right) \quad (1.33)$$

where  $\sin^2 2\theta_{ee}$  is an effective mixing angle defined as

$$\sin^2 2\theta_{ee} \equiv 4|U_{e4}|^2(1 - |U_{e4}|^2) \quad (1.34)$$

Using the specific parametrization in [35] we get  $\theta_{ee} \equiv \theta_{14}$ . In an analogous way we can write the  $\nu_\mu \rightarrow \nu_\mu^{(-)}$  disappearance probability, where instead of  $\sin^2 2\theta_{ee}$  we find  $\sin^2 2\theta_{\mu\mu} \equiv 4|U_{\mu4}|^2(1 - |U_{\mu4}|^2)$ .

The appearance probability  $\nu_\mu \rightarrow \nu_s \rightarrow \nu_e$  for short-baseline experiments can be written in the two neutrino approximation:

$$P(\nu_\mu^{(-)} \rightarrow \nu_e^{(-)}) \simeq \sin^2 2\theta_{\mu e} \sin^2 \left( \frac{\Delta m_{41}^2 L}{4E} \right) \quad (1.35)$$

where the effective mixing angle is defined as

$$\sin^2 2\theta_{\mu e} \equiv 4|U_{\mu4}|^2|U_{e4}|^2 \quad (1.36)$$

and neglecting the terms  $|U_{\alpha 4}|^4$  becomes

$$\sin^2 2\theta_{\mu e} \simeq \sin^2 2\theta_{ee} \sin^2 2\theta_{\mu\mu} \quad (1.37)$$

In this thesis a search of sterile neutrinos by looking for short baseline oscillations will be shown.

## 1.7 Motivations of the thesis work

From the previous paragraphs we have seen that neutrino oscillations are messengers of new physics, since they imply that neutrinos have mass, and a better knowledge of their properties can help to solve some of the most fundamental problems. Different scenarios can be studied at T2K by measuring both short and long baseline oscillations. The goal of this thesis is to improve the knowledge of neutrino oscillations.

First a search for a light sterile neutrinos in the 3+1 model with a mass splitting  $1 \lesssim |\Delta m_{41}^2| \lesssim 100 \text{ eV}^2/c^4$  is performed. In particular the reactor and gallium anomalies are tested by searching for short baseline  $\nu_e$  disappearance in the  $\nu_e$  intrinsic beam at the T2K near detector. This is also a way to test the unitarity of the PMNS matrix.

The following step is the measurement of the 3-flavor neutrino oscillation parameters. First the search of  $\bar{\nu}_\mu \rightarrow \bar{\nu}_e$  appearance, expected by the 3-neutrino oscillation probability but never observed so far. Then the sensitivity to  $\delta_{CP}$  is improved by combining neutrino and antineutrino data sets and comparing  $\nu_\mu \rightarrow \nu_e$  and  $\bar{\nu}_\mu \rightarrow \bar{\nu}_e$  oscillations. This is the first time such a measurement is performed. A precise measurements of the atmospheric parameters is performed as well. The presented measurements will be discussed in the light of the status of the measured oscillation parameters when this thesis work has started.

Since for a precise measurement of neutrino oscillations a very good knowledge of the predicted flux is required, the first part of the thesis work is focused on the measurement of the proton carbon hadron production performed with the NA61/SHINE experiment, needed for a drastic reduction of the T2K neutrino flux systematic uncertainties.

## Chapter 2

# The T2K experiment

T2K (Tokai-to-Kamioka) is a long-baseline neutrino experiment based in Japan that aims to measure the parameters of the PMNS matrix and to look for the first indication of CP violation in the leptonic sector by measuring  $\nu_\mu$  ( $\bar{\nu}_\mu$ ) disappearance and  $\nu_e$  ( $\bar{\nu}_e$ ) appearance in a  $\nu_\mu$  ( $\bar{\nu}_\mu$ ) beam [84]. The muon neutrino beam is produced by the J-PARC proton accelerator in Tokai, about 100 km north-west of Tokyo, by proton-carbon interactions with a nominal proton momentum of 31 GeV/c. The neutrino beam is detected by a near detector complex at  $\sim 280$  m from the neutrino source, that consists of an on-axis (INGRID) and an off-axis (ND280) detector, and a far detector (Super-Kamiokande) with a long baseline of about 295 km. The neutrino oscillations are inferred by comparing the measured neutrino spectra at the near and far detectors. The neutrino beam is produced with a beamline which direction is  $2.5^\circ$  off the axis between the target and the far detector. This configuration produces a narrow-band beam with a peak energy of about 0.6 GeV which is exactly on the first  $\nu_\mu \rightarrow \nu_e$  oscillation maximum and the background to the  $\nu_e$  appearance signal is dramatically reduced (see sec. 2.1.3).

The T2K experiment started taking data in 2010 with a muon neutrino beam and from May 2014 with a muon antineutrino beam.



Figure 2.1: Schematic of a neutrino's journey from the neutrino beamline at J-PARC to Super-Kamiokande, passing through ND280.

T2K has already reached many achievements:

- observation for the first time of non-zero  $\theta_{13}$  with a significance of about  $3\sigma$  [64] in 2011,
- discovery of  $\nu_\mu \rightarrow \nu_e$  appearance with a significance of  $7.3\sigma$  to non-zero  $\theta_{13}$  [23],

- world best measurement of  $\sin^2 \theta_{23}$  [62].

The future goals of T2K are the improvement of the measurement of the atmospheric oscillation parameters  $\Delta m_{32}^2$  and  $\sin^2 \theta_{23}$ , the first observation of  $\bar{\nu}_\mu \rightarrow \bar{\nu}_e$  appearance as well as finding the first hint of CP violation in the leptonic sector and searches for exotic physics, like sterile neutrinos.

## 2.1 The beam line

A muon neutrino beam is produced at the J-PARC Main Ring (MR) accelerator which provides a 30 GeV proton beam interacting on a graphite target. The collisions produce hadrons, mainly charged pions and kaons, that further decay into  $\nu_\mu$  with a contamination of  $\nu_e$  below 1%.

J-PARC consists of a linear accelerator (LINAC), a rapid-cycling synchrotron (RCS) and the main ring (MR) synchrotron. A beam of Hydrogen ions ( $H^-$ ) is accelerated up to 181 MeV by the LINAC and at the RCS injection is converted to a  $H^+$  beam by charge-stripping foils. Then it is accelerated up to 3 GeV by the RCS and up to 30 GeV, after being injected in the MR, where the number of extracted bunches is eight (six before June 2010). The T2K beamline consists of a primary beamline, where the protons are extracted, and a secondary beamline, where the protons interact in the carbon target, producing hadrons (mainly pions and kaons) that further decay into neutrinos. The J-PARC accelerator complex is shown in fig. 2.2



Figure 2.2: Layout of the accelerator complex at J-PARC.

### 2.1.1 Primary beamline

In the primary beamline protons are first tuned with a serie of 11 conducting magnets, then bent toward the far detector using 14 doublets of superconducting combined function magnets (SCFMs) and eventually focused by 10 conducting magnets (four steering, two dipole and four quadrupole magnets) guide onto the target. The intensity, position, profile and loss of the proton beam are precisely monitored by five current transformers (CTs), 21 electrostatic monitors (ESMs), 19 segmented secondary emission monitors (SSEMs) and 50 beam loss monitors (BLMs).

### 2.1.2 Secondary beamline

The secondary beamline consists of a target station, a decay volume and a beam dump, as shown in fig. 2.3.

The target station is connected upstream to the primary beamline by a window including two helium-cooled 0.3 mm thick titanium-alloy skins and is composed by a baffle, an optical transition radiation monitor, that measures the beam profile with a precision of  $\mu m$ , the graphite target and three magnetic horns. Everything is located inside a helium vessel in order to reduce pion absorption and to suppress tritium and  $NO_x$  production by the beam. The target is 91.4 cm long (1.9 interaction length), 2.6 cm diameter and 1.8 g/cm<sup>3</sup> and is cooled by helium gas. Each of the three horns consist of two coaxial (inner and outer) conductors which surround a closed volume and are optimized to maximize the neutrino flux at the spectrum peak of 0.6 GeV. The +250 kA current pulses magnetize the horns to focus the secondary  $\pi^+$ 's (*neutrino mode*), The  $\pi^-$ 's are focused by inverting the polarity of the horn current (*antineutrino mode*). The maximum field is 2.1 T, achieved with an operation current of 320 kA.

The produced hadrons enter the 96 m long decay volume, surrounded by 6 m thick reinforced concrete shielding, and decay mainly into muons and muon neutrinos. All the hadrons as well as the muons below 5 GeV/c are stopped by a 3.174 m long beam dump, made of 75 tons of graphite, while the neutrinos travel toward the near and far detectors. The decay volume is filled with helium gas to reduce pion absorption.

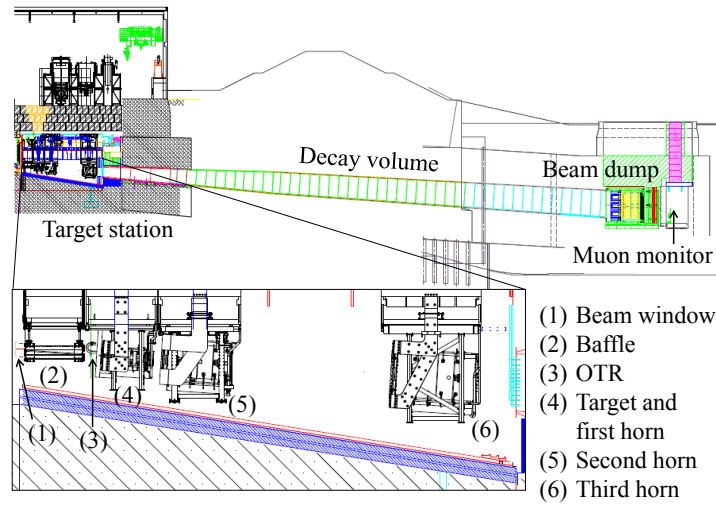


Figure 2.3: Side view of the secondary beamline.

The remaining muons reach the downstream muon pit, where a muon monitor (MUMON) measures the profile and monitors bunch-by-bunch the neutrino beam intensity, its direction with a precision better than 0.25 mrad, and the stability.

The maximum stable current beam power reached so far is 344.9 kW. The goal is to reach in the future about 750 kW by increasing the number of protons per bunch as well as the repetition rate.

### 2.1.3 Off-axis beam

The main feature of the T2K beam is the off-axis configuration [85], used for the first time in T2K. A narrow-band neutrino beam is produced by shifting its direction with respect to Super-Kamiokande by an angle  $\theta_{OA}$ , called “off-axis” angle. Considering the two-body decay  $\pi^+ \rightarrow \mu^+ + \nu_\mu$ , the energy of the neutrino can be written as a function of the off-axis angle with respect to the pion direction:

$$E_\nu = \frac{m_\pi^2 - m_\mu^2}{2(E_\pi - P_\pi \cos \theta_{OA})} \quad (2.1)$$

In fig. 2.3 the neutrino flux energy is shown for different off-axis angles. In order to maximize the sensitivity to  $\nu_\mu$  disappearance and  $\nu_e$  appearance at 295 km, the angle  $\theta_{OA} = 2.5^\circ$  was chosen in order to obtain the peak of the energy distribution at about 0.6 GeV, at the expected first oscillation maximum. This configuration reduces the fraction of high energy background events, in particular neutral current (NC) that can be misidentified as  $\nu_e$  when a  $\pi^0$  is produced and decay into two  $\gamma$ 's inside the detector. Furthermore most of the neutrino interactions are charged currents quasi-elastic (CCQE) for which the reconstructed neutrino energy is very similar to the true energy and a better energy resolution is achieved.

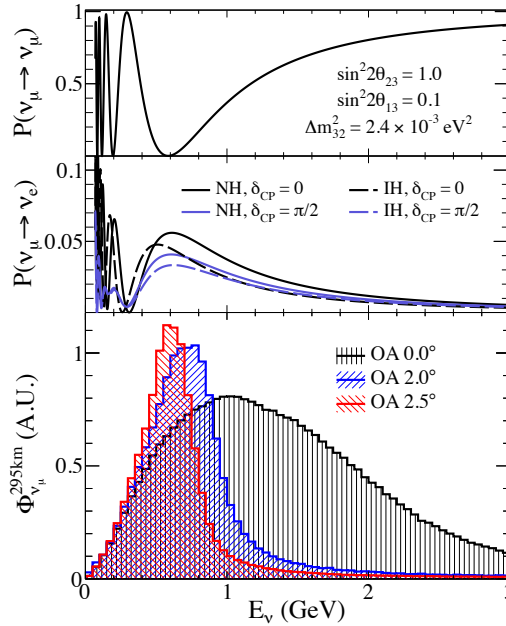


Figure 2.4: Functions of  $\nu_\mu \rightarrow \nu_\mu$  survival probability (top) and  $\nu_\mu \rightarrow \nu_e$  appearance probability (middle) at the T2K far detector are shown. In the bottom plot neutrino fluxes for different off-axis angles are shown.

## 2.2 The near detector

The function of the near detector is to measure the unoscillated neutrino flux which is then compared to the observed one at Super-Kamiokande. The near detector complex is placed at about 280 m from the graphite target and is composed by an on-axis detector (INGRID) and an off-axis magnetized detector (ND280). These detectors are placed in a pit, with a diameter of



17.5 m and a depth of 37 m, inside the near detector hall. In fig. 2.5 the near detector complex is shown.

The most upstream detector of ND280 is the  $\pi^0$  detector (P0D) [86]. Downstream of the P0D, the tracker is situated, composed by three time projection chambers (TPCs) and two fine grained detectors (FGDs), used as target for neutrino interactions as well as for the vertex reconstruction. All the three detectors are surrounded by an electromagnetic calorimeter (ECal) designed for detecting  $\gamma$  rays that have not converted neither in the TPCs nor FGDs. A side muon range detector (SMRD) that measures the ranges of muons exiting the off-axis detector is placed on the return yoke of the magnet [92]. In the following sections a more detailed descriptions of the sub-detectors important for the analyses of this thesis is given.

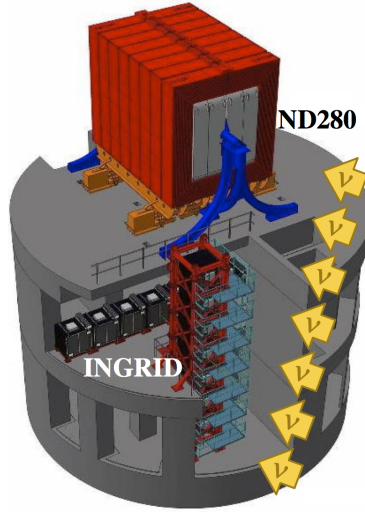


Figure 2.5: Near detector complex. ND280 is located on the upper level, while the horizontal INGRID modules are located on the level below. The vertical INGRID modules span the bottom two levels. Yellow arrows show the direction of the neutrino beam.

### 2.2.1 INGRID

The neutrino beam properties are measured by the on-axis detector INGRID (Interactive Neutrino GRID). The function of INGRID is to monitor the neutrino beam direction and intensity. An iron target provides enough interactions to measure the beam intensity and check the stability every day. The detector consists of 16 identical modules arranged in a  $10\text{ m} \times 10\text{ m}$  cross along the vertical and horizontal direction, as shown in fig. 2.6. Each module consists of 9 iron plates alternated to 11 tracking scintillator planes, surrounded by veto scintillators that reject interactions outside the modules. Another module (Proton Module), which consists of scintillator planes surrounded by a veto, has been added in the center of the INGRID cross to detect both the muons and the protons produced in it and measure the CCQE neutrino interactions.

### 2.2.2 ND280

ND280 is a magnetized off-axis tracking detector ( $\theta_{OA} \sim 2.5^\circ$ ) with the goal to determine the unoscillated  $\nu_\mu$  flux and estimate the intrinsic  $\nu_e$  beam component ( $\sim 1\%$ ), that is the irreducible background to  $\nu_\mu \rightarrow \nu_e$  appearance events at Super-Kamiokande.

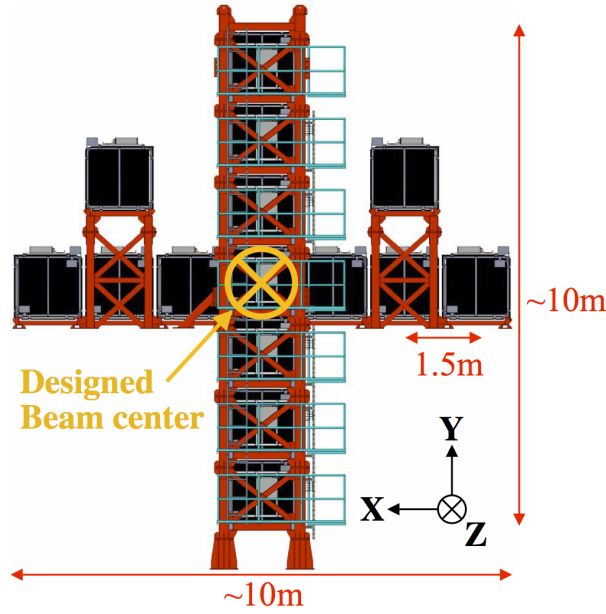


Figure 2.6: INGRID on-axis detector.

All the sub-detectors are contained inside the magnet recycled from the UA1/Nomad experiments at CERN, a solenoid that provides a uniform dipole magnetic field of 0.2 T and allows for the measurement of the charged particle track momenta with good resolution as well as to determine the sign of particle charge. The magnet consists of water-cooled aluminum coils, which creates the horizontally oriented dipole field, and a flux return yoke. All the sub-detectors are contained within the  $3.5 \times 3.6 \times 7.0 \text{ m}^3$  space inside the magnet. The x and z axes are in the horizontal plane and the y axis is vertical. The origin is at the center of the magnet and the 0.2 T magnetic field is along the +x direction. The z axis is the direction to the far detector projected onto the horizontal plane. In fig. 2.7 the view of the ND280 off-axis detector complex is shown. In fig. 2.8 the event display of a muon entering ND280 and crossing all the detectors is shown.

### The tracker: FDGs and TPCs

The particle tracking is provided by three Time Projection Chambers (TPCs) [87] and two Fine Grained Detector (FGD1 and FGD2) [88]. Neutrino interactions occur in the FGDs, that also provide the track vertex informations. The FGD1 consists of fine grained bars of polystyrene (carbon) scintillator with dimension  $9.61 \times 9.61 \times 1864.3 \text{ mm}^3$  are oriented perpendicular to the beam and allow to identify the interaction vertex with high resolution. The target material is about 1.1 tons. The FGD2 is a water-rich detector consisting of seven modules of plastic scintillator, as in FGD1, alternating with six layers of water. This configuration allows to measure the neutrino cross section in water comparing the interaction rates in the two FGDs. The read out is provided by wave-length shifter going down a hole drilled in the center of each scintillator bar and is connected to a Multi-Pixel Photon Counter (MPPC) [89], that digitizes the scintillation light signal.

The tracking of charged particles produced in the FGDs as well as their charge is provided by the TPCs. The track momentum can be determined thanks to the magnetic field. Informations

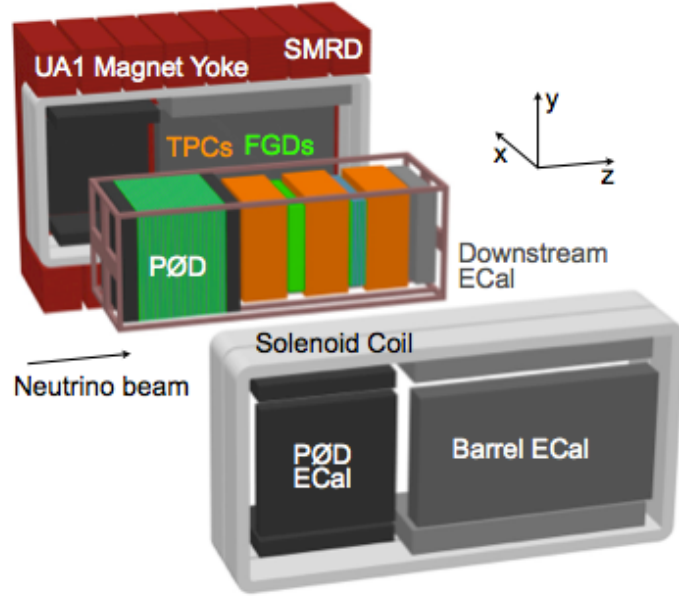


Figure 2.7: View of the ND280 off-axis detector complex. The magnet surrounds the inner detectors. The P0D is on the upstream side, three TPCs are alternated to the two FGDs and they are all covered by the electromagnetic calorimeter. The SMRD is inserted in the air gaps of the magnet iron yokes. The coordinate system is shown as well.

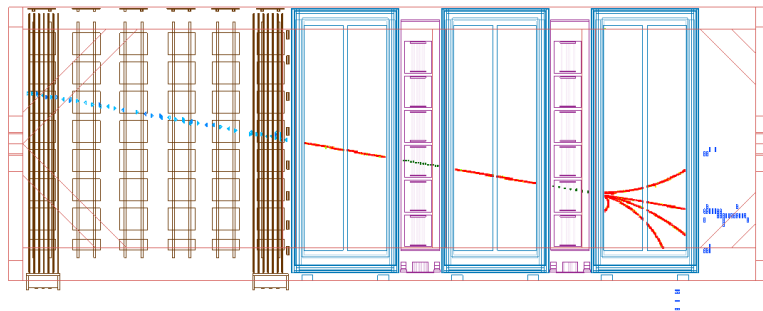


Figure 2.8: Event display with a muon track entering the P0D detector, continuing to the tracker (TPC and FGD) region and producing secondary particles then stopped in ECal.

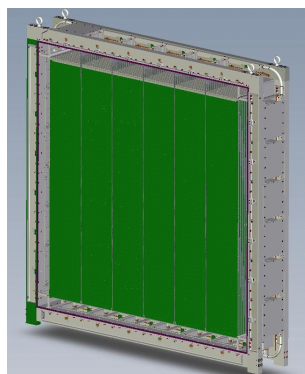


Figure 2.9: View of an FGD with the front cover removed. Scintillator modules (green) are perpendicular to the neutrino beam direction.

of particle identification are obtained by measuring the amount of ionization left by each particle that, combined with the measured momentum, allows to distinguish between different types of charged particles, providing a very good separation of muons and electrons. High purity samples of neutrino of different interaction topology can be selected. Each TPC consists of an inner box that holds an argon-based drift gas mixture  $\text{Ar}:\text{CF}_4:\text{iC}_4\text{H}_{10}$  (95%:3%:2%). An outer box of dimension  $2.3\text{ m} \times 2.4\text{ m} \times 1.0\text{ m}$  filled with  $\text{CO}_2$  is used as insulating gas. The copper strip pattern in the inner box and a central cathode panel produce a uniform electric field aligned with the magnetic field, perpendicular to the beam axis, in the volume filled with the drift gas. Charged particles ionize the argon gas producing electrons that drift toward the readout planes, where they are amplified with an electric field of  $\sim 27\text{ kV/cm}$  and sampled by micromegas detectors [90]. A schematic view of the TPC is shown in fig. 2.10. The resolution of energy loss per length ( $dE/dx$ ) for minimum ionizing particles is about 7.8% and the momentum resolution below 1 GeV/c is about 2%.

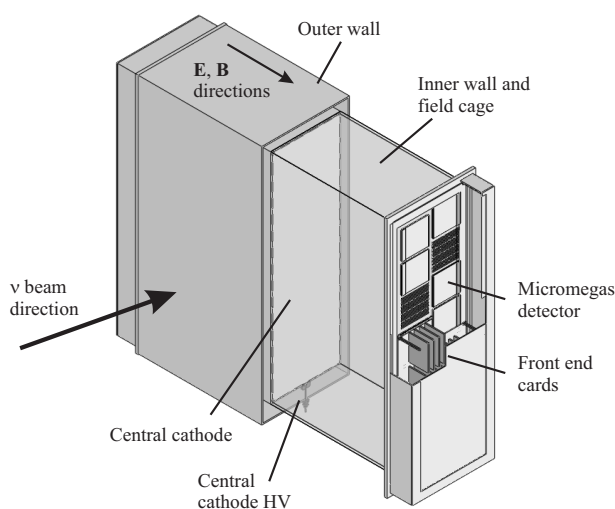


Figure 2.10: Schematic view of the TPC.

## The Electromagnetic Calorimeter (ECal)

A sampling electromagnetic calorimeter (ECal) [91], made of layers of plastic scintillator bars as active material with lead absorber sheets between layers, surrounds the P0D, FGDs and TPCs and is able to stop all the particles exiting the inner detector volume. Its main goal is the detection of photons from  $\pi^0$  decays that were produced but did not convert in the inner detector. When combined with the tracking informations from FGDs and TPCs, it provides a full event reconstruction by detecting photons and measuring their energy and direction. The detection of charged particles provides a further particle identification allowing to separate electrons, muons and pions. The ECal is composed by six modules (Barrel-ECal) around the inner volume parallel to the beam direction. One module covers the downstream side (Ds-ECal) and six modules surround the P0D detector (P0D-ECal).

## 2.3 The far detector: Super-Kamiokande

The T2K far detector is Super-Kamiokande [93], currently the world largest water Cherenkov detector, 39 m in diameter and 42 m in height. It is located at 295 km from the interaction target, where maximal  $\nu_\mu$  disappearance and  $\nu_\mu \rightarrow \nu_e$  appearance oscillations occur. It is 1 km deep inside the Ikenoyama mountain to shield the cosmic muons. The detector consists of a cylindrical pool filled with 50 kton of pure water. Separated by a cylindrical stainless steel structure, there are an inner detector (ID) with 11129 20-inches photomultiplier tubes (PMTs) that covers about the 40% of the surface, in a volume of 33.8 m in diameter and 36.2 m in height, and an outer detector (OD), 2 m thick along the radius with 1885 8-inches PMTs. A schematic view of the detector is shown in fig. 2.11. The purpose of the outer detector is to identify the neutrino interactions that occurred outside the detector, e.g. in the surrounding rock, and to act as a veto for cosmic ray muons.

When a muon (electron) neutrino with energy below 1 GeV interacts with the water it undergoes mainly CCQE interactions, producing a muon (electron) in the final state. Then the muon (electron) produces Cherenkov light that is detected by the PMTs. Muons travel through the detector producing a well defined cone of Cherenkov light with a sharp edge, while electrons, that create electromagnetic showers, produce a “fuzzy” ring pattern given by the overlap of many Cherenkov light cones. Reconstruction tools identify these different cone patterns allowing for an excellent PID. Since the recoil proton from charged current interactions at T2K is usually below the Cherenkov threshold, a single lepton is the dominant topology for beam-induced events at Super-K. For such isolated electrons (muons) the momentum and angular resolutions are estimated to be  $0.6\% + 2.6\%\sqrt{P[\text{GeV}/c]}$  ( $1.7\% + 0.7\%\sqrt{P[\text{GeV}/c]}$ ) and  $3.0^\circ$  ( $1.8^\circ$ ), respectively. In fig. 2.12 an example of reconstructed events for muon-like and electron-like rings is shown. One of the most important background for  $\nu_e$  and  $\bar{\nu}_e$  appearance consists of  $\text{NC}1\pi^0$  interactions. The  $\pi^0$  created from the neutrino interaction decays into two  $\gamma$ 's that produce Cherenkov rings similar to electrons. If one of the rings is not well reconstructed, it becomes difficult to discriminate it from pure  $\nu_e$  CC interactions.

Super-K is running since a long time (1996). For this reason the detector behavior is well understood and the calibration of the energy scale is known at the percent level.

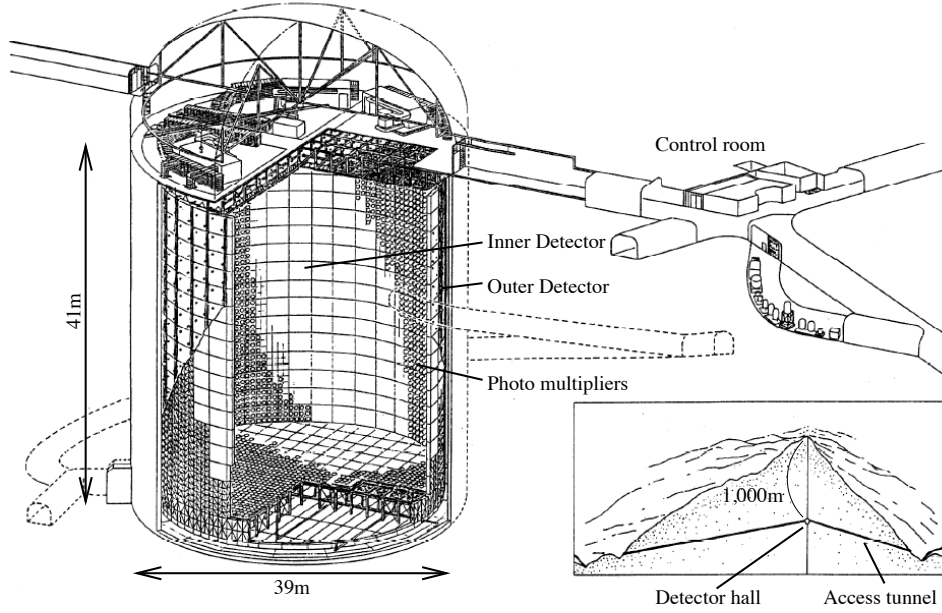


Figure 2.11: Schematic view of the Super-Kamiokande detector as well as its position inside the Ikenoyama mountain.

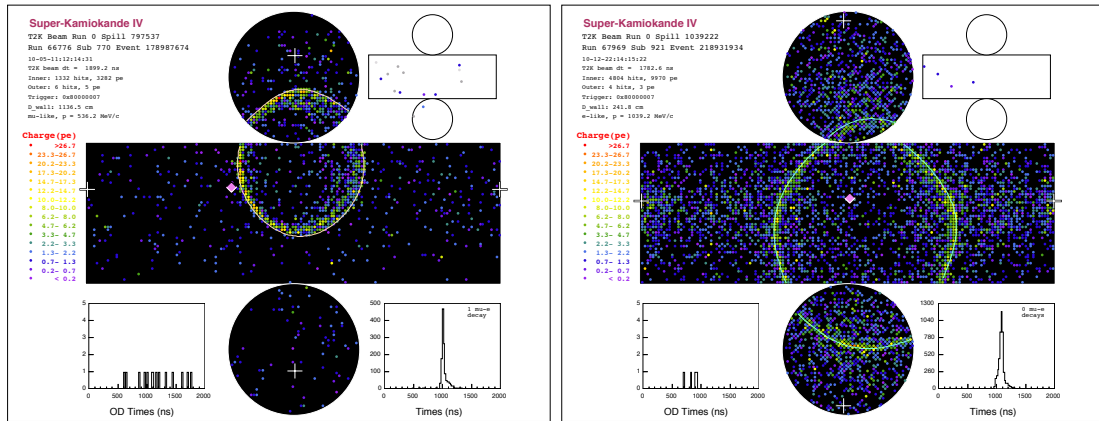


Figure 2.12: Example of event displays of reconstructed T2K events in Super-Kamiokande for a muon-like ring (left) and an electron-like ring (right). The cylindrical inner detector is unrolled onto a plane and each colored point is the light detected by a PMT where the color corresponds to the amount of charge. A line defines the reconstructed ring edge.

Run	Period	ND280 $\nu$	ND280 $\bar{\nu}$	SK $\nu$	SK $\bar{\nu}$
Run 1	Jan. 2010 - Jun. 2010	$0.17 \times 10^{20}$	—	$0.32 \times 10^{20}$	—
Run 2	Nov. 2010 - Mar. 2011	$0.79 \times 10^{20}$	—	$1.11 \times 10^{20}$	—
Run 3	Mar. 2012 - Jun. 2012	$1.56 \times 10^{20}$	—	$1.58 \times 10^{20}$	—
Run 4	Oct. 2012 - May 2013	$3.38 \times 10^{20}$	—	$3.56 \times 10^{20}$	—
Run 5	May 2014 - Jun 2014	$0.24 \times 10^{20}$	$0.43 \times 10^{20}$	$0.24 \times 10^{20}$	$0.51 \times 10^{20}$
Run 6	Oct. 2014 - Jun 2015	$0.08 \times 10^{20}$	$3.38 \times 10^{20}$	$0.10 \times 10^{20}$	$3.51 \times 10^{20}$
Total	Jan. 2010 - Jun 2015	$6.22 \times 10^{20}$	$3.81 \times 10^{20}$	$6.914 \times 10^{20}$	$4.011 \times 10^{20}$

Table 2.1: T2K run data periods at ND280 and Super-Kamiokande. The integrated number of accumulated POT is shown for each run period, for both neutrino and antineutrino modes.

## 2.4 Summary of the data taking

The T2K experiment started taking physics data in January 2010. T2K has taken data in both neutrino and antineutrino modes, respectively with polarity of the horn current set to +250 kA, selecting a neutrino beam, and -250 kA, selecting an antineutrino beam. So far the total integrated number of protons on target (POT) is  $6.914 \times 10^{20}$  POT in neutrino mode and  $4.011 \times 10^{20}$  POT in antineutrino mode at Super-K and  $6.22 \times 10^{20}$  POT in neutrino mode and  $3.81 \times 10^{20}$  POT in antineutrino mode at ND280. Since the horn current was set to 0 kA the Run 3a is not used for physics analyses. During the Run 3b the horn current was set to 205 kA. The maximum beam power reached so far is 344.9 kW. The summary of the data taking periods is shown in table 2.1 for both ND280 and Super-Kamiokande.

## 2.5 The neutrino flux prediction

In sec. 2.1 the beam line used to produce the neutrino flux has been described. Interactions of protons with the carbon target produce hadrons ( $\pi^\pm, K^\pm, K_L^0$  and  $\mu^\pm$ ) that further decay into neutrinos through the reactions shown in tab. 2.2. In fig. 2.13 the composition of the expected neutrino flux at Super-K is shown.  $\nu_\mu$  ( $\bar{\nu}_\mu$ ) are primarily produced by charged pion decays around the energy peak ( $\sim 0.6$  GeV) and two-body kaon decays. The main contribution to  $\nu_e$  ( $\bar{\nu}_e$ ) in the energy peak comes from muon decay, while, above 2 GeV,  $\nu_e$  ( $\bar{\nu}_e$ ) mainly come from three-body kaon decay. The intrinsic  $\nu_e$  beam is less than 1% below 1.5 GeV, the region where the oscillation maximum takes place. All the details on the T2K neutrino flux as well as the simulation are given in [108].

### 2.5.1 The simulation chain

A good prediction of the neutrino flux is fundamental for a precision measurement of oscillations at Super-K as well as to avoid any bias in the measurement of the oscillation parameters. The neutrino flux prediction consists of the simulation of the primary proton beam, the interaction in the graphite target with production of parent hadrons and muons that further decay into neutrinos.

FLUKA [94, 95] is used to simulate the hadronic interactions in the target and the baffle, since it has the best agreement with the external hadron production data. Incident protons with kinetic energy of 30 GeV are generated according to the measured proton beam spatial

Particle decay products	Branching ratio (%)
$\pi^+ \rightarrow \mu^+ + \nu_\mu$	99.9877
$\rightarrow e^+ + \nu_e$	$1.23 \times 10^{-4}$
$K^+ \rightarrow \mu^+ + \nu_\mu$	63.55
$\rightarrow \pi^0 + \mu^+ + \nu_\mu$	3.353
$\rightarrow \pi^0 + e^+ + \nu_e$	5.07
$K_L^0 \rightarrow \pi^- + \mu^+ + \nu_\mu$	27.04
$\rightarrow \pi^- + e^+ + \nu_e$	40.55
$\mu^+ \rightarrow e^+ + \bar{\nu}_\mu + \nu_e$	100

Table 2.2: Branching ratios of neutrino parent decay modes considered in JNUBEAM, the neutrino beam Monte Carlo simulation used at T2K. The same branching ratios are obtained for antineutrino by conjugating the charge.

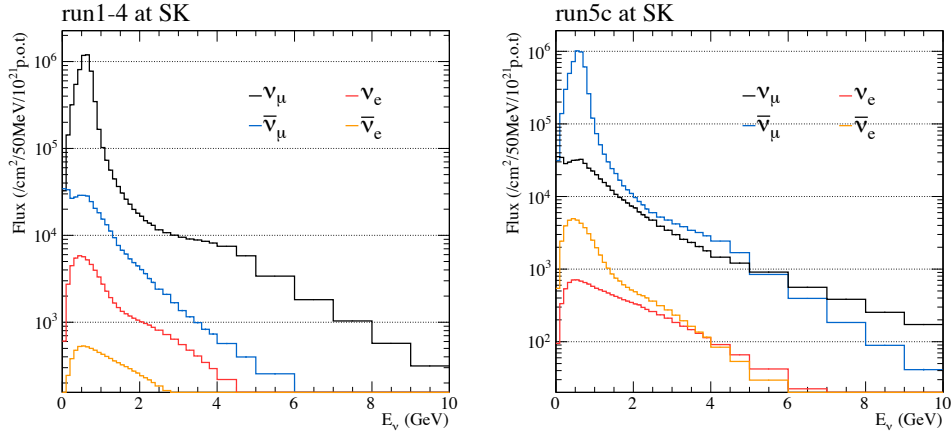


Figure 2.13: Flux expected at Super-K for run 1-4 (left), with neutrino mode beam, and run 5c (right), with antineutrino mode beam, broken down into neutrino flavor components.



Parent	$\nu_\mu$	$\bar{\nu}_\mu$	$\nu_e$	$\bar{\nu}_e$
$\pi^\pm$	97.53 %	85.20 %	1.09 %	0.36 %
$K^\pm$	2.38 %	4.34 %	26.96 %	17.39 %
$K_0^L$	0.08 %	1.24 %	11.16 %	73.25 %
$\mu$	0.01 %	9.22 %	61.06 %	9.00 %
Total	92.63 %	6.24 %	0.98 %	0.15 %

Table 2.3: Fraction of neutrino mode flux for each final hadron in the interaction chain as well as the neutrino flavor used in the simulation.

Parent	$\nu_\mu$	$\bar{\nu}_\mu$	$\nu_e$	$\bar{\nu}_e$
$\pi^\pm$	83.67 %	98.64 %	0.32 %	1.21 %
$K^\pm$	8.81 %	1.24 %	35.23 %	14.81 %
$K_0^L$	1.02 %	0.10 %	56.35 %	14.76 %
$\mu$	6.50 %	0.02 %	8.10 %	69.30 %
Total	8.89 %	90.02 %	0.23 %	0.87 %

Table 2.4: Fraction of antineutrino mode flux for each final hadron in the interaction chain as well as the neutrino flavor used in the simulation.

distribution and divergence. Parent hadrons can be generated by interactions of the original protons with the target (secondary hadrons) or by re-interactions in the target of hadrons other than the original proton (tertiary hadrons). About 40% of the hadrons are produced by tertiary interactions. In tab. 2.3 and 2.4 the neutrino flux composition is shown.

A neutrino beam Monte Carlo simulation, JNUBEAM, based on GEANT3 [96], has been developed to simulate the particle propagation. Particles are propagated through the horn magnetic field and may interact with the horn material in the target station. Particles are then propagated through the decay volume until they interact in the beam dump or decay. The hadronic interactions outside the target are simulated with the GCALOR model [97, 98]. Eventually the neutrino tracks are extrapolated to the near and far detectors.

## 2.6 Auxiliary hadron production experiment and flux tuning

The physics goal of T2K can be reached by requiring very good detector performances, reducing the cross section systematic uncertainties and with a very good knowledge of the neutrino flux, the largest source of systematic uncertainty.

The expected number of events at SK ( $\Phi_{SK}^{exp}$ ) as a function of the neutrino energy  $E_\nu$  is obtained by extrapolating the flux prediction from ND280 ( $\Phi_{ND280}$ ) with the near-to-far ratio  $R_{F/N}$ :

$$\Phi_{SK}^{exp}(E_\nu) = R_{F/N}(E_\nu) \cdot \Phi_{ND280}(E_\nu) \quad (2.2)$$

If the neutrino source is isotropic and point-like,  $R_{F/N}$  is simply given by the solid angle and is energy independent. However, in order to accumulate enough statistics, also needed to perform cross section measurements, the near detector is close to the decay tunnel such as the source is not point-like and becomes sensitive to the finite extension of the production region.

The acceptance angle becomes larger than the far detector and the far-to-near ratio becomes not trivial. Thus  $R_{F/N}$  is dependent on the neutrino energy and the momentum of the produced hadrons, as well as on the geometry of the neutrino source. For this reason a detailed knowledge of hadron production at the T2K target is needed for a correct prediction of the neutrino flux.

T2K would rely only on the models used to predict the primary and secondary interactions with JNUBEAM, that have quite large discrepancies. The predictions provided by GICALOR, GFLUKA [99] and GEISHA [99] models disagree up to a factor two at Super-K, as shown in fig. 2.14. So the total flux uncertainty is rather large and not good enough for the T2K goals, that requires about 3% of uncertainty on the near-to-far ratio.

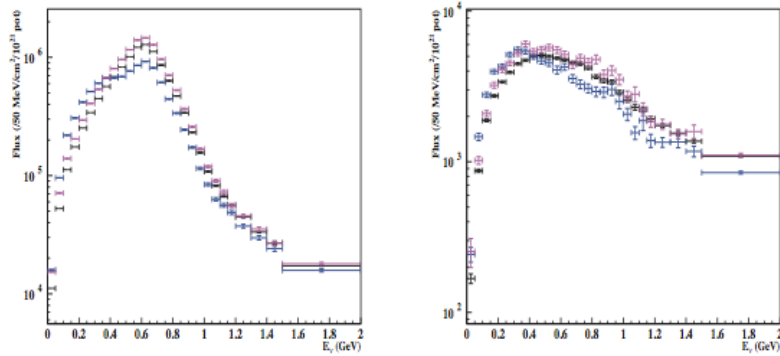


Figure 2.14:  $\nu_\mu$  (left) and  $\nu_e$  (right) spectra at the far detector. Predictions are shown for different models used for the simulation of both primary and secondary interactions: GICALOR (black), GFLUKA (purple), GEISHA (blue).

In order to reduce the uncertainty, precision hadron production measurements are needed. There are no available measurements at the T2K proton beam energy available in literature. The closest cross section measurements in energy were performed by the HARP experiment [100] at 12 GeV with a different target material and by NA49 [118] at 158 GeV. However extrapolations from the existing experimental results cannot be very reliable, since they would imply extrapolations to different energies and target materials. For this reason an auxiliary hadron production experiment, NA61/SHINE, is needed to satisfy the following requirements:

- the interaction target is of the same material (carbon) and the proton beam of the same energy as at T2K;
- both secondary and tertiary hadron production must be measured. The first component can be constrained by studying the interaction cross section of protons in a 2 cm long target (referred as “thin target”), measuring the total proton carbon production cross section and the inclusive production cross sections of the secondary hadrons. This allows to constrain up to 60% of the flux at the neutrino energy of 0.6 GeV. The secondary and tertiary hadron interactions, about 40% of the flux, can be measured by using the “T2K replica target”;
- it must cover the full T2K  $\{p, \theta\}$  phase space of the produced hadrons, where  $p$  is the momentum and  $\theta$  is the angle with respect to the beam direction;
- the statistic needed to reach the goal has been estimated to be about 10 M triggered events [101] with the thin target and 2 M triggered events with the long target.

In chap. 3 the NA61/SHINE experiment and the hadron production measurements, that I performed with the high statistic data set during the PhD, are presented.

### 2.6.1 MC reweighting procedure with external data

As explained above, T2K relies primarily on the production measurements of  $\pi^\pm, K^\pm$ , protons and  $K_S^0$  provided by the NA61/SHINE experiment [104, 102, 103]. Also measurements from other external experiments, Eichten et al. [105] and Allaby et al. [106], in the forward production region of the phase space  $\{p, \theta\}$  not covered by NA61/SHINE, were used, though on beryllium instead of carbon. Measurements of the inelastic cross section were used to reweight particle interactions and absorption rates in the T2K simulation.

The reweighting of the T2K simulation from external data is applied on the double differential multiplicity in momentum,  $p$ , of the produced particles and its angle,  $\theta$ , relative to the incident particle, written as

$$\frac{dn^2(p, \theta)}{dpd\theta} = \frac{1}{\sigma_{prod}} \frac{d^2\sigma(p, \theta)}{dpd\theta} \quad (2.3)$$

where  $\sigma_{prod}$  is the total hadronic production cross section in proton carbon interactions. The weights are calculated as the ratio between data and simulation:

$$W(p, \theta) = \left[ \frac{d^2n(p, \theta)}{dpd\theta} \right]_{data} / \left[ \frac{d^2n(p, \theta)}{dpd\theta} \right]_{MC} \quad (2.4)$$

and are applied to the FLUKA or GCALOR simulated differential productions, evaluated with the appropriate incident particle momentum and type and target material. An example of the computed weights is shown in fig. 2.15.

When interactions occur in target materials other than carbon, like aluminium in the horns, or in case of tertiary pion production from nucleon interactions at lower momentum, the extrapolation to the different material and energy is performed by applying the Feynman scaling [107].

The simulated multiplicities are reweighted by taking into account also the production cross section measured at NA61/SHINE ( $\sigma_{prod}^{data}$ ). For a particle traversing a material by a distance  $d_0$  before interacting and then by a distance  $d_1$  before exiting the material, the following weight is applied:

$$W = \frac{\sigma_{prod}^{data}}{\sigma_{prod}^{MC}} e^{-(\sigma_{prod}^{data} - \sigma_{prod}^{MC})(d_0 + d_1)} \quad (2.5)$$

$\rho$  is the density of the nuclear target and  $\sigma_{prod}^{MC}$  is the value of production cross section used in the simulation. If a particle decays before interacting, the weight is calculated only as an attenuation factor:

$$W = e^{-(\sigma_{prod}^{data} - \sigma_{prod}^{MC})(d_0 + d_1)} \quad (2.6)$$

As described more in detail in sec. 3.2, two different NA61/SHINE data sets were used for the flux tuning: the 2007 data set, a low statistic pilot run used to test the tuning method [108],

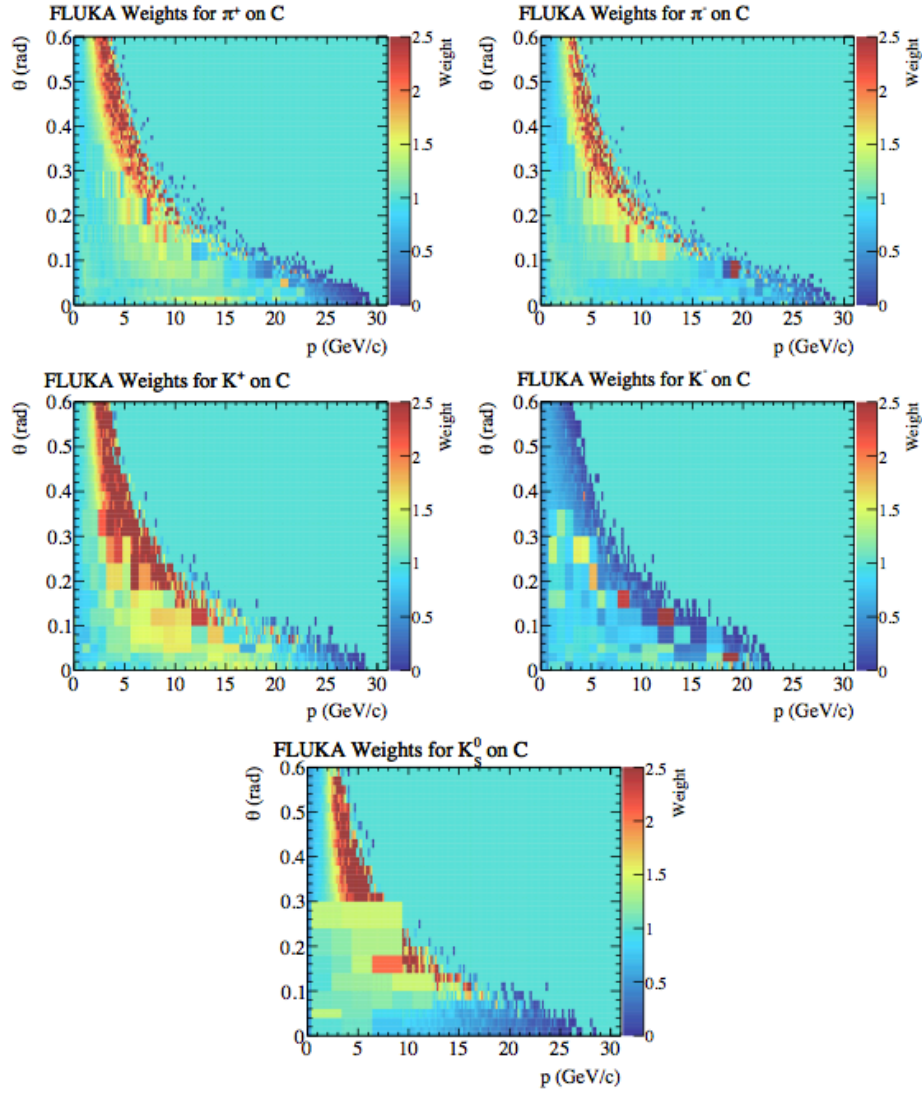


Figure 2.15: The multiplicity weights on Carbon from NA61/SHINE data over FLUKA simulation are shown. From top left to bottom right:  $\pi^+$ ,  $\pi^-$ ,  $K^+$ ,  $K^-$  and  $K_S^0$ .

and the 2009 data set, with a much higher statistic [109]. For the T2K analyses performed before 2015, the flux tuned with the 2007 data set was used, while only the more recent data analyses used the tuning with the high statistic data set. In each analysis chapter it will be explicitly noticed which NA61/SHINE dataset was used to tune the flux prediction.

As shown in fig. 2.16 the flux tunings with the two different NA61/SHINE data sets are in very good agreement.

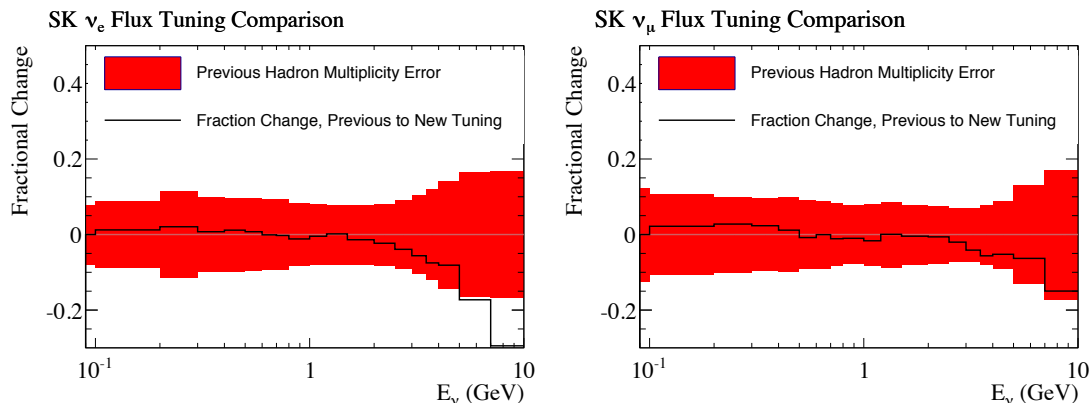


Figure 2.16: The fractional change to the Super-K  $\nu_\mu$  (left) and  $\nu_e$  (right) flux prediction for the NA61/SHINE 2009 data based tuning relative to the NA61/SHINE 2007 data based tuning (black). The red error band shows the hadron multiplicity modeling uncertainty assigned for the NA61/SHINE 2007 data based flux prediction.

### 2.6.2 Uncertainty on the flux prediction

Many sources of systematic uncertainty are considered for the neutrino flux prediction. The statistical and systematic uncertainties on the measured multiplicities provided by NA61/SHINE are taken into account. The region of the phase space  $\{p, \theta\}$ , not covered by neither NA61/SHINE, nor Eichten et al. and Allaby et al. data, is tuned by extrapolating from the NA61/SHINE data. The uncertainty on the method used for the tuning is estimated. Other systematic uncertainties are given by the incident particle energy scaling used to apply the NA61/SHINE data to interactions with lower momentum incident nucleons as well as the target material scaling method for external data where a material different from carbon was used. The production of secondary baryons in proton interactions (protons, neutrons,  $\Lambda_s^0$  and  $\Sigma_s$ ) were included in the reweighting and the corresponding uncertainties have been evaluated. The systematic uncertainty in the production cross section is conservatively taken to be represented by the magnitude of the quasi-elastic correction,  $\sigma_{qe}$ , applied to the total inelastic cross section for a given particle and at given beam energy. This is based on an apparent discrepancy between the cross section measurements for protons of Denisov et al. [133] and those of Bellettini et al. [110], Carroll et al. [132] and NA61/SHINE (sec. 3.3), which may be indicative of the difficulty in understanding whether experiments measure the inelastic or production cross sections. Finally also the systematic uncertainties on the proton beam, the neutrino off-axis angle, target and horn alignment, horn current and magnetic field are taken into account.

As shown in fig. 2.17, the largest source of flux systematic uncertainty is given by the hadron production, about 10%. Thanks to the high statistic NA61/SHINE 2009 data set the uncertainty has been reduced by about 3-4% with respect to the tuning performed with the pilot 2007 data

set. It is worth to note that currently only the 60% of the flux uncertainty is constrained with the NA61/SHINE data, since the long target data set is not used in the flux tuning yet.

In fig. 2.18 the total flux error matrix obtained after the tuning with the NA61/SHINE 2007 and 2009 data is shown. The flux parametrization used in the analyses is shown in tab. 2.5.

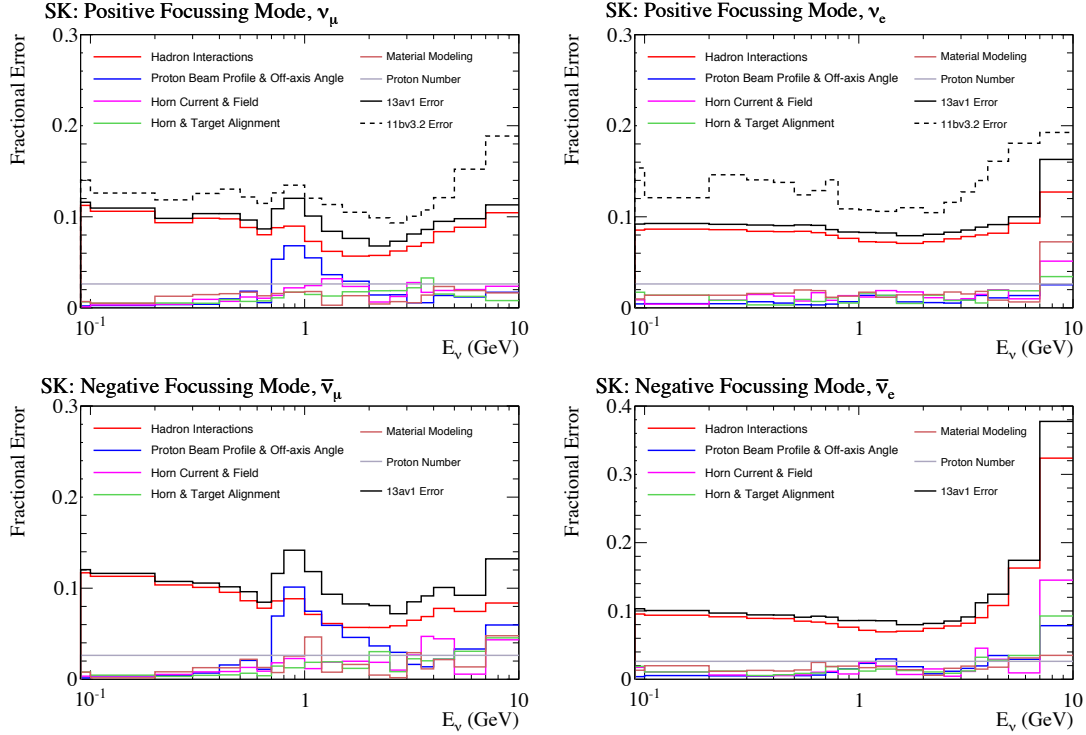


Figure 2.17: The fractional uncertainty on the Super-K prediction as a function of neutrino energy for neutrino mode (top)  $\nu_\mu$  (left) and  $\nu_e$  (right) and antineutrino mode (bottom)  $\bar{\nu}_\mu$  (left) and  $\bar{\nu}_e$  (right). The uncertainty on the flux prediction with the NA61/SHINE 2007 thin target data (dotted line) is shown only for neutrino mode, since for antineutrino mode only the 2009 data were used for the tuning. The uncertainty on the flux predicted at ND280 is similar to the Super-K one.

## 2.7 Neutrino cross sections at T2K

For neutrino oscillation experiments the knowledge of neutrino interactions is as important as a good prediction of the flux. In this section a review of the neutrino cross section models and the implications on the oscillation measurements at T2K is given. Since T2K has a neutrino beam which is mostly at an energy below 1 GeV, a particular emphasis is given to those processes that are dominant in this energy region.

In the Standard Model neutrinos can interact weakly through both neutral current (NC) and charged current (CC) interactions

$$\text{CC} : \nu_l + N \rightarrow l + X$$

$$\text{NC} : \nu_l + N \rightarrow \nu_l + X$$

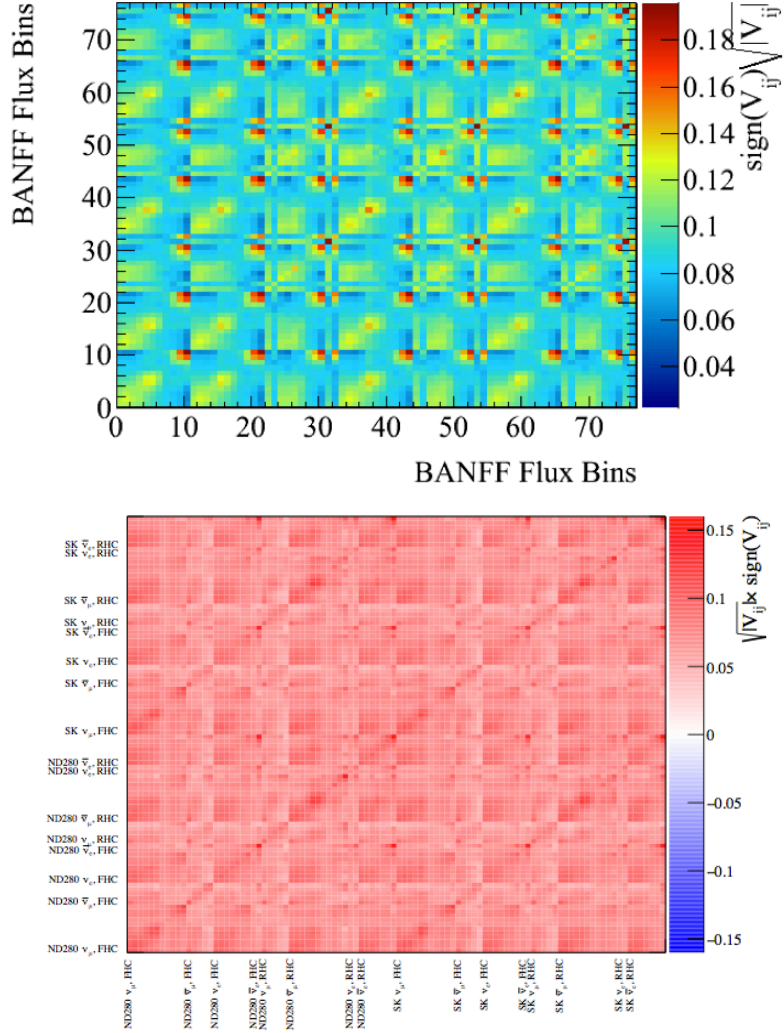


Figure 2.18: Total flux error matrix of ND280 and Super-K, for run 1-4 (top) and run 1-6 (bottom) defined as the  $\sqrt{V_{ij}} \times \text{sign}(V_{ij})$  where  $V$  is the covariance matrix. The flux is tuned with NA61/SHINE 2007 (up) and 2009 (bottom) data. Bins of the top error matrix are grouped as 0-24=ND280 neutrino mode, 25-49=Super-K neutrino mode. On the bottom error matrix: the parameters numbers are 0-24=ND280 neutrino mode, 25-49=ND280 antineutrino mode, 50-74=Super-K neutrino mode, 75-99=Super-K antineutrino mode. The flux is parametrized as described by tab. 2.5.

Flavor	Beam mode	Binning (GeV)
$\nu_\mu$	neutrino	0-0.4, 0.4-0.5, 0.5-0.6, 0.6-0.7, 0.7-1.0, 1.0-1.5, 1.5-2.5, 2.5-3.5, 3.5-5.0, 5.0-7.0, 7.0-30.0
$\nu_e$	neutrino	0-0.5, 0.5-0.7, 0.7-0.8, 0.8-1.5, 1.5-2.5, 2.5-4.0, 4.0-30.0
$\bar{\nu}_\mu$	neutrino	0-0.7, 0.7-1.0, 1.0-1.5, 1.5-2.5, 2.5-30.0
$\bar{\nu}_e$	neutrino	0-2.5, 2.5-30.0
$\nu_\mu$	antineutrino	0-0.7, 0.7-1.0, 1.0-1.5, 1.5-2.5, 2.5-30.0
$\nu_e$	antineutrino	0-2.5, 2.5-30.0
$\bar{\nu}_\mu$	antineutrino	0-0.4, 0.4-0.5, 0.5-0.6, 0.6-0.7, 0.7-1.0, 1.0-1.5, 1.5-2.5, 2.5-3.5, 3.5-5.0, 5.0-7.0, 7.0-30.0
$\bar{\nu}_e$	antineutrino	0-0.5, 0.5-0.7, 0.7-0.8, 0.8-1.5, 1.5-2.5, 2.5-4.0, 4.0-30.0

Table 2.5: Parametrization of the flux systematic parameters for each beam mode as a function of the neutrino true energy and flavor.

where  $l = e, \mu, \tau$ .  $\nu_l$  is a neutrino of flavor  $l$ ,  $N$  and  $X$  are nucleons in the initial and final state.

A purely leptonic elastic scattering is described by the following reaction

$$\text{ES} : \nu_e + e^- \rightarrow \nu_e + e^-$$

However its cross section is about four orders of magnitude smaller than scattering off nucleons at  $E \sim O(1)$  GeV.

In eq. 2.19 the CC neutrino cross sections as a function of the energy in the GeV range are shown. At low energy charge current quasi-elastic scattering (CCQE) is dominant. The neutrino has not enough energy to break the nucleons and a lepton and a free nucleon are produced. Neutrinos interact with neutrons and produce protons in the final state, while antineutrinos interact with the proton and give a neutron in the final state. This process is also called  $1p-1h$  (1 particle - 1 hole), since a free nucleon is produced as well as a hole in the nucleus. This reaction is shown in the left diagram of fig. 2.20. If the energy is around 1 GeV, the resonance in the final state is observed: the nucleon is excited, produces a resonance ( $\Delta$  or  $N^*$ ) and during the dis-excitation a pion can be released (CC1 $\pi$ ). This energy region is in the transition between the non-perturbative and perturbative regimes. At low  $Q^2$  there is also a large non-perturbative QCD (long range) contributions to the inelastic cross section and a single pion can be produced without any resonance. This is also called non-resonant single pion production background [47].

There is also a rather small probability that a pion is produced coherently (CCCoh): the neutrino scatters coherently from the entire nucleus, transferring a negligible energy to the target, resulting in a low- $Q^2$  interaction without nuclear recoil and a forward scattered pion. At higher energy, above 2 GeV, deep inelastic scattering (CCDIS) becomes the dominant contribution. The neutrino has enough energy to break the nucleon and interacts with the quarks. Since the quarks cannot be observed as free particles, they quickly recombine appearing as a hadronic shower. In an analogous way we can have NC quasi-elastic (NCQE), NC single pion (NC1 $\pi^0$ ) NC coherent scattering (NCCoh) and NC deep inelastic scattering (NCDIS).

A category which has a very big impact on oscillation neutrino experiments is the *Meson Exchange Current* (MEC) process [45, 46], also called 2p-2h (2 particles - 2 holes) since in the final state there are two free nucleons that has exchanged a meson. It corresponds to the right Feynman diagram of fig. 2.20. The reconstruction of this process is a big issue for neutrino



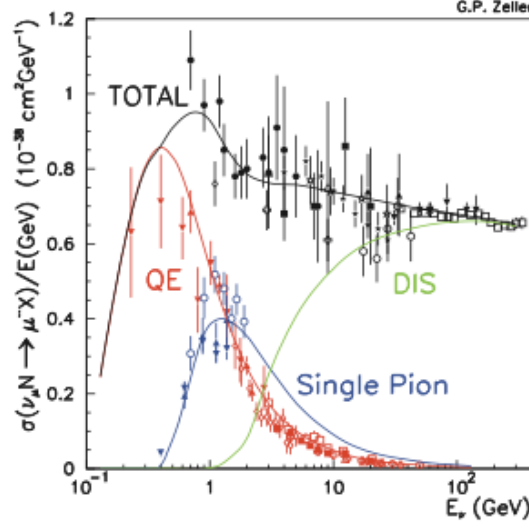


Figure 2.19: CC cross section of  $\nu_\mu$  interacting with the nucleon. CCQE (red), CC1 $\pi$  (blue), CCDIS (green) and total inclusive (black) cross sections are shown as a function of the neutrino energy. The cross sections measured by several experiments [39] are compared with the expectation obtained with the NUANCE event generator [40]. The figure is taken from [41].

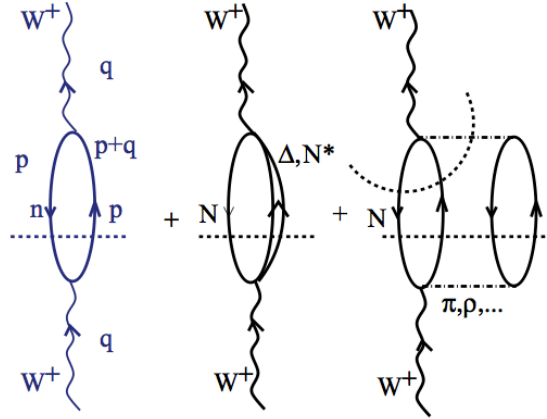


Figure 2.20: Diagrammatic representation of the mechanisms that mostly contribute to the  $W^+$  self-energy. The diagram cut by the dashed line corresponds to the channel involved in the CC interaction where a  $W^\pm$  is exchanged between the (anti)neutrino and the nucleon. The left diagram corresponds to 1p-1h CCQE interaction, in the middle a resonance ( $\Delta$  or  $N^*$ ) is produced, while the right diagram corresponds to 2p-2h with two nucleons in the final state that has exchanged a meson (MEC).

experiments since, if the nucleons in the final state are not detected, it appears as a 1p-1h interaction, producing a bias in the reconstructed neutrino energy, that for energies of about 1 GeV is calculated assuming a CCQE interaction.

Charged current interactions which are not quasi-elastic are denoted as CCnQE.

### 2.7.1 Impact of neutrino cross-sections on the energy reconstruction

A very good knowledge of neutrino cross section is fundamental in order to predict correctly the number of neutrino interactions and reconstruct the interacting (anti)neutrino energy from the informations on the detected particles in the final state: the (anti)lepton and the proton (neutron). A precise reconstruction of the neutrino energy is very important in order to obtain a good resolution on the observation of the oscillatory pattern. However it is usually very difficult to detect the nucleon in the final state, in particular at energies below 1 GeV, since most of the neutrino momentum is brought by the lepton. Given the measured lepton momentum ( $p_l$ ), angle between the expected trajectory of the interacting neutrino and the outgoing lepton ( $\theta$ ) and energy ( $E_l$ ), the proton mass ( $m_p$ ), the neutron mass ( $m_n$ ) and the mass of the lepton in the final state ( $m_l$ ), the neutrino energy of approximately 1 GeV is usually reconstructed in the CCQE hypothesis as

$$E_{Reco} = \frac{m_p^2 - (m_n - E_b)^2 - m_l^2 + 2(m_n - E_b)E_l}{2(m_n - E_b - E_l + p_l \cos \theta_l)} \quad (2.7)$$

If an antineutrino interacts, in the final state a neutron and an antilepton are present. So  $m_n$  and  $m_p$  are swapped.  $E_b$  is the nucleon binding energy which is model dependent and has to be taken into account in the calculations. Its value is 27 MeV for oxygen and 25 MeV for carbon. This formula is valid only for a target nucleon at rest. However protons and neutrons cannot be considered at rest and a *Relativistic Fermi Gas* model (RFG), defined by the *Fermi momentum*  $p_F$ , the momentum of the nucleon in the highest occupied state, and the nucleon binding energy, is usually used [42]. The model, that considers the nucleus as a degenerate gas of protons and neutrons moving as freely, smears the reconstructed energy distribution. This approximation can be good at the first order but, if a more precise energy reconstruction is needed, all the correlations between the nucleons inside the nucleus must be taken into account. Some models include the spectral function (SF) [43], giving a more realistic picture. It describes a distribution of momenta and removal energies inside the nucleus by combining the contributions from the shell model (mean field part) as well as the short-range correlations. Another model takes into account the effects given by the medium polarization in the 1p-1h contribution. It is a *Random Phase Approximation* (RPA) in many body formalism [44, 45] that gives a medium polarization effect and takes into account the propagation of a particle-hole pairs through the dense medium mediated by residual 1p-1h excitations. The effect is a nuclear screening resulting from long range inter-nucleon correlations that leads to a quenching of the CCQE cross-section at low  $Q^2$ .

Another process that can distort the reconstructed neutrino energy is the *Final State Interactions* (FSI), resulting from interactions of the nucleon or the pion, in the final state of the neutrino-nucleus interaction, that propagate through the nuclear medium before observation. Since these particles interact via the strong force, there is a significant probability of re-interaction within the nucleus like particle absorption, scattering and particle production. This masks the interaction mode of the primary vertex, making the identification of true CCQE, CC1 $\pi$ , etc. interactions difficult, therefore producing a bias on the reconstructed neutrino energy.

## Chapter 3

# Hadron production measurements with the auxiliary NA61/SHINE experiment

The NA61/SHINE (SPS Heavy Ion and Neutrino Experiment) experiment is a multi-purpose fixed target experiment at the CERN Super Proton Synchrotron (SPS), placed in the North Area, which combines a rich physics program in various fields, like the study of the onset of deconfinement and search for the critical point of strongly interacting matter [111], hadron production measurements for more reliable description of cosmic-ray air showers for the KASCADE [115] and Auger [114] experiments and precise hadron production measurements to improve calculations of the initial neutrino beam flux in the long-baseline neutrino oscillation experiments [112, 113].

NA61/SHINE inherits its main detector from the NA49 spectrometer [116], which measured proton-proton and proton-carbon interactions at 158 GeV/c [117, 118]. Upgrades to the main spectrometer were done in order to have a faster readout. New detectors were added as well in order to achieve the goals of the planned programs. Measurements of proton-carbon cross sections at 31 GeV/c were performed in order to provide to the T2K experiment the hadron multiplicities needed to tune the neutrino flux prediction. The first physics pilot run with hadron beams was recorded in 2007 and more data were collected in 2009 and 2010 with high statistic runs. Both 2007 and 2009 data sets have been analyzed, while the analysis of the 2010 data is still ongoing. My role in the NA61/SHINE experiment was to perform the proton-carbon hadron production cross section measurement at 31 GeV/c with the 2009 data set.

### 3.1 The NA61 experimental setup

The NA61/SHINE experiment is a large acceptance spectrometer with excellent capabilities in charged momentum measurements and identification. It uses the H2 beam-line of the SPS. It consists of several detectors. Five Time Projection Chambers (TPCs), two of which placed in the magnetic field produced by two superconducting dipole magnets, and a Time-of-Flight detector (TOF) compose the tracking system. The maximum combined bending power provided by the magnets is 9 Tm. The beam trajectory is precisely measured by the Beam Position Detectors (BPDs). During the 2009 data taking the magnetic field was set to a bending power of 1.14 Tm, in order to optimize the detector geometrical acceptance and provide a  $\sigma(p)/p^2$  in the track

reconstruction of about  $5 \times 10^{-3}(\text{GeV}/c)^{-1}$ .

The schematic layout of the NA61/SHINE detector as well as the coordinate system is shown in fig. 3.4. A detailed presentation of the detector is given in [119].

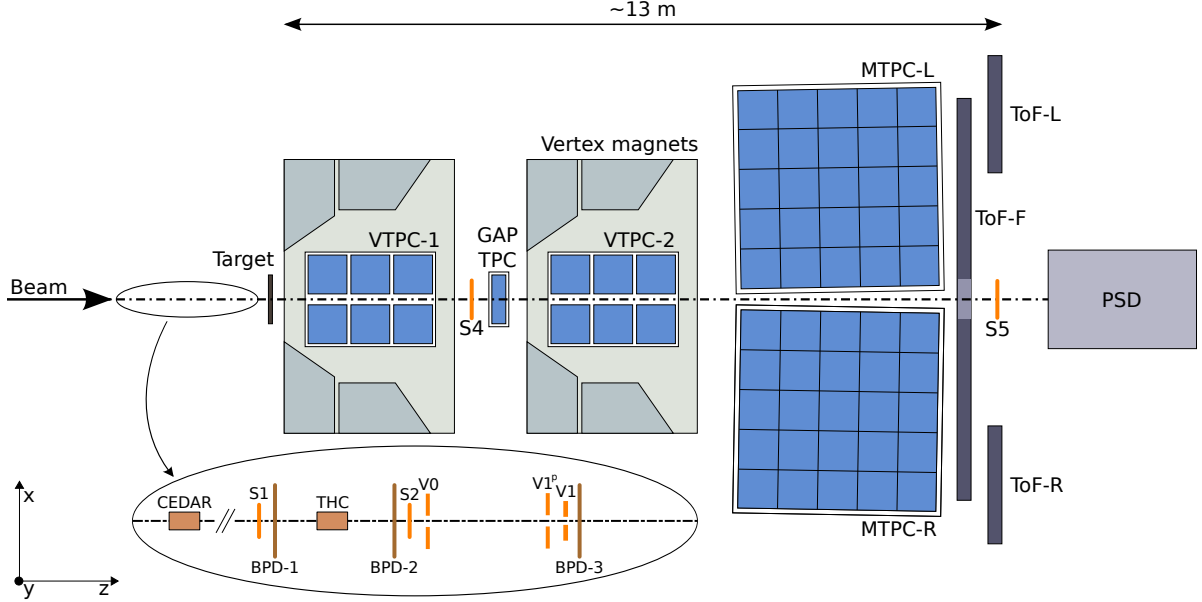


Figure 3.1: Layout of the NA61/SHINE experiment at the CERN SPS. The coordinate system is shown as well. The incoming beam direction is along the  $z$  axis. The magnetic field bends charged particle trajectories in the  $x$ - $z$  (horizontal) plane. The drift direction in the TPCs is along the  $y$  (vertical) axis.

### 3.1.1 CERN accelerator chain

The proton beam is generated from a hydrogen gas by a “duo-plasmatron” ion source and passes through a serie of accelerators. First it is focused by Radio-Frequency Quadrupoles (RFQ2) and injected in the linear accelerator (LINAC2). The 50 MeV proton beam is then distributed in the four rings of the PS Booster (PSB), which accumulates over  $10^{13}$  protons per ring. The protons accelerated up to 1.4 GeV are then sent to the Proton Synchrotron (PS) [120], that accelerates the beam up to 14 GeV/c before the injection into the Super Proton Synchrotron (SPS).

Then the beam is extracted from the SPS and focused by a set of magnets. The primary proton beam is then directed into the H2 secondary beam-line, which selects the particles in momentum, to the Experimental Hall North 1 (EHN1) where NA61/SHINE is located. The beam is focused by bending magnets (BENDs), correction dipoles (TRIMs) and quadrupoles (QUADs). Its momentum and intensity are controlled by a set of collimators. The hadrons are selected thanks to the Cherenkov Differential Counter with Achromatic Ring Focus (CEDAR) [121], that separates protons from pions and kaons. The H2 beam-line can transport charged particles in a wide range of momenta from  $\sim 9$  GeV/c up to the top SPS energy of 400 GeV/c. The proton beam used for hadron production measurements for T2K is provided with a momentum of 31 GeV/c. The CERN accelerator complex is shown in fig. 3.2.

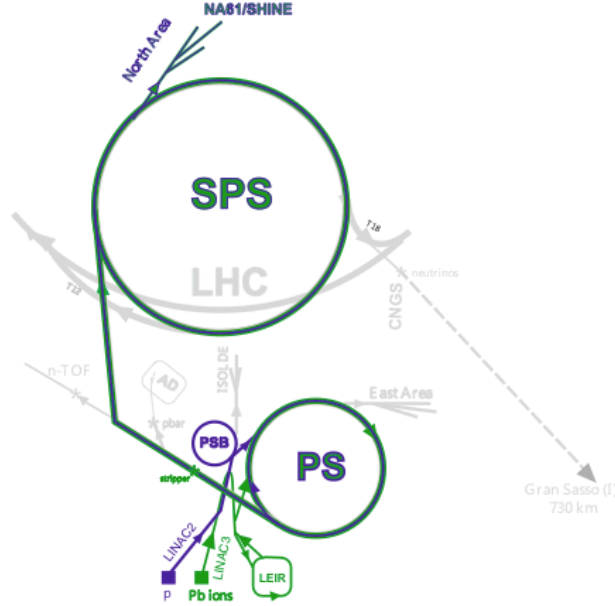


Figure 3.2: Schematic layout of the CERN accelerator complex. The colored parts are relevant for the NA61/SHINE beam operation.

### 3.1.2 Beam line and trigger system

A schematic layout of the detectors along the beamline is shown in fig. 3.3.

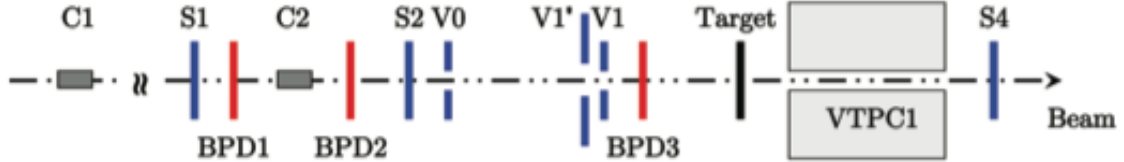


Figure 3.3: Schematic layout of the beam detectors of the beamline.

Two scintillation counters, S1 and S2, equipped with four photomultipliers directly coupled to the scintillator each, provide the beam definition and timing. In order to reduce the background of upstream interactions, three veto scintillator detectors (V0, V1 and V1p), both with a 1 cm diameter hole, are situated downstream of the S2 counter.

A Cherenkov Differential counter with Achromatic Ring Focus (CEDAR) [121] and a threshold counter (C1 and C2) are used to identify the particles in the beam and to select the proton beam with a negligible contamination: the Threshold Cherenkov counter (THC) operates at pressure lower than the proton threshold (1.65 bar) and is used in anti-coincidence in the trigger logic. The CEDAR counter, set to an absolute pressure of 3.3 bar, provides positive identification of protons with a 6-fold coincidence. Both the scintillation and Cherenkov counters provide a precise timing reference as well as the charge measurement of the incoming beam particle. The fraction of protons in the beam was about 14% and the Cherenkov detectors allowed to select a

	Thin target	T2K replica target
Material	isotropic graphite	isotropic graphite
Density [g / cm <sup>3</sup> ]	1.8395	1.831
Dimension [cm]	$2.5 \times 2.5 \times 2.0$	radius = 1.6, length = 90
Interaction length	$0.04 \lambda_I$	$1.9 \lambda_I$
z position [cm]	-580.4	-607.7

Table 3.1: Specifications of thin and T2K replica targets.

proton beam with a purity better than 99%.

### The targets

The 31 GeV/c proton beam coming from the H2 line interacts with a fixed carbon target, like at T2K, and secondary hadrons are produced. Tertiary hadrons can be produced as well by re-interactions in the target as well as in the surrounding material. First proton-carbon interactions in a 2 cm thin carbon target are produced in order to measure the total hadron production cross section as well as the multiplicities of secondary particles. Data were also collected with a T2K replica target, 90 cm long, in order to provide measurements of the produced tertiary particle components. Details of both the thin and the T2K replica target are shown in tab. 3.1.

### The interaction trigger

The beam and interaction triggers are determined by the beam counters presented in sec. 3.1.2. Up to four different triggers can be run simultaneously with a selectable 12 bit pre-scaler for each trigger. Different trigger configurations are recorded in a pattern unit on an event by event basis for off-line selection.

The proton beam before the interaction is defined by the following trigger logic (T1):

$$T_{\text{beam}}: S1 \ \& \ S2 \ \& \ \overline{V0} \ \& \ \overline{V1} \ \& \ \overline{V1^p} \ \& \ \text{CEDAR} \ \& \ \overline{\text{THC}}$$

In order to save storage space, the T1 trigger events were prescaled by a factor of 100.

A 2 cm diameter scintillation counter (S4), placed after the target between the two magnets along the expected beam trajectory, triggers the interactions of the incoming beam protons by the anti-coincidence. The minimum bias interaction trigger is based on the disappearance of the incident beam particles and is defined as

$$T_{\text{int}}: T_{\text{beam}} \ \& \ \overline{S4}$$

### The Beam Position Detectors

The transverse position of the incoming triggered proton beam is measured by three Beam Position Detectors (BDP1, BPD2 and BPD3) placed along the beam-line, upstream of the target. These detectors are proportional chambers with an active area of  $48 \times 48 \text{ mm}^2$  and Ar/CO<sub>2</sub> 85/15 gas mixture. Two orthogonal sense tungsten wire planes are alternated by three cathode planes made of  $25 \mu\text{m}$  aluminized Mylar. The outer cathode planes of these detectors are sliced into strips of 2 mm pitch which are connected to the readout electronics. Each BPD

Detector	dimensions [mm]	hole [mm]	position [m]	material budget ( $\% \lambda_I$ )
S1	$60 \times 60 \times 5$		-36.42	0.635
S2	$\phi = 28 \times 2$		-14.42	0.254
S4	$\phi = 20 \times 5$		-6.58	0.653
V0	$\phi = 80 \times 10$	$\phi = 10$	-14.16	
V1	$100 \times 100 \times 10$	$\phi = 20$	-6.72	
V1 <sup>P</sup>	$300 \times 300 \times 10$	$\phi = 20$	-6.74	
BPD1	$48 \times 48 \times 32.6$		-36.20	0.025
BPD2	$48 \times 48 \times 32.6$		-14.90	0.025
BPD3	$48 \times 48 \times 32.6$		-6.70	0.025

Table 3.2: Summary of typical beam detector parameters: dimensions, positions along the beamline (z coordinates) and the material budget (in terms of the nuclear interaction length  $\lambda_I$ ).

measures a 3-dimensional point: the two strip planes measure the transverse coordinate (x-y) and the position along the beamline correspond to the longitudinal position (z). The beam particle track is reconstructed with a resolution of  $\sim 100 \mu\text{m}$  by performing a least squares fit of straight lines to the positions measured by the three BPDs in x - z and y - z planes independently.

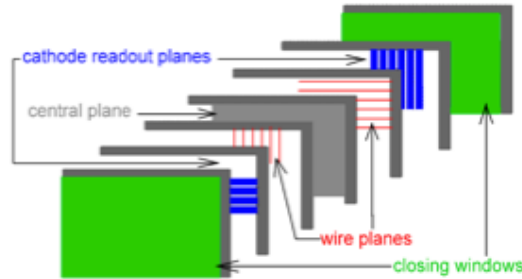


Figure 3.4: Schematic layout of the beam detectors of the beamline.

The position as well as the dimensions and material budget of the detectors along the beamline is shown in tab. 3.2

### 3.1.3 Tracking system and ToF

The main tracking system is composed by four large volume TPCs. Two Vertex TPCs (VTPC1 and VTPC2) are located between the two vertex magnets which provide a magnetic field perpendicular to the beam direction. A field cage of aluminized Mylar strips produces a uniform vertical electric field. The electrons, produced by the ionizing particles, drift toward the top cathode plates, which are subdivided into pads with an area of  $\sim 1 \text{ cm}^2$  in order to achieve a high 3-dimensional spatial resolution. Signal from different pads form a cluster. The readout chambers, shown in fig. 3.5, are in the x-y plane while the time information gives the z position.

The Vertex TPC is made of a Ar/CO<sub>2</sub> (90:10) gas mixture in a  $2.0 \times 2.5 \times 0.67$  m<sup>3</sup> box. Six proportional wire chambers on the top provide up to 72 measurements and ionization samples on the particle trajectories.

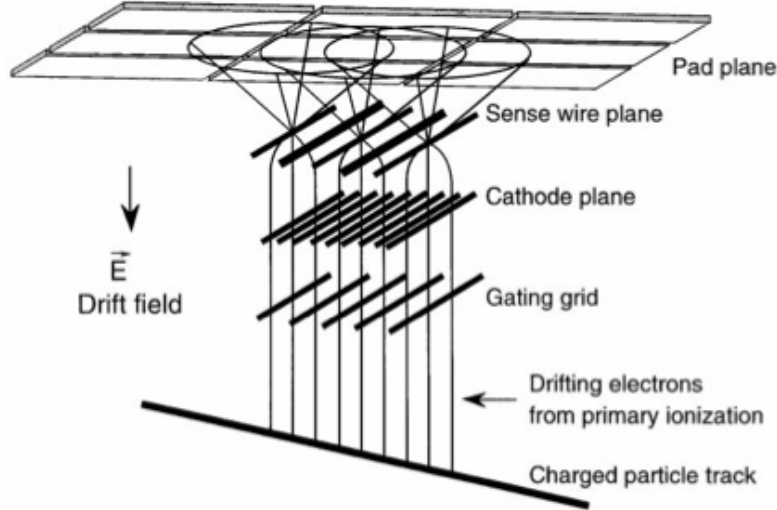


Figure 3.5: Schematic layout of the TPC readout chambers.

The Main TPC has a field cage of 1.1 m height and a readout surface at the top of  $3.9 \times 3.9$  m<sup>2</sup>. The active gas is a mixture of Ar/CO<sub>2</sub> (95:5). The readout is given by 25 proportional chambers providing up to 90 measured points and ionization samples on each particle trajectory with an accuracy of about 4% on the average ionization energy loss. A detailed description of the VTPCs and MTPCs is given in [122].

The GAP TPC (GTPC) [123] is placed between the VTPC1 and VTPC2 and detects the high momentum forward going tracks passing through the space uncovered by the VTPCs and MTPC. The material budget was minimized to 0.15% of a radiation length and 0.05% of an interaction length,

In addition to particle tracking informations, the TPCs provide also a measurement of energy loss ( $dE/dx$ ) of the detected particles. However a very good separation of kaons, protons and pions with energy higher than 1 GeV cannot be provided, since the respective Bethe-Block curves overlap. For this reason a Time of Flight system is used to improve the performance of particle identification (PID). Two Time of Flight detectors, ToF-L and ToF-R, inherited from NA49, with a total surface of 4.4 m<sup>2</sup> are placed respectively on the left and right side with respect to the beam direction. A new forward ToF (ToF-F) was constructed and placed after the MTPCs, in order to improve the geometrical acceptance. They are made of 10 scintillation bars each, with an intrinsic time resolution of about 115 ps and provide the measurement of the squared mass ( $m^2$ ) of the detected particle. A very good separation of protons, kaons and pions is given by combining the time of flight information of the particles with the energy loss measured by the TPCs.

## 3.2 Collected data

NA61/SHINE started collecting proton-carbon interaction data with a beam momentum of 30.92 GeV/c in 2007 with a low statistics pilot run. The goal was to take enough data to be able to



Target	$N_{Trig} \times 10^3$		
	2007	2009	2010
Thin	667	5598	-
T2K replica	230	$\sim 4000$	$\sim 10000$
No target	46	780	-

Table 3.3: Specifications of “thin” and “T2K replica” targets.

test the analysis method for the hadron production measurements. Data were collected with both the “thin” [124, 125] and “T2K replica” target [126]. In order to estimate the background of proton interactions occurred outside the target, data were collected also without inserting any target. Given the small amount of data, only the hadron production measurements with the “thin” target were used to tune the T2K neutrino flux.

In order to meet the T2K requirements (see sec. 2.6) a high statistic data set was collected in 2009, increasing the amount of data by a factor 10. Furthermore many improvements to the setup were done as well. In 2008 the detector was upgraded: a new interaction trigger logic was used allowing to improve the event selection and reduce the systematic uncertainty (see sec. 3.3), the DAQ as well as a new TPC readout were upgraded, the wall of the Time of Flight detector was extended and the GAP TPC detector was made available for the reconstruction of the forward-going tracks. Then a much higher beam intensity was used.

A new data run was taken also in 2010 with the “T2K replica” target.

In tab. 3.3 a summary of the collected data for T2K is shown.

In fig. 3.6 the  $\{p, \theta\}$  phase space coverage is shown for both the 2007 and 2009 data. Thanks to the upgrades and a much higher collected statistics, with the 2009 run data the phase space coverage has been improved and new particle multiplicities, like  $K_S^0$ ,  $K^-$  and protons, have been measured. Almost all the T2K phase space is covered by the NA61/SHINE experiment.

### 3.3 Hadron production cross section measurement

In this section the measurement of the total hadron production cross section of proton-carbon interactions at 31 GeV/c I performed is presented. The 2009 run data set with thin target was analyzed. This measurement is very important for the T2K neutrino flux estimation since it affects the overall flux normalization. As it will be shown in sec. 3.4, the production cross section is needed to normalize the measured hadron multiplicities. Furthermore it is an interesting measurement on its own, since it can help to better understand the hadron interaction models.

The same measurement was already performed with the 2007 run data set [127, 124]. However, even if the method is quite similar, there are several differences between the two analyses. The first difference is given by the different trigger logic which allowed for an event by event selection with the 2009 data set. Some different event selections are applied as well. Furthermore the study of the systematic uncertainties has been improved and more possible sources have been investigated. A new approach for the correction of the experimental biases is now used. The advantage is that a more reliable event selection can be applied, resulting in a drastic

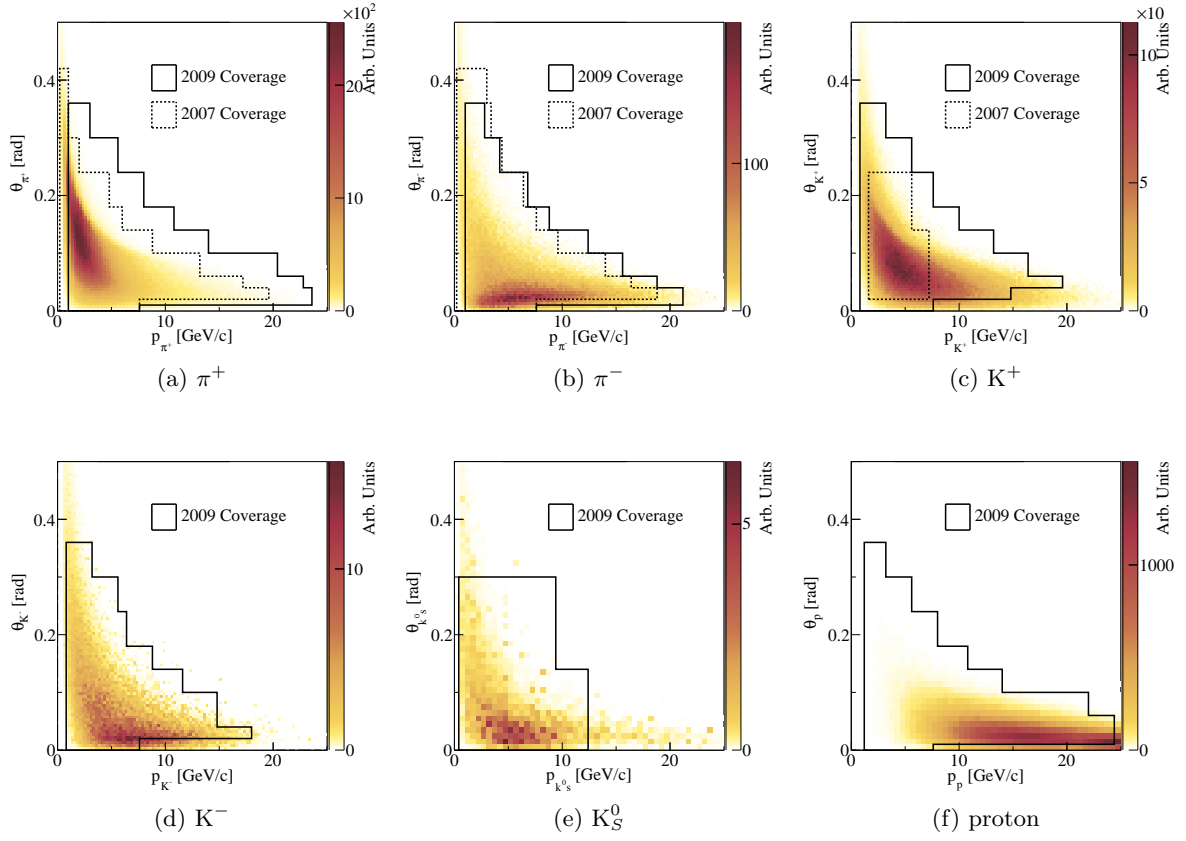


Figure 3.6: The phase space of  $\pi^\pm$ ,  $K^\pm$ ,  $K_S^0$  and  $p$  contributing to the predicted neutrino flux at the T2K far detector in the “positive” focusing configuration (color), and the regions covered by the previously published NA61/SHINE measurements [124, 125] (black dashed line) as well as by the new results obtained with 2009 run data (black solid line) are shown.

reduction of the detector systematic uncertainty. On the other hand, in 2009 it was not possible to register all the beam trigger informations for each single event and, in order to reduce the amount of storage, only 1 out of 100 beam events was randomly stored. For this reason the statistical uncertainty in 2009 was a bit larger than in 2007. However in 2007 the total uncertainty was dominated by the systematic uncertainty.

The inelastic ( $\sigma_{inel}$ ) and production cross ( $\sigma_{prod}$ ) sections have been measured. They correspond to the total cross section minus respectively the elastic ( $\sigma_{el}$ ) and quasi-elastic ( $\sigma_{qel}$ ) cross sections. However only an effective total cross section, the interaction trigger cross section ( $\sigma_{trig}$ ), which is affected by the detector configuration, like the angular acceptance, is measured. In order to obtain the final production cross section, corrections that take into account these bias must be applied.

### 3.3.1 The interaction trigger cross section

The probability to have an interaction in the target, given a beam proton in the event, is called trigger probability. The beam trigger  $T_{beam}$  is used to select events with a beam proton. The interaction in the target is assumed to occur when the beam proton does not reach the scintillator counter S4. The trigger logic  $T_{int}$  is used.

Following the notation for the trigger shown in sec. 3.1.2, the trigger probability can be calculated as

$$P_{Tint} = \frac{N(T_{beam} \wedge T_{int})}{N(T_{beam})}, \quad (3.1)$$

where  $N(T_{beam})$  is the number of events which satisfy the beam trigger condition and  $N(T_{beam} \wedge T_{int})$  is the number of events which satisfy both the beam and interaction triggers.

The interaction trigger probability was measured for both target inserted,  $P_{Tint}^I$ , and target removed,  $P_{Tint}^R$ , configurations. The beam protons can interact both inside and outside of the carbon target, e.g. in the surrounding material. By measuring the trigger probability with the target removed, the amount of the *out-of-target* background interactions can be estimated. The effective proton-carbon interaction probability is obtained with the data-driven background subtraction method used in [127]:

$$P_{int} = \frac{P_{Tint}^I - P_{Tint}^R}{1 - P_{Tint}^R}. \quad (3.2)$$

The interaction trigger cross section can be directly derived from the interaction probability of eq. 3.2:

$$\sigma_{trig} = \frac{1}{\rho L_{eff} N_A / A} P_{int} \quad (3.3)$$

where  $N_A$ ,  $\rho$ ,  $A$  are respectively the Avogadro number, the target density, its atomic number.  $L_{eff}$  is the effective target length, that takes into account the exponential beam attenuation. It is computed according to

$$L_{eff} = \lambda_{abs} \left( 1 - \exp^{-L/\lambda_{abs}} \right) \quad (3.4)$$

where the absorption length is

$$\lambda_{abs} = \frac{A}{\rho N_A \sigma_{trig}} \quad (3.5)$$

L [cm]	2
$\rho$ [g/cm <sup>3</sup> ]	$1.8395 \pm 0.0010$
$N_A$ [mol <sup>-1</sup> ]	$6.022 \times 10^{23}$
A [g/mol]	12.011

Table 3.4: Summary table of constants for the evaluation of the trigger cross section.

Substituting eq. 3.4 and eq. 3.5 into eq. 3.3, the exact formula for the trigger cross section is obtained:

$$\sigma_{trig} = \frac{A}{L\rho N_A} \cdot \ln \left( \frac{1}{1 - P_{int}} \right) \quad (3.6)$$

The values of the constants used in the formula are summarized in tab. 3.4.

The trigger cross section has been calculated after applying the event selection described in sec. 3.3.2 needed to reduce the background.

### 3.3.2 Event selection

During the 2009 run approximately 578k triggered beam events for inserted target operation (I) and 257k for removed target operation (R) were registered.

An event selection is applied in order to improve the signal over background ratio, improving the rejection of out-of-target interactions. Two quality event cuts are applied: the first one, called *BPD cut*, is based on the beam position measurements performed with the BPDs, while the second one, called *WFA cut*, was based on the beam proton passage timing measured with the Wave Form Analyzer of the S1 counter (WFA).

#### BPD cut

The informations provided by the BPDs (see sec. 3.1.2) can be used to apply quality selection on the beam position. This selection requires that the beam hits all the BPDs, releasing a well defined cluster in each of them, and that its position on the transverse  $xy$  plane is well reconstructed.

This selection rejects about 30% of the events and reduces the fraction of out-of-target background from 20% to 12%.

#### WFA cut

The Wave Form Analyzer (WFA) collects the time informations of each beam that crosses the scintillator S1, with a resolution of 100 ns, in a time window of  $\pm 25 \mu\text{s}$  around the trigger beam, the beam that triggers the event. In each event the beam consists of a bunch of protons (9 on average). All the other protons in the bunch are called *off-time beams*, which can interact as well in the target, but do not participate to the event. In fig. 3.7 both the distribution of all the recorded beam protons as well as the distribution of the number of beam protons in a event are shown.

The WFA cut rejects an event if there is at least an off-time beam close to the trigger beam within a certain time window  $\Delta T$ . The off-time beam protons affect the measurement of the trigger cross section: since the trigger logic has a time window smaller than 10 ns, the WFA cut is not able to reject these off-time beam protons because its resolution is not good

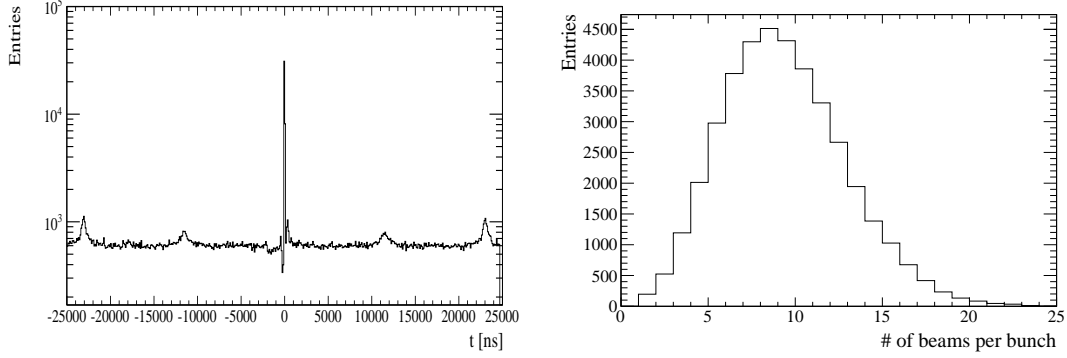


Figure 3.7: Left: time distribution of all the recorded beam protons; the trigger beam has a time reference of either 0 ns or -100 ns. Right: distribution of the number of beam protons in an event. On average there are 9 beam protons in an event.

enough. Furthermore the off-time beam particles can distort the beam position measurement in the BPDs: when an off-time beam interacts before the trigger beam, the charge clusters from the two different protons can overlap, as shown in fig. 3.8.

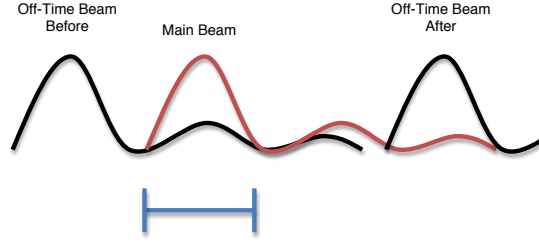


Figure 3.8: Example of how an off-time beam can distort the charge distribution of the trigger beam. The tails of the off-time beam overlaps the charge distribution of the trigger beam. When the distortion becomes not negligible the BPD cut rejects wrongly the event.

This effect can be studied by looking to the distribution of the beam times or the time difference between the trigger beam and the closest off-time beam, shown in fig. 3.9. From -2 to 0  $\mu s$  the distributions are not symmetric only when the BPD event selection is applied. This is due to the distortion of the BPD informations.

In order to obtain a reliable and suitable BPD quality selection, the WFA cut rejects all the events with at least one off-time beam particle in the time window  $t = [-2, 0] \mu s$  around the trigger beam.

### 3.3.3 Interaction probability after the event selection

The event selection rejects about 43% of events for both the target inserted and target removed samples. In tab. 3.5 the number of events after each cut is shown.

The values of trigger probabilities were found to be

$$P_{\text{Tint}}^I = (6.20 \pm 0.04)\% \quad (3.7)$$

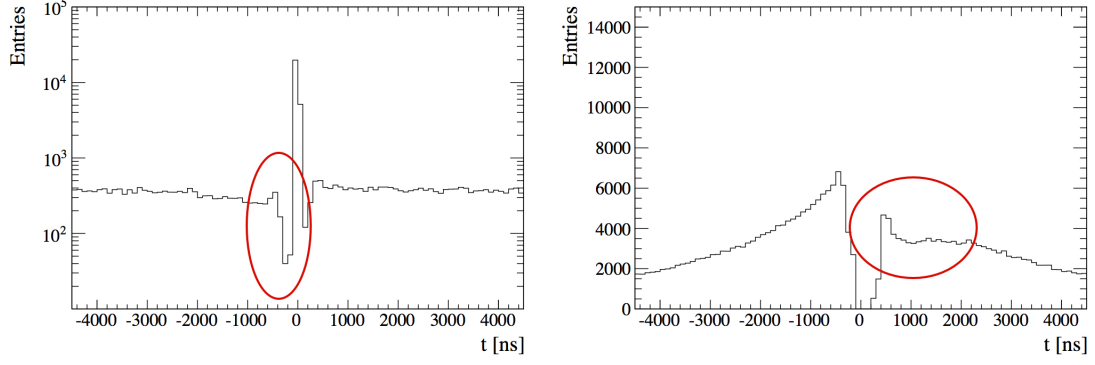


Figure 3.9: Distribution of the beam times (left) and of the time difference between the trigger beam and the closest off-time beam after the BPD quality selection. The red circles evidence the asymmetry given by the distorted measurement of the beam position by the BPDs.

	Target inserted	Target removed
$N(T_{beam})$ before cuts	577894	257430
$N(T_{beam} \wedge T_{int})$ before cuts	39644	3705
$N(T_{beam})$ after cuts	331735	145682
$N(T_{beam} \wedge T_{int})$ after cuts	20578	1110

Table 3.5: Number of beam trigger,  $N(T_{beam})$ , and interaction trigger,  $N(T_{beam} \wedge T_{int})$ , events before and after the event selection.

$$P_{\text{Tint}}^{\text{R}} = (0.76 \pm 0.02)\% \quad (3.8)$$

Thanks to the event selection, the probability to trigger an interaction occurred out of the target has been reduced by about 50%. The ratio between the target removed and target inserted trigger probabilities  $\epsilon = P_{\text{Tint}}^{\text{R}}/P_{\text{Tint}}^{\text{I}}$  is

$$\epsilon = 12.3 \pm 0.4\% \quad (3.9)$$

The interaction probability is obtained by inserting eq. 3.7 and eq. 3.8 into eq. 3.2:

$$P_{\text{int}} = 5.48 \pm 0.05\% \quad (3.10)$$

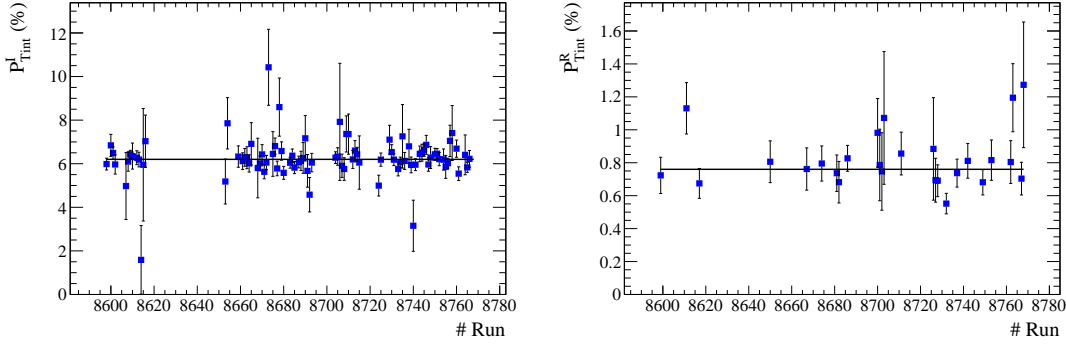


Figure 3.10: Trigger probability for target inserted (left) and target removed (right) configurations as a function of the run number after the even selection. The solid lines correspond to the measured mean values of the interaction trigger probabilities presented in eq. 3.7 and eq. 3.8. Points far away from the measured values correspond to the runs with low number of events.

After quality selection the beam position is better defined, as shown in fig. 3.11.

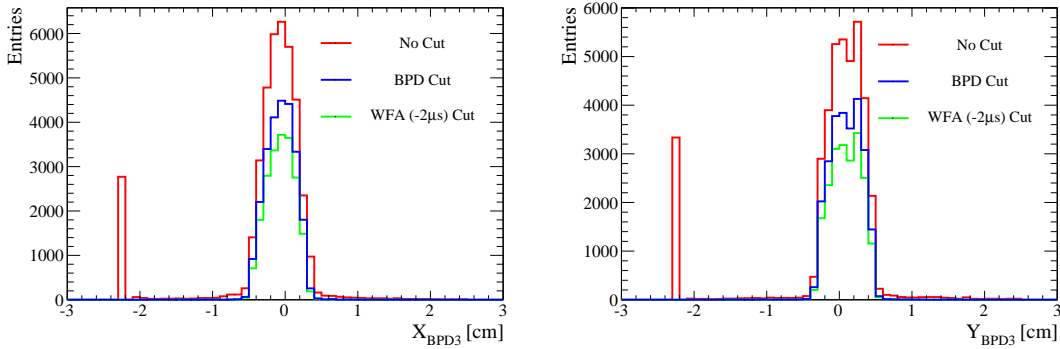


Figure 3.11: X (left) and Y (right) beam position measured by BPD3 after each event selection cut.

### 3.3.4 Systematic uncertainties on trigger cross section

The following source of detector systematic uncertainties on the trigger cross section have been carefully studied. A possible bias due to the event selection, the effect of elastic scattering of

the beam along the beam line which can preclude any interaction in the target, the pile-up, the beam contamination and the trigger efficiency have been investigated.

### Event selection

The first source of systematic uncertainty is conservatively evaluated as the difference of the measured trigger cross section before and after the event selection, in order to consider any possible bias given by the quality selection. This systematic uncertainty was taken into account in the 2007 normalization analysis as well. Now the detector is well understood and the possibility to apply selection cuts event-by-event has drastically reduced the corresponding uncertainty from 7.3 mb down to 1.0 mb, about the 0.3% of the measured trigger cross section.

### Elastic scattering

A possible bias to the measurement of trigger cross section can be due to elastic scattering along the beam line. The beam measured with the BPDs was extrapolated to the target plane. The number of beams measured with the BPDs and extrapolated outside the target area was found to be negligible.

### Pile up

Another source of systematic uncertainty is related to the pile-up in the trigger system. The trigger logic has a time resolution of about 9 ns and the probability to have two beam protons in the same trigger time window ( $P_{2\text{beam}}$ ) can be written as

$$P_{\text{beam}} = P_{\text{beam}}^{\text{true}} (1 - P_{2\text{beam}}) + (P_{\text{beam}}^{\text{true}})^2 P_{2\text{beam}} + 2P_{\text{beam}}^{\text{true}} (1 - P_{\text{beam}}^{\text{true}}) P_{2\text{beam}} \quad (3.11)$$

where  $P_{\text{beam}}^{\text{true}}$  and  $P_{\text{beam}}$  are respectively the true and measured probability that a beam proton is triggered by S4, i.e. the proton did not interact in the target. The first term of the equation describes the probability that the beam proton is triggered by S4, the second term gives the probability that two beam protons are in the same time window and both are triggered by S4 and the last term corresponds to the case where two protons are in the same time window and only one is triggered by S4. Solving the equation, neglecting the terms at the second order and substituting  $P_{\text{beam}}^{\text{corr}} = 1 - P_{\text{Tint}}^{\text{corr}}$  and  $P_{\text{beam}} = 1 - P_{\text{Tint}}$  in eq. 3.11, one obtains:

$$P_{\text{Tint}}^{\text{corr}} = \frac{P_{\text{Tint}}}{1 - P_{2\text{beam}}} \quad (3.12)$$

where  $P_{\text{Tint}}^{\text{corr}}$  is the corrected interaction trigger probability and  $P_{\text{Tint}}$  is defined as in eq. 3.1. The probability  $P_{2\text{beam}}$  was found to be  $(0.18 \pm 0.07)\%$ , thus the correction to  $\sigma_{\text{trig}}$  is negligible and no systematic uncertainty was assigned.

### Beam contamination

The beam composition at 31 GeV/c in the H2 beam-line is 83% of pions, 15% of protons and 2% of kaons. The proton beam is then selected by requiring the coincidence of the CEDAR and the anti-coincidence of the THC Cherenkov counters as explained in sec. 3.1.2. Nevertheless there could be a small contamination from  $\pi$ 's or K's that must be quantified. If some contamination still remains after the Cherenkov selection, a correction to the trigger cross section is needed,



that would correspond also to an additional systematic uncertainty. This systematic effect is investigated.

In order to quantify the beam contamination two special runs, with respectively 30253 events and 29986 events, with 30.6 GeV protons, target removed and maximum magnetic field (9 Tm) were used. Thanks to this configuration it was possible to obtain the distribution of the energy loss by the beam in the TPCs and to identify the incoming particles.

A quality selection of the tracks in the TPCs is applied. First the main vertex must be defined in the event. Since the magnetic field deflects the beam towards VTPC-2, only positive charge tracks with no clusters in VTPC-1 are required. Good quality tracks are assured by requiring a total of at least 35 clusters (15 clusters in the VTPC-2, 5 clusters in the GTPC and at least 15 clusters in the MTPC). Since the beam tracks correspond to forward-going particles, a hit in the ToF-F is required. The cut  $29 \text{ GeV}/c < P < 31 \text{ GeV}/c$  on the beam momentum is applied as well. In fig. 3.12 the event display of a beam event with target removed and maximum magnetic field is shown.

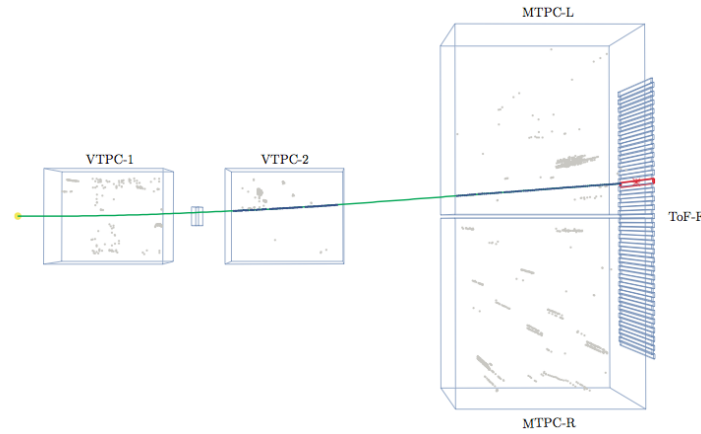


Figure 3.12: Event display for a special removed target run with full magnetic field.

Since off-time beam particles are not affected by the selection of the CEDAR and THC counters, they are affected by a much higher contamination of pions than the trigger beam. For this reason a cut on the  $y$  position of the last cluster ( $Y$ ) in the MTPC is applied.  $Y$  depends on the length of the particle drift. Indeed large  $Y$  values mean that the off-time particle passed through the MTPC earlier than the trigger beam, while small values correspond to particles that did not cross a large part of the MTPC. The selection is applied on the variable

$$\Delta Y = |Y_{\text{mean}} - Y| \quad (3.13)$$

where  $Y$  is the  $y$  position of the last MTPC cluster.  $Y_{\text{mean}}$  corresponds to the average  $y$  position of the trigger beam particles. In order to reject most of the off-time beam particles, which are not affected by the Cherenkov counter selection, and make a reliable estimation of the beam contamination, the cut  $\Delta Y \leq 1 \text{ cm}$  is applied. In fig. 3.13 the distribution of the  $y$  position of the last cluster in the MTPC as well as the selected region are shown.

In fig. 3.14 the energy loss distribution is shown. If one looks to the energy loss distribution of the off-time beam particles, by applying the cut  $\Delta Y \geq 3 \text{ cm}$ , the beam composition without the selection of the CEDAR and THC counters is observed. The first peak of the distribution

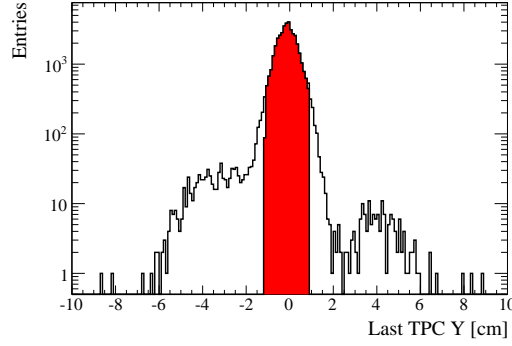


Figure 3.13: The distribution of the last cluster Y position in the MTPC is shown. The red region corresponds to events selected by the cut  $\Delta Y = |Y_{\text{mean}} - Y| \leq 1$  cm.

at about 1.2 arbitrary units corresponds to protons, while pions are centered at 1.4 arbitrary units. The kaons are centered at about 1.3 arbitrary units but, since they give a very small contribution to the total beam composition, they cannot be clearly observed. After rejecting the off-time beam particles the pion contamination is evaluated to be lower than 0.2% and is considered to be negligible. This result is in agreement with the estimation performed on the 2007 run data.

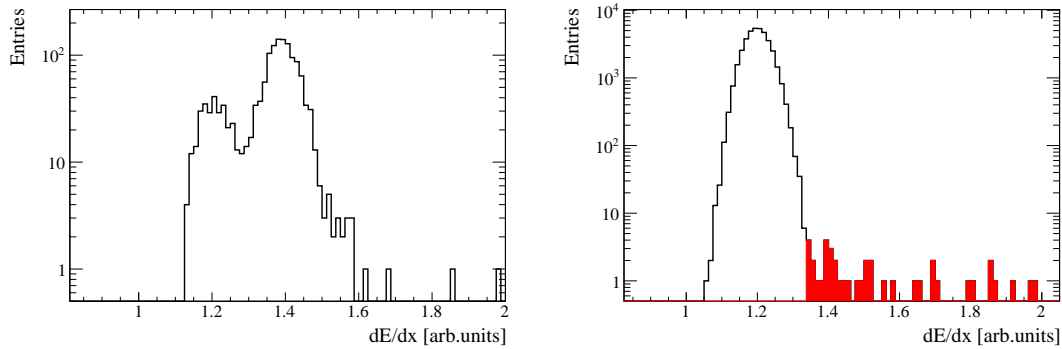


Figure 3.14: Energy loss distribution after applying the cut  $\Delta Y \geq 3$  cm (left) and  $\Delta Y \leq 1$  cm (right).

### S4 efficiency

The efficiency ( $\epsilon_{\text{trig}}$ ) of the interaction trigger was estimated using the ADC information from the S4 scintillator counter. Since the ADC signal of S4 can be distorted by off-time beam particles close in time to the triggered proton, at least one beam particle within  $\pm 4\mu\text{s}$  around the trigger beam particle was rejected.

In fig. 3.15 the distribution of the ADC signal is shown after requiring either the beam ( $T_{\text{beam}}$ ) or both interaction and beam trigger ( $T_{\text{int}} \wedge T_{\text{beam}}$ ). If a beam proton does not interact in the target and hits S4, ADC counts are larger than 70. In the case of  $T_{\text{int}} \wedge T_{\text{beam}}$ , the ADC counts are distributed as the pedestal, between 56 and 70 counts ( $\Delta_{\text{adc}}$ ).

The S4 counter efficiency is defined as the ratio between the number of ADC counts in  $\Delta_{\text{adc}}$  interval after requiring  $T_{\text{int}} \wedge T_{\text{beam}}$  and the total number of ADC counts in the  $\Delta_{\text{adc}}$  requiring

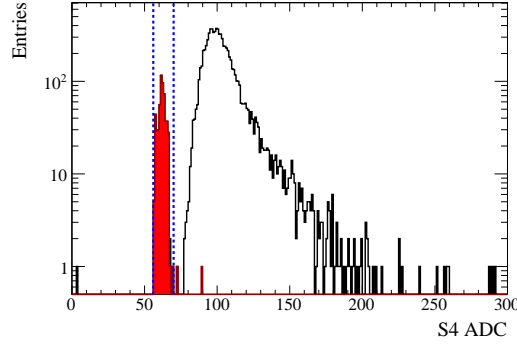


Figure 3.15: Distribution of S4 ADC counts for the beam trigger  $T_{\text{beam}}$ . Red histogram corresponds to the interaction trigger subsample  $T_{\text{beam}} \wedge T_{\text{int}}$ .

only  $T_{\text{beam}}$ . The measured value of S4 counter efficiency is  $\epsilon_{\text{trig}} = (99.8 \pm 0.2)\%$ , compatible with 100%. The corresponding systematic uncertainty is negligible. This estimate has been cross-checked also using the GTPC. Beam tracks reconstructed in the GTPC were extrapolated to the  $z$  position of S4 and the fraction of the number of extrapolations hitting S4 as well as satisfying  $T_{\text{int}}$  was estimated. This method provides another estimate of the S4 efficiency which agrees very well with the previous one.

### Measured interaction trigger cross section

The total systematic uncertainty is estimated to be 1.0 mb. The measured trigger cross section is obtained by inserting eq. 3.10 in eq. 3.3:

$$\sigma_{\text{trig}} = 305.7 \pm 2.7(\text{stat}) \pm 1.0(\text{det}) \text{ mb} \quad (3.14)$$

where “stat” is the statistical uncertainty and “det” is the detector systematic uncertainty. The result is in agreement with the measurement performed with the 2007 data within the errors:  $298.1 \pm 1.9(\text{stat}) \pm 7.3(\text{syst}) \text{ mb}$  [127, 124]. The statistical uncertainty in 2009 is a bit larger, as explained at the beginning of sec. 3.3, but the systematic uncertainty is much lower because in 2007 data it was not possible to apply an event-by-event quality selection.

### 3.3.5 Inelastic and production cross section

The inelastic cross section includes all the contributions from strong interactions except the coherent elastic proton-carbon component. Then the hadron production cross section is obtained by subtracting the quasi-elastic cross section. The measurement of both the inelastic and production cross sections are very interesting as they represent physical quantities that can be compared to measurements from other experiments, helping to improve the hadron production models.

Once the trigger interaction cross section has been measured the inelastic and production cross sections can be written as following:

$$\sigma_{\text{inel}} = \left( \sigma_{\text{trig}} - \sigma_{\text{el}}^f \right) \frac{1}{f_{\text{inel}}} \quad (3.15)$$

$$\sigma_{\text{prod}} = \left( \sigma_{\text{trig}} - \sigma_{\text{el}}^f - \sigma_{\text{qe}}^f \right) \frac{1}{f_{\text{prod}}} \quad (3.16)$$

$$\sigma_{\text{el}}^f = \sigma_{\text{el}} f_{\text{el}} \quad (3.17)$$

$$\sigma_{\text{qe}}^f = \sigma_{\text{qe}} f_{\text{qe}} \quad (3.18)$$

where  $f_{\text{el}}$ ,  $f_{\text{qe}}$ ,  $f_{\text{inel}}$  and  $f_{\text{prod}}$  are the fractions of elastic, quasi-elastic, inelastic and production events, respectively, in which all the charged particles miss the S4 counter and are accepted as interactions by the  $T_{\text{int}}$  trigger. Their values depend upon the efficiency of  $T_{\text{int}}$  for selecting elastic, quasi-elastic, inelastic and production events.  $\sigma_{\text{el}}^f$  and  $\sigma_{\text{qe}}^f$  are the contributions of elastic and quasi-elastic interactions to  $\sigma_{\text{trig}}$  which must be subtracted in order to obtain  $\sigma_{\text{inel}}$  and  $\sigma_{\text{prod}}$ . Since  $\sigma_{\text{el}}$ ,  $f_{\text{el}}$  and  $\sigma_{\text{qe}}$ ,  $f_{\text{qe}}$  are correlated, the systematic uncertainties are based on those of  $\sigma_{\text{el}}^f$  and  $\sigma_{\text{qe}}^f$ . This method differs from the one used for the 2007 data analysis [127, 124], where the simulated values of  $\sigma_{\text{prod}}$  and  $\sigma_{\text{inel}}$  were implicitly part of the corrections. This is avoided with the new approach, since only the magnitude of fractions  $f$  are estimated with MC.

The corrections to  $\sigma_{\text{trig}}$  were estimated with GEANT4.9.5 [128, 129] using the FTF\_BIC physics list (see [130] for a detailed description of the simulation).

In literature two proton-carbon elastic cross section measurements are available at energies not far from NA61: Bellettini et al. [110], at 21 GeV/c, and Schiz et al. [131], at 70 GeV/c. Bellettini et al. provided the total elastic proton-carbon cross section, while Schiz et al. published only the differential cross section, parametrized as

$$\left( \frac{d\sigma}{dt} \right)_{\text{el}} = \frac{N_0 N_N^2}{16\pi \hbar^2} e^{-b_A(-t)} \quad (3.19)$$

The parameters  $N_0$ ,  $N_N$  and  $b_A$  are provided with the corresponding uncertainties. The total elastic cross section is obtained by integrating eq. 3.19 over the whole range of  $t$ , the square of the four-momentum transfer. The systematic uncertainty on the integrated cross section is computed by making 50k toys MC: for each toy MC all the parameters of eq. 3.19 were randomly varied within their uncertainties, assuming a gaussian prior distribution, and the total elastic cross section is calculated. The total systematic uncertainty is given by the standard deviation of the distribution of the integrated cross section. The estimated elastic proton-carbon cross section at 70 GeV/c is

$$\sigma_{\text{el}}(70 \text{ GeV}/c) = 76.6 \pm 6.9(\text{sys}) \text{ mb} \quad (3.20)$$

The elastic cross section measured by Bellettini et al. is

$$\sigma_{\text{el}}(21.5 \text{ GeV}/c) = 81.0 \pm 5.0(\text{sys}) \text{ mb}$$

The elastic cross section at the NA61/SHINE momentum was obtained by a linear interpolation between these two measurements:

$$\sigma_{\text{el}}(30.92 \text{ GeV}/c) = 80.1 \pm 5.4(\text{sys}) \text{ mb}$$

The  $\pm 1\sigma$  range covers the interval [74.8, 85.5] mb. The deviations between the extremes of the interval and the nominal value of  $\sigma_{el}$  estimated with GEANT4 are taken into account as a model systematic uncertainty.

The values of elastic and quasi-elastic cross section, estimated with GEANT4, are

$$\sigma_{el}^f = 50.4^{+0.6}_{-0.5}(\text{det})^{+4.9}_{-2.0}(\text{mod}) \text{ mb} \quad (3.21)$$

$$\sigma_{qe}^f = 26.2^{+0.4}_{-0.3}(\text{det})^{+3.9}_{-0.0}(\text{mod}) \text{ mb} \quad (3.22)$$

The fractions of events accepted by the interaction trigger are:

$$f_{inel} = 0.988^{+0.001}_{-0.008}(\text{det})^{+0.000}_{-0.008}(\text{mod}) \quad (3.23)$$

$$f_{prod} = 0.993 \pm 0.000(\text{det})^{+0.001}_{-0.012}(\text{mod}) \quad (3.24)$$

where “det” is the detector systematic uncertainty obtained by performing a simulation where the position of S4 along both x and y directions is varied by 0.05 cm, the S4 radius is changed by  $\pm 0.02$  cm and finally changing the target density from 1.8395 g/cm<sup>3</sup> to 1.84 g/cm<sup>3</sup>. Also the beam divergence measured from the data is taken into account. The uncertainty “mod” is the cross section model systematic uncertainty, calculated as the largest difference between the contributions estimated for  $\sigma_{qe}^f$  with different GEANT4 physics models (FTFP\_BERT, QBBC, QGSP\_BERT and FTF\_BIC) and from measured data for  $\sigma_{el}^f$  as already described above.

### 3.3.6 Final result of inelastic and production cross section

The final results of total inelastic and production cross section are obtained by inserting eq. 3.14, eq. 3.21, eq. 3.22, eq. 3.23 or eq. 3.24 in eq. 3.15 and eq. 3.16.

The measured inelastic and production cross sections are

$$\sigma_{inel} = 258.4 \pm 2.8(\text{stat}) \pm 1.2(\text{det})^{+5.0}_{-2.9}(\text{mod}) \text{ mb} \quad (3.25)$$

$$\sigma_{prod} = 230.7 \pm 2.8(\text{stat}) \pm 1.2(\text{det})^{+6.3}_{-3.5}(\text{mod}) \text{ mb} \quad (3.26)$$

where “stat” is the statistical uncertainty, “det” is the detector systematic uncertainty and “mod” is the physics model uncertainty. The result is in a very good agreement with the analysis performed with the 2007 run data. The total uncertainty on  $\sigma_{prod}$  is  $^{+7.0}_{-4.6}$  mb, significantly smaller than the one obtained by the analysis of the 2007 data. The dominant uncertainty is given by the choice of the physics model used to correct the trigger cross section.

In fig. 3.16 a comparison of the measured inelastic and production cross sections with the previously published results is shown. They are in agreement within the uncertainty with all the measurements except for Denisov et al. [133] with which there is some tension. It could come from the different experimental techniques used to measure  $\sigma_{inel}$ . In [135] it is pointed out as different experimental approaches could lead to differences in the measured  $\sigma_{inel}$  up to 8 mb.

The cross section measurement described in this chapter has been published in [104].

## 3.4 Normalization of the measured hadron multiplicities with 2009 run data

Several measurements of particle yields in the  $\{p, \theta\}$  phase space are performed at NA61/SHINE in order to provide all the informations on the hadron production to T2K. Multiplicities have

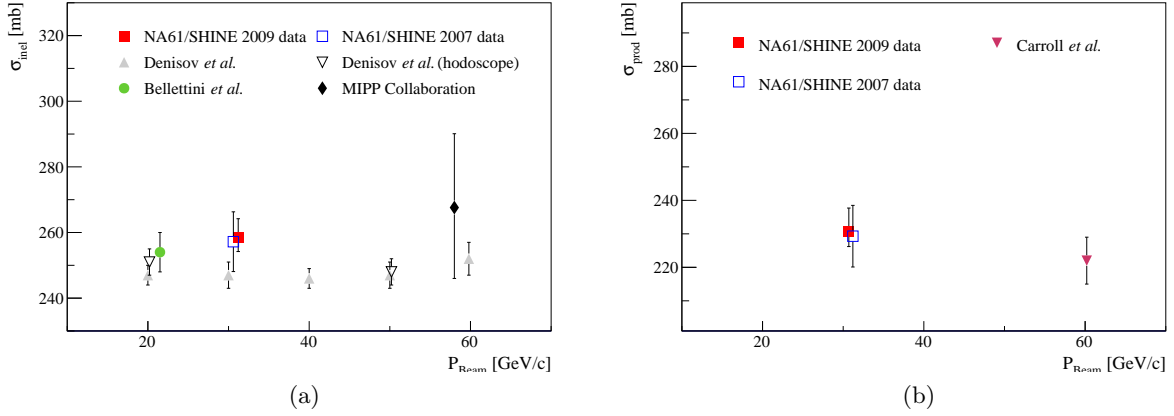


Figure 3.16: A comparison of the measured inelastic (left) and production (right) cross sections at different momenta with previously published results. Bellettini *et al.* (green full circle) [110], Denisov *et al.* (grey full triangles) [133] and MIPP (black full diamond) [134] measured the inelastic cross section while Carroll *et al.* (pink full inverted triangle) [132] result corresponds to the production cross section. Inelastic cross section measurements performed by Denisov *et al.* with the hodoscope method are shown as well (open inverted triangles). The NA61/SHINE measurements with 2007 (blue open square) and 2009 (red full square) data samples are shown.

been measured for  $\pi^\pm$ ,  $K^\pm$ ,  $K_S^0$ ,  $\Lambda$  and protons by combining the measured energy loss in the TPCs and the ToF informations, being able to have a very good particle identification above 1 GeV/c. The spectra are then corrected for geometrical acceptance, reconstruction efficiency, contamination from other particles, secondary interactions and weak decays. One of the main sources of background to  $\pi^\pm$  production is given by the decays  $K_S^0 \rightarrow \pi^+\pi^-$  and  $\Lambda \rightarrow \pi^-p$ . In order to reduce it, the measured spectra of  $K^0$  and  $\Lambda$  are used to correct the pion multiplicity.

The double differential inclusive cross section was calculated as

$$\frac{d^2\sigma_h}{dpd\theta} = \frac{\sigma_{\text{trig}}}{1-\epsilon} \left( \frac{1}{N^I} \frac{\Delta n_h^I}{\Delta p \Delta \theta} - \frac{\epsilon}{N^R} \frac{\Delta n_h^R}{\Delta p \Delta \theta} \right) \quad (3.27)$$

where  $\sigma_{\text{trig}}$  is given by eq. 3.14,  $N^I$  and  $N^R$  are the numbers of events with the target inserted and removed,  $\Delta p$  and  $\Delta \theta$  are the bin size in momentum and polar angle and  $\epsilon$  is given by eq. 3.9.

The multiplicities, in order to be used for the reweighting of the T2K flux prediction, need to be normalized to the total hadron production cross section, which includes only processes due to strong interactions. The particle spectra normalized to the mean particle multiplicity in production interactions was calculated as

$$\frac{d^2n_h}{dpd\theta} = \frac{1}{\sigma_{\text{prod}}} \cdot \frac{d^2\sigma_h}{dpd\theta}, \quad (3.28)$$

where  $\sigma_{\text{prod}}$  is given by eq. 3.26.

In fig. 3.17 the measured normalized spectra of  $\pi^+$  used for the T2K neutrino flux reweighting are shown.

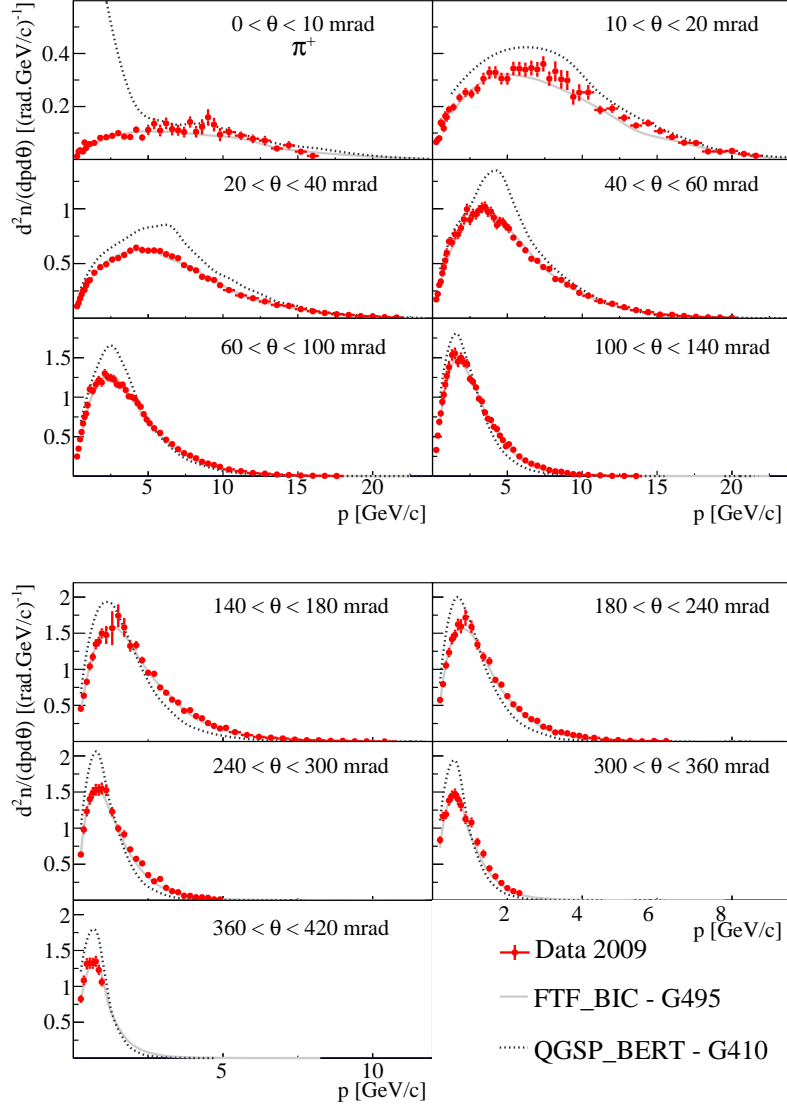


Figure 3.17: Laboratory momentum distributions of  $\pi^+$  mesons produced in proton-carbon interactions at 31 GeV/c in different polar angle intervals. Distributions are normalized to the mean  $\pi^+$  multiplicity in all production proton-carbon interactions. The vertical bars correspond to the total uncertainty, while the horizontal bars indicate the size of the momentum bin. The spectra are compared to predictions of the FTF\_BIC-G496 and QGSP\_BERT-G410 models.





## Chapter 4

# Search for short baseline $\nu_e$ disappearance at T2K

### 4.1 Overview of the analysis

In this chapter the search for short baseline  $\nu_e$  disappearance at ND280 is presented. As described in sec. 1.5 there are several hints of short baseline oscillations, which could be explained introducing one sterile neutrino (3+1 model), though some of them are discordant. The goal of this analysis is to test the reactor and the gallium anomalies. This is the first search for short baseline oscillations performed at T2K. A paper has been written on this work [136] and more details can be found in [137].

T2K has a  $\nu_\mu$  beam with a 1% of intrinsic  $\nu_e$  contamination. An optimized selection at ND280 is applied in order to obtain a sample of electron neutrinos ( $\nu_e$  sample) with high purity and efficiency. A control sample is selected in order to measure “in situ” the background. The data set corresponds to the run 1-4 data set collected at ND280 (see tab. 2.1) for a total of  $5.9 \times 10^{20}$  POT.

A deficit of the number of  $\nu_e$  depending on the reconstructed energy is searched for, in order to be sensitive to any oscillation pattern. The short baseline  $\nu_e \rightarrow \nu_s$  oscillations are described by the survival probability in the approximation of two neutrino mass states

$$P(\nu_e^{(-)} \rightarrow \nu_e^{(-)}) = 1 - \sin^2 2\theta_{ee} \sin^2 \left( 1.267 \frac{\Delta m_{\text{eff}}^2 L_\nu}{E_\nu} \right) \quad (4.1)$$

where  $\sin^2 2\theta_{ee}$  is the oscillation amplitude,  $\Delta m_{\text{eff}}^2$  ( $\text{eV}^2/c^4$ ) is the mass squared difference between the new sterile mass state and the weighted average of the active standard mass states,  $L_\nu$  (m) and  $E_\nu$  (MeV) are respectively the neutrino travelled distance and reconstructed energy. Since in the 3+1 model there is not any CP phase, the oscillation probability is exactly the same for neutrinos and antineutrinos. It is the analogue of eq. 1.33, which is instead in natural units. Examples of oscillation probability functions are shown in fig. 4.1 for different values of the oscillation parameters. In fig. 4.2 the predicted distribution of the neutrino travelled distance is shown.

In this analysis it is assumed that oscillations do not affect the  $\nu_\mu$  beam and consequently there cannot be  $\nu_\mu \rightarrow \nu_s \rightarrow \nu_e$  appearance. This assumption can be justified by the fact that

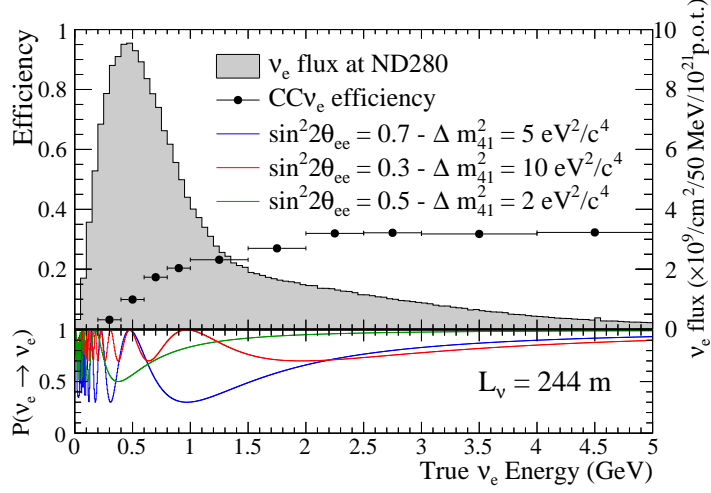


Figure 4.1: Expected  $\nu_e$  flux at ND280 and CC  $\nu_e$  selection efficiency as a function of the true neutrino energy are shown. Oscillation probabilities for different oscillation hypothesis are shown as well for the average neutrino travelled distance, 244 m.

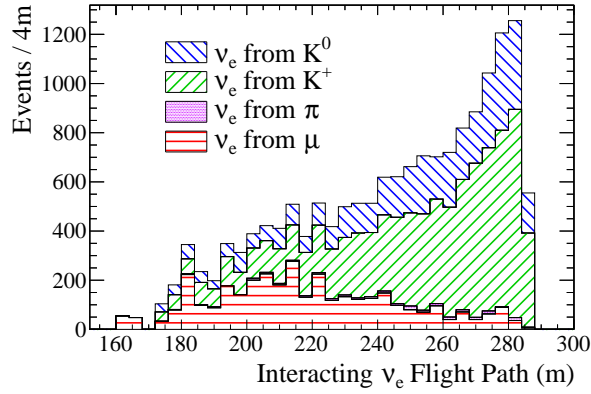


Figure 4.2: Distribution of the expected neutrino flight path for  $\nu_e$  interacting in the ND280 FV, broken down by the neutrino parent meson.

so far there are no hints of short baseline  $\nu_\mu$  disappearance from other experiments which put limits and excluded a wide range of the oscillation parameters (see sec. 1.5).

The used approach, common to all the oscillation analyses at T2K, consists to measure  $\nu_\mu$  CC interactions at ND280, assuming that oscillations did not occur. Then, taking into account the correlations between  $\nu_\mu$  and  $\nu_e$  flux and cross sections, the total systematic uncertainty in the  $\nu_e \rightarrow \nu_s$  analysis can be drastically reduced. This is possible since the ND280 CC  $\nu_\mu$  sample is mutually exclusive with both the  $\nu_e$  and the control samples used in this analysis. Once the samples are selected and systematic uncertainties are defined, the analysis templates, i.e. the expected distributions of events, are built as a function of the reconstructed energy. The parameters  $\sin^2 2\theta_{ee}$  and  $\Delta m_{\text{eff}}^2$  of the oscillation probability eq. 4.1 are inferred by comparing the templates for different oscillation hypotheses with data. Confidence intervals are built in the  $\{\sin^2 2\theta_{ee}, \Delta m_{\text{eff}}^2\}$  parameters space and the p-value with respect to the null oscillation hypothesis is computed.

## 4.2 Analysis templates

The templates used in the analysis are built as a function of the neutrino reconstructed energy in the CCQE electron hypothesis. For each event the neutrino reconstructed energy is defined in eq. 2.7, with an electron and a proton in the final state of the interaction. The templates are used to compare the MC expectation with the data.

The systematic uncertainties are represented by parameters that reweight each event depending on the neutrino flavor, interaction type, true energy and reconstructed energy. The considered neutrino interactions are: CCQE, CC1 $\pi$  resonance, CC coherent scattering (CC-Coh), all the remaining charged current interactions (CCOth) that include CC deep inelastic scattering (CCDIS), NC1 $\pi^0$  resonance (NC1 $\pi^0$ ) and all the other NC interactions (NCOth).

The expected total number of events in the “j-th” template bin of reconstructed neutrino energy is calculated with Monte Carlo (MC) as

$$n_{\text{exp}}^j(\sin^2 2\theta_{ee}, \Delta m_{\text{eff}}^2) = \sum_{i=1}^{N_{\text{events}}} P(\sin^2 2\theta_{ee}, \Delta m_{\text{eff}}^2; t, \nu) \cdot S(\vec{f}; m, t, \nu, r) \quad (4.2)$$

where  $P(\sin^2 2\theta_{ee}, \Delta m_{\text{eff}}^2; t, \nu)$ , the neutrino oscillation probability defined in eq. 4.1, is applied to each event with  $\nu_e$  or  $\bar{\nu}_e$  and depends on the neutrino true energy  $t$ .  $S(\vec{f}; m, t, \nu, r)$  is an overall, multiplicative, systematic error factor depending on the reaction mode  $m$ , the neutrino flavor  $\nu$ , the true energy  $t$ , the reconstructed energy  $r$  and a vector of parameters,  $\vec{f}$ , which includes flux, cross section and detector systematic uncertainties that are applied to each single event. The systematic uncertainties used in the analysis are presented in details in sec. 4.4.

## 4.3 The event selection

In this section the event selection, used in order to obtain the  $\nu_e$  and control samples, as well as the detector systematic uncertainties used in the analysis are described. More details can be found in [137, 138, 139]. The  $\nu_e$  sample used for this analysis is composed by electron neutrino candidates which are selected in the ND280 Tracker (FGDs, TPCs and ECAL) by combining together informations of the TPC and ECAL PID. A control sample is used to measure “in situ” the main background,  $\nu_\mu N \rightarrow \pi^0 X$  interactions, where  $N$  and  $X$  is the nucleon respectively in

Flavor	$\nu_e$ sample	Control sample
$\nu_e$	420.5	130.2
$\bar{\nu}_e$	1.8	11.6
$\nu_\mu$	234.9	1061.3
$\bar{\nu}_\mu$	8.1	32.7
Total	665.3	1235.9
Data	614	989

Table 4.1: Number of predicted events in the null oscillation hypothesis for each selected sample and each flavor are shown and compared to the selected events in the run 1-4 data set. The systematic parameter values measured with the CC  $\nu_\mu$  ND280 data shown in tab. 4.4.

the initial and final state. The  $\pi^0$  can decay into 2  $\gamma$ 's which convert into  $e^+e^-$ . If only the  $e^-$  is reconstructed, a  $\nu_e$  interaction can be faked.

The chosen range of reconstructed energy is from 0.2 to 10 GeV, since the low energy region is mostly populated by  $\nu_\mu N \rightarrow \pi^0 X$  background. In tab. 4.1 the number of predicted events is compared with the number of events observed in the run 1-4 data set.

#### 4.3.1 The electron neutrino selection

The goal of the selection is to reject the  $\nu_\mu$  interactions background. The main background is given by  $\nu_\mu N \rightarrow \pi^0 X$  interactions, inside or outside the FGDs.

The following criteria to select  $\nu_e$  candidates are applied:

- events associated to beam trigger and compatible with one of the proton bunches are selected;
- the lepton candidate is selected as the most energetic negative track of the event entering the TPCs, with momentum larger than 200 MeV/c;
- the interaction vertex of the lepton candidate is in one of the FGDs fiducial volume;
- the track, which must cross at least half of the TPC in the direction parallel to the beam, has more than 36 reconstructed points;
- electron candidates are selected based on the TPC and ECAL PID, which rejects the 99.9% of muons;
- the contamination from photons, which can convert into electron pairs ( $\gamma \rightarrow e^+e^-$ ), is reduced by requiring no other reconstructed tracks in the P0D, TPC or Barrel ECAL in the same bunch;
- events containing an electron-like positive track, starting within 100 mm of the electron candidate, and an  $e^+e^-$  pair with an invariant mass less than 100 MeV/c<sup>2</sup>, are rejected in order to reduce the  $\gamma \rightarrow e^+e^-$  contamination from 65% to 30%.

In fig. 4.1 the  $\nu_e$  selection efficiency is shown as a function of the true neutrino energy.

$\nu_e$  CC interactions are selected with an overall efficiency of 26% and a purity of 63%. About the 72% of the background, which is dominant at low energy, consists of electrons from conversion of  $\pi^0$  decay photons ( $\nu_\mu N \rightarrow \pi^0 X$ ). The remaining background is given by  $\nu_\mu$  interactions where

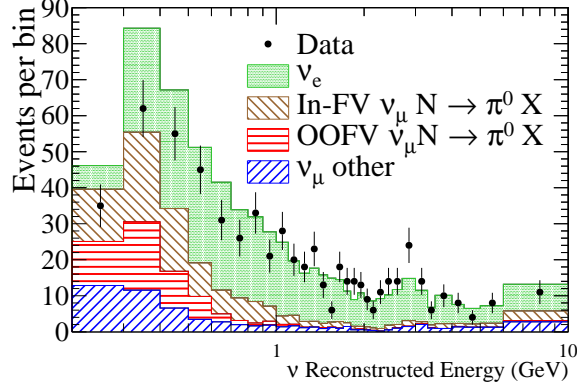


Figure 4.3: Reconstructed energy distributions of the  $\nu_e$  sample. The expected distributions is broken down by  $\nu_e$  interactions (signal), background inside the fiducial volume due to  $\nu_\mu N \rightarrow \pi^0 X$  (In-FV  $\nu_\mu N \rightarrow \pi^0 X$ ), background outside the fiducial volume due to  $\nu_\mu N \rightarrow \pi^0 X$  (OOFV  $\nu_\mu N \rightarrow \pi^0 X$ ) and all other sources of background, like muon and pion misidentification ( $\nu_\mu$  other). Both  $\nu$  and  $\bar{\nu}$  are included in the samples. Black dots represent the data with the statistical uncertainty. Systematic uncertainties are taken into account and neutrino oscillations are not assumed.

muons (14%) or protons and pions (14%) are misidentified as electrons. About 35% of the background is given by particles produced outside the FV, like in the magnet, dead materials of the FGDs and TPCs, ECal, P0D or surrounding material. They correspond to neutrino interactions on heavier nuclei (e.g. iron, aluminium, lead) with larger cross section uncertainties (30%). A total of 614  $\nu_e$  CC candidates are selected in the  $\nu_e$  sample and  $665 \pm 51$  (syst) events are expected, assuming no oscillation and with the systematic uncertainties described in sec. 4.4.

In fig. 4.3 the distribution of the reconstructed energy used in the analysis for the selected  $\nu_e$  sample is shown.

#### 4.3.2 The control sample selection

As explained above the main background contribution is given by  $\nu_\mu N \rightarrow \pi^0 X$  interactions, where the  $\pi^0$  decays into photons which convert into  $e^+e^-$ . If the positron is not reconstructed in the TPC the event is topologically equivalent to a  $\nu_e$  CC interaction.

A control sample is selected in order to measure this background component. The selection requires:

- two electron-like tracks in the TPC with a common vertex in the FGD
- the distance between the starting points of the two tracks less than 100 mm
- invariant mass less than  $50 \text{ MeV}/c^2$

The control sample has an overall selection efficiency with respect to the total number of photons converting in the FGDs of about 12% but a very high purity of photon conversion from  $\nu_\mu N \rightarrow \pi^0 X$  in NC and CCDIS interactions, about 92%. About 62% of the  $\nu_\mu$  events are interactions outside the FGDs fiducial volume (OOFV), Since the kinematics of the photons in the control and  $\nu_e$  samples are similar it provides a direct constraint to the  $\nu_e$  sample  $\nu_\mu N \rightarrow \pi^0 X$

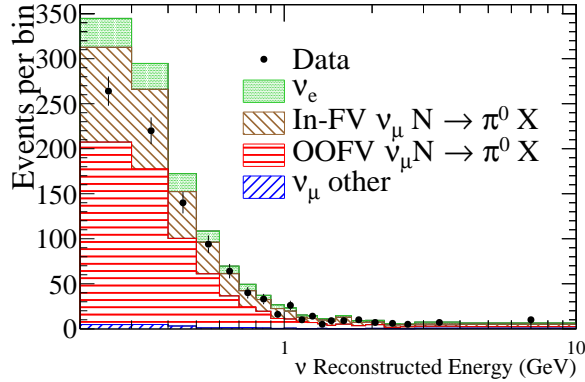


Figure 4.4: Reconstructed energy distributions of the control sample. The expected distributions are broken down by  $\nu_e$  interactions (signal), background inside the fiducial volume due to  $\nu_\mu N \rightarrow \pi^0 X$  (In-FV  $\nu_\mu N \rightarrow \pi^0 X$ ), background outside the fiducial volume due to  $\nu_\mu N \rightarrow \pi^0 X$  (OOFV  $\nu_\mu N \rightarrow \pi^0 X$ ) and all other sources of background like muon and pion misidentification ( $\nu_\mu$  other). Both  $\nu$  and  $\bar{\nu}$  are included in the samples. Black dots represent the data with the statistical uncertainty. Systematic uncertainties are taken into account and neutrino oscillations are not assumed.

background as well as most of the OOFV interactions, which is one of the main systematic uncertainties in the analysis.

The number of selected events in the control sample is 989 in data, with an expectation of  $1236 \pm 246$  (syst) where the systematic uncertainties described in sec. 4.4 are taken into account.

In fig. 4.4 the distribution of the reconstructed energy used in the analysis for the selected control sample is shown.

## 4.4 The systematic uncertainties

The systematic uncertainties of a neutrino oscillation analysis have several sources. As shown in sec. 2.5 and 2.6, the first source of systematic uncertainty is the poor knowledge of the neutrino flux. The predicted flux is tuned with the NA61/SHINE hadron production measurements performed with the 2007 run data set since the analysis of the 2009 run data was not finalized yet. Other source of systematic uncertainties are given by neutrino cross sections (sec. 2.7) and detector systematics. Each systematic parameter reweights each selected MC event as shown in eq. 4.2.

### 4.4.1 Detector systematic uncertainties

The detector systematic uncertainties are studied for the TPCs, the FGDs and ECAL, the sub-detectors used in the analysis.

The TPC systematic uncertainty is due to several sources. The first one comes from the capability to find clusters and tracks with an assigned charge. The TPC reconstruction efficiency is 99.8% and the probability to assign a wrong charge is below 1% for tracks with momenta less than 5 GeV/c. Uncertainty on the magnetic field strength as well as the momentum resolution are taken into account. Systematic uncertainties on the TPC particle identification converted into systematic uncertainties on the energy loss is computed as well.

The source of systematic uncertainties for the FGDs are the following: a potential mis-modelling of the track-finding efficiency, and the FGD mass, highly correlated to the neutrino interaction probability. A track in the TPC upstream or downstream must implies the presence of a track in the FGD as well. The efficiency with which TPC and FGD tracks in the same event are matched is taken into account. Also the uncertainty on pion secondary interactions with the other nuclei after the neutrino interaction is taken into account. This effect can misidentify a CC1 $\pi$  event as a CCQE event.

The ECAL systematic uncertainties take into account the particle identification, the energy resolution, the energy scale and the efficiency to match a reconstructed ECAL object with TPC tracks.

The effect of the detector systematic uncertainties on the analysis is evaluated with toy MC experiments. A different parameter with an uncertainty has been assigned to each systematic effect. Then all the parameters were varied randomly taking into account the existing correlations and the final covariance matrix is built. Each detector systematic parameter, which is used as nuisance parameter in the analysis, corresponds to a different bin of the covariance matrix, which depends on the selected sample, neutrino reconstructed energy and flavor, as shown in tab. 4.2. A total of 10 systematic parameters with nominal value 1 are used to normalize the number of events in each template bin. This approximated approach, that gives an effective systematic variation of the template, is needed since the implementation of each different detector systematic effect would be complicated and difficult to manage in the analysis.

Parameter	Central value	Flavor	Selected sample	Reconstructed energy (GeV)
0	1	$\nu_e, \bar{\nu}_e$	$\nu_e$ sample	0 - 0.6
1	1	$\nu_e, \bar{\nu}_e$	$\nu_e$ sample	0.6 - 2
2	1	$\nu_e, \bar{\nu}_e$	$\nu_e$ sample	2- 2.5
3	1	$\nu_e, \bar{\nu}_e$	$\nu_e$ sample	2.5 - 10
4	1	$\nu_\mu, \bar{\nu}_\mu$	$\nu_e$ sample	0 - 0.5
5	1	$\nu_\mu, \bar{\nu}_\mu$	$\nu_e$ sample	0.5 - 1
6	1	$\nu_\mu, \bar{\nu}_\mu$	$\nu_e$ sample	1 - 10
7	1	all	control sample	0 - 0.5
8	1	all	control sample	0.5 - 1
9	1	all	control sample	1 - 10

Table 4.2: Parametrization used for the detector-like parameters (detector and FSI systematic parameters). It depends on the selected sample, neutrino reconstructed energy and flavor.

#### 4.4.2 Flux systematic uncertainties

The flux systematics are normalization parameters which reweight the expected number of events and are based on the external hadron production measurements, with priority to NA61/SHINE 2007 run data as described in sec. 2.6. The flux parametrization used in the analysis is shown in tab. 2.5 (neutrino mode). It consists of a total of 25 parameters which differentiate in true neutrino energy and flavor. The flux covariance matrix that describes the uncertainty on the flux prediction is shown in fig. 2.18 (top plot).

#### 4.4.3 Cross section systematic uncertainties

Neutrino interactions can occur either in water or polystyrene scintillator and the dominant interaction topology is CC scattering off neutrons. The neutrino event generator NEUT [140] simulates the neutrino interactions at ND280.

Uncertainties in the neutrino-nucleus cross section models are estimated by comparing the NEUT prediction with external neutrino data [141]. A set of parameters, with large prior uncertainties between 20% and 40%, is assigned to each cross section.

The cross section parameters are treated in two different ways: normalization parameters, which simply modify the normalization of a given neutrino interaction, and parameters that change the cross-section in a not trivial way, and reweight the event through dedicated functions.

The normalization parameters are CCQE, CC1 $\pi$ , CC Coherent, NC1 $\pi^0$ , NC Other, that normalize the corresponding interaction mode templates,  $\sigma_{\nu_e}$ , that takes into account the uncertainty on the difference between  $\nu_e$  and  $\nu_\mu$  cross sections, due to radiative corrections which are affected by the lepton mass in the final state or differences in the nucleon form factors [143],  $\sigma_{\bar{\nu}}$ , due to the uncertainty on the difference between the  $\nu$  and  $\bar{\nu}$  cross section, the normalization of the  $\nu_\mu N \rightarrow \pi^0 X$  OOFV component and the normalization of the other OOFV events.

For the CCQE, CC1 $\pi$  systematic uncertainties a systematic parameter is assigned for each energy bin shown in tab. 4.3, while the other parameters are constant for all the energy range.

Interaction	Energy (GeV)
CCQE 1	$0 < E < 1.5$
CCQE 2	$1.5 < E < 3.5$
CCQE 3	$3.5 < E < 30$
CC1 $\pi$ 1	$0 < E < 2.5$
CC1 $\pi$ 2	$2.5 < E < 30$

Table 4.3: True energy binning used for CCQE and CC1 $\pi$  systematic parameters.

The second group of cross section systematic parameters changes the expected energy distribution through response functions that depend on the neutrino true energy, flavor, reconstructed energy, interaction mode and are different for each single event. The response function represents the weight of the corresponding event as a function of the cross section parameter and gives both a normalization and shape effect to the reconstructed neutrino energy distribution. This kind of implementation of the cross section systematic uncertainties directly modifies the cross section model used in the analysis and does not correspond to an effective impact of the cross section systematic uncertainty like the normalization parameters described above. The parameters handled with response functions are:

- CCQE axial-mass scaling factor ( $M_A^{QE}$ ), that takes into account variations of the spectra due to the uncertainty on the axial mass for CCQE interactions;
- resonance-production axial-mass scaling factor ( $M_A^{RES}$ ), the systematic uncertainty on the cross section axial mass of events with resonances;
- CC other shape (CCOth), which is applied to neutrino interactions with deep inelastic scattering and other charge current interactions not treated by the other systematic parameters, modifies the neutrino energy dependence of the cross section;



- $P_F$ , the Fermi momentum systematic uncertainty, that describes the target nucleus as a relativistic Fermi gas in CCQE interactions. A variation of the Fermi momentum can affect the energy distribution;
- the uncertainty on the nucleus binding energy ( $E_b$ ) in CCQE interactions;
- the uncertainty on the spectral function ( $S_F$ ) model (see sec. 2.7.1); the default model for the target nucleus assumes a relativistic Fermi gas model. A systematic parameter takes into account the possibility that the spectral function model ( $S_F = 1$ ) is favored by the data with respect to the relativistic Fermi gas model ( $S_F = 0$ ).
- W shape, an empirical parameter introduced in order to improve the agreement between the prediction and external data of the MiniBooNE experiment for NC1 $\pi^0$  events.
- $\pi$ -less  $\Delta$  decay ( $\Delta + N \rightarrow N + N$ ), due to the uncertainty on the fraction of resonant events in which a  $\Delta$  particle interacts and has not time to decay into pions. The NEUT software simulates a 20% of events with  $\pi$ -less  $\Delta$  decay. A variation of the number of events with  $\pi$ -less  $\Delta$  decay is taken into account.

An example of response function is given in fig. 4.5. A more detailed description of the cross section systematic uncertainties can be found in [142].

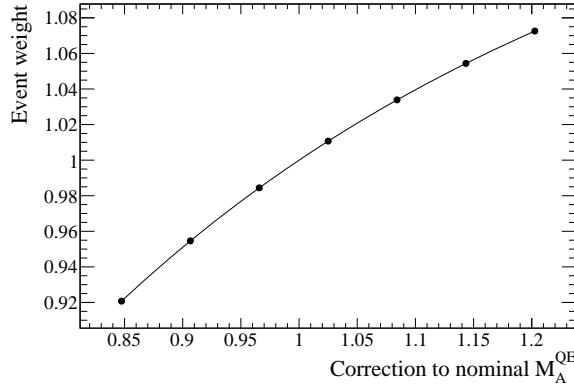


Figure 4.5: An example of response function of the  $M_A^{QE}$  cross section systematic parameter is shown for a single event. The points correspond to variation of  $-3\sigma, -2\sigma, -1\sigma, +0\sigma, +1\sigma, +2\sigma, +3\sigma$  of the parameter, where  $\sigma$  is its systematic uncertainty. The correction to the nominal  $M_A^{QE}$  value is given as input and the output event weight is computed by the interpolation between the two closest points.

#### 4.4.4 Final state interactions

The final state interaction systematic uncertainty (FSI) describes the different observables in the final state exiting the nucleus, compared to the initial state. Pions produced by CC1 $\pi$  interactions can interact inside the nucleus before being detected and the event is misidentified as CCQE. The poor knowledge on the nuclear processes involved forces the introduction of an additional systematic uncertainty. The same reconstructed energy parametrization as for the detector systematics is used. A covariance matrix is built and added in quadrature to the detector one and common parameters, with nominal value 1, are used.

#### 4.4.5 Constraining the systematic uncertainties with the near detector

The measurement of  $\nu_\mu$  CC interactions at ND280 assuming no  $\nu_\mu$  disappearance, is used to reduce the flux and the following cross section systematic uncertainties:  $M_A^{QE}$ ,  $M_A^{Res}$ , CC Other Shape, CCQE, CC1 $\pi$ , spectral function, Fermi Momentum, Binding Energy,  $\pi$ -less  $\Delta$  decay, NC1 $\pi^0$ , NC Other and CC coherent. The same technique as used in [23] is adopted. This approach is made possible by the fact that  $\nu_\mu$  and  $\nu_e$  cross sections are expected to be identical, except possible minor differences which are taken into account with the  $\sigma_{\nu_e}$  systematic parameter, and the fluxes to be highly correlated.

Three different samples of  $\nu_\mu$  CC events are selected: events without pions (CC-0 $\pi$ ), events with one  $\pi^+$  (CC- $\pi^+$ ) and other interactions which produce a  $\pi^-$ ,  $\pi^0$  or more than one pion (CC-Oth), in order to provide more sensitivity respectively to CCQE, CC1 $\pi$  resonance and CCDIS interactions. The ND280 CC  $\nu_\mu$  samples are mutually exclusive with the  $\nu_e$  and control samples. The distributions of events of the three samples, binned in muon momentum and angle with respect to the z-axis, are shown in fig. 4.6.

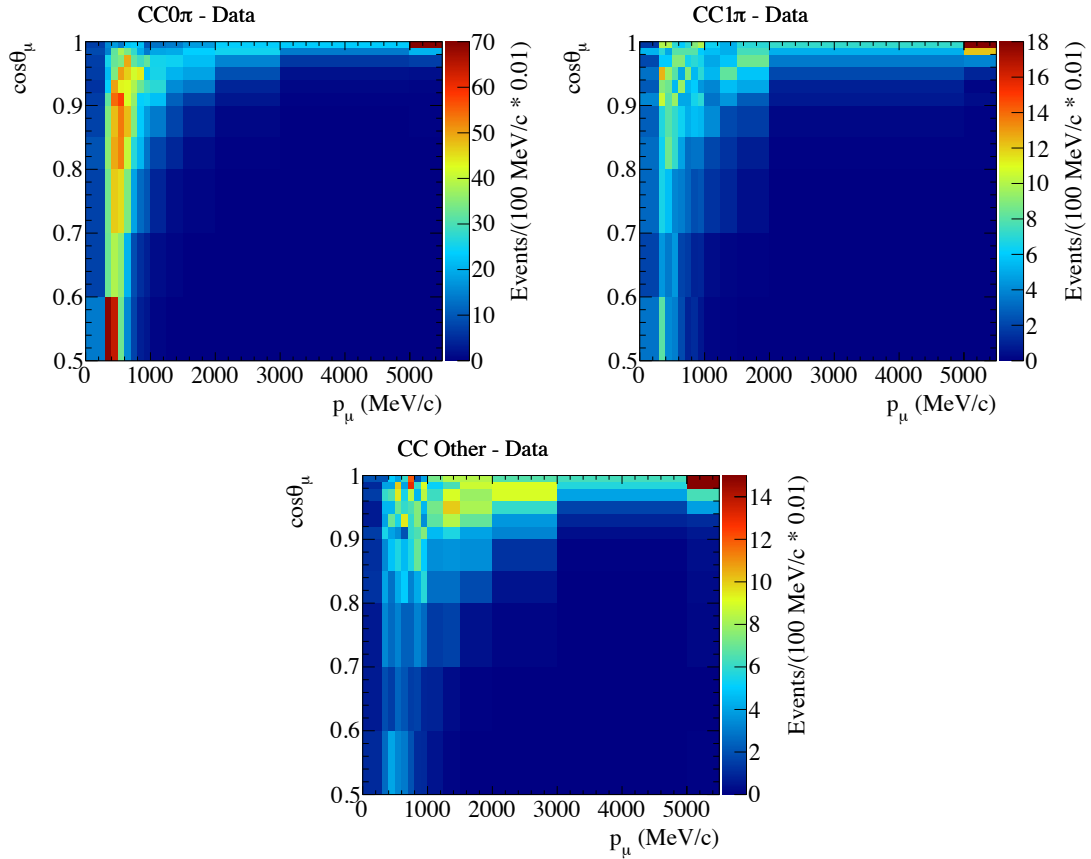


Figure 4.6: Muon momentum ( $p$ ) and angle ( $\cos\theta$ ) distributions for the CC-0 $\pi$ , CC- $\pi^+$  and CC-Oth selected data samples used for the measurement of  $\nu_\mu$  CC interactions at ND280.

The flux and cross section parameters are inferred by performing a fit which compares the expected distributions with the data without considering neutrino oscillations.

#### 4.4.6 Summary of systematic uncertainties

A total of 55 systematic parameters are used in the analysis and their uncertainties are taken into account through a covariance matrix.

The binning of the covariance matrix as well as the nominal values of the systematic parameters are shown in tab. 4.4.

Parameter	Description	Nominal value	Error
0-10	$\nu_\mu$ flux	$\sim 0.9-1.00$	$\sim 0.07-0.9$
11-17	$\nu_e$ flux	$\sim 0.9-1.01$	$\sim 0.06-0.10$
18-22	$\bar{\nu}_\mu$ flux	$\sim 0.98-1.01$	$\sim 0.09-0.14$
23-24	$\bar{\nu}_e$ flux	$\sim 0.9-1.0$	$\sim 0.07-0.16$
25	$M_A^{QE}$ (GeV/c <sup>2</sup> )	1.24	0.07
26	$M_A^{RES}$ (GeV/c <sup>2</sup> )	0.96	0.07
27	CC Other Shape (GeV)	0.23	0.28
28	Spectral Function	0.24	0.13
29	$P_F$ (MeV/c)	266.3	10.1
30	CCQE 1	0.97	0.08
31	CCQE 2	0.93	0.10
32	CCQE 3	0.85	0.11
33	CC1 $\pi$ 1	1.26	0.16
34	CC1 $\pi$ 2	1.12	0.17
35	NC1 $\pi^0$	1.13	0.25
36	NC Other	1.41	0.22
37	CC Coherent	0.45	0.16
38	$\sigma_{\nu_e}$	1	0.03
39	$\sigma_{\bar{\nu}}$	1	0.4
40	W shape (MeV/c <sup>2</sup> )	87.7	45.3
41	$\pi$ -less $\Delta$ decay	0.206	0.085
42	$E_b$ (MeV/c)	30.9	5.2
43	$\nu_\mu N \rightarrow \pi^0 X$ OOFV	1	0.3
44	Other OOFV	1	0.3
45-54	Detector + FSI	1	$\sim 0.05-0.11$

Table 4.4: Summary of nominal values and uncertainties of systematic parameters used in the fit. The parametrization of the flux and detector+FSI systematic uncertainties is shown respectively in tab. 2.5 (neutrino mode) and tab. 4.2.

The detector and FSI covariance matrices are added in quadrature. The parametrization of the Detector + FSI systematic parameters is given in tab. 4.2 and the corresponding covariance matrix is shown in fig. 4.8.

In tab. 4.5 the effect of each group of systematic uncertainties on the total number of events for each sample is shown and in fig. 4.9 the effect of a  $\pm 1\sigma$  variation of the systematic uncertainties on the analysis templates is shown.

Error source (# param.)	$\nu_e$ sample (sig+bkg)	$\nu_e$ sample (sig only)	control sample
Flux + cross section constrained (40)	4.4	5.2	6.7
Cross section unconstrained (5)	3.7	3.0	17.9
Detector + FSI (10)	5.1	5.5	5.5
Total (55)	7.6	8.1	19.9

Table 4.5: Fractional variation (RMS/mean in %) of the expected total number of events for  $\nu_e$  (all events and signal only) and control sample in the null oscillation hypothesis due to the effect of the systematic uncertainties. The following groups of systematic uncertainties are shown: flux and cross section constrained with the ND280 CC  $\nu_\mu$  data, cross section unconstrained and detector + FSI. Existing correlations between systematics are taken into account.

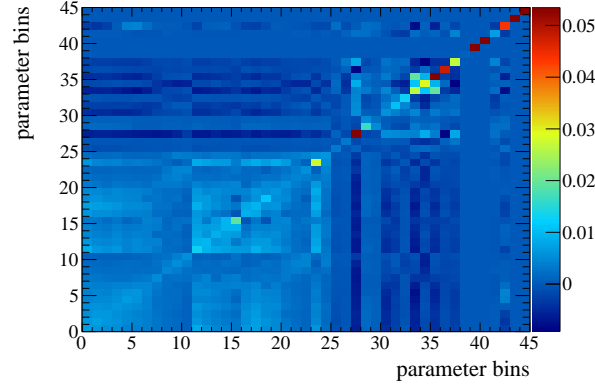


Figure 4.7: The flux and cross section covariance matrix used in the analysis is shown. The binning of the matrix, defined in tab. 4.4, is: 0-24=flux parameters, 25-44=cross section parameters.

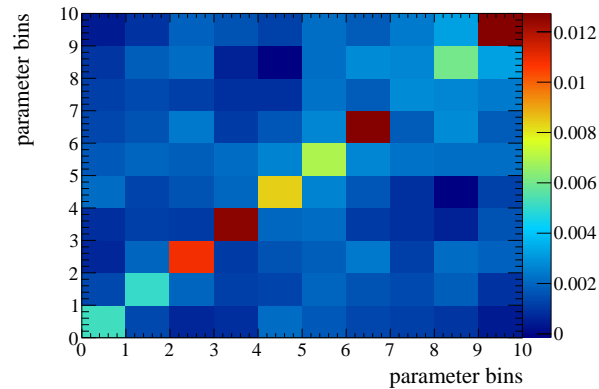


Figure 4.8: Detector + FSI covariance matrix used in the analysis. Each bin of the matrix corresponds to a different parameter, as shown in tab. 4.2.

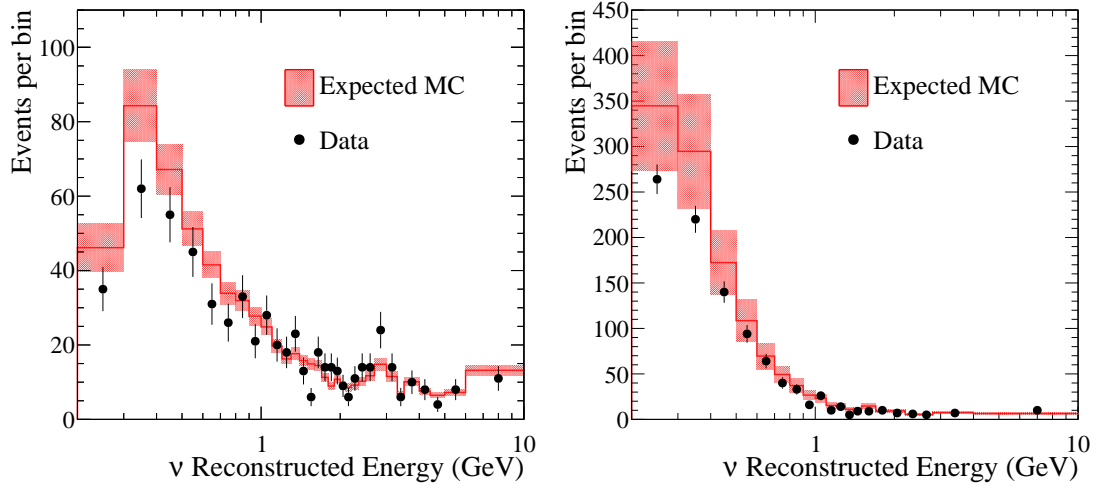


Figure 4.9: The effect of the systematic uncertainties on the expected distributions of reconstructed energy for the  $\nu_e$  (left) and control (right) samples is shown. The red bars represent the  $\pm 1\sigma$  variation of the number of events of each bin of reconstructed energy. 10k toys MC are performed taking into account the existing correlations between the systematic parameters. Black dots shown the data and the corresponding statistical uncertainties.

## 4.5 Analysis method

The oscillation parameters,  $\sin^2 2\theta_{ee}$  and  $\Delta m_{\text{eff}}^2$ , are extracted by performing a binned likelihood ratio fit, where the expected reconstructed energy distributions shown in fig. 4.3 and 4.4 are used as templates and compared to the data. The negative log-likelihood function used in the analysis is

$$-2 \ln \mathcal{L}(\vec{\theta}, \vec{f}; \text{data}) = -2 \ln \mathcal{L}_{\nu_e}(\vec{\theta}, \vec{f}; \text{data}) - 2 \ln \mathcal{L}_{\text{control}}(\vec{\theta}, \vec{f}; \text{data}) - 2 \ln \mathcal{L}_{\text{syst}}(\vec{f}) \quad (4.3)$$

where  $\vec{\theta}$  is the vector of parameters of interest, in this analysis  $\sin^2 2\theta_{ee}$  and  $\Delta m_{\text{eff}}^2$ . The first two terms compare the templates of respectively the  $\nu_e$  and control samples with the selected data and are both generally written as

$$-2 \ln \mathcal{L}(\vec{\theta}, \vec{f}; \text{data}) = 2 \sum_i^{N_{\text{bins}}} \left\{ n_{\text{exp}}^i - n_{\text{data}}^i + n_{\text{data}}^i \times \ln \left( \frac{n_{\text{data}}^i}{n_{\text{exp}}^i} \right) \right\}. \quad (4.4)$$

$N_{\text{bins}}$  is the total number of bins of the analysis template,  $n_{\text{exp}}^i$  is the number of expected events defined by eq. 4.2, while  $n_{\text{data}}^i$  is the observed number of events in the “i-th” template bin. It is function of both oscillation ( $\vec{\theta}$ ) and systematic ( $\vec{f}$ ) parameters as well as the fitted data set.  $n_{\text{data}}^i$  could correspond either to the T2K data set, used when the measurement is performed, or the Asimov data set [144], the most probable data set that corresponds to the nominal expected distribution ( $n_{\text{exp}}^i$ ) in a given oscillation hypothesis that is used for sensitivity studies, or a single toy MC experiment.

This likelihood function, built as a product of Poisson and multinomial probability density functions [145], is recommended for low statistic data analyses such as neutrino oscillations, since it works perfectly with low number of events as well as when the Gaussian regime is satisfied.

If the number of entries in each bin is distributed as Gaussian  $-2 \ln \mathcal{L}(\vec{\theta}, \vec{f}; \text{data})$  converges to a chi-square distribution. For this reason sometimes it can be also denoted as  $\chi^2(\vec{\theta}, \vec{f}; \text{data})$ .

The last term is a gaussian penalty term which constrains the systematic parameters, treated as nuisance parameters, and is defined as

$$-2 \ln \mathcal{L}_{\text{syst}}(\vec{f}) = (\vec{f} - \vec{f}_0)^T V^{-1} (\vec{f} - \vec{f}_0) \quad (4.5)$$

where  $\vec{f}_0$  is the vector of the nominal values of the nuisance parameters (see tab. 4.4),  $\vec{f}$  is the vector of the fitted nuisance parameters and  $V$  is the total covariance matrix (see fig. 4.7 and 4.8). The analysis method called *profiling* is used. The minimum of eq. 4.3 is searched for and the best-fit values (*bf*) of oscillation and nuisance parameters are obtained. The method gets rid of the nuisance parameters by fixing them to their best-fit values. It is used to say the nuisance parameters are *profiled*. More details about statistical methods can be found in app. C.1.

## 4.6 Sensitivity study

A sensitivity study for the parameters  $\sin^2 2\theta_{\text{ee}}$  and  $\Delta m_{\text{eff}}^2$  was performed using the Asimov data set in the null oscillation hypothesis which is shown in fig. 4.3 and 4.4. The *constant*  $\Delta\chi^2$  method described in app. C.2 is followed. Expected contours at 68%, 90% and 95% CL for the null oscillation hypothesis are shown in fig. 4.10.

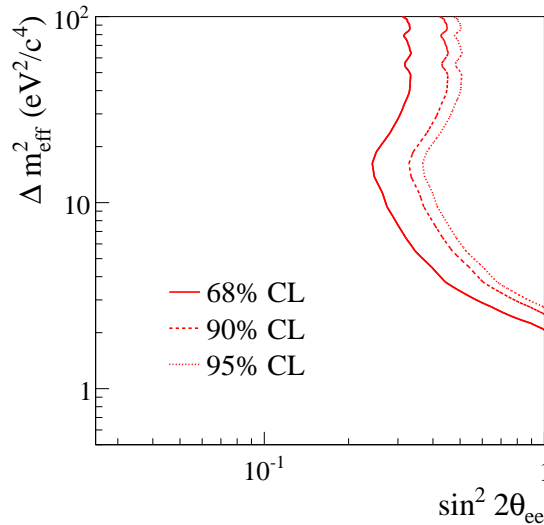


Figure 4.10: The sensitivity at 68% CL, 90% CL and 95% CL for the null oscillation hypothesis is shown for the  $\sin^2 2\theta_{\text{ee}}$  and  $\Delta m_{\text{eff}}^2$  parameters.

## 4.7 Oscillation results

The oscillation parameters are measured with a binned likelihood ratio method, minimizing eq. 4.3. The reconstructed neutrino energy templates of the  $\nu_e$  and control samples are simultaneously compared to the data, as explained in sec. 4.5.

The best-fit oscillation parameters are  $\sin^2 2\theta_{ee} = 1$  and  $\Delta m_{\text{eff}}^2 = 2.05 \text{ eV}^2/\text{c}^4$  and the  $\chi^2/\text{ndf}$  is 42.16/49, obtained by minimizing eq. 4.3. If the oscillation parameters are fixed to the null oscillation hypothesis and only the nuisance parameters are allowed to float the  $\chi^2/\text{ndf}$  is 45.86/51.

As shown in fig. 4.4 the number of expected events in the control sample is higher than the data, especially at low energy. Hence the systematic parameter corresponding to the normalization of the  $\nu_\mu N \rightarrow \pi^0 X$  OOFV component is reduced by 31%, about  $1\sigma$ . Since the control sample only contains a small fraction of  $\nu_e$  events (about 11%), it is not sensitive to  $\nu_e$  disappearance. Indeed, if the fit is performed without considering neutrino oscillations, the systematic parameter is reduced by about the same amount. The best fit reconstructed energy distributions for both  $\nu_e$  and control sample are shown in fig. 4.11.

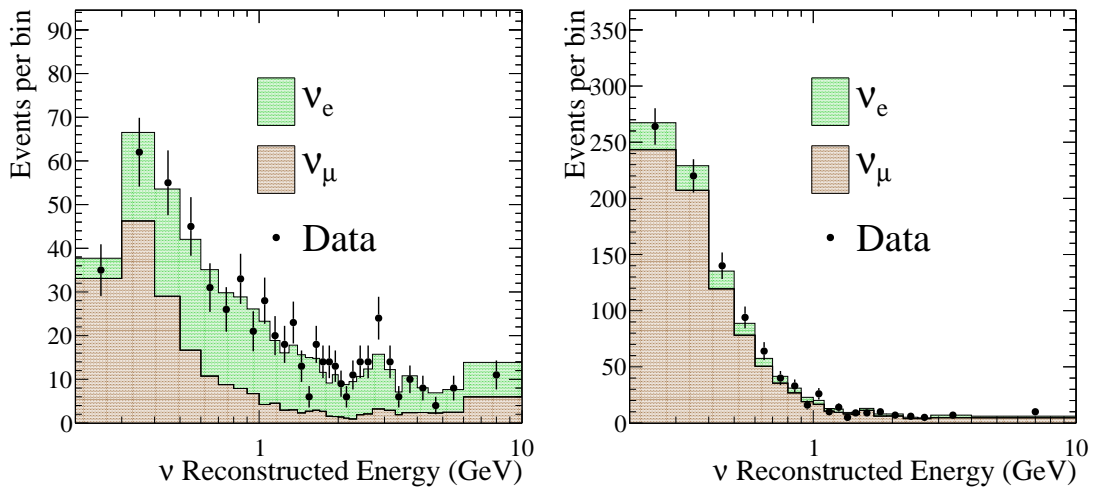


Figure 4.11: Best fit reconstructed neutrino energy distributions for the  $\nu_e$  sample (left) and the control sample (right). Both the  $\nu_e + \bar{\nu}_e$  signal (green) and  $\nu_\mu + \bar{\nu}_\mu$  background components are shown. The data with statistical uncertainties are shown by black dots.

In fig. 4.12 the ratio between the best-fit and the expected non-oscillated MC distributions is shown as a function of the reconstructed neutrino energy for both the  $\nu_e$  and the control samples. The ratios are showed both performing the fit with and without oscillations. From the figure it is clear that the control sample is independent from  $\nu_e$  disappearance since the ratios with and without oscillations are very similar. Instead in the  $\nu_e$  sample the oscillations allow to match better the data at low energy, where a deficit of events with respect to the expectation is present.

#### 4.7.1 P-value

In order to characterize how anomalous the data are with respect to the null oscillation hypothesis, the p-value has been calculated using a profile likelihood ratio as a test statistic:

1. 10k toy MC experiments were performed without oscillations, taking into account statistical and systematic uncertainties
2. for each toy eq. 4.3 is minimized first fixing the oscillation parameters to the null oscillation hypothesis ( $\sin^2 2\theta_{ee} = 0$  and  $\Delta m_{\text{eff}}^2 = 0 \text{ eV}^2/\text{c}^4$ ) and fitting only the nuisance parameters

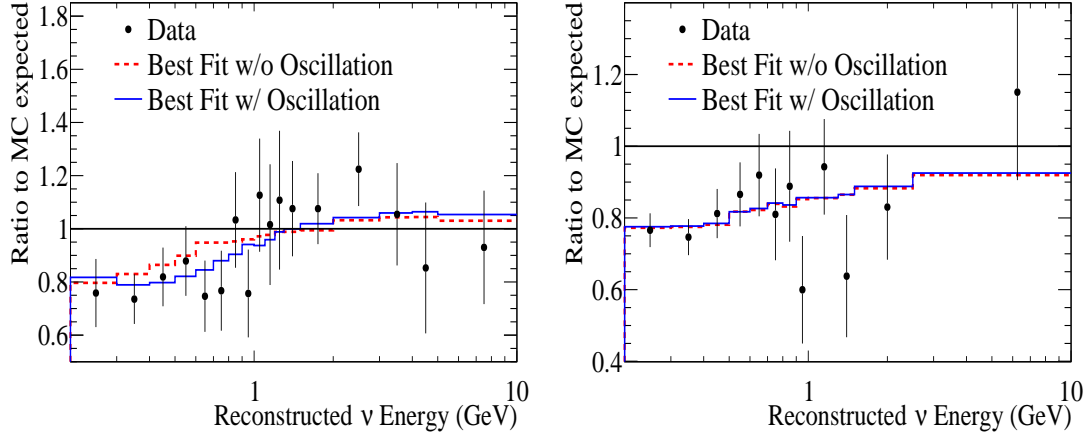


Figure 4.12: The ratio of the best fit spectrum to the expected MC distribution is shown. The blue line corresponds to the case where both nuisance and oscillation parameters are fitted, while the red line shows the case where oscillation parameters are fixed to the null oscillation hypothesis and nuisance parameters only are fitted. The plots show the  $\nu_e$  sample (left) and the control sample (right). The black line corresponds to the expected non-oscillated MC before the fit. The black dots show the data with statistical uncertainties.

$(-2 \ln \mathcal{L}_{fix})$ , then fitting both oscillation and nuisance parameters  $(-2 \ln \mathcal{L}_{bf})$ . The test statistic is calculated as

$$\Delta\chi^2(\sin^2 2\theta_{ee}, \Delta m_{eff}^2, \vec{f}; \text{data}) = (-2 \ln \mathcal{L}_{fix}(\sin^2 2\theta_{ee} = 0, \Delta m_{eff}^2 = 0; \text{data})) - (-2 \ln \mathcal{L}_{bf}(\sin^2 2\theta_{ee}, \Delta m_{eff}^2, \vec{f}; \text{data})) \quad (4.6)$$

where “data” corresponds to a single toy MC data set and the expected distribution of  $\Delta\chi^2$ ,  $\mathcal{F}(\Delta\chi^2)$ , is obtained;

3. eq. 4.6 is calculated using the run 1-4 data set and  $\Delta\chi_{obs}^2$  is obtained (see fig. 4.13).
4. the p-value is defined as

$$\text{p-value} = \int_{\Delta\chi_{obs}^2}^{+\infty} \mathcal{F}(\Delta\chi^2) d(\Delta\chi^2) \quad (4.7)$$

In fig. 4.13 the expected  $\Delta\chi^2$  distribution in the null oscillation hypothesis as well as  $\Delta\chi_{obs}^2$  are shown. The p-value is calculated as the number of entries on the right side of  $\Delta\chi_{obs}^2$  (red line) divided by the total number of toy MC experiments. A discussion about the p-value can be found in app. C.3.

The p-value of the null oscillation hypothesis is 0.085, which is not significant enough to claim any hint of oscillations.

#### 4.7.2 Confidence intervals

The two-dimensional confidence intervals in the  $\sin^2 2\theta_{ee} - \Delta m_{eff}^2$  parameter space were computed using the same method as in sec. 4.6 on the run 1-4 data set, with the only difference that critical



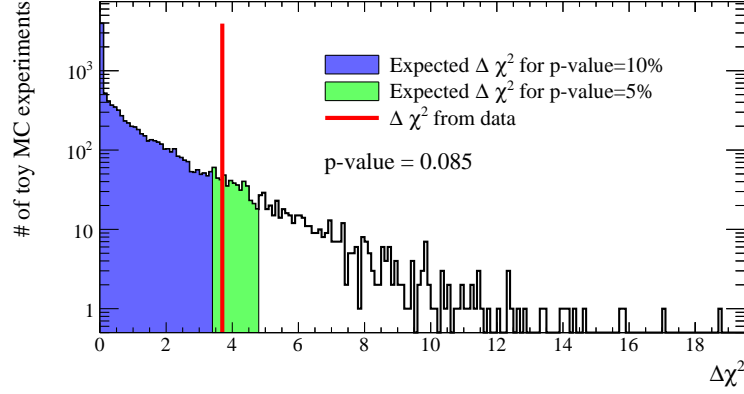


Figure 4.13: Expected distribution of  $\Delta\chi^2$  computed with 10k toys. The violet and green regions show the  $\Delta\chi^2$  values corresponding respectively to p-value = 0.1 and p-value=0.05. The red line shows  $\Delta\chi_{obs}^2$  obtained from the data. The p-value of the null oscillation hypothesis is 0.085.

values  $\Delta\chi_{crit}^2$  were calculated using the *Feldman-Cousins* method, described in app. C.2.1.

The 68%, 90% and 95% confidence regions are shown in fig. 4.14. The exclusion region at 95% CL is approximately given by  $\sin^2 2\theta_{ee} > 0.3$  and  $\Delta m_{eff}^2 > 7 \text{ eV}^2/c^4$ .

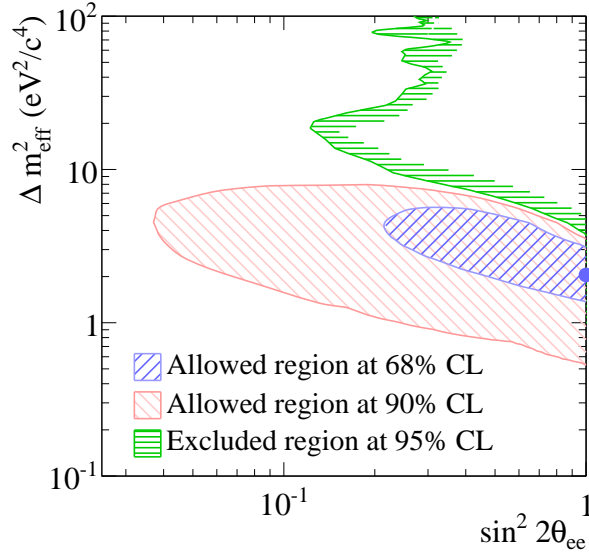


Figure 4.14: The 68% and 90% CL allowed regions and 95% CL exclusion region for the  $\sin^2 2\theta_{ee}$  -  $\Delta m_{eff}^2$  parameters measured with the T2K near detector run 1-4 data set is shown.

In fig. 4.15 the T2K confidence region at 90% and 95% CL is compared with allowed regions of the gallium and reactor anomalies as well as the excluded regions from  $\nu_e + {}^{12}\text{C} \rightarrow {}^{12}\text{N} + e^-$  scattering data of KARMEN [149, 150], LSND [151] experiments and solar neutrino and KamLAND data [152, 153, 154, 155, 156, 157, 158, 159, 160, 161, 162, 163, 164]. At 90% CL the T2K allowed region is compatible with both the reactor and gallium anomalies, but in part excluded by the global fit on the solar neutrino data. However other analyses which combine the solar neutrino data with the reactor neutrino data shows weaker limits on  $\sin^2 2\theta_{ee}$ , moving

it to about 0.20 [165, 68]. The T2K result excludes part of the gallium anomaly and a small part of the reactor anomaly allowed regions.

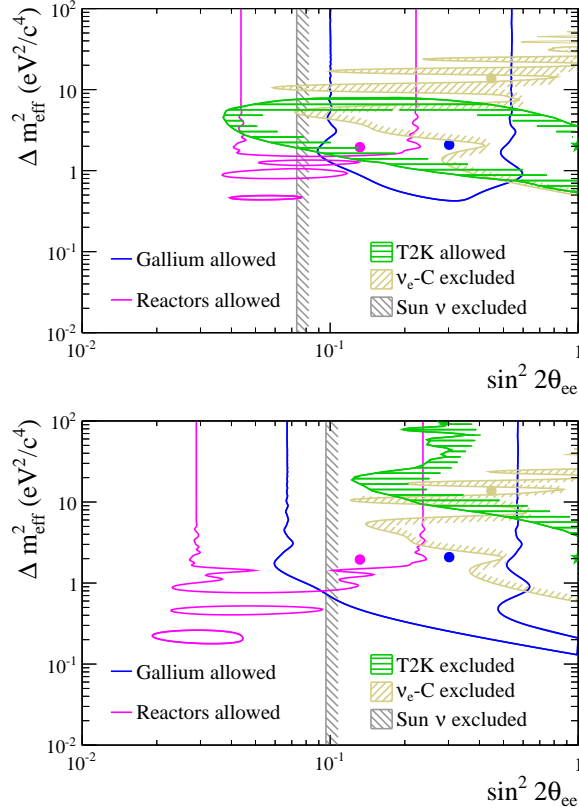


Figure 4.15: The T2K confidence interval in the  $\sin^2 2\theta_{ee}$  -  $\Delta m_{\text{eff}}^2$  parameter space at 90% CL (top) and 95% CL (bottom) is compared with allowed regions of gallium and reactor anomalies and excluded regions by  $\nu_e$ -carbon interaction data and solar neutrino data [72]. The T2K best fit is marked by a green star, while the best fit of other experimental results corresponds to circles of the same coloring as the contours.

## 4.8 Summary

A search for short baseline  $\nu_e$  disappearance, due to mixing with sterile neutrinos, has been performed with the T2K near detector run 1-4 data set. A deficit of events is present at low energy both in  $\nu_e$  and control samples, though in the second one it is within the systematic uncertainties. The best-fit oscillation parameters are  $\sin^2 2\theta_{ee} = 1$  and  $\Delta m_{\text{eff}}^2 = 2.05 \text{ eV}^2/\text{c}^4$ . The 90% CL allowed region is compatible with both the reactor and gallium anomalies. However the p-value of the null oscillation hypothesis is 0.085 and is not significant enough to claim any possible indication of new physics. The excluded region at 95% CL is approximately  $\sin^2 2\theta_{ee} > 0.3$  and  $\Delta m_{\text{eff}}^2 > 7 \text{ eV}^2/\text{c}^4$ . In order to improve the measurement and confirm or not the result it will be important to both increase the statistics as well as reducing the systematic uncertainties.

## Chapter 5

# Framework for oscillation analyses at Super-K

T2K is currently the only neutrino experiment, with NO $\nu$ A [167, 168], that have some sensitivity in the search of CP violation in the leptonic sector if  $\delta_{CP} \sim -\pi/2$ . After the first observation with  $3\sigma$  CL of non-zero  $\theta_{13}$  and the discovery of  $\nu_e$  appearance in a  $\nu_\mu$  beam (see sec. 1.3.3), now the goals of T2K are to observe for the first time  $\bar{\nu}_\mu \rightarrow \bar{\nu}_e$  appearance, which is expected by the standard 3-neutrino framework but never observed so far, and find a first hint of CP violation. In order to have a more precise and reliable measurement both neutrino and antineutrino data must be jointly analyzed. After having collected data in neutrino mode, T2K is now taking antineutrino data since May 2014 (see sec. 2.4), about  $4.011 \times 10^{20}$  POT so far. The first analysis of antineutrino data at T2K was the measurement of  $\bar{\nu}_\mu$  disappearance in a  $\bar{\nu}_\mu$  beam with the run 5-6 data [169]. The further steps are the search for  $\bar{\nu}_\mu \rightarrow \bar{\nu}_e$  appearance and finally the  $\nu/\bar{\nu}$  joint analysis, where both neutrino and antineutrino mode data are analyzed. CP violation is searched for by measuring simultaneously  $\nu_\mu$  /  $\bar{\nu}_\mu$  disappearance and  $\nu_\mu \rightarrow \nu_e$  /  $\bar{\nu}_\mu \rightarrow \bar{\nu}_e$  appearance.

In the following chapters the first search ever performed for  $\bar{\nu}_\mu \rightarrow \bar{\nu}_e$  appearance as well as the  $\nu/\bar{\nu}$  joint analysis are presented. In the  $\bar{\nu}_\mu \rightarrow \bar{\nu}_e$  appearance analysis a normalization parameter ( $\bar{\beta}$ ) that reweights only  $\bar{\nu}_\mu \rightarrow \bar{\nu}_e$  events is introduced. The significance to  $\bar{\nu}_e$  appearance is quoted by comparing the cases  $\bar{\beta} = 0$ , background only, and  $\bar{\beta} = 1$ , appearance, consistent with the oscillation parameters measured by the past T2K run 1-4 analysis [83]. The sample of  $\bar{\nu}_e$  candidates selected from the run 5-6 data set in antineutrino mode is analyzed. In the  $\nu/\bar{\nu}$  joint analysis the oscillation parameters  $\sin^2 \theta_{13}$ ,  $\sin^2 \theta_{23}$ ,  $\Delta m_{32}^2$  ( $\Delta m_{13}^2$ ) and  $\delta_{CP}$  are measured and confidence intervals are quoted. Since CP violation can be discovered only by observing different oscillations between neutrinos and antineutrinos, all the samples for both neutrino and antineutrino modes must be analyzed simultaneously.

### 5.1 Analysis templates

The procedure used to make the analysis templates is common to both the search for  $\bar{\nu}_\mu \rightarrow \bar{\nu}_e$  appearance as well as the  $\nu/\bar{\nu}$  joint analysis. Binned templates are used to fit the data and are built as the number of predicted neutrino events at Super-K as a function of either the reconstructed neutrino energy ( $E_{reco}$ ) in the  $\bar{\nu}_\mu \rightarrow \bar{\nu}_e$  appearance analysis or  $E_{reco}$  and  $\theta$ , the angle between the neutrino beam direction and the outgoing lepton produced in the interaction, in the  $\bar{\nu}/\nu$  joint analysis.

In general, given a selected sample of neutrino events, the predicted number of events in each bin of the template,  $N_{SK}$ , is function of both the oscillation parameters,  $\vec{\sigma}$ , and the systematic parameters,  $\vec{f}$ , and is computed as follows:

$$N_{SK}(\vec{\sigma}, \vec{f}; r, \theta) = \sum_m \sum_t \sum_\nu P(\vec{\sigma}; t, \nu) \cdot T(f_E^{SK}; r \rightarrow r) \cdot S(\vec{f}; m, t, \nu, r, \theta) \cdot N_{SK}^{MC}(m, \nu, t, r, \theta) \quad (5.1)$$

where  $N_{SK}^{MC}(m, \nu, t, r, \theta)$  is the input Super-K Monte Carlo (MC) template containing the number of selected events with true neutrino interaction mode  $m$  and neutrino flavor  $\nu$  in the true energy bin  $t$  and the reconstructed energy bin  $r$ .  $\vec{\sigma}$  is the vector of oscillation parameters.  $S(\vec{f}; m, t, \nu, r, \theta)$  is an overall, multiplicative, systematic error factor depending on the reaction mode  $m$ , the neutrino flavor  $\nu$ , the true energy bin  $t$ , the reconstructed energy bin  $r$  and the angle  $\theta$  and a vector of nuisance (systematic) parameters  $\vec{f}$ , which includes flux, cross section and detector systematic uncertainties.  $T(f_E^{SK}; r \rightarrow r)$  is a transfer function describing the migration of events between the reconstructed energy bins  $r$  and  $r$  due to the uncertainty in the Super-K reconstructed energy scale, expressed here in terms of the nuisance parameter  $f_E^{SK}$ . Finally,  $P(\vec{\sigma}; t, \nu)$  is the 3-flavour oscillation probability, described by eq. 1.8, 1.9 and 1.10, applied to the true energy bin  $t$  of the Super-K MC template which corresponds to the neutrino flavor  $\nu$ . In sec. 5.4 the systematic parameters  $\vec{f}$  and  $f_E^{SK}$  will be discussed more in detail.

Different template parametrizations have been used for the  $\bar{\nu}_\mu \rightarrow \bar{\nu}_e$  appearance and joint fit analyses and they will be treated respectively in chap. 6 and chap. 7.

The neutrino interaction modes ( $m$ ) considered are: CCQE, CC MEC, CC1 $\pi$ , CC coherent, CC other, NC1 $\pi^\pm$ , NC1 $\pi^0$ , NC coherent, NC other and NC 1 $\gamma$ <sup>1</sup>, produced by radiative decay of weak resonances, mainly  $\Delta \rightarrow N\gamma$ . The flavor components  $\nu$  are:  $\nu_\mu$ ,  $\nu_e$ ,  $\bar{\nu}_\mu$ ,  $\bar{\nu}_e$ , oscillated  $\nu_\mu \rightarrow \nu_e$ , oscillated  $\bar{\nu}_\mu \rightarrow \bar{\nu}_e$  and NC, that is not affected by oscillations since the flavor cannot be distinguished.

## 5.2 Fit method

A binned likelihood-ratio method is adopted as in sec. 4.5. For each selected sample a different template, calculated as shown by eq. 5.1, is used and a likelihood term  $\mathcal{L}_s(\vec{\theta}, \vec{f}; \text{data})$  is calculated using eq. 4.4. The total likelihood is given by the product of the likelihood terms of each selected sampled,

$$\mathcal{L}(\vec{\theta}, \vec{f}; \text{data}) = \prod_{s=1}^{N_{samples}} \mathcal{L}_s(\vec{\theta}, \vec{f}; \text{data}) \quad (5.2)$$

where  $N_{samples}$  is the number of selected samples used in the analysis. The adopted statistical method is quite different from what was used in the search for  $\nu_e \rightarrow \nu_s$  disappearance at ND280: instead of the fully frequentist approach (*profiling*) described in sec. 4.5, now a hybrid bayesian-frequentist method, called *marginalization*, is used [147]. The nuisance parameters are *marginalized* and the so-called marginal likelihood, that depends only on the parameters of interest  $\vec{\theta}$ , is computed as

---

<sup>1</sup>The NC 1 $\gamma$  component was included in the NC other component during the  $\bar{\nu}_\mu \rightarrow \bar{\nu}_e$  appearance analysis at Super-K and the oscillation analysis at ND280.

$$\mathcal{L}_{\text{marg}}(\vec{\theta}; \text{data}) = \int_F \mathcal{L}(\vec{\theta}, \vec{f}; \text{data}) \pi(\vec{f}) d\vec{f} = \frac{1}{n} \sum_{i=1}^n \mathcal{L}(\vec{\theta}, \vec{f}_i; \text{data}) \quad (5.3)$$

where  $\mathcal{L}(\vec{\theta}, \vec{f}; \text{data})$  is defined by eq. 5.2,  $n$  is the number of toys MC,  $\vec{f}$  is the vector of nuisance parameters,  $\pi(\vec{f})$  is the corresponding prior distribution, that includes correlations between the parameters as well, and  $\vec{f}_i$  is the particular set of nuisance parameters randomly extracted in one toy MC according to  $\pi(\vec{f})$ . Many toys are performed in order to sample most of the nuisance parameters space  $F$ . When marginalization is used the gaussian penalty term of eq. 4.5 is not included any longer, since the nuisance parameters  $\vec{f}_i$  are extracted according to their priors.

In order to simplify the notation, since  $-2 \ln \mathcal{L}(\vec{\theta}; \text{data})$  converges to a  $\chi^2(\vec{\theta}; \text{data})$  distribution when the Poissonian distribution of the number of events in each bin behaves as gaussian, the marginal log-likelihood will be denoted as

$$\chi_{\text{marg}}^2(\vec{\theta}; \text{data}) = -2 \ln \mathcal{L}_{\text{marg}}(\vec{\theta}; \text{data}) \quad (5.4)$$

Finally  $\chi_{\text{marg}}^2(\vec{\theta}; \text{data})$  is minimized and the best-fit parameters  $\vec{\theta}$  are found. The advantage of this method compared to the profiling is that the full prior information of the systematic parameters is exploited in the fit. When  $\chi_{\text{marg}}^2(\vec{\theta}; \text{data})$  is calculated, also the parameters of interest  $\vec{\theta}$  can be constrained using a gaussian penalty term, in the same way as it is done in sec. 4.5. In this case the total likelihood function becomes

$$\chi_{\text{constr}}^2(\vec{\theta}; \text{data}) = \chi_{\text{marg}}^2(\vec{\theta}; \text{data}) + (\vec{\theta} - \vec{\theta}_0)^T V^{-1} (\vec{\theta} - \vec{\theta}_0) \quad (5.5)$$

where  $\vec{\theta}_0$  is the nominal value of the parameters of interest,  $\vec{\theta}$  is its fitted value and  $V$  is the covariance matrix which relates all the free parameters. If the constrained parameter  $\theta^{\text{constr}}$ , included in  $\vec{\theta}$ , is not correlated with the other parameters of interest,  $V$  is reduced to the uncertainty  $\Delta\theta^{\text{constr}}$ , and eq. 5.5 becomes

$$\chi_{\text{constr}}^2(\vec{\theta}; \text{data}) = \chi_{\text{marg}}^2(\vec{\theta}; \text{data}) + \frac{(\theta^{\text{constr}} - \theta_0^{\text{constr}})^2}{(\Delta\theta^{\text{constr}})^2} \quad (5.6)$$

A more detailed discussion on the statistical methods, *marginalization* and *profiling*, is given in app. C.1.

### 5.3 Event selection

Super-K is a Cherenkov detector that cannot distinguish neutrinos from antineutrinos, since it is not magnetized. However, thanks to the hadron production measurements (see sec. 2.6) and the measurement of the neutrino interactions at the near detector (see sec. 5.4.6), the neutrino flux composition is well known. Two different event selections for both neutrino and antineutrino modes are applied and the following samples are obtained:

- muon-like samples, that contains  $\nu_\mu$  or  $\bar{\nu}_\mu$  candidates
- electron-like samples, which includes  $\nu_e$  or  $\bar{\nu}_e$  candidates

CCQE-like events, with only a lepton in the neutrino interaction final state, are selected for both samples, since the energy region around the expected oscillation maximum is mostly populated by CCQE events. Since in Super-K each particle is observed as a different Cherenkov light ring, events with more than one ring are rejected. In CCQE-like events only the lepton ring is observed because the proton produced in the final state rarely reaches Cherenkov threshold. In antineutrino interactions a neutron is produced and it can never be detected because neutral.

In fig. 5.1 the event display of  $\nu_\mu$  CCQE,  $\nu_e$  CCQE and NC1 $\pi^0$  candidates are shown. The first two event displays show one single Cherenkov ring. The muon-like ring is better defined than the electron-like ring, since the electron traveling in water produces photons and consequently other electrons creating an envelope of rings. When NC1 $\pi^0$ -like interaction occurs, two Cherenkov rings are produced. This is one of the most important background sources, since these events can be mis-identified as a  $\nu_e$  CCQE interaction.

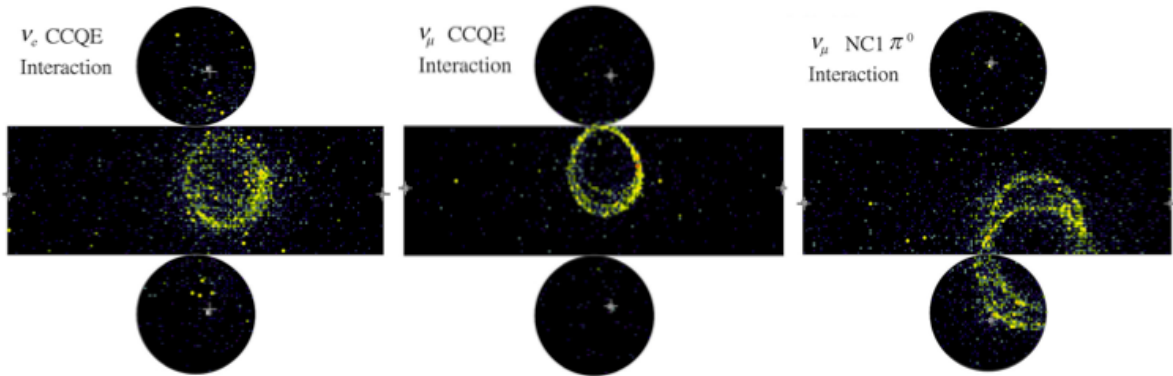


Figure 5.1: Event displays for the Super-K simulation of  $\nu_e$  CCQE (left),  $\nu_\mu$  CC (middle) and NC1 $\pi^0$  (right) event.

### 5.3.1 Electron-like samples

A sample of  $\nu_e/\bar{\nu}_e$  candidates is selected by looking for a Cherenkov ring compatible with an electron in the final state. An irreducible background for  $\nu_\mu \rightarrow \nu_e$  events is the intrinsic contamination of  $\nu_e$  in the  $\nu_\mu$  beam. Another important source of background is given by the NC1 $\pi^0$  events. Indeed the  $\pi^0$  decays into two photons and, if one of the two rings is not properly reconstructed, it can be misidentified as an electron.

The following event selection is applied:

- events are timed with respect to the leading edge of the beam spill, taking into account the time of flight of the neutrino and all the possible sources of delay;
- the neutrino event is fully contained in the fiducial volume (FCFV). There is little or no outer detector activity (fully contained). Then the distance from the reconstructed vertex to inner detector wall is larger than 200 cm and the visible energy, i.e. the sum of energy from all the rings identified in the event, assuming the rings to be electron-like, is required to be above 30 MeV (fiducial volume);
- the number of rings found by the ring counting algorithm is one;
- the Cherenkov ring is identified as electron-like by the PID algorithm;

- the visible energy is greater than 100 MeV. This cut rejects low energy events, such as NC backgrounds and Michel electrons produced by invisible muons;
- the number of decay electrons is zero. A decay electron can be produced by invisible or un-identified muons or pions, indicating either  $\nu_\mu$  or CCnQE events. Such background can be rejected even when the muon or pion does not exceed the Cherenkov threshold. The efficiency for tagging electrons from muon decays within the inner detector is 89.1%;
- events with reconstructed neutrino energy less than 1250 MeV are selected, since higher energy neutrinos are mainly from  $\nu_e/\bar{\nu}_e$  beam contamination;
- a large fraction of NC1 $\pi^0$  background is rejected by the cut  $\ln(L_{\pi^0}/L_e) < 175 - 0.875 \times m_{\gamma\gamma}$ , where  $L_{\pi^0}$  and  $L_e$  are the maximum likelihoods in the hypothesis the ring is produced respectively by an electron and a  $\pi^0$ . The event reconstruction framework, fitQun [170], performs the maximum likelihood fit of particle kinematic parameter, using the charge and time information from the PMT's in the detector.

Exactly the same selection is applied for both neutrino and antineutrino modes. In fig. 5.2 the number of events passing each selection stage is shown.

In neutrino mode the nominal expected numbers of  $\nu_\mu \rightarrow \nu_e$  appearance and background events in the final electron-like sample for  $\sin^2 2\theta_{13} = 0.1$  and  $\delta_{CP} = 0$  obtained by reweighting the neutrino flux with external hadron production data (see sec. 2.6.1), are 19.26 and 4.96 respectively. The background comes predominantly from intrinsic beam  $\nu_e$  CC interactions. After all the selection cuts 31 events were selected in the run 1-6 data sample.

In antineutrino mode the nominal expected numbers of  $\bar{\nu}_\mu \rightarrow \bar{\nu}_e$  appearance and background events are 2.51 and 1.67 respectively. As for the neutrino mode, most of the background comes from intrinsic beam  $\bar{\nu}_e$ . In the run 5-6 data sample 3 events were selected.

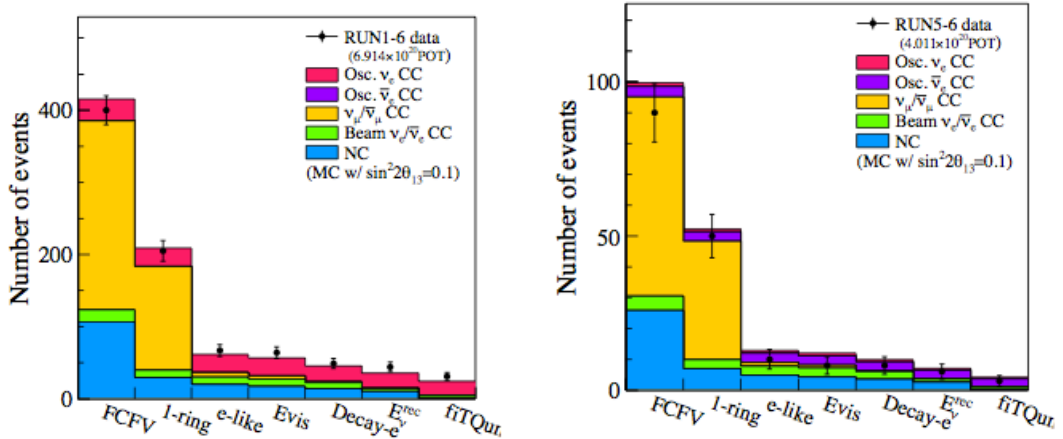


Figure 5.2: The number of electron-like events passing each selection stage is shown for both neutrino (left) and antineutrino (right) modes. Both distributions correspond to the statistic collected during runs 1-6. The data are shown by the black dots. MC distributions are made using  $\sin^2 2\theta_{13} = 0.1$  and  $\delta_{CP} = 0$ . The expected neutrino flux is reweighted with external hadron production data (see sec. 2.6.1).

### 5.3.2 Muon-like samples

Most of the event cuts are common to the selection used for the electron-like sample. The event selection criteria for  $\nu_\mu$  candidates is as follows:

- Neutrino events are fully contained in the fiducial volume.
- The number of rings is one.
- The Cherenkov ring is identified as muon-like by the PID algorithm.
- The reconstructed momentum is greater than 200 MeV/c.
- The number of  $\mu \rightarrow e + \nu_e + \nu_\mu$  decay electrons is equal or less than one, since only one muon must be observed in a CCQE-like event.

The selection is identical for both neutrino and antineutrino modes. In fig. 5.3 the number of events passing each selection cut is shown.

In neutrino mode the nominal expected total number of events for is 120.1, while the  $\nu_e/\bar{\nu}_e$  and NC background events are respectively 0.40 and 9.11 (NC). After all the selection cuts 124 events were selected in the run 1-6 data sample.

In antineutrino mode the expected number of events is 36.14 with only 2.01 NC and 0.06  $\nu_e/\bar{\nu}_e$  background events. After all the selection cuts 34 events were selected in the run 1-6 data sample.

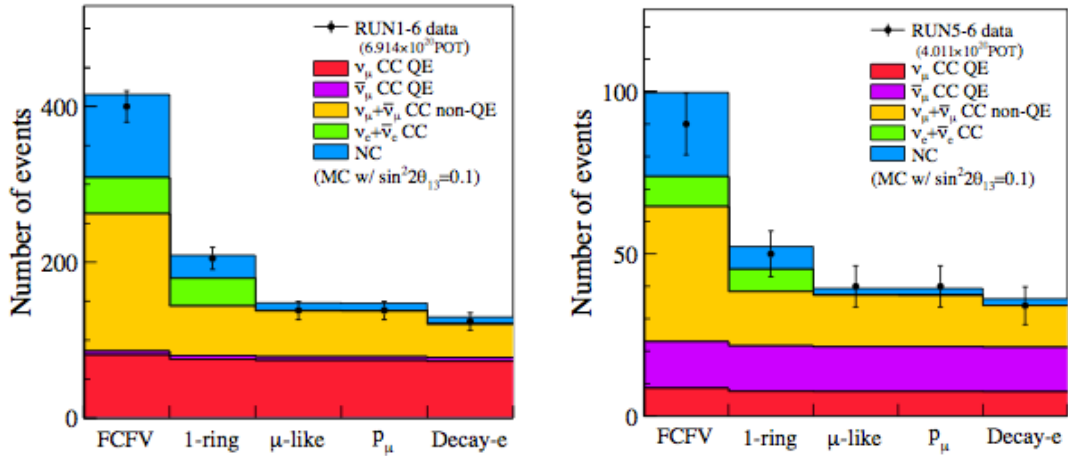


Figure 5.3: The number of muon-like events passing each selection stage for both neutrino (left) and antineutrino (right) modes are shown. Both distributions correspond to the statistic collected during runs 1-6. The data are shown by the black dots. MC distributions are made using  $\sin^2 2\theta_{13} = 0.1$  and  $\delta_{CP} = 0$ . The expected neutrino flux is reweighted with external hadron production data (see sec. 2.6.1).

## 5.4 Systematic uncertainties

The systematic uncertainties considered for both the  $\bar{\nu}_\mu \rightarrow \bar{\nu}_e$  appearance as well as the neutrino and antineutrino joint analysis can be grouped into four categories:



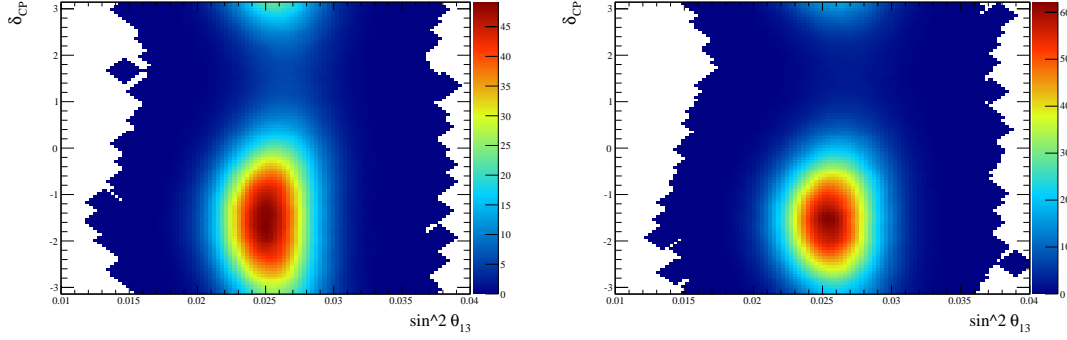


Figure 5.4: Prior distributions used to randomly extract  $\sin^2 \theta_{13}$  and  $\delta_{CP}$  for NH (left) and IH (right). The correlations between the parameters are taken into account. The distributions are from the T2K run 1-4 data bayesian analysis [83]. The analysis was performed only with neutrino mode data and the prior probability  $\sin^2 2\theta_{13} = 0.095 \pm 0.01$  from [65] was used as constraint in the analysis.

- uncertainty on the oscillation parameter
- uncertainties on the neutrino flux prediction
- cross section model uncertainties
- Super-K detector systematic uncertainties

All the systematic uncertainties are introduced in the fit as nuisance parameters, that modify the number of events in each bin of the analysis templates (see sec. 5.1), and are marginalized as described in sec. 5.2.

#### 5.4.1 Uncertainty on the oscillation parameters

The oscillation probability depends on all the parameters of the PMNS matrix (see eq. 1.10). If only a few parameters are measured, it is important to take into account the uncertainties on the other oscillation parameters, which are marginalized. The uncertainty on the oscillation parameters is treated in a slightly different way in the two oscillation analyses at Super-K.

Since in the  $\bar{\nu}_\mu \rightarrow \bar{\nu}_e$  appearance analysis only the run 5-6 data in antineutrino mode are analyzed, the posterior distributions of the bayesian analysis of the T2K run 1-4 data [83] were used as priors in the marginalization. A discrete prior is used for the mass hierarchy: the probability for normal hierarchy (NH) and inverted hierarchy (IH) is respectively 0.684 and 0.326. Different priors of the oscillation parameters are used for NH and IH as well. Values of  $\sin^2 \theta_{13}$  and  $\delta_{CP}$  are extracted from the 2D prior distributions shown in fig. 5.4 taking into account the existing correlations.  $\sin^2 \theta_{23}$  and  $|\Delta m_{32}^2|$  for NH ( $|\Delta m_{31}^2|$  for IH) are randomly extracted from the 2D prior distributions shown in Fig. 5.5. All the oscillation parameters were marginalized in the fit, except  $\sin^2 \theta_{12}$  and  $\Delta m_{21}^2$ , which were fixed, given the negligible effect on the oscillation probability with the T2K baseline.

In the  $\bar{\nu}/\nu$  joint analysis the prior distributions used for the  $\bar{\nu}_\mu \rightarrow \bar{\nu}_e$  appearance analysis cannot be used, because the full T2K run 1-6 data set is analyzed. The priors used for this analysis come from external measurements and are shown in tab. 5.2.

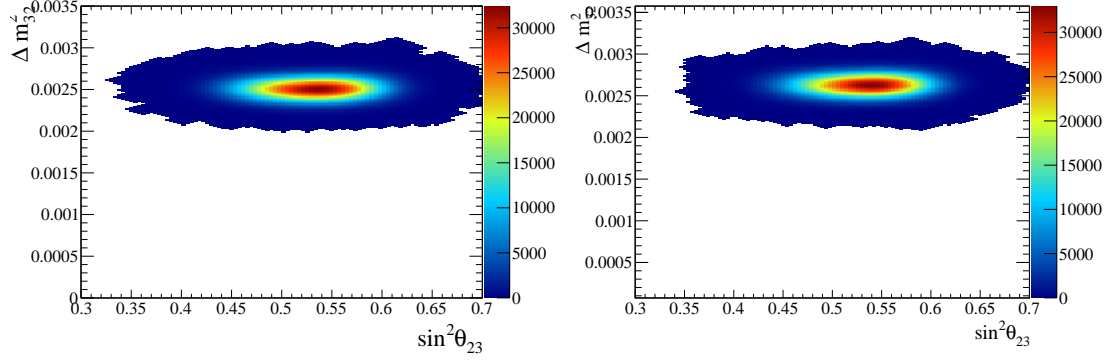


Figure 5.5: Prior distributions used to randomly extract  $\sin^2 \theta_{23}$  and  $|\Delta m_{32}^2|$  for NH (left),  $\sin^2 \theta_{23}$  and  $|\Delta m_{31}^2|$  for IH (right). The correlations between the parameters are taken into account. The distributions are from the T2K run 1-4 data bayesian analysis [83]. The analysis was performed only with neutrino mode data and the prior probability  $\sin^2 2\theta_{13} = 0.095 \pm 0.01$  from [65] was used as constraint in the analysis.

Parameter(s)	Nominal value	Treatment
$\sin^2 \theta_{23}$	0.528	T2K run 1-4 posterior
$\sin^2 \theta_{13}$	0.025	T2K run 1-4 posterior
$\sin^2 \theta_{12}$	0.306	fixed
$ \Delta m_{32}^2 $ (NH) / $ \Delta m_{31}^2 $ (IH)	$2.509 \times 10^{-3} \text{ eV}^2/\text{c}^4$	T2K run 1-4 posterior
$\Delta m_{21}^2$	$7.5 \times 10^{-5} \text{ eV}^2/\text{c}^4$	fixed
$\delta_{CP}$	-1.601	T2K run 1-4 posterior
Mass Hierarchy	NH	T2K run 1-4 posterior

Table 5.1: Treatment of the oscillation parameters in the  $\bar{\nu}_\mu \rightarrow \bar{\nu}_e$  appearance analysis. The values of the fixed oscillation parameters correspond to the most probable parameters of the bayesian analysis on the T2K run 1-4 data described in [83]. The mass hierarchy is marginalized. The T2K run 1-4 posterior probability distributions, used to marginalize the oscillation parameters, are shown in fig. 5.4 and 5.5.

Parameter(s)	Nominal value	Prior	Range
$\sin^2 \theta_{23}$	0.528	uniform	[0.3; 0.7]
$\sin^2 2\theta_{13}$ (reactors)	0.085	gauss	$0.085 \pm 0.005$
$\sin^2 2\theta_{13}$ (T2K data only)	0.085	uniform	[0; 0.4]
$\sin^2 2\theta_{12}$	0.846	gauss	$0.846 \pm 0.021$
$ \Delta m_{32}^2 $ (NH) / $ \Delta m_{31}^2 $ (IH)	$2.509 \times 10^{-3} \text{ eV}^2/\text{c}^4$	uniform	$[2; 3] \times 10^{-3} \text{ eV}^2/\text{c}^4$
$\Delta m_{21}^2$	$7.53 \times 10^{-5} \text{ eV}^2/\text{c}^4$	gauss	$(7.53 \pm 0.18) \times 10^{-5} \text{ eV}^2/\text{c}^4$
$\delta_{CP}$	-1.601	uniform	$[-\pi; +\pi]$
Mass Hierarchy	NH	fixed	NH or IH

Table 5.2: Treatment of the oscillation parameters in the  $\nu/\bar{\nu}$  joint analysis. All the gaussian priors are from [66]. The parameter  $\sin^2 2\theta_{13}$  can be constrained with the measurement of reactor experiments using the gaussian prior, otherwise a uniform prior is used and the measurement relies only on the T2K data. The nominal values of  $\sin^2 2\theta_{13}$ ,  $\sin^2 2\theta_{12}$  and  $\Delta m_{21}^2$  are from [66], while all the other nominal values correspond to the most probable values obtained by the bayesian analysis on the T2K run 1-4 neutrino mode data [83]. The mass hierarchy is not marginalized but fixed to either NH or IH.

#### 5.4.2 Flux systematic uncertainties

The flux systematic uncertainties are treated in the same way as in sec. 5.4.2, as normalization parameters which reweight the expected number of events in each true energy bin. The only difference is that the flux covariance matrix obtained after the tuning with the NA61/SHINE high statistics 2009 run data is used. The flux parametrization is given in tab. 2.5. For the  $\bar{\nu}_\mu \rightarrow \bar{\nu}_e$  analysis only the 25 Super-K antineutrino mode parameters are used, while for the  $\nu/\bar{\nu}$  joint analysis a total of 50 parameters that include both neutrino and antineutrino modes parameters at Super-K are needed. The covariance matrix is shown in fig. 2.18 (bottom plot).

#### 5.4.3 Cross section systematic uncertainties

The cross section model used in these analyses is partially different from what presented in sec. 4.4.3. Indeed in 2014 more theoretical models were studied by the T2K Neutrino Interaction Working Group (NIWG) and in 2015 new cross section parametrizations were introduced. In this section the new systematic uncertainties are presented. The MEC component, described in [46], which systematic uncertainty was partially taken into account by the  $\pi$ -less  $\Delta$  decay one, has been added to the simulation [174]. Also the relativistic RPA model is now implemented [176], as a function of  $Q^2$ , and is associated with a relativistic Fermi gas (RFG) (see sec. 2.7.1).

As already shown in sec. 4.4.3, there are both systematic parameters which simply normalize the analysis templates and parameters that change the expected distribution in a non-linear way through response functions. In these analyses the response functions are built for each bin of the analysis template shown in sec. 5.1 and are not applied event by event as in sec. 4.4.3.

The new systematic parameters are:

- Meson exchange current (MEC) parameter [171]. It applies a normalization to all the MEC events.
- An additional meson exchange current normalization parameter for antineutrino interactions on oxygen is applied since MEC cross section is different between neutrinos and

antineutrinos. It is applied only to antineutrino interactions (MEC- $\bar{\nu}$ ). This systematic parameter has not been applied in the  $\bar{\nu}_\mu \rightarrow \bar{\nu}_e$  analysis since it was still under study. However the antineutrino mode samples are dominated by antineutrino events and this systematic uncertainty would have a small effect, in particular when compared to the statistical uncertainty.

- Normalization of the neutrino cross section axial form factor when a pion is produced from a resonance ( $C_5^A$ ) [173]. Differently from the parameter of the axial mass, that controls both the overall cross section and the shape of the  $d\sigma^2/dQ^2$  differential cross section, to first order  $C_5^A$  controls only the overall normalization. Response functions are used.
- Rescale of the isospin  $I = 1/2$  non-resonant single pion background (BgRes) through response functions [173]. The non-resonant single pion background (see sec. 2.7), is assumed to be entirely  $I = 1/2$ . However it is known there could be  $I = 3/2$  non-resonant background, which is not included in the simulation and would affect the  $\nu_\mu + n \rightarrow \mu^- + p + \pi^0$  and  $\nu_\mu + n \rightarrow \mu^- + n + \pi^+$  CC channels.
- Normalization of NC coherent (NCCoh) interactions, that in sec. 4.4.3 was included in the NC other component.
- The NC1 $\gamma$  component was rescaled by a factor two and a normalization parameter is assigned as systematic uncertainty. Previously it was included in the NC other component. This systematic uncertainty was not implemented in the  $\bar{\nu}_\mu \rightarrow \bar{\nu}_e$  analysis, since it was still under study. However its effect is small compared to the total systematic and statistical uncertainty and becomes more important only when also the neutrino mode samples are used, since they contain much more events.
- Normalization of CC- $\nu_e$  ( $\sigma_{\nu_e}$ ) and CC- $\bar{\nu}_e$  ( $\sigma_{\bar{\nu}_e}$ ) events that take into account possible differences between  $\nu_\mu$  and  $\nu_e$  ( $\bar{\nu}_\mu$  and  $\bar{\nu}_e$ ) cross sections. Studies have shown that the uncertainty is smaller than what was used in sec. 4.4.3 and should be reduced from 3% to 2% [175]. Now also the possibility of the existence of second class currents, that are associated with form factors of the CCQE neutrino cross section, are taken into account. While theoretically possible, the existence of such currents requires charge or time symmetry violation, and measurements show the size of these violations to be small. In the context of T2K, they would stand as a proxy for possible un-modelled nuclear effects [172]. The result is an anti-correlation between the parameters  $\sigma_{\nu_e}$  and  $\sigma_{\bar{\nu}_e}$ , corresponding to a covariance of 2%. In the  $\bar{\nu}_\mu \rightarrow \bar{\nu}_e$  analysis  $\sigma_{\nu_e}$  and  $\sigma_{\bar{\nu}_e}$  were fully correlated and a single parameter was used for both, since the implementation of the second class currents was not available yet. However the antineutrino mode sample is dominated by  $\bar{\nu}_e$ , so the effect of the anti-correlation between  $\sigma_{\nu_e}$  and  $\sigma_{\bar{\nu}_e}$  is negligible. Furthermore the  $\bar{\nu}_\mu \rightarrow \bar{\nu}_e$  analysis is totally dominated by the statistical uncertainty.

The cross section systematic parameters common to the search for short-baseline  $\nu_e$  disappearance analysis, whose description can be found in sec. 4.4.3, are

- CCQE axial-mass scaling factor ( $M_A^{QE}$ )
- Fermi momentum (PF)
- Binding energy ( $E_b$ )

- Resonance-production axial-mass scaling factor ( $M_A^{RES}$ )
- CC other shape (CCOth)
- CC coherent (CCCoh)
- NC other normalization (NCOth)

The list of all the cross section systematic uncertainties with nominal values and uncertainties used in the analysis can be found in tab. B.1 for the  $\bar{\nu}_e \rightarrow \bar{\nu}_\mu$  appearance analysis and tab. B.3 for the  $\bar{\nu}/\nu$  joint analysis.

#### 5.4.4 Detector systematic uncertainties

Control samples that are not related to the T2K beam spills are used to assess systematic uncertainties. Muons and neutrinos, produced by interactions of cosmic rays in the atmosphere, are used to evaluate the systematic uncertainty due to the cuts on the fully contained fiducial volume and muon decay electrons. A systematic uncertainty is assigned also to the event reduction consisting of good spill selection, including the GPS timing synchronization with the beam-line.

Other sources of systematic uncertainty come from the topological cuts used to select the neutrino candidate samples and possible mismodeling of ring counting, particle identification and  $\pi^0$  rejection are evaluated using 1417.4 days Super-K atmospheric neutrinos samples fully contained in the fiducial volume. In order to obtain the error size, the MC expectation was compared to the data through a fit.

For the estimation of the  $\pi^0$  (NC) background systematics, a hybrid  $\pi^0$  sample, where real electron events from cosmic rays and atmospheric neutrinos are combined with simulated gamma events assuming the  $\pi^0$  kinematics, was developed and the systematic error of the selection efficiency of single  $\pi^0$  events was estimated.

Finally the uncertainty on the selection of NC1 $\gamma$  events, which can produce a charge pattern very similar to the one of an electron and are background to  $\nu_e$  CC candidates, is estimated.

As described in sec. 2.3, the Super-K angular resolution is very good and no systematic uncertainty is assigned because negligible compared to the other systematics.

A covariance matrix parametrized in reconstructed neutrino energy is produced by performing toys MC, in analogue way as described in sec. 4.4.1. The corresponding systematic parameters, that for both electron-like and muon-like samples are shown in tab. 5.3, are used to normalize the number of events in each template bin. The same parametrization is used for both neutrino and antineutrino mode samples and a total of 36 systematic parameters with nominal value 1 are used. All the correlations between the systematic parameters of the different samples are taken into account. In fig. 5.6 the detector error matrix used in the analyses is shown. A more detailed description of the detector systematic uncertainties can be found in [177] and [178].

The systematic parameter that takes into account the uncertainty on the Super-K reconstructed neutrino energy scale is included. It is estimated to be 2.4% [179]. Its effects are calculated by scaling the energy bin edges of the MC templates and, assuming uniform distribution of events within the bins, calculating the number of events gained from (lost to) neighbouring bins.

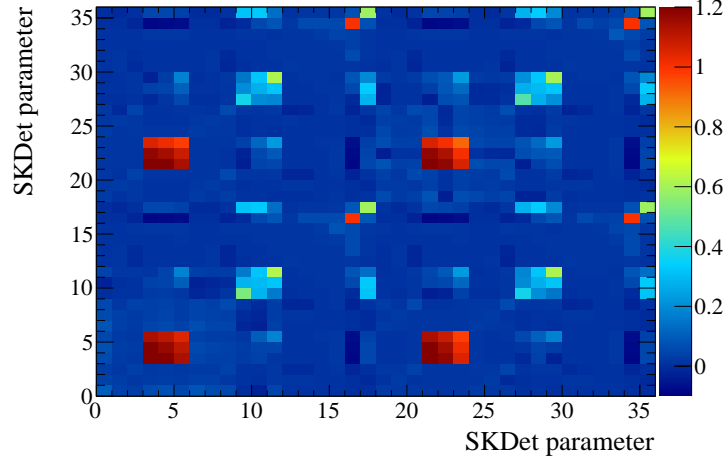


Figure 5.6: Super-K detector error matrix defined as  $\text{sign}(V_{ij}) \times \sqrt{V_{ij}}$  where  $V_{ij}$  is an element of the covariance matrix. Elements from 0 to 17 correspond to the neutrino mode, while elements from 18 to 35 correspond to antineutrino mode. For each beam mode the parametrization shown in tab. 5.3 is used.

Parameter	Sample	Category	Energy range (GeV)
0   18	electron-like	oscillated $\nu_e/\bar{\nu}_e$ CC	$E_{reco} < 0.35$
1   19	electron-like	oscillated $\nu_e/\bar{\nu}_e$ CC	$0.35 < E_{reco} < 0.80$
2   20	electron-like	oscillated $\nu_e/\bar{\nu}_e$ CC	$0.80 < E_{reco} < 1.25$
3   21	electron-like	$\nu_\mu/\bar{\nu}_\mu$ CC	$E_{reco} < 0.35$
4   22	electron-like	$\nu_\mu/\bar{\nu}_\mu$ CC	$0.35 < E_{reco} < 0.80$
5   23	electron-like	$\nu_\mu/\bar{\nu}_\mu$ CC	$0.80 < E_{reco} < 1.25$
6   24	electron-like	$\nu_e/\bar{\nu}_e$ CC	$E_{reco} < 0.35$
7   25	electron-like	$\nu_e/\bar{\nu}_e$ CC	$0.35 < E_{reco} < 0.80$
8   26	electron-like	$\nu_e/\bar{\nu}_e$ CC	$0.80 < E_{reco} < 1.25$
9   27	electron-like	all NC	$E_{reco} < 0.35$
10   28	electron-like	all NC	$0.35 < E_{reco} < 0.80$
11   29	electron-like	all NC	$0.80 < E_{reco} < 1.25$
12   30	muon-like	$\nu_\mu/\bar{\nu}_\mu$ CCQE	$E_{reco} < 0.40$
13   31	muon-like	$\nu_\mu/\bar{\nu}_\mu$ CCQE	$0.40 < E_{reco} < 1.10$
14   32	muon-like	$\nu_\mu/\bar{\nu}_\mu$ CCQE	$1.10 < E_{reco} < 30.0$
15   33	muon-like	all $\nu_\mu/\bar{\nu}_\mu$ CCnQE	$E_{reco} < 30.0$
16   34	muon-like	$\nu_e/\bar{\nu}_e$ CC	$E_{reco} < 30.0$
17   35	muon-like	all NC	$E_{reco} < 30.0$

Table 5.3: Binning of Super-K selection efficiency systematic parameters in covariance matrices for both electron- and muon-like samples for each category and reconstructed neutrino energy range. The same parametrization is used for both neutrino and antineutrino mode samples. The parameter number is shown for both neutrino (0-17) and antineutrino (18-35) mode.

### 5.4.5 Final State and secondary interaction uncertainty and photo-nuclear effect

The uncertainty on the final state interaction (FSI) and secondary pion interactions with other nuclei (SI) is taken into account and treated in the same way as already described in sec. 4.4.4.

At Super-K also the photo-nuclear (PN) effect, given by interactions of a photon with a nucleus, becomes important because it could affect the rejection of  $\pi^0$  in the final state: the photon can be absorbed without a subsequent emission above the Cherenkov threshold. If one of the two photons is not detected, the NC1 $\pi^0$  event is misidentified as a  $\nu_e$  CCQE event.

The same parametrization as adopted for Super-K detector systematics, shown in tab. 5.3, is used and the FSI+SI+PN covariance matrix, which is added in quadrature to the Super-K detector one. The same parameters of Super-K detector systematics are used.

In fig. 5.7 the fractional error for both FSI+SI and PN systematic uncertainties is shown.

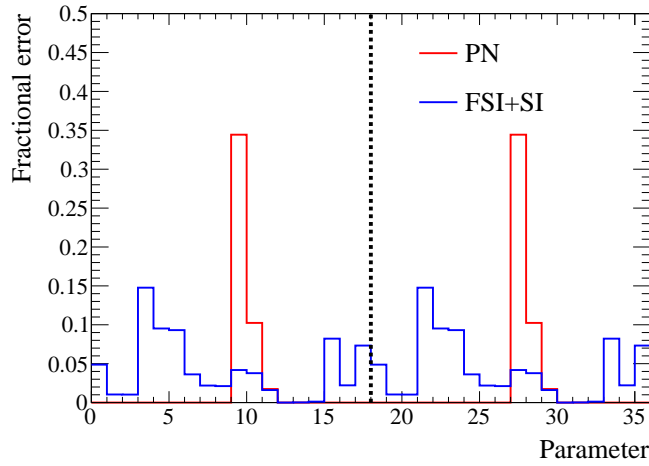


Figure 5.7: Fractional errors for FSI+SI and PN systematic uncertainties for neutrino (bins from 0 to 17) and antineutrino (bins from 18 to 35) modes. Each bin corresponds to a different systematic parameter. The same parametrization shown in tab. 5.3 is used.

### 5.4.6 Near detector measurement

In order to reduce the total systematic uncertainty the flux and cross section systematic parameters have been measured at ND280, where the neutrino beam is not affected by oscillations [180]. The constraints on the model from the fit are used to predict the neutrino event rates at Super-K. The same procedure described in sec. 4.4.5 is performed again but including also the run 5-6 data set (see tab. 2.1). The flux covariance matrix for run 1-6 data, shown in fig. 2.18, is used. The correlations between the flux at ND280 and Super-K as well as between neutrino and antineutrino modes are taken into account. In order to better constrain the antineutrino flux as well as those cross sections systematic parameters which can be different for neutrinos and antineutrinos, four more samples from the run 5-6 data set were added to the three already available  $\nu_\mu$ -candidate samples (CC-0 $\pi$ , CC-1 $\pi$  and CC-0th) of the run 1-4 data set:  $\bar{\nu}_\mu$ -candidate CC-1track, that is dominated by CCQE interactions since only the antimuon track is detected,  $\bar{\nu}_\mu$ -candidate CC-Ntracks, where more tracks are required in order to select CC1 $\pi$  and CCDIS interactions,  $\nu_\mu$ -candidate CC-1track and  $\nu_\mu$ -candidate CC-Ntracks. The analysis

templates are built as a function of the lepton momentum ( $p$ ) and the angle between the lepton and the neutrino direction ( $\cos \theta$ ). A binned likelihood fit is performed and the flux and cross section parameters are measured. For the first time the neutrino interaction data in both FGD1 and FGD2 are used in order to measure with more precision the neutrino cross section in water. The fit result shows that FGD1 and FGD2 data are in very good agreement. In fig. 5.8 the momentum distributions measured at ND280 as well as the total systematic error before and after the fit are shown. In fig. 5.9 the flux plus cross section covariance matrix obtained by the fit of the ND280 data and used in the analysis is shown. For the  $\bar{\nu}_\mu \rightarrow \bar{\nu}_e$  appearance analysis an analogue matrix corresponding to the subset of parameters, shown in tab. B.1, is used.

#### 5.4.7 Summary of systematic uncertainties

In tab. B.1 the flux and cross section systematic parameters used as nuisance parameters in the  $\bar{\nu}_\mu \rightarrow \bar{\nu}_e$  analysis are shown, while the systematic parameters used in the joint fit analysis are presented in tab. B.2 and B.3.

The cross section systematic parameters that are not extrapolated from ND280 to Super-K are NCOther, NC1 $\gamma$ ,  $\sigma_{\nu_e}$  and  $\sigma_{\bar{\nu}_e}$  for which ND280 has weak sensitivity.

For the  $\bar{\nu}_\mu \rightarrow \bar{\nu}_e$  appearance and  $\nu/\bar{\nu}$  joint analyses a different fit with the near detector data was performed. As already anticipated in sec. 5.4.3, the cross section model was updated in order to provide new inputs to the  $\nu/\bar{\nu}$  joint analysis: the MEC normalization parameter for  $\bar{\nu}$  was added. Furthermore the FGD2 data with interactions on water were not used to constrain the systematic uncertainties for the  $\bar{\nu}_\mu \rightarrow \bar{\nu}_e$  appearance analyses. Conservatively the parameters such as the CC Coherent normalization, Fermi momentum, binding energy and MEC, which are correlated between carbon and oxygen interactions, were set as uncorrelated. This means that these parameters were largely unconstrained by the fit to ND280 data. However the  $\bar{\nu}_\mu \rightarrow \bar{\nu}_e$  appearance is dominated by the statistical uncertainty and a conservative treatment of the systematic uncertainties does not have a large impact on the final result.



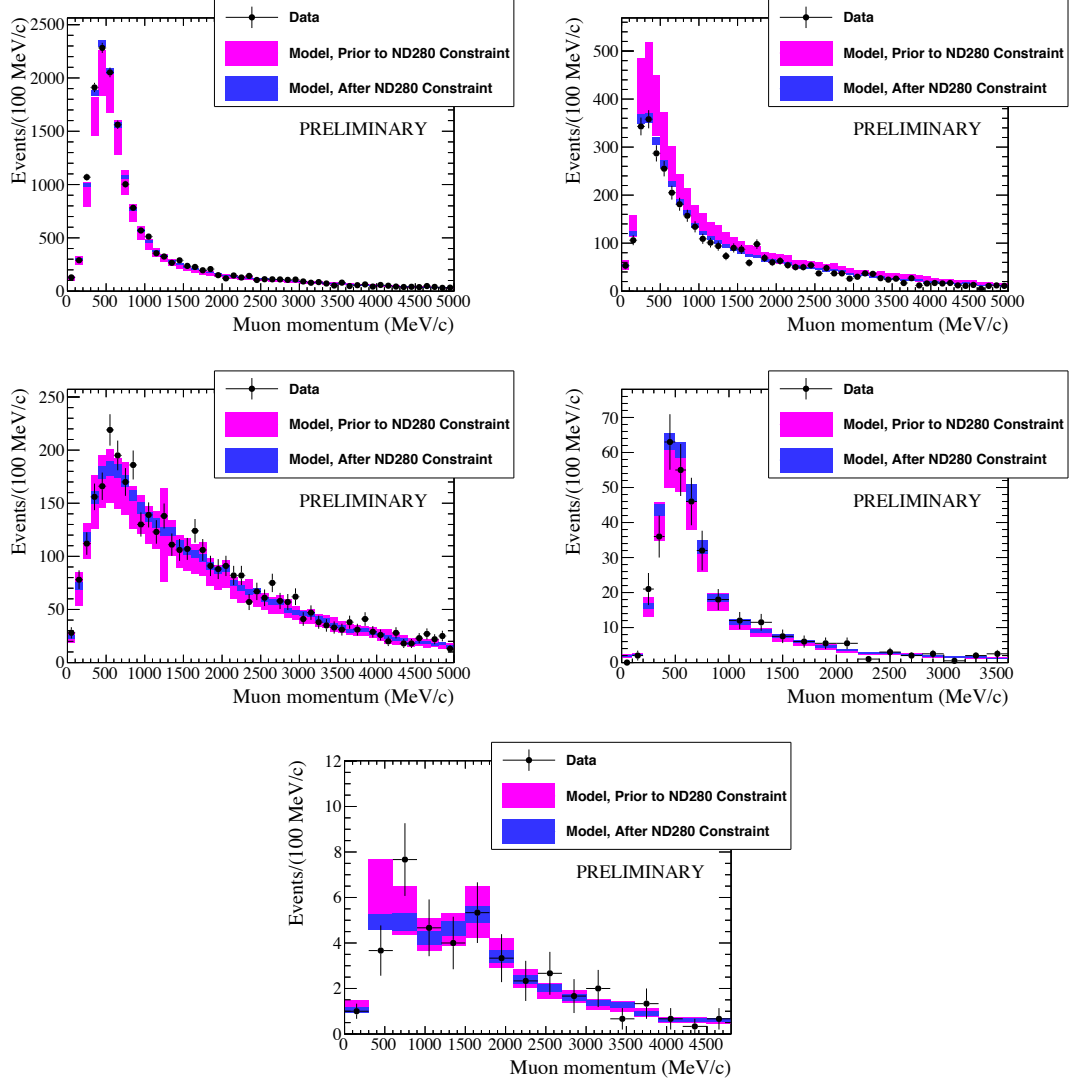


Figure 5.8: The plots on top and in the middle, from left to right, show the momentum distribution of the  $\mu^-$  candidates from the  $\nu_\mu$  CC0 $\pi$ , CC1 $\pi$  and CC0th samples in neutrino mode. The plots on the bottom are the momentum distributions of  $\mu^+$  candidates from the  $\bar{\nu}_\mu$  CC-1Track sample in antineutrino mode. The MC predictions, before and after the fit of the run 1-6 ND280 data, are shown including errors on flux, cross section and detector systematics as well as MC statistical errors.

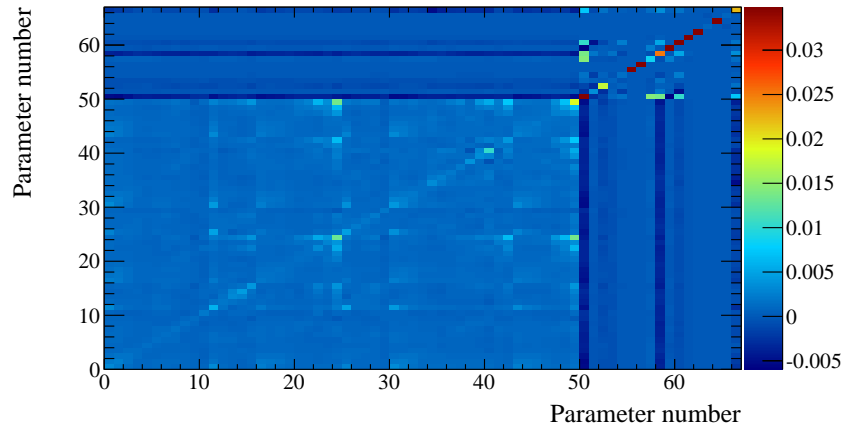


Figure 5.9: Covariance matrix of the flux and cross section systematic parameters used in the analyses. The parameter number is the same as shown in tab. B.2 and B.3: neutrino mode flux (0-24), antineutrino mode flux (25-49) and cross section (50-66).

## Chapter 6

# Search for $\bar{\nu}_\mu \rightarrow \bar{\nu}_e$ appearance at Super-K

The goal of this analysis is to search for  $\bar{\nu}_\mu \rightarrow \bar{\nu}_e$  appearance at Super-K. This neutrino oscillation channel is predicted by the PMNS matrix in the 3-neutrino framework but has never been observed so far. Its measurement is important also because it is the first step toward the search for CP violation in the neutrino sector, that requires the comparison of  $\nu_\mu \rightarrow \nu_e$  and  $\bar{\nu}_\mu \rightarrow \bar{\nu}_e$  oscillations. As already explained, in this analysis only the electron-like sample selected from the antineutrino beam mode run 5-6 data set is used. The collected data correspond to  $4.011 \times 10^{20}$  POT (see sec. 2.4).

The analysis template given by eq. 5.1 is built as a function of the reconstructed neutrino energy with bins of 50 MeV between 0 and 1.25 GeV. The energy spectrum used in the analysis is shown in fig. 6.1. The significance to  $\bar{\nu}_\mu \rightarrow \bar{\nu}_e$  appearance is computed introducing a normalization parameter  $\bar{\beta}$  that takes only values 0 or 1 and is applied to the oscillation probability as following:

$$\bar{\beta} \times P(\bar{\nu}_\mu \rightarrow \bar{\nu}_e)$$

where  $P(\bar{\nu}_\mu \rightarrow \bar{\nu}_e)$  is the  $\bar{\nu}_\mu \rightarrow \bar{\nu}_e$  oscillation probability given by eq. 1.10 and the oscillation parameters shown in tab 5.1.

If  $\bar{\beta} = 0$  the signal  $\bar{\nu}_\mu \rightarrow \bar{\nu}_e$  appearance component, the green part of the energy spectrum in fig. 6.1, disappears and only  $\nu_\mu \rightarrow \nu_e$ , NC and other (intrinsic  $\bar{\nu}_e$ ,  $\bar{\nu}_\mu$ ,  $\nu_e$ ,  $\nu_\mu$  beam) background components are included. If  $\bar{\beta} = 1$ , also the  $\bar{\nu}_\mu \rightarrow \bar{\nu}_e$  appearance component is added and the full spectrum is obtained. If  $\bar{\beta} = 1$ , 3.729 electron-like events are expected with 1.961 signal events, while if  $\bar{\beta} = 0$  the number of expected events is 1.768.

A total of 55 systematic parameters describing the effect of oscillation, flux, cross section and detector systematic uncertainties are introduced in the analysis as nuisance parameters (see sec. 5.4). The prior distributions, shown in fig. 5.4 and 5.5, are used to take into account the uncertainty on the oscillation parameters, as described in tab. 5.1. The effect of all the systematic uncertainties on the total number of events is shown in tab. 6.1. The total systematic uncertainty is dominated by the oscillation parameters and the MEC systematic uncertainty which is almost unconstrained by the fit of the near detector data (see sec. 5.4.6) and gives an effect of about 9%. The effect of all the systematic uncertainties on the reconstructed neutrino energy spectrum for both  $\bar{\beta} = 0$  and  $\bar{\beta} = 1$  is shown in fig. 6.2.

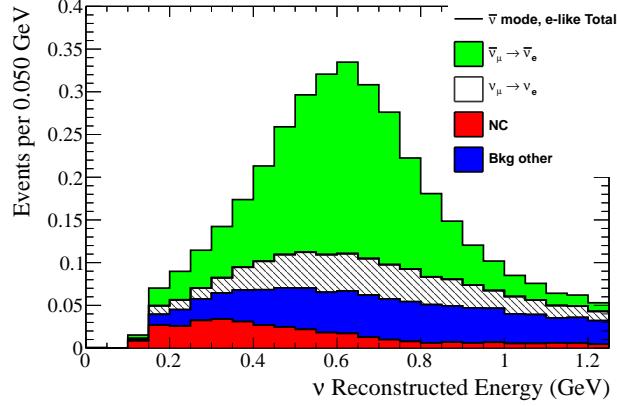


Figure 6.1: Predicted reconstructed-energy spectrum of electron-like ring events with oscillations for an exposure of  $4.011 \times 10^{20}$  POT in antineutrino mode. The distribution is broken down by the following components:  $\bar{\nu}_\mu \rightarrow \bar{\nu}_e$  signal (green),  $\nu_\mu \rightarrow \nu_e$  (grey) background, NC background (red) and background other (blue) components. The spectrum was generated using the systematic parameters measured with the ND280 data shown in tab. B.1, and the oscillation parameters shown in tab. 5.1.

## 6.1 Sensitivity study

The only free parameter of the analysis is  $\bar{\beta}$ . The significance to  $\bar{\nu}_\mu \rightarrow \bar{\nu}_e$  appearance is presented by quoting the p-value given the hypothesis of null signal ( $\bar{\beta} = 0$ ), i.e. the probability that data are compatible with a fluctuation of the background. A procedure slightly different from the one used in sec. 4.7.1, described more in detail in app. C.3, is used. Two different analyses were performed:

- rate-only analysis: the p-value is computed using the distribution of the total number of events obtained with toys MC as test statistic. The shape of the reconstructed neutrino energy spectrum in fig. 6.1 is not exploited, since only a counting of the total number of events is performed.

Source of uncertainty	$\delta N_{SK} / \langle N_{SK} \rangle$ ( $\bar{\beta} = 0$ )	$\delta N_{SK} / \langle N_{SK} \rangle$ ( $\bar{\beta} = 1$ )
SuperK detector	5.05%	3.03%
FSI + SI + PN	4.34%	2.45%
SuperK detector + FSI + SI + PN	6.66%	3.90%
Flux + Cross section (w/ ND280 constraint)	9.72%	10.29%
Oscillation parameters	4.72%	13.38%
Total	12.75%	17.21%

Table 6.1: Effect of  $1\sigma$  variations of the groups of systematics parameters on total number of 1-ring electron-like events ( $N_{SK}$ ) in the antineutrino mode sample obtained by performing 10k toys MC. The effect of each group of systematics is computed as the standard deviation divided by the mean of the distribution of the total number of Super-K events.

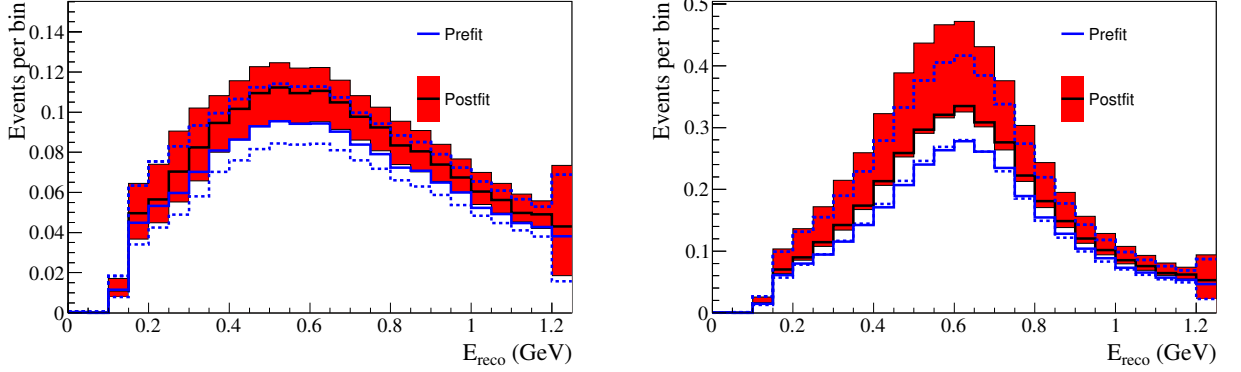


Figure 6.2: Error envelopes for the energy spectrum as a result of all systematic parameters, with (red) and without (blue) the constraint from the fit of the ND280 data, for  $\bar{\beta} = 0$  (left) and  $\bar{\beta} = 1$  (right) are shown. 10k toy MC experiments were generated with randomized systematic parameters and the  $1\sigma$  spread of bin contents was calculated. Existing correlations between the systematic parameters were taken into account.

- rate+shape analysis: the fit procedure described in sec. 5.2 is used and a distribution of  $\Delta\chi^2 = \chi_{\text{marg}}^2(\bar{\beta} = 0) - \chi_{\text{marg}}^2(\bar{\beta} = 1)$  is obtained with toys MC by fixing  $\bar{\beta}$  to 0 and 1. In this case the shape of the reconstructed neutrino energy spectrum is exploited by likelihood fit.

A sensitivity study for  $4.011 \times 10^{20}$  POT is performed by using the Asimov data set [144], in the  $\bar{\nu}_\mu \rightarrow \bar{\nu}_e$  appearance hypothesis consistent with the T2K run 1-4 data ( $\bar{\beta} = 1$ ), shown in fig. 6.1. In order to quote the significance to  $\bar{\nu}_e$  appearance a 1-sided p-value (right tail) is computed.

The expected number of events is 3.729 for  $4.011 \times 10^{20}$  POT and the quoted rate-only p-value is 0.109. The expected rate+shape p-value is 0.0699. The toy MC distributions of the test statistics used to quote both the rate-only and rate+shape p-values are shown in fig. 6.3. The p-value is given by the number of entries on the right side of the red line, the test statistic computed using the Asimov data set, divided by the total number of entries. In fig. 6.4 the p-value is shown for different numbers of expected events. If more than 4 events are observed, the rate+shape p-value is smaller than 0.05.

## 6.2 Result of run 5-6 data set analysis

The total number of electron-like events observed in the run 5-6 data set is 3, while 3.728 events are expected. In figure 6.5 the expected reconstructed neutrino energy distribution is compared to data.

The rate-only and rate+shape p-values for  $\bar{\nu}_\mu \rightarrow \bar{\nu}_e$  appearance are performed with the run 5-6 data set following the same procedure as in section 6.1. A summary of the observed p-values is given in table 6.2. The measured  $\Delta\chi_{\text{obs}}^2$  is 0.164. The p-value given null  $\bar{\nu}_\mu \rightarrow \bar{\nu}_e$  appearance ( $\bar{\beta} = 0$ ) is 0.1589 for rate+shape analysis and 0.2637 for rate-only analysis. The result does not allow to claim any hint of appearance.

Studies were performed also to check whether data prefer the background only hypothesis

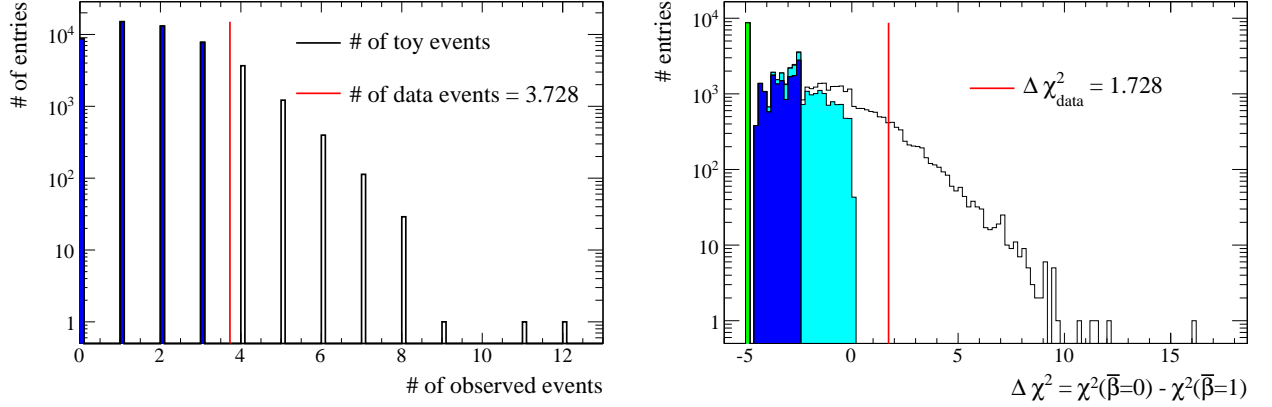


Figure 6.3: The distribution of the total number of events from 50k toy MC experiments, used to quote the rate-only p-value, is shown on the left. The red line corresponds to the total number of events given by the Asimov dataset. The distribution of the  $\Delta\chi^2$  from 50k toy MC experiments, used to quote the rate+shape p-value, is shown on the right. The red line corresponds to  $\Delta\chi_{obs}^2$  obtained from the Asimov dataset. The colored green entries correspond to toys MC with no observed events while the blu and the cyan colored entries correspond respectively to toys with 1 and 2 events. The distributions are for  $4.011 \times 10^{20}$  POT. The p-value is given by the area of the distribution on the right side of the red line divided by the total number of entries.

( $\bar{\beta} = 0$ ) or  $\bar{\nu}_\mu \rightarrow \bar{\nu}_e$  appearance ( $\bar{\beta} = 1$ ). In order to quantify it, the 1-sided p-value given  $\bar{\nu}_\mu \rightarrow \bar{\nu}_e$  appearance is computed as well: the same procedure as described in sec. C.3 is still used but the distribution of the test statistic is obtained by making 50k toys with  $\bar{\beta} = 1$  instead of  $\bar{\beta} = 0$ . In this case the p-value gives the probability that data are compatible with a fluctuation of signal plus background. As shown in tab. 6.2 the p-value given  $\bar{\nu}_e$  appearance is slightly larger than the background only hypothesis, that means the data slightly prefer the  $\bar{\nu}_\mu \rightarrow \bar{\nu}_e$  hypothesis. The distributions of the rate+shape test statistic ( $\Delta\chi^2$ ) used to compute the p-values for both background only ( $\bar{\beta} = 0$ ) and  $\bar{\nu}_\mu \rightarrow \bar{\nu}_e$  ( $\bar{\beta} = 1$ ) hypotheses are shown in fig. 6.6. It is clear that the measured  $\Delta\chi^2$  value does not strongly prefer any of the two distributions. In order to improve the sensitivity more data must be collected. This would separate more the two distributions and reduce the p-value of either of the two hypotheses.

hypothesis	p-value (rate-only)	p-value (rate+shape)
$\bar{\beta} = 0$	0.2637	0.1589
$\bar{\beta} = 1$	0.3752	0.2770

Table 6.2: Summary of 1-sided rate-only and rate+shape p-values from the combined run 5-6 data set. The 1-sided p-values are obtained by performing 50k toys with  $\bar{\beta} = 0$  for background only hypothesis and  $\bar{\beta} = 1$  for background plus  $\bar{\nu}_\mu \rightarrow \bar{\nu}_e$  appearance, in order to get the distribution of the test statistic. In the first case the p-value given null  $\bar{\nu}_e$  appearance is obtained on the right tail of the expected distribution, while for  $\bar{\beta} = 1$  the 1-sided p-value is obtained on the left tail of the expected distribution.

It is interesting to note that the observation of 3 events seems to prefer  $\delta_{CP} = -\pi/2$ , which corresponds to the best-fit result of the T2K run 1-4 data analysis shown in tab. 5.1. Indeed if  $\delta_{CP} = 0$  and  $\delta_{CP} = +\pi/2$  respectively 4.315 and 4.851 events are expected. However, given the

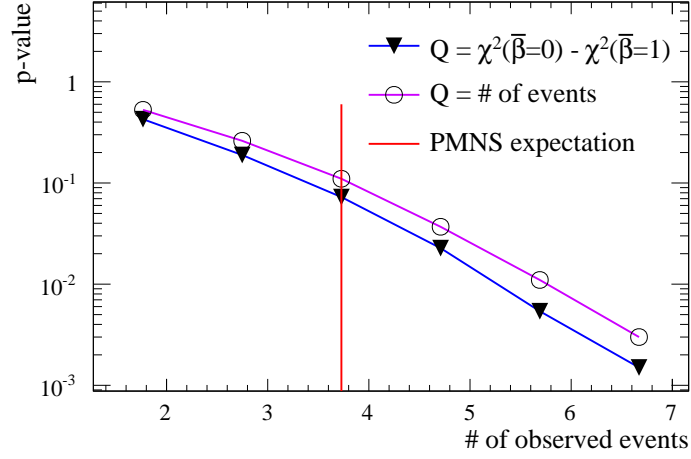


Figure 6.4: Rate-only (violet) and rate+shape (blue) p-value (logarithmic scale) for different number of observed events given by Asimov data sets. A different test statistic  $Q$  is used, respectively the number of observed events and  $\Delta\chi^2 = \chi^2(\bar{\beta} = 0) - \chi^2(\bar{\beta} = 1)$ . The red line corresponds to the PMNS expectation given by the T2K run 1-4 data ( $\bar{\beta} = 1$ ). The study is performed with  $4.011 \times 10^{20}$  POT and 10k toys MC.

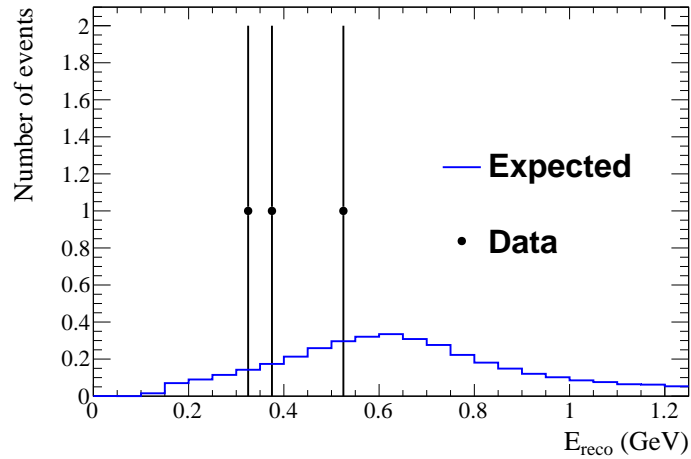


Figure 6.5: The expected reconstructed neutrino energy distribution (blue) is compared to the run 5-6 data set (black dots), corresponding to  $4.011 \times 10^{20}$  POT. The expected distribution corresponds to the oscillation parameters shown in tab. 5.1.

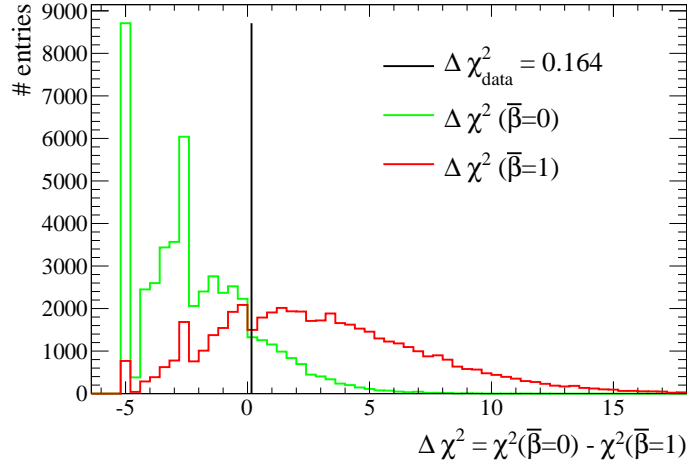


Figure 6.6: The distribution of the test statistic  $\Delta\chi^2$  from 50k toy MC experiments is shown for both  $\bar{\beta} = 0$  (green) and  $\bar{\beta} = 1$  (red). The black line corresponds to the  $\Delta\chi^2$  value measured in the run 5-6 dataset. Data and MC distributions correspond to  $4.011 \times 10^{20}$  POT.

low statistics available in run 5-6, the result is also affected by statistical fluctuations. In order to quantify the compatibility of the T2K data with different values of  $\delta_{CP}$  the  $\nu/\bar{\nu}$  joint analysis is needed, whose result is shown in the next chapter.

A sensitivity study performed with the statistic that the T2K collaboration expects to collect by summer 2016,  $9.5 \times 10^{20}$  POT in antineutrino mode, shows that the significance to  $\bar{\nu}_\mu \rightarrow \bar{\nu}_e$  appearance should improve up to 99% CL if  $\delta_{CP} = -\pi/2$  and become better than  $3\sigma$  if  $\delta_{CP} = +\pi/2$ . If the PMNS matrix gives a reliable description of neutrino oscillations, the T2K experiment will probably be able to observe the first hint of  $\bar{\nu}_\mu \rightarrow \bar{\nu}_e$  appearance in about one year.

The results presented in this section are also shown in [185].



## Chapter 7

# Neutrino and antineutrino joint analysis at Super-K

The  $\nu/\bar{\nu}$  joint analysis of neutrino and antineutrino mode data is needed in order to precisely measure the parameters of the PMNS matrix. In particular the possibility to directly compare  $\bar{\nu}_\mu \rightarrow \bar{\nu}_e$  and  $\nu_\mu \rightarrow \nu_e$  oscillation channels increases the sensitivity to  $\delta_{CP}$ . All the four event samples selected from the run 1-6 data set, described in sec. 5.3, are analyzed simultaneously. In this way the correlations between all the oscillation parameters are better taken into account. Furthermore analyzing more samples simultaneously allows to better constrain the systematic uncertainties. The muon-like samples are needed to observe  $\nu_\mu$  and  $\bar{\nu}_\mu$  disappearance and measure the atmospheric parameters  $\Delta m_{32}^2$  ( $\Delta m_{13}^2$ ) and  $\sin^2 \theta_{23}$ , while, thanks to the electron-like samples, the parameters  $\theta_{13}$  and  $\delta_{CP}$  can be inferred by looking to  $\bar{\nu}_\mu \rightarrow \bar{\nu}_e$  and  $\nu_\mu \rightarrow \nu_e$  oscillations.

An analysis template, used to compare the data with the expected MC, is built for each selected sample following the procedure described in sec. 5.1. For muon-like distributions 1-dimensional templates as a function of the reconstructed neutrino energy, from 0 to 30 GeV, were used. For what concern the electron-like samples, 2-dimensional templates, which consist of the number of events as a function of both the reconstructed neutrino energy, from 0 to 1.25 GeV, and the angle between the neutrino and the outgoing lepton directions ( $\theta$ ), are used. The CCQE differential cross section is different for neutrinos and antineutrinos interacting off free nucleons [181]. Adding a variable to the template provides more informations about the kinematic of the interaction and helps to better separate  $\bar{\nu}_\mu \rightarrow \bar{\nu}_e$ ,  $\nu_\mu \rightarrow \nu_e$  and NC components, improving the sensitivity to  $\delta_{CP}$ . Furthermore a better discrimination of the background reduces the probability to have a bias in the measurement. In fig. 7.1 the templates used in the  $\nu/\bar{\nu}$  joint analysis are shown. More details are given in app. D, where the electron-like 2-dimensional templates are shown for each neutrino flavor and oscillation channel component.

In the  $\nu/\bar{\nu}$  joint analysis all the oscillation channels are important for the measurement of the PMNS parameters. The background to  $\bar{\nu}_\mu \rightarrow \bar{\nu}_e$  and  $\nu_\mu \rightarrow \nu_e$  appearance in the electron-like samples is given by NC interactions,  $\nu_\mu/\bar{\nu}_\mu$  and  $\nu_e/\bar{\nu}_e$  beam. In order to measure the atmospheric parameters  $\sin^2 \theta_{23}$  and  $\Delta m_{32}^2$  ( $\Delta m_{13}^2$ ), the muon-like samples are needed and the oscillation pattern is measured in the  $\nu_\mu$  and  $\bar{\nu}_\mu$  spectra. In tab. 7.1 the number of predicted events, compared to the number of selected events in the run 1-6 data set, are shown for all the selected samples.

The systematic uncertainties used in the analysis are described in sec. 5.4. The impact of the systematic uncertainties on each sample is shown in tab. 7.2.

Category	electron-like		muon-like	
	neutrino	antineutrino	neutrino	antineutrino
$\nu_\mu \rightarrow \nu_e$	21.508	0.551	0.345	0.010
$\bar{\nu}_\mu \rightarrow \bar{\nu}_e$	0.138	1.500	0.002	0.019
$\nu_\mu$	1.469	0.141	117.643	14.508
$\bar{\nu}_\mu$	0.069	0.235	7.602	19.664
$\nu_e + \bar{\nu}_e$	3.409	0.791	0.322	0.083
NC	1.488	0.377	8.067	1.768
Total (oscillated)	26.594	3.218	120.123	34.284
Total (not oscillated)	5.698	1.253	484.737	99.020
Data	31	3	124	34

Table 7.1: Number of events for each selected sample for both neutrino and antineutrino modes. The prediction is compared with the number of events selected in the run 1-6 data set, corresponding to  $6.914 \times 10^{20}$  POT in neutrino mode and  $4.011 \times 10^{20}$  POT in antineutrino mode. The systematic parameter values measured with the ND280 data shown in tab. B.2 and B.3 and the oscillation parameters shown in tab. 5.2 are used. Also the total number of events when the spectra are not affected by oscillations is shown. The numbers of predicted events for each different category is calculated taking into account oscillations.

Since  $\delta_{CP} \neq 0, \pi$  introduces an asymmetry in neutrino versus antineutrino oscillations, it is important to understand how differently the systematic uncertainties affect neutrino and antineutrino mode samples. Those systematic uncertainties that are anti-correlated between neutrinos and antineutrinos are critical, because if not well reproduced the maximal CP violation could be faked. In tab. 7.3 the impact of the systematic uncertainties on the ratio of the total number of events between neutrino and antineutrino mode for both electron- and muon-like samples is shown. The errors cancellation, given by the simultaneous analysis of neutrino and antineutrino mode samples, is better for the muon-like than for the electron-like sample. Indeed systematic parameters  $\sigma_{\nu_e}$  and  $\sigma_{\bar{\nu}_e}$  are anti-correlated (see sec. 5.4). In fig. 7.2 the effect of the systematic uncertainties on the reconstructed neutrino energy spectra is shown.

Source of uncertainty	electron-like		muon-like	
	neutrino	antineutrino	neutrino	antineutrino
Super-K detector	2.28%	3.11%	3.85%	3.36%
FSI+SI+PN	2.63%	2.43%	1.44%	2.05%
Flux	3.67%	3.84%	3.61%	3.80%
Cross section	5.21%	5.55%	4.09%	4.20%
Flux+Cross section	4.17%	4.60%	2.90%	3.36%
Oscillations	4.20%	4.00%	0.03%	0.03%
Total	6.91%	7.38%	5.17%	5.17%

Table 7.2: Effect of  $1\sigma$  variations of the groups of systematics parameters on total number of 1-ring electron- and muon-like events for both neutrino and antineutrino modes obtained by performing 10k toys MC. The systematic parameter values measured with the ND280 data shown in tab. B.2 and B.3 and the oscillation parameters shown in tab. 5.2 are used. Since the parameters  $\theta_{23}$  and  $\Delta m_{32}^2$  ( $\Delta m_{13}^2$ ) will be measured, only the uncertainty on the parameters  $\sin^2 \theta_{13}$ ,  $\sin^2 \theta_{12}$  and  $\Delta m_{21}^2$  are taken into account.

Source of uncertainty	muon-like	electron-like
Super-K detector	0.7%	1.6%
FSI+SI+PN	2.6%	3.5%
Flux	1.7%	1.7%
XSec Tot	1.7%	4.3%
Flux+XSec	1.9%	4.1%
Oscillations	0.0%	0.8%
Total	3.3%	5.8%

Table 7.3: Effect of  $1\sigma$  variations of the several sources of systematic uncertainties on the ratio between the total number of events in neutrino and antineutrino modes for 1-ring electron- and muon-like samples obtained by performing 10k toys MC. The systematic parameter values measured with the ND280 data shown in tab. B.2 and B.3 and the oscillation parameters shown in tab. 5.2 are used. Since the parameters  $\theta_{23}$  and  $\Delta m_{32}^2$  ( $\Delta m_{13}^2$ ) will be measured and priors are uniform over a wide range, only the uncertainties on the parameters  $\sin^2 \theta_{13}$ ,  $\sin^2 \theta_{12}$  and  $\Delta m_{21}^2$  are taken into account.

## 7.1 Sensitivity study

The fit procedure is described in sec. 5.2. Differently from the  $\bar{\nu}_\mu \rightarrow \bar{\nu}_e$  appearance analysis, all the four selected samples are included in the likelihood of eq. 5.2.

Sensitivity studies for the full run 1-6 data set are performed by using the *constant*  $\Delta\chi^2$  method, described in app. C.2, with the Asimov data set corresponding to the oscillation parameters shown in tab. 5.2.

All the oscillation parameters which are not parameters of interest are marginalized using the prior distributions shown in tab. 5.2. When the reactor constraint is applied, the parameter  $\theta_{13}$  is constrained using the nominal value and the gaussian error from the measurements of the reactor experiments: if  $\theta_{13}$  is a free parameter, eq. 5.6 is used, while if  $\theta_{13}$  is marginalized the standard procedure described in sec. 5.4.1 is followed. For example, in order to obtain the confidence intervals of  $\delta_{CP}$  with reactor constraint,  $\theta_{13}$  is marginalized, while the contour  $\sin^2 \theta_{13}$  Vs  $\delta_{CP}$  with reactor constraint is obtained by using eq. 5.6.

Contours at 68.27% CL and 90% CL are set for the following combinations of oscillation parameters:

- $\delta_{CP}$  1-dimensional fit with reactor constraint
- $\sin^2 \theta_{13}$  Vs  $\delta_{CP}$  2-dimensional fit with reactor constraint
- $\sin^2 \theta_{13}$  Vs  $\delta_{CP}$  2-dimensional fit T2K only data
- $\sin^2 \theta_{23}$  Vs  $\Delta m_{32}^2$  ( $\Delta m_{13}^2$ ) 2-dimensional fit with reactor constraint

In fig. 7.3 the expected confidence intervals corresponding to the run 1-6 data set are shown. T2K has some sensitivity to  $\delta_{CP}$  when the reactor constraint is used and  $\delta_{CP} \sim -\pi/2$  and has the power to perform a precise measurement of the atmospheric parameters.

## 7.2 Results of run 1-6 data analysis

The run 1-6 data, corresponding to  $6.914 \times 10^{20}$  POT in neutrino mode and  $4.011 \times 10^{20}$  POT in antineutrino mode, are analyzed. The measured oscillation parameters are:  $\delta_{CP}$ ,  $\sin^2 \theta_{13}$ ,  $\sin^2 \theta_{23}$  and  $\Delta m_{32}^2$  ( $\Delta m_{13}^2$ ).  $\sin^2 \theta_{12}$  and  $\Delta m_{21}^2$  cannot be measured since the T2K baseline of 295 km is too short to give good sensitivity to these parameters (see sec. 1.3.1). The fit method described in sec. 5.2 is used. The observed number of events are listed in tab. 7.1 and compared to the prediction.

The confidence intervals are set using the same procedure as in sec. 7.1 and are shown in fig. 7.4 and 7.5. Since  $\theta_{13}$  and  $\delta_{CP}$  are degenerate, as shown in eq. 1.24 and 1.25, the constraint on  $\theta_{13}$  with the measurements from reactor experiments helps to improve the sensitivity and exclude a wider region of  $\delta_{CP}$ . Indeed when  $\theta_{13}$  is not constrained, T2K has little sensitivity and none of the  $\delta_{CP}$  values for normal hierarchy are excluded at 90% CL. The reactor constraint is also used when the parameters  $\sin^2 \theta_{23}$  and  $\Delta m_{32}^2$  ( $\Delta m_{13}^2$ ) are measured, though it does not help much to improve the significance. As shown in fig. 7.6, for  $\delta_{CP}$  1-dimensional confidence interval, which is the most important result of the  $\nu/\bar{\nu}$  joint analysis, also the *Feldman-Cousins* method, described in app. C.2.1, is adopted. Indeed the likelihood function has a non linear dependence with  $\delta_{CP}$ . Also for the confidence intervals of the other combinations of oscillation parameters the *Feldman-Cousins* method would be needed. However since a lot of CPU time would be required and the main goal of this analysis release is the 1-dimensional confidence interval for  $\delta_{CP}$ , the *constant*  $\Delta\chi^2$  method is used. Furthermore the likelihood as a function of  $\sin^2 \theta_{13}$  and  $\sin^2 \theta_{23}$  is more gaussian and at the first order has a linear dependence (see sec. 1.2.2), so the *Feldman-Cousins* method should not give critical values very different from the *constant*  $\Delta\chi^2$  method.

For each oscillation parameter the allowed ranges are obtained by marginalizing all the other oscillation parameters using the prior distributions shown in tab. 5.2. The best-fit parameters and the  $1\sigma$  CL ranges are shown in tab. 7.4.

The best-fit spectra, shown in fig. 7.7, are obtained by performing a simultaneous fit of  $\delta_{CP}$ ,  $\sin^2 \theta_{23}$  and mass hierarchy, which are then fixed to their best-fit values, marginalizing all the nuisance parameters and applying the reactor constraint. The method described in app. C.1 is used.

The results presented in this section are also shown in [186].

## 7.3 Discussion of the results and future sensitivities

The results shown in sec. 7.2 can be compared to the global fit of experimental data released until 2012 (sec. 1.4), the year I started to work on this thesis. The readers should carefully interpret the global fit result since existing correlations between different experiments may not be taken into account. Furthermore the treatment of the systematic uncertainties is not as accurate as it can be in the analysis performed in a single experiment. However a comparison can help to understand how much the precision on the 3-flavor neutrino oscillation parameters has been improved by the T2K experiment since then. The 1-dimensional  $\Delta\chi^2$  distributions shown in fig. 7.4 can be directly compared with fig. 1.5.

The T2K experiment cannot measure  $\theta_{13}$  with a precision better than the reactor experiments, since the neutrino flux rate from nuclear reactors is much higher than what an accelerator experiment can reach. However in 2014 T2K measured  $\theta_{13}$  with a significance higher than  $5\sigma$  and observed for the first time  $\nu_\mu \rightarrow \nu_e$  appearance [23]. This is also shown in the  $\Delta\chi^2$  distri-

	Reactors	Normal			Inverted		
Parameter		Best-fit	$\chi^2_{min}$	$\pm 1\sigma$	Best-fit	$\chi^2_{min}$	$\pm 1\sigma$
$\delta_{CP}$	YES	-1.854	296.51	[-2.737; -0.859]	-1.351	298.16	- ([-2.369; 0.082])
$\delta_{CP}$	NO	-2.231	299.49	$[-\pi; -0.640]$ & $[2.793; +\pi]$	1.100	300.20	$[-1.735; 0.469]$  $([-2.176; -0.591])$
$\sin^2 \theta_{13}$	NO	0.0299	297.09	[0.0224; 0.0387]	0.0339	298.09	- ([0.0258; 0.0441])
$\sin^2 \theta_{23}$	YES	0.534	295.92	[0.478; 0.577]	0.536	297.98	- ([0.482; 0.577])
$\Delta m_{32}^2$ or $\Delta m_{13}^2$ ( $10^{-3}$ eV <sup>2</sup> /c <sup>4</sup> )	YES	2.545	295.36	[2.455; 2.634]	2.510	297.56	- ([2.422; 2.599])

Table 7.4: The measured oscillation parameter best-fit and minimum  $\chi^2$  values as well as the  $1\sigma$  CL intervals are shown, for both normal and inverted hierarchy. The  $\pm 1\sigma$  interval is obtained by using the *constant*  $\Delta\chi^2$  method. All the parameters are measured using the reactor constraint  $\sin^2 \theta_{13} = 0.0219 \pm 0.0012$  [66], except for  $\delta_{CP}$  where specified (T2K only) and  $\sin^2 \theta_{13}$ . For the inverted hierarchy the intervals are calculated both with respect to the global minimum, i.e. normal hierarchy, as well as independently for inverted hierarchy (between parenthesis in second row).

bution as a function of  $\sin^2 \theta_{13}$ , where  $\sin^2 \theta_{13} = 0$  is excluded with a significance better than  $5\sigma$  ( $\Delta\chi^2 > 25$ ). The measurement performed by reactor experiments is in agreement with the T2K results at about  $1\sigma$  level.

The measured  $\sin^2 \theta_{23}$  is slightly different from the 2012 global fit result, where the lower octant is favored. The T2K data prefer maximal  $\nu_\mu/\bar{\nu}_\mu$  disappearance though the significance to the octant discrimination is not very high. This is also reflected on the shape of the  $\Delta\chi^2$  distribution which is quite different from what is shown in fig. 1.5. Also for this reason it becomes quite difficult to compare the  $1\sigma$  allowed ranges. However it is clear that the measurement of  $\theta_{23}$  has been improved by the T2K data when looking to the region excluded at  $3\sigma$  level, which is tighter.

The excluded range of  $\Delta m_{32}^2$  ( $\Delta m_{13}^2$ ) is slightly smaller than the one obtained by the 2012 global fit and is in very good agreement. The precision on  $\Delta m_{32}^2$  ( $\Delta m_{13}^2$ ) could be definitely improved by collecting more neutrino data in the next few years.

The best improvement is given to the measurement of  $\delta_{CP}$ . The exclusion of  $\delta_{CP}$  ranges is much stronger compared to the 2012 global fit. The maximal  $\Delta\chi^2$  is about 7 for normal hierarchy and 12 for inverted hierarchy, while the largest  $\Delta\chi^2$  obtained by the 2012 global fit is smaller than 4. The excluded regions are wider also compared to the sensitivity study shown in fig. 7.3. This is mainly driven by the excess of the number of  $\nu_e$  candidates in the T2K data since the antineutrino mode  $\Delta\chi^2$  distribution is statistically less significant, as shown in fig. 7.8, because affected by larger statistical fluctuations. However it is interesting to see that neutrino and antineutrino data gives best-fit values of  $\delta_{CP}$  very close. The value of  $\delta_{CP}$  favored by the joint fit analysis when the reactor constraint is applied is -1.854 and corresponds to normal hierarchy. As shown in fig. 7.6,  $\delta_{CP} = 0$  is excluded with more than 2 standard deviations, while  $\delta_{CP} = \pi$  is not excluded at 90% CL. A large fraction of the range between  $\delta_{CP} = 0$  and  $+\pi$  is excluded with a significance of  $2\sigma$ . Basically with the Run 1-6 data set we cannot exclude the

hypothesis of no CP violation in the leptonic sector at 90% CL.

The inverted hierarchy is disfavored at more than  $1\sigma$  level, using the *constant*  $\Delta\chi^2$  method, and is partially excluded at  $3\sigma$  for values of  $\delta_{CP}$  around  $+\pi/2$ . It has been shown this exclusion, stronger than what is expected from the fit of the Asimov data sets for  $\delta_{CP} = -1.601$ , is due to the small excess of events in the neutrino mode  $e$ -like sample. Indeed the impact of antineutrino mode samples on the result is quite small. If the reactor constraint is not applied, the best-fit value of  $\delta_{CP}$  is still quite close to  $-\pi/2$ . However the exclusion is much weaker than when the reactor constraint is applied. The contour of  $\sin^2\theta_{13}$  vs  $\delta_{CP}$  shows an agreement at the level of  $1\sigma$  with the measurement of the reactors if  $\delta_{CP} \sim -\pi/2$ .

It is now very important to collect more neutrino and antineutrino data, in order to reduce the statistical uncertainties and improve the sensitivity to  $\delta_{CP}$ . As shown in fig. 7.9, if  $12.5 \times 10^{21}$  POT for both neutrino and antineutrino modes are collected, CP violation in the leptonic sector could be confirmed with a significance higher than  $3\sigma$  if  $\delta_{CP}$  is exactly  $-\pi/2$ . This could be possible if the neutrino beam intensity is increased up to 750 MW and the data taking period is extended by about 5-6 years. Furthermore more data will allow to perform a more precise measurement of both  $\sin^2\theta_{23}$  and  $\Delta m_{32}^2$  ( $\Delta m_{13}^2$ ).

The T2K experiment is becoming very important for future long-baseline neutrino oscillation experiments, such as Hyper-Kamiokande [184], a 1 Mtons water Cherenkov detector, that aims to measure  $\delta_{CP}$  with a precision better than  $19^\circ$ . Indeed Hyper-K will use the same detector technology as T2K, though at a much larger scale, as well as the same neutrino beam energy and off-axis configuration. It will be also very important to improve the neutrino flux measurement below the 1% uncertainty as well as the understanding and constraining of the neutrino cross section. All the experience gained with the T2K experiment will be fundamental to proceed toward the measurement of  $\delta_{CP}$ .

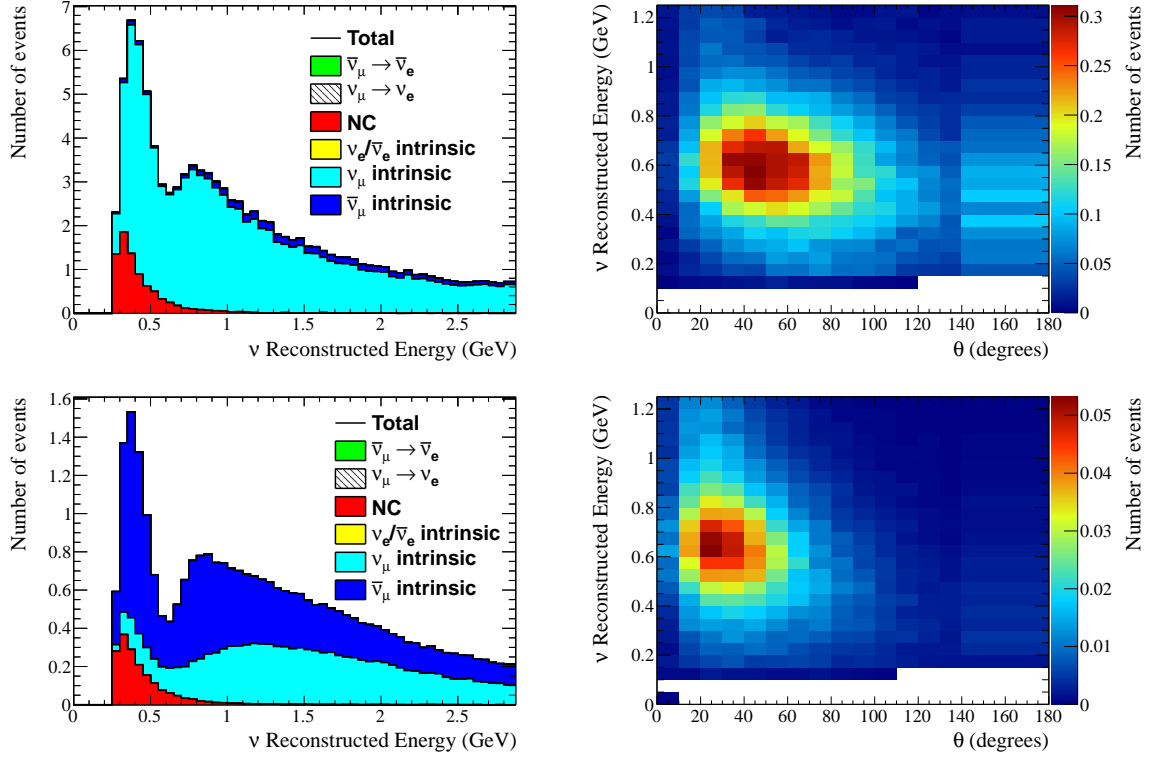


Figure 7.1: Predicted spectra of neutrino mode muon-like (top left) and electron-like (top right), antineutrino mode muon-like (bottom left) and electron-like (bottom right) events. Muon-like distributions are function of the reconstructed neutrino energy, while the electron-like distributions are function of both the reconstructed neutrino energy and the angle between the outgoing lepton and the neutrino direction. The distributions correspond to the statistics collected in the full run 1-6 data set for an exposure of  $6.914 \times 10^{20}$  POT in neutrino mode and of  $4.011 \times 10^{20}$  POT in antineutrino mode. The muon-like distributions are broken down by the following components:  $\bar{\nu}_\mu \rightarrow \bar{\nu}_e$  (green),  $\nu_\mu \rightarrow \nu_e$  (black/white), NC (red),  $\nu_e + \bar{\nu}_e$  intrinsic beam (yellow),  $\nu_\mu$  intrinsic beam (light blue) and  $\bar{\nu}_\mu$  intrinsic beam (blue). The spectra were generated with the systematic parameters measured with the ND280 data shown in tab. B.2 and B.3 and the oscillation parameters shown in tab. 5.2.

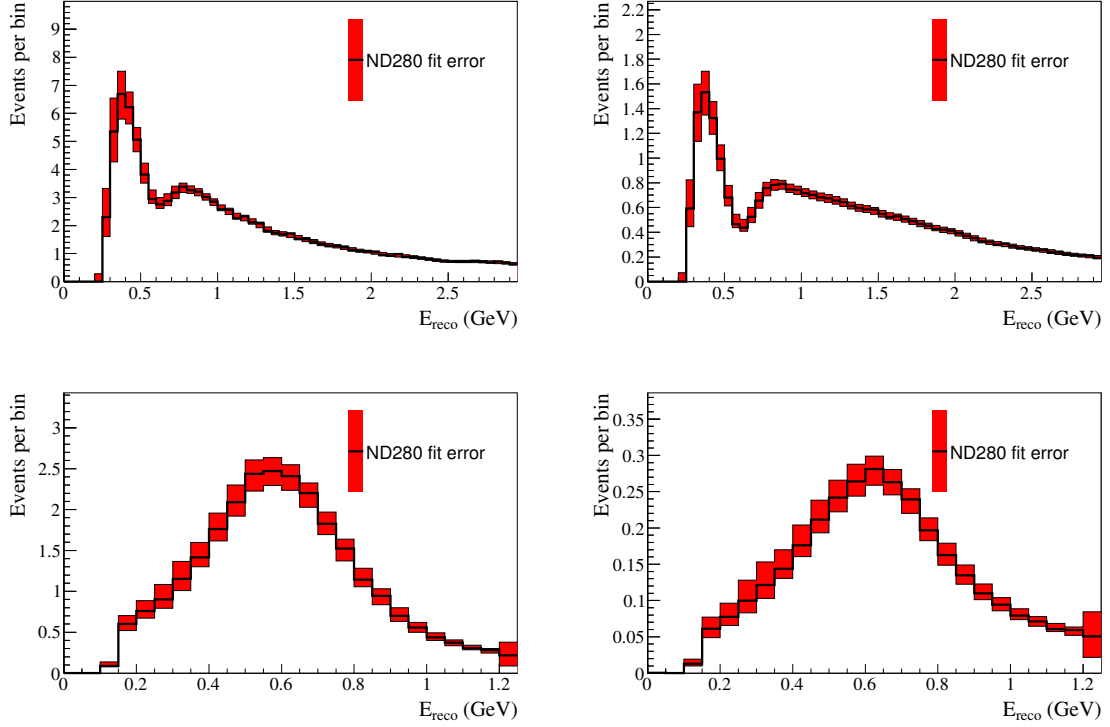


Figure 7.2: Error envelopes for the energy spectrum as a result of all systematic parameters for all the selected samples, from top left to bottom right: neutrino mode muon-like, antineutrino mode muon-like, neutrino mode electron-like and antineutrino mode electron-like. 10k toy MC experiments were generated with randomized systematic parameters and the  $1\sigma$  spread of bin contents was calculated. Existing correlations between the systematic parameters are taken into account. The distributions correspond to the collected statistics in the full run 1-6 data set for an exposure of  $6.914 \times 10^{20}$  POT in neutrino mode and of  $4.011 \times 10^{20}$  POT in antineutrino mode. The spectra were generated with the systematic parameters measured with the ND280 data shown in tab. B.2 and B.3 and the oscillation parameters shown in tab. 5.2.



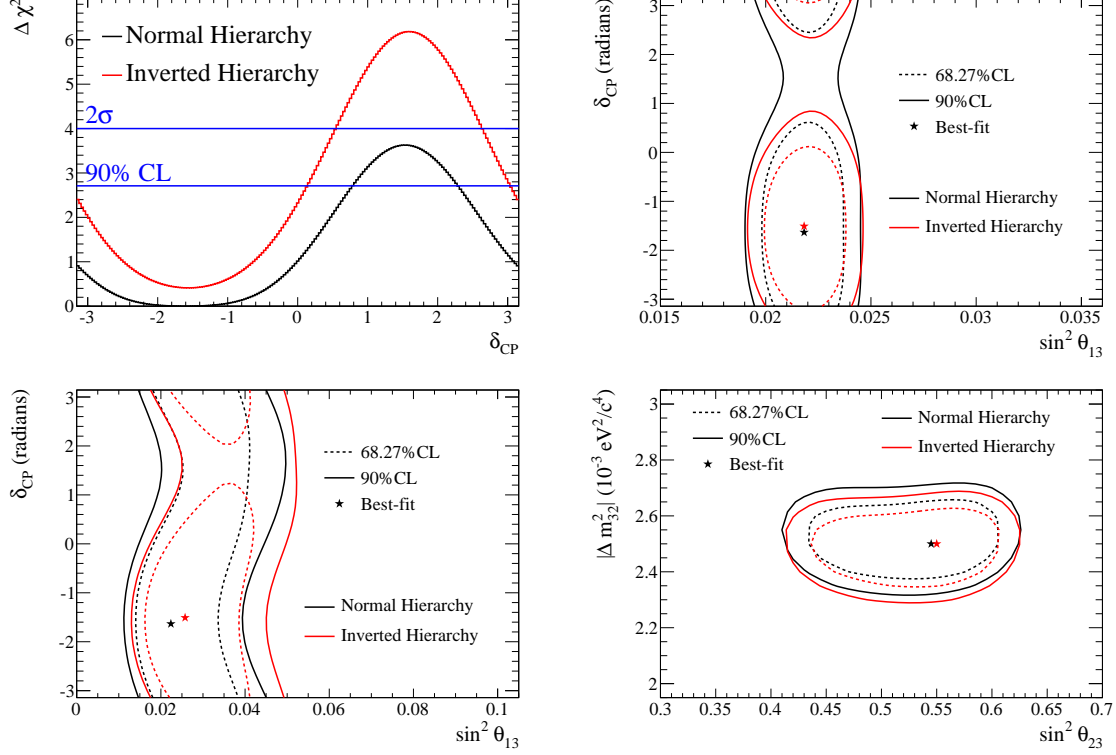


Figure 7.3: Expected confidence intervals for the full run 1-6 statistics with the Asimov data set corresponding to tab. 5.2. Sensitivities for both normal (black) and inverted (red) hierarchy are shown. From top left to bottom right the following combinations of oscillation parameters are shown:  $\delta_{CP}$  with reactor constraint,  $\sin^2 \theta_{13}$  Vs  $\delta_{CP}$  with reactor constraint,  $\sin^2 \theta_{13}$  Vs  $\delta_{CP}$  with T2K only data and  $\sin^2 \theta_{23}$  Vs  $|\Delta m_{32}^2|$  ( $\Delta m_{32}^2$  for normal hierarchy or  $\Delta m_{13}^2$  for inverted hierarchy) with reactor constraint. For  $\delta_{CP}$  the 90% and  $2\sigma$  CL are shown: the values of  $\delta_{CP}$  with  $\Delta\chi^2$  above the blue lines are excluded at a certain CL. For the 2-dimensional contours the 68.27% CL (dashed line) and 90% CL (solid line) are shown. The *constant*  $\Delta\chi^2$  method is used to compute the confidence intervals. The contours for normal and inverted hierarchy in the 2-dimensional sensitivities are independent, while for the  $\delta_{CP}$  1-dimensional sensitivity both normal and inverted hierarchy  $\Delta\chi^2$  distributions are shifted with respect to the same global minimum. All the oscillation parameters which are not parameters of interest are marginalized using the prior distributions shown in tab. 5.2.

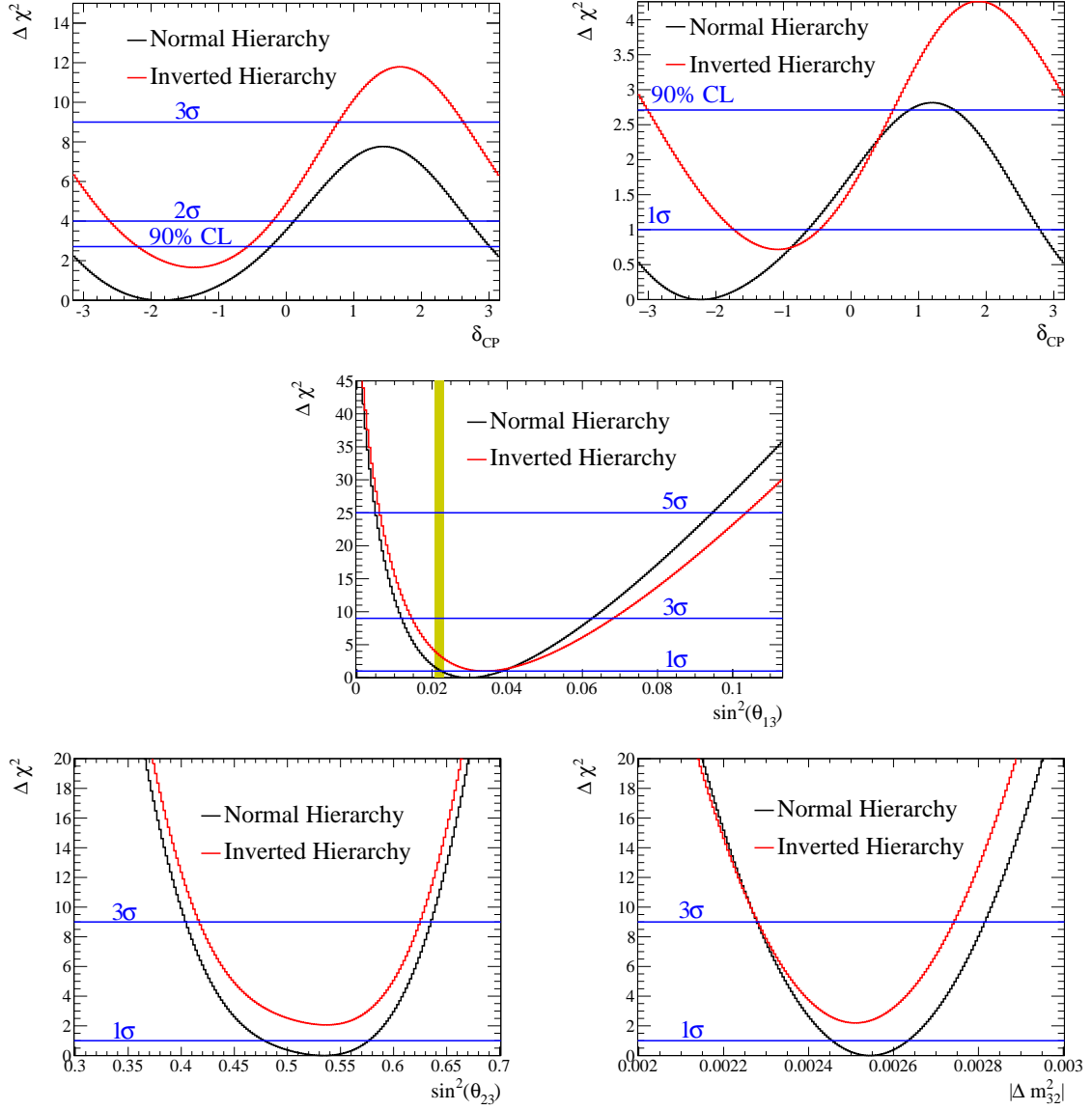


Figure 7.4: Measured  $\Delta\chi^2$  distributions with the full run 1-6 data set as a function of  $\delta_{CP}$  with reactor constraint,  $\delta_{CP}$  with T2K data only,  $\sin^2 \theta_{13}$  with T2K data only,  $\sin^2 \theta_{23}$  with reactor constraint and  $|\Delta m_{32}^2|$  ( $\Delta m_{32}^2$  for normal hierarchy or  $\Delta m_{13}^2$  for inverted hierarchy) with reactor constraint. Both normal (black) and inverted (red) hierarchies are shown. The *constant*  $\Delta\chi^2$  method is used (see app. C.2). Both normal and inverted hierarchy  $\Delta\chi^2$  distributions are shifted with respect to the same global minimum. All the oscillation parameters which are not parameters of interest are marginalized using the prior distributions shown in tab. 5.2. The measured  $\Delta\chi^2$  distribution as a function of  $\sin^2 \theta_{13}$  is compared with the value given by the global analysis of the reactor measurements,  $\sin^2 \theta_{13} = 0.0219 \pm 0.0012$  [66], shown by the yellow bar.

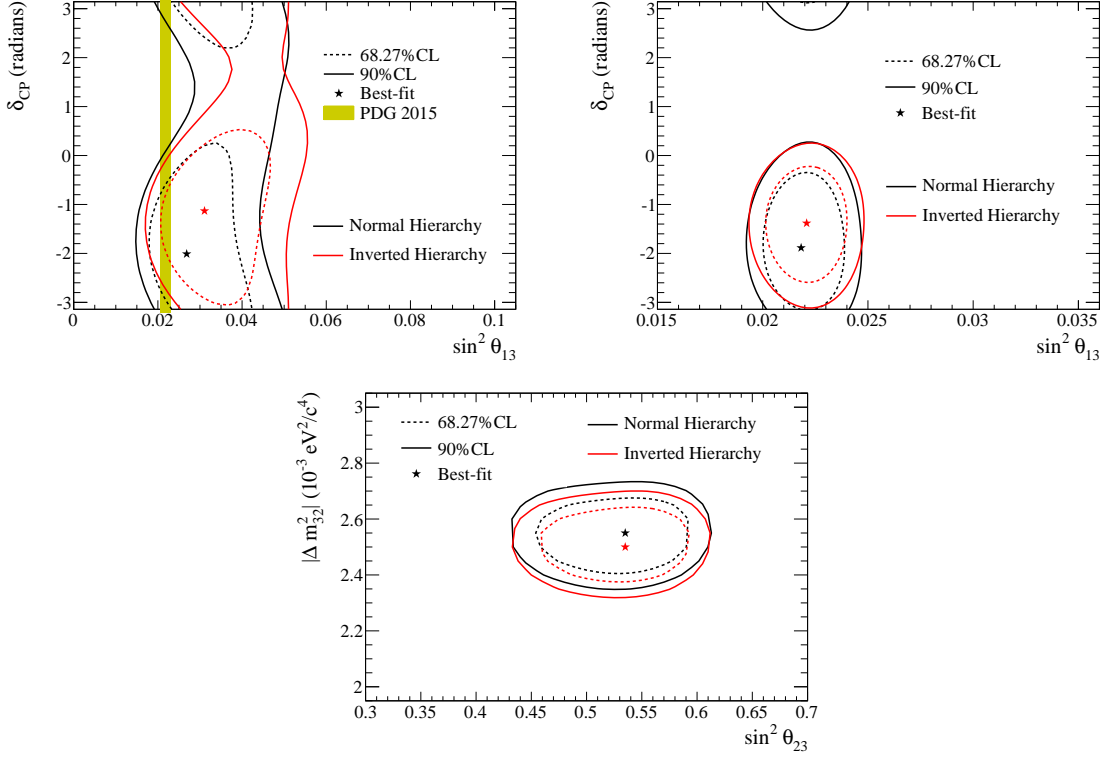


Figure 7.5: Measured confidence intervals with the full run 1-6 data set. Both normal (black) and inverted (red) hierarchies are shown. From top left to bottom right the following combinations of oscillation parameters are shown:  $\sin^2 \theta_{13}$  Vs  $\delta_{CP}$  with T2K data only,  $\sin^2 \theta_{13}$  Vs  $\delta_{CP}$  with reactor constraint and  $\sin^2 \theta_{23}$  Vs  $|\Delta m_{32}^2|$  ( $\Delta m_{32}^2$  for normal hierarchy or  $\Delta m_{13}^2$  for inverted hierarchy) with reactor constraint. Both 68.27% (dashed line) and 90% CL (solid line) are shown. Confidence intervals are performed using the *constant*  $\Delta\chi^2$  method (see app. C.2). Contours for normal (black) and inverted (red) hierarchy are computed independently with respect to the global minimum of each hierarchy (star). All the oscillation parameters which are not parameters of interest are marginalized using the prior distributions shown in tab. 5.2. The measured contour of  $\sin^2 \theta_{13}$  Vs  $\delta_{CP}$  without reactor constraint is compared with the measurement performed by the reactor experiments,  $\sin^2 \theta_{13} = 0.0219 \pm 0.0012$  [66], shown by the yellow bar.

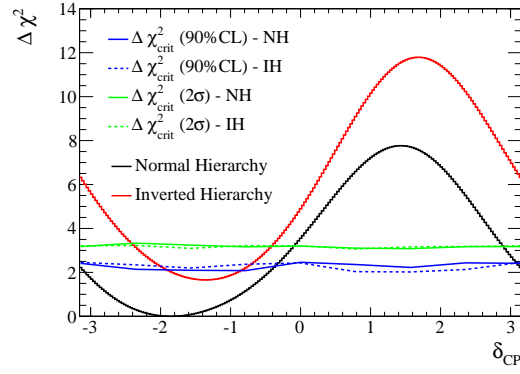


Figure 7.6: Measured  $\Delta\chi^2$  distributions as a function of  $\delta_{CP}$  with reactor constraint with the full run 1-6 statistics. The *Feldman-Cousins* method is used to compute the critical values for 90% (blue) and  $2\sigma$  (green) confidence levels, both normal (solid line) and inverted (dashed line) hierarchy. Both normal (black line) and inverted (red line) hierarchy  $\Delta\chi^2$  distributions are shifted with respect to the same global minimum. The region of  $\delta_{CP}$  and mass hierarchy for which the  $\Delta\chi^2$  values are above the critical values are excluded at a certain confidence level. All the other oscillation parameters are marginalized using the prior distributions shown in tab. 5.2.

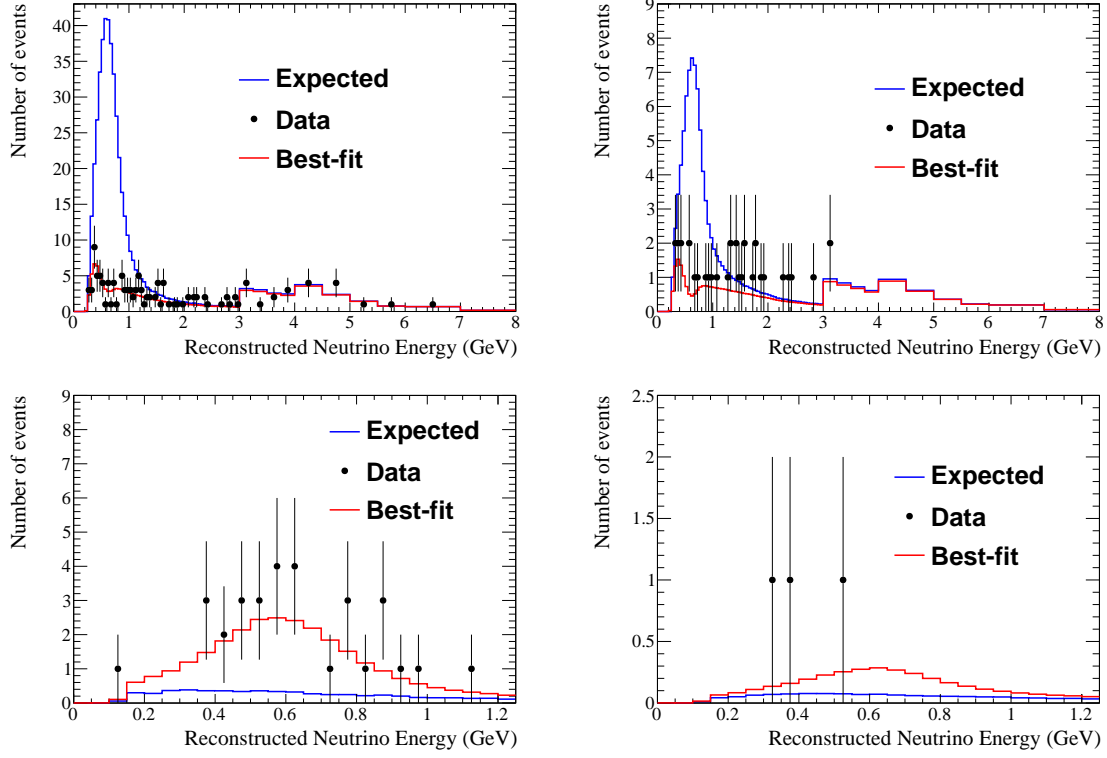


Figure 7.7: The best-fit spectra as a function of the neutrino reconstructed energy shown for each selected sample of the run 1-6 data set. They correspond to the fit of  $\sin^2 \theta_{23}$ ,  $\delta_{CP}$  and mass hierarchy with reactor constraint where all the nuisance parameters are marginalised. From top left to bottom right the neutrino mode muon-like, neutrino mode electron-like, antineutrino mode muon-like and antineutrino mode electron-like samples are shown. The best-fit distributions are compared with the predicted unoscillated spectrum (all the oscillation parameters are set to 0), generated with the systematic parameters measured with the ND280 data shown in tab. B.2 and B.3.

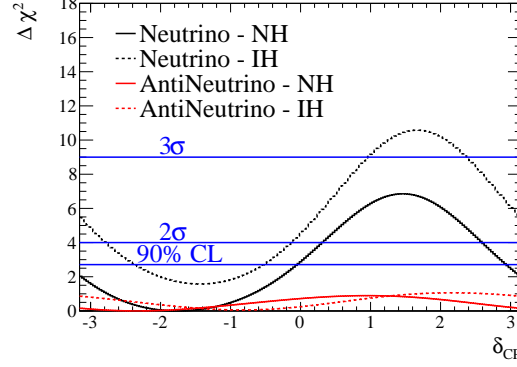


Figure 7.8: Measured  $\Delta\chi^2$  distributions as a function of  $\delta_{CP}$  with reactor constraint with the full run 1-6 data set for neutrino (black) and antineutrino (red) modes. Both normal (solid line) and inverted (dashed line) hierarchies are shown. The *constant*  $\Delta\chi^2$  method is used (see app. C.2). Normal and inverted hierarchy  $\Delta\chi^2$  distributions are shifted with respect to the same global minimum. All the oscillation parameters which are not parameters of interest are marginalized using the prior distributions shown in tab. 5.2.

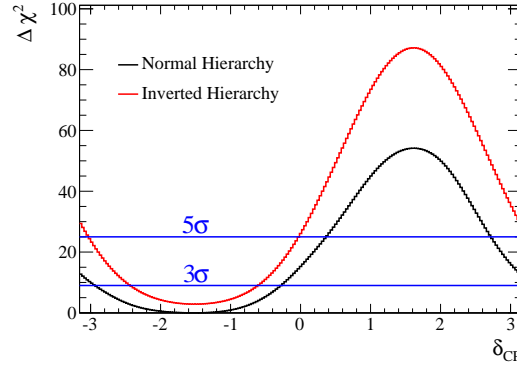


Figure 7.9: Expected  $\Delta\chi^2$  distribution as a function of  $\delta_{CP}$  with  $12.5 \times 10^{21}$  POT for both neutrino and antineutrino modes with the Asimov data set corresponding to tab. 5.2. Sensitivities for both normal (black) and inverted (red) hierarchy are shown. Both normal and inverted hierarchy  $\Delta\chi^2$  distributions are shifted with respect to the same global minimum. The other oscillation parameters are marginalized using the prior distributions shown in tab. 5.2. The parameter  $\sin^2 \theta_{13}$  is constrained with the measurements of the reactor experiments.

# Conclusions

This thesis shows the latest measurement of the neutrino oscillation parameters performed by the T2K experiment. One of the main issues in neutrino oscillation experiments is the poor knowledge of the neutrino flux. Indeed theoretical models show discrepancies up to about 30%. In order to drastically reduce its systematic uncertainty, the total hadron production cross section was measured with the NA61/SHINE experiment, by measuring interactions of protons at 30.8 GeV on a carbon target, the same as at T2K. The cross section has been measured with a precision of about 3%.

Then, since there exist some experimental hints of short baseline oscillations, consistent with active to sterile neutrino oscillations, the data at the T2K near detector were analyzed and a search for  $\nu_e \rightarrow \nu_s$  disappearance was performed in order to test the *reactor* and *gallium* anomalies. If sterile neutrinos exist, the PMNS matrix would not be unitary any more and the 3-neutrino framework should be extended to a 3+N framework. No evidence of sterile neutrinos has been found and the quoted p-value for the null oscillation hypothesis is 0.085.

Finally, assuming the PMNS matrix to be unitary, the antineutrino data collected at the T2K far detector since May 2014 has been analyzed. A search of  $\bar{\nu}_\mu \rightarrow \bar{\nu}_e$  appearance was performed. This oscillation mode is expected in the 3-neutrino framework but never observed so far. No clear evidence of such oscillation has been found. However this could be an interesting result in prospective of the measurement of  $\delta_{CP}$ . Indeed the observation of only 3  $\bar{\nu}_e$  candidates is consistent with  $\delta_{CP} = -\pi/2$ , which corresponds to maximal  $\nu_\mu \rightarrow \nu_e$  appearance, and minimal  $\bar{\nu}_\mu \rightarrow \bar{\nu}_e$  appearance. In order to improve the precision on the oscillation parameters, the neutrino and antineutrino data were jointly analyzed. All the oscillation parameters, except  $\sin^2 \theta_{12}$  and  $\Delta m_{21}^2$ , were measured with a precision comparable or better than the global fit of neutrino experimental data released until 2012, the year I started this thesis work. In particular the significance to  $\delta_{CP}$  has been improved. The data still do not show any clear evidence of CP violation, for which more statistic is required. However the T2K data prefer values of  $\delta_{CP}$  close to  $-\pi/2$ . If about 20 times more data are collected, which is possible by increasing the neutrino beam intensity by a factor 2 and extending the full data taking period by about 5-6 years, CP violation could be observed with a significance better than  $3\sigma$  if the true value of  $\delta_{CP}$  is exactly  $-\pi/2$  and the current systematic uncertainties are assumed.





# Appendices



# Appendix A

## Theory of neutrinos

### A.1 Neutrinos in the Standard Model

The Standard Model describes the strong, electromagnetic, and weak interactions of elementary particles.

The neutrinos are introduced as mass-less fermions (particles with spin  $\frac{1}{2}$ ) which interact via the weak force, exchanging a  $W^\pm$  or a  $Z^0$  boson, but do not carry electric charge. Like all the fermions, neutrinos follow the Dirac equation

$$(i\not{\partial} - m) \psi(x) = 0 \quad (\text{A.1})$$

There are three neutrino electroweak fields  $\nu_e, \nu_\mu, \nu_\tau$  and each of them couples with the corresponding charged lepton field ( $e^-, \mu^-$  and  $\tau^-$ ) in the charged weak current. The symmetry group that describes electroweak interactions is  $SU(2)_L \times U(1)_Y$ , where  $SU(2)$  is called “weak isospin” and its subscript “L” indicates that the elements of the group act in a nontrivial way only on the left-handed chiral components of the fermion fields. The right-handed chiral components are singlets under weak isospin transformations. The generators of the group are  $I_a = \tau_a/2$  ( $a = 1, 2, 3$ ), where  $\tau_1, \tau_2, \tau_3$  are the Pauli matrices. The weak isospin doublets of left-handed leptons are

$$L_e \equiv \begin{pmatrix} \nu_{eL} \\ e_L \end{pmatrix} L_\mu \equiv \begin{pmatrix} \nu_{\mu L} \\ \mu_L \end{pmatrix} L_\tau \equiv \begin{pmatrix} \nu_{\tau L} \\ \tau_L \end{pmatrix} \quad (\text{A.2})$$

while  $e_R, \mu_R$  and  $\tau_R$  are singlets which correspond to the right-handed components. In the Standard Model it is assumed that the neutrino fields have only left-handed components because of the parity violated nature of the electroweak theory. This assumption follows from the two-component theory of Landau [25], Lee and Yang [26] and Salam [27], implying that neutrinos are mass-less. The symmetry group  $U(1)_Y$  is called “hypercharge” and is generated by the hypercharge operator  $Y$ , which is connected to  $I_3$  and the charge operator  $Q$ :

$$Q = I_3 + \frac{Y}{2}. \quad (\text{A.3})$$

A vector gauge boson is associated to each generator. If neutrinos are mass-less only left-helicity neutrinos ( $\nu_L$ ) or right-helicity anti-neutrinos ( $\bar{\nu}_R$ ) exist. The chirality left- (right-) handed states are described by  $\nu_{L(R)} \equiv [(1 \mp \gamma^5)/2] \nu$ , where  $\gamma^5 \equiv i\gamma^0\gamma^1\gamma^2\gamma^3\gamma^4$  and  $\gamma^\mu$  are the Dirac matrices, and correspond to the helicity states, if mass-less.

The gauge invariance of the weak interaction Lagrangian is spontaneously broken via the Higgs mechanism [24] by adding the Higgs lagrangian term

$$\mathcal{L}_{Higgs} = (D_\mu \phi)^\dagger (D^\mu \phi) - V(\phi) \quad (\text{A.4})$$

$$V(\phi) = \mu^2 \phi^\dagger \phi + \lambda (\phi^\dagger \phi)^2 \quad (\text{A.5})$$

to the Standard Model lagrangian, where  $D_\mu$  is the covariant derivative,  $\lambda > 0$  and  $\mu^2 < 0$  in order to realize the spontaneous symmetry breaking.  $\phi^+$  and  $\phi^0$ , with electric charge +1 and 0 respectively, are the components of the Higgs weak isospin doublet

$$\phi(x) \equiv \begin{pmatrix} \phi^0(x) \\ \phi^+(x) \end{pmatrix}. \quad (\text{A.6})$$

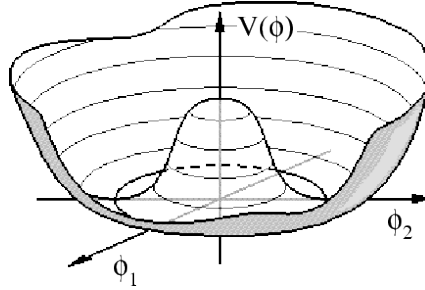


Figure A.1: Potential described by eq. A.5 which gives rise to the symmetry breaking. The vacuum, i.e. the minimum, has clearly a non-zero value.

An interaction with the higgs potential, given by eq. A.5, that has the shape of a “mexican hat”, allows particles to acquire mass.

A doublet of scalar fields couples to the fermions via the Higgs-lepton Yukawa Lagrangian term

$$\mathcal{L}_{H,L} = - \sum_{\alpha,\beta=e,\mu,\tau} y_{\alpha\beta} (\bar{\nu}_{\alpha L} \phi^+ l_{\beta R} + \bar{l}_{\alpha L} \phi^0 l_{\beta R}) + h.c. \quad (\text{A.7})$$

where  $y_{\alpha\beta}$  is the Yukawa coupling.

After the symmetry breaking with the choice

$$\tilde{\phi}(x) = \frac{1}{\sqrt{2}} \begin{pmatrix} v + H(x) \\ 0 \end{pmatrix} \quad (\text{A.8})$$

where  $H(x)$  is the Higgs field and  $v \simeq 246$  GeV is the vacuum expectation value of the Higgs field (VEV), eq. A.7 becomes

$$\mathcal{L}_{H,L} = - \sum_{\alpha=e,\mu,\tau} \frac{y_{\alpha} v}{2} \bar{l}_{\alpha R} l_{\alpha L} - \sum_{\alpha=e,\mu,\tau} \frac{y_{\alpha}}{2} \bar{l}_{\alpha R} l_{\alpha L} H \quad (\text{A.9})$$

where the first term is a Yukawa mass term for the charged leptons, whose masses are given by  $m_{\alpha} = \frac{y_{\alpha} v}{2}$  ( $\alpha = e, \mu, \tau$ ), unknown parameters that cannot be predicted and must be obtained

from experimental measurements. The right term shows a trilinear coupling with constant  $\frac{m_\alpha}{v}$  between the charged leptons and the Higgs boson, proportional to the lepton mass. All the fermions (with the exception of neutrinos) as well as  $W^\pm$  and  $Z^0$  gauge bosons acquire mass. A fermion mass term must involve a coupling of left-handed and right-handed fields, so in the Standard Model neutrinos are massless because their fields do not have a right-handed component. Since after the symmetry breaking the neutrinos remain massless, the analogue of eq. A.9 for neutrinos is not present, so they do not couple with the Higgs boson. In order to have the electroweak symmetry breaking the energy must be comparable to the VEV. Indeed for energies higher than the electroweak symmetry breaking, the “mexican hat” potential of eq. A.5, shown in fig. A.1, becomes negligible and the symmetry cannot be broken by the Higgs mechanism.

The lepton numbers  $L_e$ ,  $L_\mu$  and  $L_\tau$  are singularly conserved and  $L(\nu) = -L(\bar{\nu})$ . Consequently the total lepton number  $L = L_e + L_\mu + L_\tau$  is conserved as well.

The coupling with  $W^\pm \nu l$  gives charged-current interaction with a neutrino in the initial state and a charged lepton in the final state is described by the charged current Lagrangian term

$$\mathcal{L}_{CC} = -\frac{g}{\sqrt{2}} W_\rho^- \bar{l}_L \gamma^\rho \nu_L + h.c. \quad (\text{A.10})$$

where  $g$  is the electroweak coupling constant and  $\bar{l}_L \equiv l_L^\dagger \gamma^0$

The NC interaction is described by the coupling  $Z^0 \nu \nu$  with a neutrino both in the initial and final state and the corresponding Lagrangian is

$$\mathcal{L}_{NC} = -\frac{g}{\sqrt{2} \cos \theta_W} Z_\rho^0 \bar{\nu}_L \gamma^\rho \nu_L + h.c. \quad (\text{A.11})$$

where  $\theta_W$  is the Weinberg angle.

Experimental evidences show that neutrinos oscillate between different flavor states. As it is explained in sec. 1.2 and app. A.2, this implies that neutrinos must have a mass, which corresponds to new physics beyond the Standard Model.

## A.2 Neutrinos masses

The mass of neutrinos can be introduced in the theory by some extensions of the Standard Model. A Dirac neutrino mass, that follows eq. A.1, could be generated with the same Higgs mechanism that gives mass to quarks and charged leptons in the Standard Model, as shown in app. A.1, with the extension that also right-handed neutrinos  $\nu_{\alpha R}$  ( $\alpha = e, \mu, \tau$ ) are introduced. The asymmetry between the lepton and quark sectors would be eliminated, since right-handed quarks are already predicted. This model is also called minimally extended Standard Model with three right-handed neutrino fields. However the right-handed neutrinos are different from the other elementary fermion fields because they are invariant under the symmetries of the Standard Model as  $SU(3)_C \times SU(2)_L$  and have hyper-charge  $Y = 0$ . We will call these right-handed neutrinos as *sterile* because they do not undergo electroweak and strong interactions and can interact only with the gravitational force. The standard neutrinos  $\nu_e$ ,  $\nu_\mu$  and  $\nu_\tau$  participate in weak interactions and are called *active*. The presence of sterile right-handed neutrinos is irrelevant for the cancellation of quantum anomalies, which constrain the properties of the other

elementary fermion fields. For this reason the number of right-handed neutrino fields is not constrained by the theory. These fields would be singlets under the Standard Model symmetries and hence sterile.

The Standard Model Higgs-lepton Yukawa term of eq. A.7 can be extended by adding the terms that correspond to three right-handed neutrinos and left-handed antineutrino fields:

$$\mathcal{L}_{H,L} = - \sum_{\alpha=e,\mu,\tau} m_D^\alpha \bar{\nu}_{\alpha L} \nu_{\alpha R} + h.c. \quad (\text{A.12})$$

where  $m_D^\alpha = \frac{y_\alpha^\nu v}{2}$ .

It is important to know that the neutrino masses obtained with this mechanism are proportional to the Higgs VEV, as the masses of charged leptons and quarks. However, it is known that neutrino masses are much smaller than those of the charged leptons and quarks and a very small Higgs-neutrino Yukawa coupling would be required. However there is no explanation for a very small value of the coupling.

Another possible way to introduce neutrino masses in the Standard Model is to assume that neutrinos are Majorana particles [3], i.e. neutrinos and antineutrinos are the same entity. The only thing that differentiates neutrinos and anti-neutrinos is the helicity. An ultrarelativistic Majorana neutrino with positive helicity interacts as a Dirac antineutrino with positive helicity and ultrarelativistic Majorana neutrino with negative helicity interacts as a Dirac neutrino with negative helicity. It is used to call Majorana neutrinos with negative helicity *neutrinos* and Majorana neutrinos with positive helicity *anti-neutrinos*.

Considering only one neutrino and omitting the flavor, given  $C$  the charge conjugation operator and  $\nu_C$  the charged conjugate of the neutrino field  $\nu$  defined as

$$\nu^C = C^\dagger \nu C = C \bar{\nu}^T \quad (\text{A.13})$$

the fermion field can be written as

$$\nu = \nu_L + \nu_R = \nu_L + C \bar{\nu}_L^T \quad (\text{A.14})$$

If neutrinos and anti-neutrinos are the same particle we can define the Majorana neutrino field as

$$\nu = \nu_L + \nu_R = \nu_L + \nu_L^C \quad (\text{A.15})$$

and the condition

$$\nu^C = \nu \quad (\text{A.16})$$

is satisfied.

Only neutral particles, like neutrinos, can follow eq. A.16.

The absence of a conserved lepton number is evident from the fact that Dirac neutrinos have  $L = +1$  and Dirac antineutrinos have  $L = -1$ . Since in the Majorana case neutrinos

and antineutrinos are the same object, it is clear that there cannot be a conserved lepton number. However, since neutrino masses are very small and the Lagrangian is invariant under the global  $U(1)$  gauge transformations, it is possible to assign to charged leptons and neutrinos an effective total lepton number  $L_{eff}$  which is conserved in all the processes that are not sensitive to the Majorana mass of neutrinos. In these processes, the neutrinos can be considered to be massless. These assignments of the effective lepton number lead to its conservation in all the weak interaction processes, because in such processes a charged lepton with  $L_{eff} = +1$  can produce only a negative helicity neutrino and a charged antilepton with  $L_{eff} = -1$  can produce only a positive helicity neutrino. The Dirac and Majorana descriptions of a neutrino have different phenomenological consequences only if the neutrino is massive.

Majorana mass terms can be constructed from the left-handed neutrino states alone ( $\nu_L$ ), from right-handed neutrino states only ( $\nu_R$ ), or from both. The left-handed Majorana mass term is

$$\mathcal{L}_{M,L} = \frac{1}{2} m_L \bar{\nu}_L^C \nu_L + h.c. \quad (\text{A.17})$$

and the right-handed one is

$$\mathcal{L}_{M,R} = \frac{1}{2} m_R \bar{\nu}_R^C \nu_R + h.c. \quad (\text{A.18})$$

where  $m_L$  and  $m_R$  are dimensionless free parameter with the characteristic of a mass.

If the Majorana mass terms in eq. A.17 and eq. A.18 are considered as a perturbation of the massless Lagrangian, it generates transitions with  $\Delta L_{eff} = \pm 2$ . The most promising process which could allow the discovery of such transitions is the neutrinoless double  $\beta$ -decay  ${}^A_Z X \rightarrow {}^A_{Z+2} X' + 2e^-$ . Many experiments are searching for this process which would not only lead to the discovery of the Majorana nature of neutrinos, but also to the measurement of the absolute neutrino mass scale.

Considering only one generation and assuming that both  $\nu_L$  and  $\nu_R$  exist, a general mass term can be obtained from the combination of all the possible terms of the Dirac and Majorana Lagrangians, shown in eq. A.12, eq. A.17 and eq. A.18:

$$\mathcal{L}_{D+M} = \frac{1}{2} m_L \bar{\nu}_L^C \nu_L + \frac{1}{2} m_R \bar{\nu}_R^C \nu_R - m_D \bar{\nu}_L \nu_R + h.c. \quad (\text{A.19})$$

$$= \frac{1}{2} (\bar{\nu}_L^C, \bar{\nu}_R) \begin{pmatrix} m_L & m_D \\ m_D & m_R \end{pmatrix} \begin{pmatrix} \nu_L \\ \nu_R^C \end{pmatrix} + h.c. \quad (\text{A.20})$$

where  $m_L$  and  $m_R$  are respectively the left-handed and right-handed Majorana neutrino masses while  $m_D$  is the Dirac mass. It is interesting to see that the Dirac-Majorana lagrangian is invariant under  $SU(2)_L \times U(1)_Y$  if  $m_L = 0$ , since the mass term in eq. A.17 is not allowed by the Standard Model symmetry. Since there are off-diagonal Dirac terms, the chiral fields  $\nu_L$  and  $\nu_R$  have not a definite mass and the diagonalization of the mass matrix is needed. If we define the Majorana massive neutrino field as in eq. A.15, the resulting Lagrangian is

$$\mathcal{L}_{D+M} = \frac{1}{2} \sum_{k=1,2} m_k \nu_{kL}^T C^\dagger \nu_{kL} + H.c. = -\frac{1}{2} \sum_{k=1,2} m_k \bar{\nu}_k \nu_k \quad (\text{A.21})$$

where  $\nu_k$  are the mass neutrino fields and  $m_k$  are the eigenvalues of the diagonalized mass matrix:

$$m_{1,2} = \frac{1}{2} \left[ m_L + m_R \pm \sqrt{(m_L - m_R)^2 + 4m_D^2} \right] \quad (\text{A.22})$$

If  $m_D \ll m_R$  and  $m_L = 0$  from eq. A.22 we obtain

$$m_1 \simeq \frac{m_D^2}{m_R} \quad (\text{A.23})$$

$$m_2 \simeq m_R \quad (\text{A.24})$$

Therefore  $\nu_2$  is as heavy as  $\nu_R$  while  $\nu_1$  is very light. This is the so-called *see-saw mechanism* for which the heavy mass  $m_2$  of  $\nu_2$  is responsible for the lightness of  $\nu_1$ . From eq. A.23 it becomes clear how the existence of a heavy sterile neutrino could explain the very light active neutrino masses. The mixing angle between the active and sterile states is defined as

$$\tan 2\theta = 2 \frac{m_D}{m_R} \quad (\text{A.25})$$

and becomes very small if the sterile neutrino mass is very large. This would imply that  $\nu_1$  is mainly composed of the active chiral state  $\nu_L$  and  $\nu_2$  is composed mainly of the sterile state  $\nu_R$ . The Dirac mass  $m_D$  can be generated through the Standard Model Higgs mechanism and is expected not to be much larger than the electroweak scale, of the order of  $10^2$  GeV. On the other hand the Majorana mass state could be at the grand unification scale, i.e.  $10^{14}$ - $10^{16}$  GeV, and would explain the reason why the active neutrinos have a very small mass. It should be noted that the light neutrino mass scale,  $m_1$ , is not a fundamental scale, but is derived from the combination of  $m_D$  and  $m_R$ , at a much bigger scale. For this reason the neutrino physics in the context of the *see-saw* mechanism can be seen as a portal, at low energies, of new physics at very high energies, close to the GUT energy. Following the procedure described above, more than one sterile neutrino can be introduced in the model, also with different masses, both heavy and light.

The same result of the See-Saw mechanism can be obtained by constructing a lagrangian term that is not renormalizable and violates the lepton number. If we take eq. A.20 for  $m_L = 0$  we obtain

$$\mathcal{L}^{D+M} = -m_D (\bar{\nu}_R \nu_L + \bar{\nu}_L \nu_R) + \frac{1}{2} m_R (\nu_R^T C^\dagger \nu_R + \nu_R^\dagger C \nu_R^*) \quad (\text{A.26})$$

that above the electroweak symmetry scale becomes

$$\mathcal{L}^{D+M} = -y^v (\bar{\nu}_R \tilde{\phi}^\dagger L_L + \bar{L}_L \tilde{\phi} \nu_R) + \frac{1}{2} m_R (\nu_R^T C^\dagger \nu_R + \nu_R^\dagger C \nu_R^*) \quad (\text{A.27})$$

where  $y^v$  is a Yukawa coupling,  $\tilde{\phi}$  is the transformed Higgs doublet ( $\tilde{\phi} = i\tau_2 \phi^*$ ) and  $L_L$  is the Standard Model lepton doublet in eq. A.2. Below the electroweak symmetry-breaking scale



the Dirac mass  $m_D = \frac{y^v v}{\sqrt{2}}$  is generated. If the mass  $m_R$  is very heavy, at the Standard Model energies the right-handed chiral field can be integrated away by considering it in the static limit, where the kinetic energy of the motion term is negligible, and we get

$$\nu_R \simeq -\frac{y^v}{m_R} \tilde{\phi}^T C \bar{L}_L^T \quad (\text{A.28})$$

Substituting eq. A.28 in eq. A.27 we get

$$\mathcal{L}_5 \simeq -\frac{1}{2} \frac{(y^v)^2}{m_R} (L_L^T \tau_2 \phi) C^\dagger (\phi^T \tau_2 L_L) \quad (\text{A.29})$$

where 5 indicates the energy dimension. This lagrangian term is not renormalizable, since it would need an energy dimension not larger than four. However this is the lowest dimension term which could generate a Majorana neutrino mass.

Below the electroweak symmetry-breaking scale, where the Higgs mechanism is valid, if we define  $\nu_{1L} \simeq -i\nu_L$ , eq. A.29 becomes

$$\mathcal{L}_5 \simeq \frac{1}{2} \frac{m_D^2}{m_R} \left( \nu_{1L}^T C^\dagger \nu_{1L} + \nu_{1L}^\dagger C \nu_{1L}^* \right) \quad (\text{A.30})$$

This is a Majorana mass term for  $\nu_{1L}$ , whose mass  $m_1$  is given by the *see-saw* formula in eq. A.23. The alternative derivation above shows that the *see-saw* mechanism is a particular case of an effective Lagrangian approach. The lagrangian term  $\mathcal{L}_5$  is not acceptable in the framework of Standard Model because it is not renormalizable. However the Standard Model cannot be considered as a final theory but only an effective low-energy theory produced by the symmetry breaking of a high-energy unified theory. So it is reasonable that there are effective low-energy lagrangian terms which respect the symmetries of Standard Model but are non-renormalizable. There are different versions of *see-saw* mechanism, where the Higgs sector is expanded and Higgs multiplets are added to the theory. The version of *see-saw* described in this section is called of *type-I*.

### A.3 Leptogenesis

The possibility that neutrinos are Majorana particles is fundamental for the understanding of the matter/antimatter asymmetry in the universe. The non observation of primordial antimatter in the Universe could be related to fundamental properties of particle physics. As Sakharov pointed out in 1967 [37], there are three necessary conditions that must be satisfied to allow the *baryogenesis* process to produce the baryon asymmetry:

- the existence of an elementary process that violates the baryon number;
- violation of charge conjugation C and CP, the combination of parity transformation P, corresponding to flipping the sign of all space coordinates, and charge conjugation C, a flip of the sign of all charges of the elementary particles. The violation of the CP symmetry implies that laws of the nature are different for matter and antimatter;
- a departure from thermal equilibrium during the baryogenesis.

The  $CP$  symmetry is partially violated in the Standard Model baryon sector by the weak force, but it is not enough to account for all the present baryon asymmetry. The most promising mechanism that can explain the matter/antimatter asymmetry is called *leptogenesis* [36]. The minimal version of *leptogenesis*, that will be described in this section, is a cosmological consequence of the *type I see-saw* mechanism described in app. A.2 with three heavy right-handed neutrinos ( $N_i$ ,  $i = 1, 2, 3$ ). In the very early stage of the Universe, after the inflation period, when matter was in the form of plasma, the temperature was  $T \sim 10^{15}$  GeV. At these temperatures the heavy neutrinos were produced by the Yukawa interactions of leptons and Higgs bosons in the thermal bath and then decay either into leptons, through  $N_i \rightarrow l_i + \phi$ , or into antileptons. Since both the heavy right-handed neutrino  $N$ , with mass  $m_N$ , and the Higgs boson  $\phi$  do not carry any lepton number, both inverse processes and decays violate the lepton number by  $\Delta L = 1$ ,  $CP$  and  $B - L$ . When  $T < m_N$ , the heavy right-handed neutrinos are not produced by inverse process any longer and can only decay. This satisfies the third Sakharov condition. If  $CP$  symmetry is violated in the leptonic sector, then the decay rate into leptons,  $\Gamma(N \rightarrow l\phi)$ , is different from the decay rate into antileptons,  $\Gamma(N \rightarrow l^C\phi^C)$  and a lepton/antilepton asymmetry would be produced. The  $CP$  violation asymmetry can be written as

$$\epsilon = \frac{\Gamma(N \rightarrow l + \phi) - \Gamma(N \rightarrow \bar{l} + \phi^\dagger)}{\Gamma(N \rightarrow l + \phi) + \Gamma(N \rightarrow \bar{l} + \phi^\dagger)} \quad (\text{A.31})$$

At temperatures  $T \gg 100$  GeV, Standard Model processes in equilibrium, called *sphalerons*, converted the lepton asymmetry into a baryon asymmetry conserving  $B-L$ . About  $1/3$  of the  $B - L$  asymmetry is converted in the form of baryon asymmetry, while  $-2/3$  of the  $B - L$  asymmetry is converted in the form of lepton number. All the three Sakharov conditions are clearly satisfied.

In order to prove the *leptogenesis* it becomes fundamental to observe that neutrinos are Majorana-like and that  $CP$  is violated in the leptonic sector. The first problem is that  $CP$  violation involving the heavy right-handed neutrinos cannot be proved, since these neutrinos are too massive and cannot be produced by any experiment. However it has been shown that the  $CP$  violation asymmetry in eq. A.31 can depend only on the  $CP$  violation of light active neutrinos shown in sec. 1.2. If  $T \gtrsim m_N \sim 10^{12}$  GeV all the interactions mediated by the charged lepton Yukawa coupling are out of equilibrium and the lepton flavor composition does not play any role in the final asymmetry. Only the total lepton number affects the asymmetry [38]. At this energy all the relevant interactions are flavor blind and the lepton quantum states evolve coherently between the production from  $N$ -decay and the subsequent inverse decay with the Higgs boson.

However at  $T \sim m_N \sim 10^{12}$  GeV the interaction mediated by the charged  $\tau$  Yukawa coupling come into equilibrium as well as the  $\mu$  Yukawa coupling at  $T \sim m_N \sim 10^9$  GeV. At these energies the flavor becomes physical. The final value of the baryon asymmetry is the sum of the contribution of  $CP$  violation from each active flavor.

Assuming all the Majorana  $CP$  violation phases are null and only the  $CP$  violation phase of active flavor neutrinos ( $\delta_{CP}$ ) can play a role in the total baryon asymmetry, for a temperature in the range  $10^9 \gtrsim m_N \gtrsim 10^{12}$  GeV, a lower bound on the  $CP$  violation asymmetry is obtained:

$$\epsilon \propto |\sin \theta_{13} \sin \delta_{CP}| \gtrsim 0.11 \quad (\text{A.32})$$

Since, as it will be shown in sec. 1.3.3,  $\theta_{13}$  has been measured to be relatively large ( $\sin \theta_{13} \sim 0.15$ ) a large value of  $\sin \delta_{CP}$  could be sufficient to explain the full baryon asymmetry through

*leptogenesis*. The discovery of CP violation in the leptonic sector, by looking for a different oscillation probability between  $\nu_\mu \rightarrow \nu_e$  and  $\bar{\nu}_\mu \rightarrow \bar{\nu}_e$  oscillations, and Majorana neutrinos will be a strong indication of *leptogenesis* as the origin of the matter/antimatter asymmetry.

## A.4 Light sterile neutrinos

As shown in sec. A.2 and A.3 the existence of heavy right-handed neutrinos, introduced by the *see-saw* mechanism, can explain why active neutrinos have a very small mass. They also play a fundamental role in the *leptogenesis*, a possible solution to the baryon asymmetry problem.

There also exist some experimental hints that are consistent with oscillations between active and sterile neutrinos (see sec. 1.5) and if sterile neutrino masses are in the range  $1 \text{ eV} \lesssim M \lesssim 1 \text{ MeV}$  (keV is preferred) they are an interesting warm dark matter candidate [81].

For the *see-saw* mechanism all the mass values of the right-handed neutrinos are technically natural, but it also turns out that, while neutrinos are Majorana fermions, for large masses the active and right-handed neutrinos are decoupled and mixing does not occur (see eq. A.25). These oscillations could happen if neutrinos are *pseudo-Dirac* like ( $m_D \gg m_L, m_R$ ) or in the *active sterile* case ( $m_D$  is comparable to  $m_L$  and  $m_R$ ). However the *pseudo-Dirac* case is excluded, as shown in fig. A.2 [80]. This figure also shows that for mass splittings higher than  $\sim 1 \text{ eV}^2$  the oscillation amplitudes becomes smaller.

A significant *active sterile* mixing requires that at least some Dirac masses ( $m_D$ ) and some Majorana masses ( $m_R$  or  $m_L$ ) are simultaneously very small but non-zero. Furthermore both *pseudo-Dirac* and *active sterile* cases cannot explain the small mass of the active neutrinos.

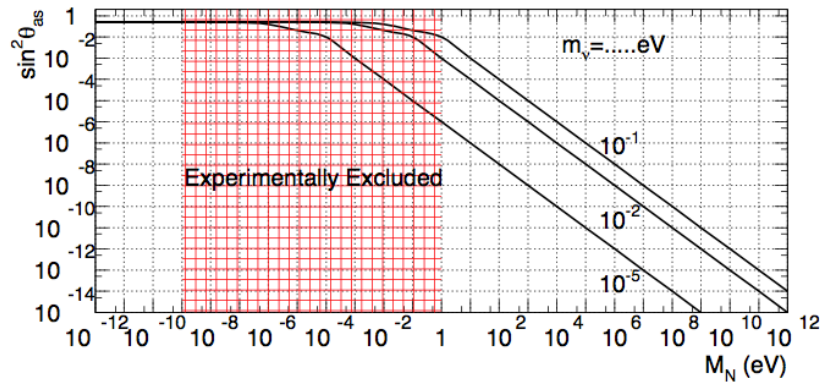


Figure A.2: Estimate of the magnitude of the mixing between active and sterile neutrinos  $\sin^2 \theta$  as a function of the right-handed neutrino mass  $M_N$ , for different values of the mostly active neutrino masses,  $m_\nu = 10^{-1}, 10^{-2}$ , and  $10^{-5} \text{ eV}$ . The hatched region qualitatively indicates the values of  $M_N$  that are currently excluded by the world's particle physics data [80].

If light sterile neutrinos exist a new theory, as the *split see-saw* mechanism [82], should be introduced. It consists of the Standard Model with three right-handed neutrinos and assumes the space-time to be five dimensional. If two heavy right-handed neutrinos are localized on a brane separated from the Standard Model one, the wave function overlap between them and the lighter states is very weak and the *see-saw* mechanism is preserved. In this way one can explain the matter-antimatter asymmetry of the Universe, the warm dark matter and the oscillations between active and sterile neutrinos in a more natural way, instead of introducing effective

Yukawa couplings.

Sterile neutrinos with mass of the order of  $O(1 \text{ keV})$  can be a good candidate for non-baryonic warm Dark Matter. Cosmological data do not favor the existence of a fourth right-handed neutrino with a mass of the order of 1 eV, which is distinct from cold and warm dark matter [77]. However these analyses are strongly model dependent and light sterile neutrinos with eV or sub-eV mass have been shown to help reconcile the tensions in the cosmological data between current measurements of the present and early Universe [78]. These sterile neutrinos can be studied by experiments with a longer baseline like the Daya Bay experiment that put quite strong limits in the mass splitting range  $10^{-3} < |\Delta m_{41}^2| < 0.1 \text{ eV}^2/c^4$  [79].

## Appendix B

# Flux and cross section systematic uncertainties used in the analysis at Super-K

A more detailed description of the flux and cross section systematic uncertainties used in the  $\bar{\nu}_\mu \rightarrow \bar{\nu}_e$  appearance analysis is shown in tab. B.1. In tab. B.2 and B.3 the flux and cross section systematics used in the  $\nu/\bar{\nu}$  joint analysis at Super-K are shown.

Parameter	Description	Energy range (GeV)	Nominal value	$1\sigma$ pre/postfit
0	$\nu_\mu$ flux	0.0 - 0.7	1.142	0.094 / 0.071
1	$\nu_\mu$ flux	0.7 - 1.0	1.091	0.079 / 0.053
2	$\nu_\mu$ flux	1.0 - 1.5	1.079	0.077 / 0.052
3	$\nu_\mu$ flux	1.5 - 2.5	1.074	0.081 / 0.060
4	$\nu_\mu$ flux	2.5 - 30.0	1.050	0.080 / 0.053
5	$\bar{\nu}_\mu$ flux	0.0 - 0.4	1.204	0.104 / 0.069
6	$\bar{\nu}_\mu$ flux	0.4 - 0.5	1.210	0.102 / 0.058
7	$\bar{\nu}_\mu$ flux	0.5 - 0.6	1.180	0.096 / 0.051
8	$\bar{\nu}_\mu$ flux	0.6 - 0.7	1.128	0.085 / 0.041
9	$\bar{\nu}_\mu$ flux	0.7 - 1.0	1.123	0.125 / 0.077
10	$\bar{\nu}_\mu$ flux	1.0 - 1.5	1.118	0.105 / 0.068
11	$\bar{\nu}_\mu$ flux	1.5 - 2.5	1.121	0.080 / 0.053
12	$\bar{\nu}_\mu$ flux	2.5 - 3.5	1.121	0.074 / 0.049
13	$\bar{\nu}_\mu$ flux	3.5 - 5.0	1.122	0.094 / 0.067
14	$\bar{\nu}_\mu$ flux	5.0 - 7.0	1.112	0.093 / 0.064
15	$\bar{\nu}_\mu$ flux	7.0 - 30.0	1.093	0.130 / 0.108
16	$\nu_e$ flux	0.0 - 2.5	1.109	0.069 / 0.047
17	$\nu_e$ flux	2.5 - 30.0	1.090	0.085 / 0.067
18	$\bar{\nu}_e$ flux	0.0 - 0.5	1.193	0.095 / 0.054
19	$\bar{\nu}_e$ flux	0.5 - 0.7	1.184	0.091 / 0.047
20	$\bar{\nu}_e$ flux	0.7 - 0.8	1.167	0.091 / 0.049
21	$\bar{\nu}_e$ flux	0.8 - 1.5	1.141	0.084 / 0.044
22	$\bar{\nu}_e$ flux	1.5 - 2.5	1.120	0.080 / 0.054
23	$\bar{\nu}_e$ flux	2.5 - 4.0	1.123	0.089 / 0.068
24	$\bar{\nu}_e$ flux	4.0 - 30.0	1.180	0.156 / 0.144
25	MEC	0.0 - 30.0	1.031	1.041 / 1.015
26	$C_5^A$	0.0 - 30.0	0.854	0.119 / 0.073
27	BgRes	0.0 - 30.0	1.143	0.154 / 0.146
28	$M_A^{QE}$	0.0 - 30.0	0.948	0.058 / 0.028
29	$M_A^{RES}$	0.0 - 30.0	0.762	0.158 / 0.055
30	PF	0.0 - 30.0	0.997	0.055 / 0.054
31	CCOth	0.0 - 30.0	0.023	0.400 / 0.193
32	$E_b$	0.0 - 30.0	1.002	0.333 / 0.326
33	CCCoh	0.0 - 30.0	1.076	1.000 / 0.972
34	NCCoh	0.0 - 30.0	0.980	0.300 / 0.299
35	NCOth	0.0 - 30.0	1.413	0.300 / 0.186
36	$\sigma_{\nu_e}$	0.0 - 30.0	1.001	0.030 / 0.030

Table B.1: Summary of antineutrino beam mode flux and correlated cross-section systematics included in the  $\bar{\nu}_\mu \rightarrow \bar{\nu}_e$  analysis. The nominal value used in the fit as well as the  $1\sigma$  fractional error on the systematic parameter before and after the fit of the ND280 data is shown.

Parameter	Description	Beam mode	Energy range (GeV)	Nominal value	$1\sigma$ pre/postfit
0	$\nu_\mu$ flux	neutrino	0.0 - 0.4	1.128	0.099 / 0.064
1	$\nu_\mu$ flux	neutrino	0.4 - 0.5	1.156	0.103 / 0.061
2	$\nu_\mu$ flux	neutrino	0.5 - 0.6	1.148	0.096 / 0.051
3	$\nu_\mu$ flux	neutrino	0.6 - 0.7	1.128	0.087 / 0.043
4	$\nu_\mu$ flux	neutrino	0.7 - 1.0	1.104	0.113 / 0.046
5	$\nu_\mu$ flux	neutrino	1.0 - 1.5	1.100	0.092 / 0.045
6	$\nu_\mu$ flux	neutrino	1.5 - 2.5	1.127	0.070 / 0.044
7	$\nu_\mu$ flux	neutrino	2.5 - 3.5	1.124	0.074 / 0.048
8	$\nu_\mu$ flux	neutrino	3.5 - 5.0	1.121	0.087 / 0.049
9	$\nu_\mu$ flux	neutrino	5.0 - 7.0	1.075	0.098 / 0.053
10	$\nu_\mu$ flux	neutrino	7.0 - 30.0	1.064	0.114 / 0.065
11	$\bar{\nu}_\mu$ flux	neutrino	0.0 - 0.7	1.100	0.103 / 0.081
12	$\bar{\nu}_\mu$ flux	neutrino	0.7 - 1.0	1.112	0.079 / 0.048
13	$\bar{\nu}_\mu$ flux	neutrino	1.0 - 1.5	1.111	0.084 / 0.060
14	$\bar{\nu}_\mu$ flux	neutrino	1.5 - 2.5	1.116	0.086 / 0.070
15	$\bar{\nu}_\mu$ flux	neutrino	2.5 - 30.0	1.162	0.086 / 0.069
16	$\nu_e$ flux	neutrino	0.0 - 0.5	1.134	0.090 / 0.052
17	$\nu_e$ flux	neutrino	0.5 - 0.7	1.135	0.090 / 0.049
18	$\nu_e$ flux	neutrino	0.7 - 0.8	1.135	0.086 / 0.047
19	$\nu_e$ flux	neutrino	0.8 - 1.5	1.119	0.081 / 0.043
20	$\nu_e$ flux	neutrino	1.5 - 2.5	1.115	0.079 / 0.046
21	$\nu_e$ flux	neutrino	2.5 - 4.0	1.111	0.084 / 0.050
22	$\nu_e$ flux	neutrino	4.0 - 30.0	1.118	0.094 / 0.067
23	$\bar{\nu}_e$ flux	neutrino	0.0 - 2.5	1.121	0.074 / 0.057
24	$\bar{\nu}_e$ flux	neutrino	2.5 - 30.0	1.153	0.128 / 0.117
25	$\nu_\mu$ flux	antineutrino	0.0 - 0.7	1.098	0.094 / 0.072
26	$\nu_\mu$ flux	antineutrino	0.7 - 1.0	1.121	0.079 / 0.052
27	$\nu_\mu$ flux	antineutrino	1.0 - 1.5	1.130	0.077 / 0.048
28	$\nu_\mu$ flux	antineutrino	1.5 - 2.5	1.155	0.081 / 0.054
29	$\nu_\mu$ flux	antineutrino	2.5 - 30.0	1.111	0.080 / 0.055
30	$\bar{\nu}_\mu$ flux	antineutrino	0.0 - 0.4	1.118	0.104 / 0.071
31	$\bar{\nu}_\mu$ flux	antineutrino	0.4 - 0.5	1.127	0.102 / 0.060
32	$\bar{\nu}_\mu$ flux	antineutrino	0.5 - 0.6	1.117	0.096 / 0.052
33	$\bar{\nu}_\mu$ flux	antineutrino	0.6 - 0.7	1.121	0.085 / 0.044
34	$\bar{\nu}_\mu$ flux	antineutrino	0.7 - 1.0	1.155	0.125 / 0.066
35	$\bar{\nu}_\mu$ flux	antineutrino	1.0 - 1.5	1.132	0.105 / 0.057
36	$\bar{\nu}_\mu$ flux	antineutrino	1.5 - 2.5	1.139	0.080 / 0.053
37	$\bar{\nu}_\mu$ flux	antineutrino	2.5 - 3.5	1.141	0.074 / 0.054
38	$\bar{\nu}_\mu$ flux	antineutrino	3.5 - 5.0	1.151	0.094 / 0.071
39	$\bar{\nu}_\mu$ flux	antineutrino	5.0 - 7.0	1.133	0.093 / 0.070
40	$\bar{\nu}_\mu$ flux	antineutrino	7.0 - 30.0	1.082	0.130 / 0.110
41	$\nu_e$ flux	antineutrino	0.0 - 2.5	1.117	0.069 / 0.051
42	$\nu_e$ flux	antineutrino	2.5 - 30.0	1.112	0.085 / 0.071
43	$\bar{\nu}_e$ flux	antineutrino	0.0 - 0.5	1.126	0.095 / 0.058
44	$\bar{\nu}_e$ flux	antineutrino	0.5 - 0.7	1.127	0.091 / 0.051
45	$\bar{\nu}_e$ flux	antineutrino	0.7 - 0.8	1.133	0.091 / 0.052
46	$\bar{\nu}_e$ flux	antineutrino	0.8 - 1.5	1.132	0.084 / 0.046
47	$\bar{\nu}_e$ flux	antineutrino	1.5 - 2.5	1.125	0.080 / 0.056
48	$\bar{\nu}_e$ flux	antineutrino	<sup>143</sup> 2.5 - 4.0	1.119	0.089 / 0.071
49	$\bar{\nu}_e$ flux	antineutrino	4.0 - 30.0	1.166	0.156 / 0.141

Table B.2: Nominal values and fractional errors, before and after the measurement with the near detector data, of neutrino flux in both neutrino and antineutrino beam modes used in the joint fit analysis. The neutrino flavor and the true energy range specified.

Parameter	Description	Best fit	$1\sigma$ pre/postfit
50	MEC	1.546	- / 0.343
51	$C_5^A$	0.789	0.119 / 0.062
52	BgRes	1.042	0.154 / 0.134
53	$M_A^{QE}$	0.931	- / 0.028
54	$M_A^{RES}$	0.889	0.158 / 0.041
55	PF	1.041	- / 0.105
56	CCOth	-0.022	0.400 / 0.208
57	$E_b$	0.882	0.333 / 0.282
58	CCCoh	0.858	0.300 / 0.228
59	NCCoh	0.931	0.300 / 0.298
60	NCOth	1.000	0.300 / 0.300
61	$\sigma_{\nu_e}$	1.000	0.028 / 0.028
62	NC $1\gamma$	1.000	1.000 / 1.000
63	$\sigma_{\bar{\nu}_e}$	1.000	0.028 / 0.028
64	MEC- $\bar{\nu}$	0.578	- / 0.177

Table B.3: Nominal values used and fractional errors before and after the measurement with the near detector data of the cross section systematic parameters used in the joint fit analysis. The cross section systematic parameters are applied to the whole range of true energy. MEC, MEC- $\bar{\nu}$ ,  $M_A^{QE}$  and PF are free parameters in the fit of the near detector data.



# Appendix C

## Statistical methods

In this chapter a detailed description of the statistical method used in the performed analyses is given. More informations can be found in [66].

### C.1 Discussion of marginalization and profiling and best-fit spectra

In sec. 4.5 and 5.2 different statistical methods are described, respectively *profiling* and *marginalization*. The aim of both procedures is to get rid of the nuisance parameters, those fit parameters that are not measured in the data analysis but that can affect the result. At the end the likelihood,  $\mathcal{L}(\vec{\theta}; \text{data})$ , is only function of the parameters of interest ( $\vec{\theta}$ ) and the data set (data). Confidence intervals can be easily set as a function of only  $\vec{\theta}$ .

The *profiling* method can be explained by the following equation:

$$\mathcal{L}_{prof}(\vec{\theta}; \text{data}) = \max_{\vec{f}} \mathcal{L}(\vec{\theta}, \vec{f}; \text{data}) \quad (\text{C.1})$$

The nuisance parameters are fixed to the best-fit values, i.e. the values that correspond to the maximum of the likelihood (or minimum of  $-2 \ln \mathcal{L}$ ). It is also called fully-frequentist approach, since the result is, in principle, only determined by the data.

In the *marginalization* method [147] the nuisance parameters are not fixed to their best-fit values, but a sort of average of the likelihood weighted with the prior distribution  $\pi(\vec{f})$  of the nuisance parameters is performed:

$$\mathcal{L}_{marg}(\vec{\theta}; \text{data}) = \int_F \mathcal{L}(\vec{\theta}, \vec{f}; \text{data}) \pi(\vec{f}) d\vec{f} \quad (\text{C.2})$$

In this way the full knowledge of  $\vec{f}$ , coming from previous independent measurements, is exploited. This approach is based on the Bayes theorem, that, applied only on the nuisance parameters, looks like

$$P(\vec{f}|\text{data}) \propto \mathcal{L}(\text{data}|\vec{f}) \pi(\vec{f}) \quad (\text{C.3})$$

where  $P(f|\text{data})$  is the posterior probability distribution of  $\vec{f}$  given the data set and  $\mathcal{L}(\text{data}|\vec{f})$  is simply the likelihood function. The final result depends on the prior  $\pi(\vec{f})$  that is chosen by the analyzer. This is the weakness of *marginalization*. Indeed the goal of *profiling* is to provide a final result which depends only on the data and is not affected by the choice of the prior.

However priors  $\pi(\vec{f})$ , when measured, are usually used also when *profiling* is adopted, by adding a gaussian penalty term like eq. 4.5.

In the gaussian regime *profiling* and *marginalization* gives exactly the same result. This can also be seen by the following relation between  $\mathcal{L}_{prof}$  and  $\mathcal{L}_{marg}$ , shown in [182] and obtained by the Laplace approximation [183]:

$$-2 \ln \mathcal{L}_{marg}(\vec{\theta}; \text{data}) \approx -2 \ln \mathcal{L}_{prof}(\vec{\theta}; \text{data}) + \ln \left[ \left| \frac{d^2 (\ln \mathcal{L}(\vec{\theta}, \vec{f}; \text{data}))}{d\vec{f}^2} \right|_{\hat{\vec{f}}_{\vec{\theta}}} \right] \quad (\text{C.4})$$

If the likelihood function is gaussian the correction factor is a constant and the confidence intervals performed with *profiling* and *marginalization* methods are identical.

In the physics community there is not any general preference for either *marginalization* or *profiling* and, depending on the experiment, results are provided using either of these approaches. My personal point of view is that *marginalization* is better when the prior distribution is well known, thanks to an independent measurement already performed. Indeed the information of the full range of  $\vec{f}$ , given by the prior distribution, is exploited. However, *marginalization* becomes weak when there are no measurements of the nuisance parameters (or estimation of their uncertainties). This could be the case when more physical parameters are measured, but the results are shown as a function of only one or two parameters, given the difficulty to perform  $> 2$  dimensions confidence intervals. When this happens, usually a uniform prior, that reflects the total ignorance of the physical parameter, is used. However a problem here is that if the prior p.d.f is flat for a certain parameter, then it is not flat for a nonlinear function of the same parameter, and so a different parametrization of the problem would lead in general to a non-equivalent posterior p.d.f. The risk is to bias the result by introducing an information on the parameters of interest which has been decided by a choice of the analyzer, since there is not any reason to choose a prior instead of another one. In this case it is maybe better to use the prior information as less as possible and profile these parameters. However the decision of the T2K collaboration was to release the 2015 oscillation analysis results using *marginalization* for all the nuisance parameters, while in the past the analyzers were free to choose the preferred approach.

The best-fit spectrum is the distribution of MC events that corresponds to the parameter values obtained by fitting the data. It is straightforward to obtain it when the nuisance parameters are profiled, since both the free and the nuisance parameters are fixed to their best-fit values. Instead, when the marginalization method is used, the nuisance parameter values are not fixed to their best-fit, but correspond to an effective set of values  $\vec{f}_{marg}$  given by the average of the likelihoods from many toys. However the fit itself cannot show these effective values, since the marginalization gets rid of the nuisance parameters, and in order to show best-fit spectra consistent with *marginalization*, a new method has been developed.

From each toy MC  $i$ , used to marginalize the nuisance parameters, a different spectrum, with  $N^j(\vec{\theta}_{bf}; \vec{f}_i)$  number of events in each bin  $j$ , is produced as well as a likelihood  $\mathcal{L}(\vec{\theta}_{bf}, \vec{f}_i; \text{data})$  value, calculated using eq. 5.2, where  $\vec{\theta}_{bf}$  is the best-fit value of the free parameters vector and  $\vec{f}_i$  is the vector of nuisance parameters corresponding to the toy  $i$ . The best-fit number of events in the bin  $j$  of the spectrum is calculated by the weighted average

$$N_{marg}^j = \frac{\sum_{i=1}^n \mathcal{L}(\vec{\theta}_{bf}; \vec{f}_i; \text{data}) \cdot N^j(\vec{\theta}_{bf}; \vec{f}_i)}{\sum_{i=1}^n \mathcal{L}(\vec{\theta}_{bf}; \vec{f}_i; \text{data})} \quad (\text{C.5})$$

where  $n$  is the number of toys MC and the likelihood value of each toy is used as a weight.

It is easy to find a relation between the best-fit spectrum corresponding to *profiling* and *marginalization*. Assuming that one of the toys MC is generated with the nuisance parameters vector  $\vec{f}_{bf}$ , which is approximately true if many toys MC are performed, the marginal likelihood of eq. 5.3 can be written as

$$\mathcal{L}_{marg}(\vec{\theta}_{bf}; \text{data}) = \frac{1}{n} \sum_{i=1, i \neq bf}^n \left[ \mathcal{L}(\vec{\theta}_{bf}; \vec{f}_i; \text{data}) + \mathcal{L}_{prof} \right] \quad (\text{C.6})$$

where  $\mathcal{L}_{prof} = \mathcal{L}(\vec{\theta}_{bf}; \vec{f}_{bf}; \text{data})$  is the best-fit likelihood obtained with *profiling*. Given  $N_{prof}^j = N_i^j(\vec{\theta}_{bf}; \vec{f}_{bf})$  the number of events in the bin  $j$  for the best-fit spectrum obtained with *profiling*, eq. C.5 can be written as

$$N_{marg}^j = \frac{\sum_{i=1, i \neq bf}^n \mathcal{L}(\vec{\theta}_{bf}; \vec{f}_i; \text{data}) \cdot N^j(\vec{\theta}_{bf}; \vec{f}_i) + \mathcal{L}_{prof} \cdot N_{prof}^j}{\sum_{i=1}^n \mathcal{L}(\vec{\theta}_{bf}; \vec{f}_i; \text{data})} \quad (\text{C.7})$$

## C.2 Methods for confidence intervals

In high energy physics results are usually provided by showing the confidence intervals of the physical parameters, in this case the oscillation parameters. The confidence interval at  $X\%$  confidence level (CL) is the interval range of the parameters vector  $\vec{\theta} = (\theta_0, \theta_1, \dots, \theta_N)$  that, if the same experiment is performed an infinite number of times, contains the true value of  $\vec{\theta}$  the  $X\%$  of the times. The confidence intervals are performed by using the likelihood ratio as a test statistic [144].

The procedure consists of the following steps:

- all the points of the  $\vec{\theta}$  parameters grid are scanned.
- at each point, that corresponds to a different oscillation hypothesis, the negative log-likelihood  $-2 \ln \mathcal{L}(\vec{\theta}; \text{data})$  (eq. 4.3 or eq. 5.6) is minimized keeping the oscillation parameters fixed to the grid point and profiling (see sec. 4.5) or marginalizing (see sec. 5.2) the nuisance parameters. A grid of  $-2 \ln \mathcal{L}(\vec{\theta}_{fix}; \text{data})$  values is obtained. If a sensitivity study is performed, “data” corresponds to the Asimov data set, while, if the measurement is performed, the T2K data set is used.
- the global minimum of the grid of  $\vec{\theta}$ ,  $-2 \ln \mathcal{L}(\vec{\theta}_{bf}; \text{data})$ , is computed by minimizing eq. 4.3 or eq. 5.6, leaving also the oscillation parameters free in the fit, which are then set to their best-fit values ( $bf$ ), i.e. the set of values given by the minimum of the negative log-likelihood.
- In each grid point the value  $-2 \ln \mathcal{L}(\vec{\theta}_{fix}; \text{data})$  is shifted with respect to the global minimum as following:

$$\Delta\chi^2(\vec{\theta}; \text{data}) = -2 \ln \mathcal{L}(\vec{\theta}_{fix}; \text{data}) - (-2 \ln \mathcal{L}(\vec{\theta}_{bf}; \text{data})) \quad (\text{C.8})$$

and the  $\Delta\chi^2(\vec{\theta}; \text{data})$  distribution as a function of all the  $\vec{\theta}$  points of the grid is obtained.

- the confidence interval is defined by the region of  $\vec{\theta}$  that corresponds to

$$\Delta\chi^2(\vec{\theta}; \text{data}) < \Delta\chi_{crit}^2(\vec{\theta}) \quad (\text{C.9})$$

where  $\Delta\chi_{crit}^2(\vec{\theta})$  is a precomputed critical value that defines the confidence levels. The region of the  $\vec{\theta}$  values which do not accomplish the condition of eq. C.9 is excluded at a certain confidence level.

In the gaussian regime, i.e. the likelihood function has a linear dependence with all the fit parameters which are also distributed as gaussian, already precomputed values of  $\Delta\chi_{crit}^2(\vec{\theta})$  can be used to set the confidence intervals. If there is only one free parameter, the critical value corresponding to  $N\sigma$  confidence interval is given by  $\Delta\chi_{crit}^2(\vec{\theta}) = N^2$  and does not depend on  $\vec{\theta}$ . If the number of free parameters is two,  $\Delta\chi_{crit}^2(\vec{\theta}) = 2.30, 4.61, 5.99$  can be used respectively to set the 68.27% CL, 90% CL and 95% CL contours. This method is called *constant  $\Delta\chi^2$*  and works well only in the gaussian regime. However, since it does not require much computational time, it is widely used to perform sensitivity studies. Sometimes also the results are provided using this method, if the gaussian approximation is still good. Usually the sensitivity studies are performed using the Asimov dataset [144], that is the most probable data set, i.e. the nominal MC spectrum for a given oscillation hypothesis.

### C.2.1 Feldman-Cousins method

If the gaussian regime is not satisfied the *constant  $\Delta\chi^2$*  method is not reliable and new  $\Delta\chi_{crit}^2(\vec{\theta})$  critical values must be calculated following the *Feldman-Cousins* method [146]. The nuisance parameters can be both marginalized (sec. 4.5) or profiled [148] (sec. 5.2). For each point of the  $\vec{\theta}$  grid a different critical value  $\Delta\chi_{crit}^2(\vec{\theta})$  is calculated. The procedure consists of the following steps:

1. many toys MC (usually at least 10k) are performed assuming the oscillation hypothesis of the grid point  $\vec{\theta}$  and taking into account both the statistical and systematic uncertainties;
2. for each toy first  $-2 \ln \mathcal{L}(\vec{\theta}_{fix}; \text{data})$  is obtained by minimizing  $-2 \ln \mathcal{L}(\vec{\theta}; \text{data})$  where the oscillation parameters  $\vec{\theta}$  are kept fixed to the values corresponding to the grid point and the nuisance parameters are either profiled or marginalized. Then  $-2 \ln \mathcal{L}(\vec{\theta}; \text{data})$  is minimized, leaving the oscillation parameters  $\vec{\theta}$  as free in the fit and  $-2 \ln \mathcal{L}(\vec{\theta}_{bf}; \text{data})$  is obtained. “data” corresponds in this case to the single toy MC data set.
3.  $\Delta\chi^2(\vec{\theta}; \text{data})$  is calculated using eq. C.8.
4. The steps 2 and 3 are repeated for each toy MC and a distribution of  $\Delta\chi^2(\vec{\theta}; \text{data})$  ( $f(\Delta\chi^2)$ ) is obtained.
5. The critical value for  $X\%$  CL,  $\Delta\chi_{crit}^2(\vec{\theta})$ , can be defined as:

$$\Delta\chi_{crit}^2 : \int_{-\infty}^{\Delta\chi_{crit}^2} f(\Delta\chi^2) d(\Delta\chi^2) = X\% \quad (\text{C.10})$$

An example of  $\Delta\chi^2$  distribution is given in fig. C.1. The computed critical value at the 90% CL is the  $\Delta\chi^2$  value which contains the fraction 90% of entries on its left side.

6. This procedure is repeated for all the points of the  $\vec{\theta}$  grid and several critical values are computed

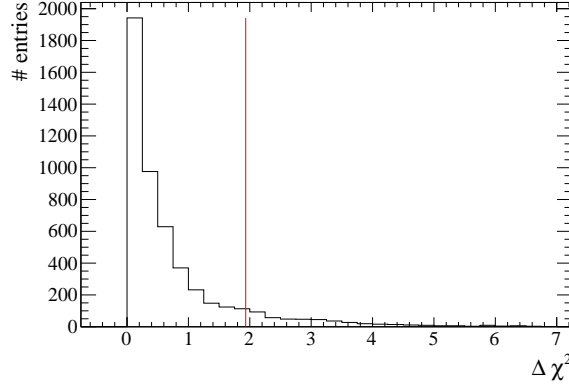


Figure C.1: Example of a  $\Delta\chi^2$  distribution,  $f(\Delta\chi^2)$ , obtained by following the procedure described above by performing 10k toys MC. The red line shows the critical value  $\Delta\chi_{crit}^2(\vec{\theta})$  corresponding to the 90% CL. It is calculated as the  $\Delta\chi^2$  value which contains the 90% of entries on its left side.

Once a critical value,  $\Delta\chi_{crit}^2(\vec{\theta})$ , is computed for each oscillation hypothesis in the  $\vec{\theta}$  grid, the confidence intervals are set by the condition of eq. C.9.

### C.3 P-value and method for $\bar{\nu}_\mu \rightarrow \bar{\nu}_e$ appearance analysis

The p-value describes how anomalous the data are with respect to a certain physics hypothesis. In general hints of new physics are considered when the p-value has a significance of at least  $3\sigma$ , i.e. p-value  $< 0.027$ , while  $5\sigma$  corresponds to discovery.

There are different test statistics that can be used to quote a p-value. One possible way has been already described in sec. 4.7.1, where the parameters of interest are left free in the fit. Since the goal of the  $\bar{\nu}_\mu \rightarrow \bar{\nu}_e$  appearance analysis is not to measure any parameter but to quote a significance for a particular oscillation hypothesis, the free parameter  $\bar{\beta}$  is not left free, but fixed to 0 and 1. Indeed any value of  $\bar{\beta}$  between 0 and 1 has not any physical meaning. Since the analysis is still dominated by the statistical uncertainty and the information on the shape of the reconstructed neutrino energy spectrum cannot be fully exploited, two different p-values were quoted:

- p-value with rate-only analysis: the number of events is used as test statistics, without using the shape information of the reconstructed neutrino energy distribution. The parameter of interest,  $\bar{\beta}$ , is set to 0 and many toys MC ( $N_{toys} \geq 10k$ ), are performed by randomly extracting all the systematic parameters taking into account the existing correlations and fluctuating the reconstructed energy spectrum using the Poisson statistic. For each toy MC “ $i$ ” the total number of events,  $N_{SK}^i$ , is computed and the distribution  $f(N_{SK})$  of the total number of Super-K events is obtained. Then the number of events is measured from the T2K or Asimov data set ( $N_{SK}^{obs}$ ) and the 1-sided (right tail) p-value can be computed

as following:

$$\text{p-value (right tail)} = \int_{N_{SK}^{obs}}^{+\infty} f(N_{SK}) dN_{SK} = \frac{\sum_{i=1}^{N_{toys}} w(N_{SK}^i \geq N_{SK}^{obs})}{N_{toys}} \quad (\text{C.11})$$

where  $w(N_{SK}^i \geq N_{SK}^{obs})$  is 1 if  $N_{SK}^i \geq N_{SK}^{obs}$ , otherwise 0. The distribution  $f(N_{SK})$  is expected to be discrete since it follows the Poisson statistic.

In an analogous way the left tail 1-sided p-value is computed as following:

$$\text{p-value (left tail)} = \int_{-\infty}^{N_{SK}^{obs}} f(N_{SK}) dN_{SK} = \frac{\sum_{i=1}^{N_{toys}} w(N_{SK}^i \leq N_{SK}^{obs})}{N_{toys}} \quad (\text{C.12})$$

- p-value with rate+shape analysis: the shape information of the reconstructed energy distribution is used. In this case the test statistic is used to compare the case of  $\bar{\beta} = 0$  with  $\bar{\beta} = 1$ :

$$\Delta\chi^2(\text{data}) = \chi^2(\bar{\beta} = 0; \text{data}) - \chi^2(\bar{\beta} = 1; \text{data}) \quad (\text{C.13})$$

where  $\chi^2(\bar{\beta} = 0; \text{data})$  and  $\chi^2(\bar{\beta} = 1; \text{data})$  are computed using eq. 5.4. It is worth to note that the parameter  $\bar{\beta}$  is not fitted, i.e. the value corresponding to the  $\chi^2(\bar{\beta}; \text{data})$  minimum is not found, but fixed either to 0 or 1. Toy MC experiments, performed as described for the rate-only p-value, are used as “data”. For each toy  $i$ , the test statistic  $\Delta\chi_i^2$  is calculated and the distribution  $f(\Delta\chi^2)$  is obtained. Then the test statistic  $\Delta\chi_{obs}^2$  is calculated using eq. C.13 on either the Asimov or T2K data set, in order to perform respectively a sensitivity study or the measurement. The 1-sided p-value (right tail) is calculated as:

$$\text{p-value (right tail)} = \int_{\Delta\chi_{obs}^2}^{+\infty} f(\Delta\chi^2) d\Delta\chi^2 = \frac{\sum_{i=1}^{N_{toys}} w(\Delta\chi_i^2 \geq \Delta\chi_{obs}^2)}{N_{toys}} \quad (\text{C.14})$$

where  $w(\Delta\chi^2 \geq \Delta\chi_{obs}^2)$  is 1 if  $\Delta\chi^2 \geq \Delta\chi_{obs}^2$  otherwise 0.

The 1-sided p-value (left tail) is calculated as:

$$\text{p-value (left tail)} = \int_{-\infty}^{\Delta\chi_{obs}^2} f(\Delta\chi^2) d\Delta\chi^2 = \frac{\sum_{i=1}^{N_{toys}} w(\Delta\chi_i^2 \leq \Delta\chi_{obs}^2)}{N_{toys}} \quad (\text{C.15})$$

The p-value is calculated on the left or right tail depending on the position of the observed test statistic in the expected distribution and the physics hypothesis assumed in the toys MC generation.

## Appendix D

# Templates of joint fit analysis

The templates used in the  $\nu/\bar{\nu}$  joint analysis are presented in this section.

For the muon-like samples spectra of reconstructed neutrino energy were used (see fig. D.1).

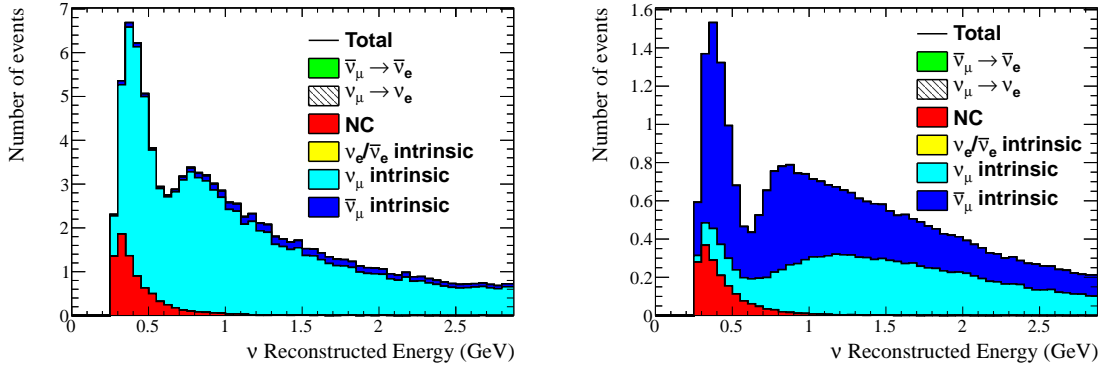


Figure D.1: Predicted muon-like reconstructed neutrino energy spectra of neutrino mode (left) and antineutrino mode (right) events. The distributions correspond to the collected statistics in the full run 1-6 data set for an exposure of  $6.914 \times 10^{20}$  POT in neutrino mode and of  $4.011 \times 10^{20}$  POT in antineutrino mode and are broken down by the following components:  $\bar{\nu}_\mu \rightarrow \bar{\nu}_e$  (green),  $\nu_\mu \rightarrow \nu_e$  (black/white), NC (red),  $\nu_e + \bar{\nu}_e$  intrinsic beam (yellow),  $\nu_\mu$  intrinsic beam (light blue) and  $\bar{\nu}_\mu$  intrinsic beam (blue). The spectra were generated with the systematic parameters measured with the ND280 data shown in tab. B.2 and B.3 and the oscillation parameters shown in tab. 5.2.

In fig. D.2 the  $\bar{\nu}_\mu \rightarrow \bar{\nu}_e$ ,  $\nu_\mu \rightarrow \nu_e$  and background components are shown for the electron-like samples. It is clear that, in particular for the antineutrino mode, it is not possible to separate the  $\bar{\nu}_\mu \rightarrow \bar{\nu}_e$  and  $\nu_\mu \rightarrow \nu_e$  components by looking only to the reconstructed neutrino energy, since the shapes are similar. This problem does not show up in the neutrino mode sample since the contamination of  $\bar{\nu}_\mu \rightarrow \bar{\nu}_e$  is very small. The shape of the background component, dominated by NC, is slightly different since is more flat, but still not easy to discriminate.

In order to improve the sensitivity to  $\delta_{CP}$  a good separation of the  $\bar{\nu}_\mu \rightarrow \bar{\nu}_e$  and  $\nu_\mu \rightarrow \nu_e$  components is very important. For this reason 2-dimensional spectra, functions of both the reconstructed neutrino energy and the angle between the neutrino and the outgoing lepton directions, were used for the electron-like samples. In fig. E.1 and E.2 the 2-dimensional templates are shown for each neutrino flavor and oscillation component. It is clear that for both neutrino

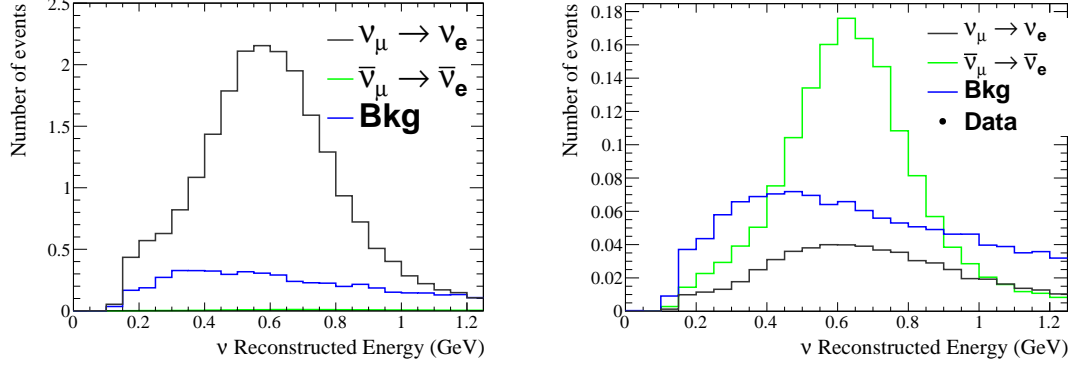


Figure D.2: Predicted spectra of reconstructed neutrino energy for electron-like neutrino mode (left) and antineutrino mode (right) events. The distributions correspond to the collected statistics in the full run 1-6 data set for an exposure of  $6.914 \times 10^{20}$  POT in neutrino mode and of  $4.011 \times 10^{20}$  POT in antineutrino mode. The distributions are broken down by the following components:  $\bar{\nu}_\mu \rightarrow \bar{\nu}_e$  (green),  $\nu_\mu \rightarrow \nu_e$  (black/white), background, which includes NC,  $\nu_e + \bar{\nu}_e$  intrinsic beam (yellow),  $\nu_\mu$  intrinsic beam (light blue) and  $\bar{\nu}_\mu$  intrinsic beam (blue). The spectra were generated with the systematic parameters measured with the ND280 data shown in tab. B.2 and B.3 and the oscillation parameters shown in tab. 5.2.

and antineutrino modes the distributions of  $\nu_\mu \rightarrow \nu_e$  and  $\bar{\nu}_\mu \rightarrow \bar{\nu}_e$  are quite well separated since events populate different regions in the  $\{E_{reco}; \theta\}$  space, though some overlap is still present. The same happens for the NC background. In fig. D.5 the 1-dimensional distributions of the reconstructed neutrino energy and the angle between neutrino and outgoing lepton are shown.



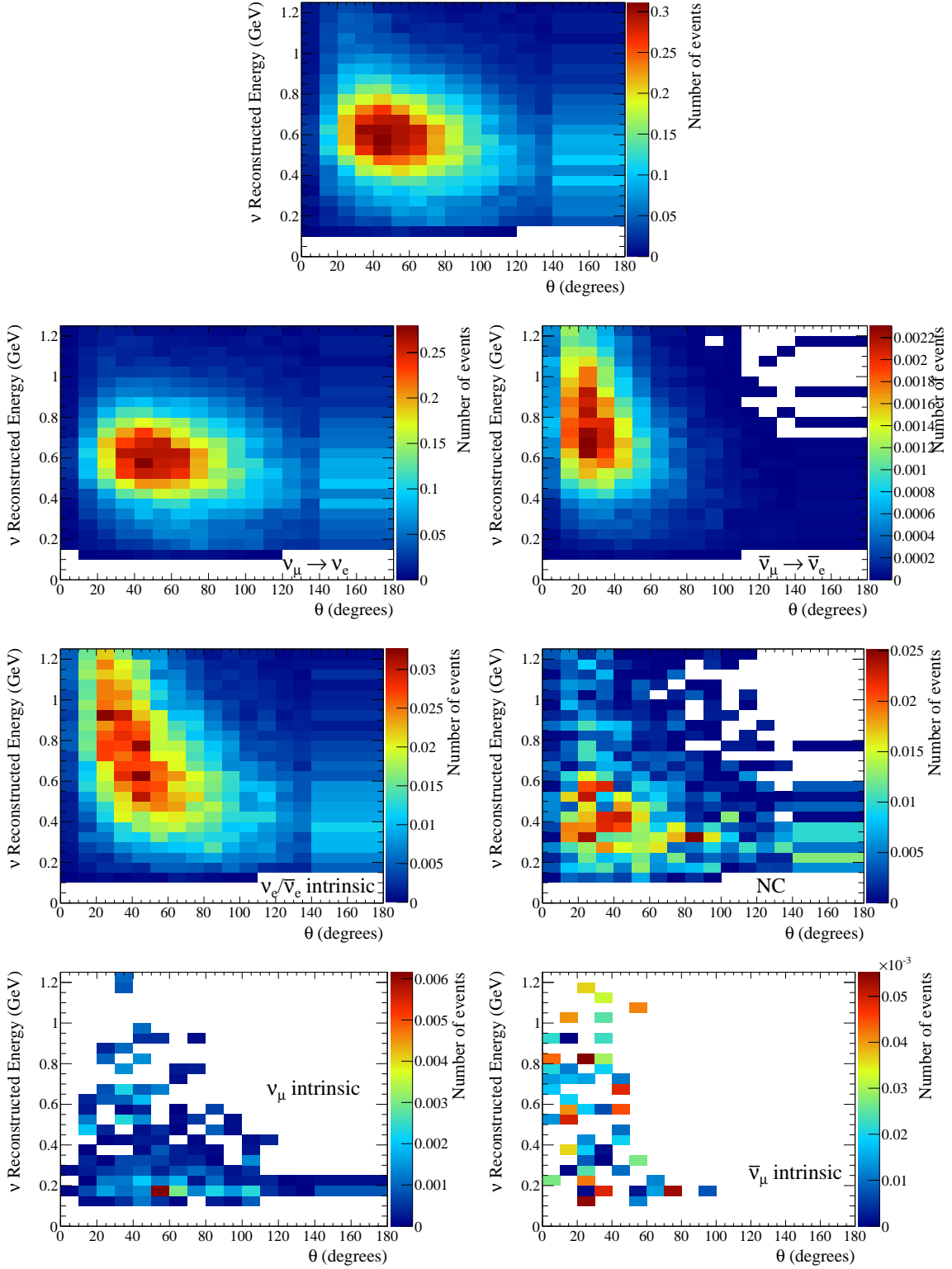


Figure D.3: Predicted spectra of electron-like events as a function of the reconstructed neutrino energy and the angle between the outgoing lepton and the neutrino direction. The distributions correspond to the collected statistics in the full run 1-6 data set for an exposure of  $6.914 \times 10^{20}$  POT in neutrino mode. From top left to bottom right the following components are shown: total,  $\nu_\mu \rightarrow \nu_e$ ,  $\bar{\nu}_\mu \rightarrow \bar{\nu}_e$ ,  $\nu_e + \bar{\nu}_e$  intrinsic beam, NC,  $\nu_\mu$  intrinsic beam and  $\bar{\nu}_\mu$  intrinsic beam. The spectra were generated with the systematic parameters measured with the ND280 data shown in tab. B.2 and B.3 and the oscillation parameters shown in tab. 5.2.

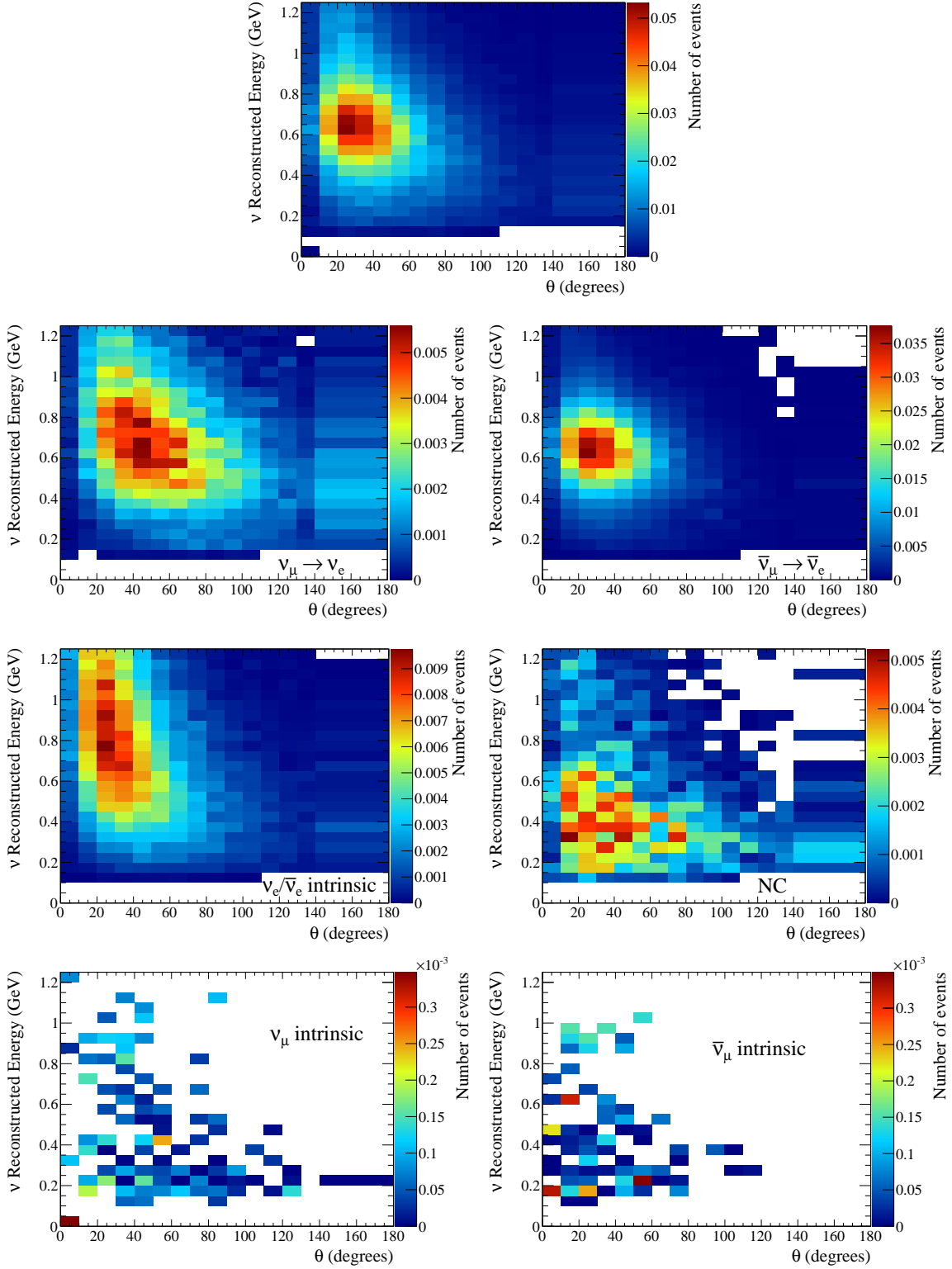


Figure D.4: Predicted spectra of electron-like events as a function of the reconstructed neutrino energy and the angle between the outgoing lepton and the neutrino direction. The distributions correspond to the collected statistics in the full run 1-6 data set for an exposure of  $4.011 \times 10^{20}$  POT in antineutrino mode. From top left to bottom right the following components are shown: total,  $\nu_\mu \rightarrow \nu_e$ ,  $\bar{\nu}_\mu \rightarrow \bar{\nu}_e$ ,  $\nu_e + \bar{\nu}_e$  intrinsic beam, NC,  $\nu_\mu$  intrinsic beam and  $\bar{\nu}_\mu$  intrinsic beam. The spectra were generated with the systematic parameters measured with the ND280 data shown in tab. B.2 and B.3 and the oscillation parameters shown in tab. 5.2.

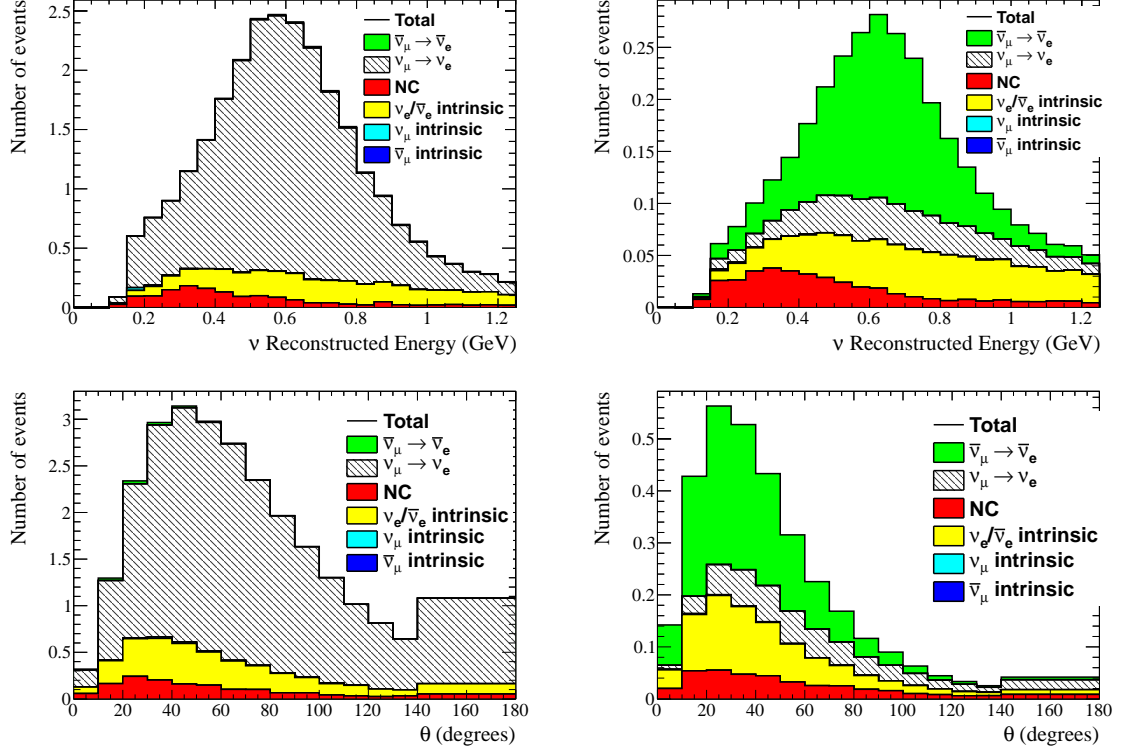


Figure D.5: Predicted spectra of the reconstructed neutrino energy (top) and the angle between the neutrino and the outgoing lepton directions (bottom) for electron-like neutrino mode (left) and antineutrino mode (right) events. The distributions correspond to the collected statistics in the full run 1-6 data set for an exposure of  $6.914 \times 10^{20}$  POT in neutrino mode and of  $4.011 \times 10^{20}$  POT in antineutrino mode. The distributions are broken down by the following components:  $\bar{\nu}_\mu \rightarrow \bar{\nu}_e$  (green),  $\nu_\mu \rightarrow \nu_e$  (black/white), NC (red),  $\nu_e + \bar{\nu}_e$  intrinsic beam (yellow),  $\nu_\mu$  intrinsic beam (light blue) and  $\bar{\nu}_\mu$  intrinsic beam (blue). The spectra were generated with the systematic parameters measured with the ND280 data shown in tab. B.2 and B.3 and the oscillation parameters shown in tab. 5.2.



## Appendix E

# Comparison of data with expected MC for electron-like T2K run 1-6 data sample

The predicted spectra of reconstructed neutrino energy and angle for electron-like samples in neutrino and antineutrino modes and full run 1-6 data set are compared to the observed events and are shown in fig. E.1 and E.2. Each single neutrino flavor component and NC is compared to the data.

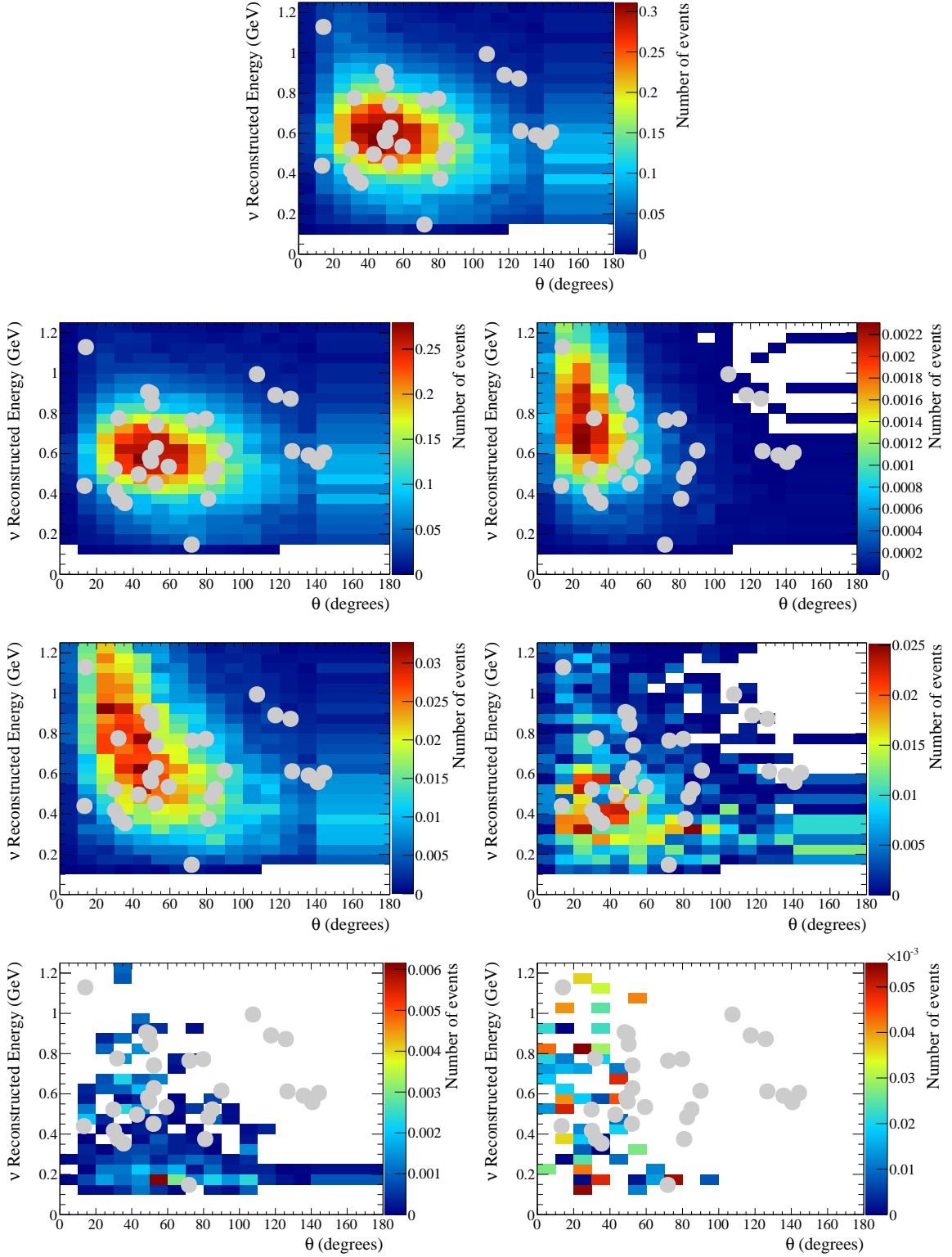


Figure E.1: Predicted spectra of electron-like events as a function of the reconstructed neutrino energy and the angle between the outgoing lepton and the neutrino direction. The distributions correspond to the collected statistics in the full run 1-6 data set for an exposure of  $6.914 \times 10^{20}$  POT in neutrino beam mode. From top left to bottom right the following components are shown: total,  $\nu_\mu \rightarrow \nu_e$ ,  $\bar{\nu}_\mu \rightarrow \bar{\nu}_e$ ,  $\nu_e + \bar{\nu}_e$  intrinsic beam, NC,  $\nu_\mu$  intrinsic beam and  $\bar{\nu}_\mu$  intrinsic beam. The spectra were generated with the systematic parameters measured with the ND280 data shown in tab. B.2 and B.3 and the oscillation parameters shown in tab. 5.2.

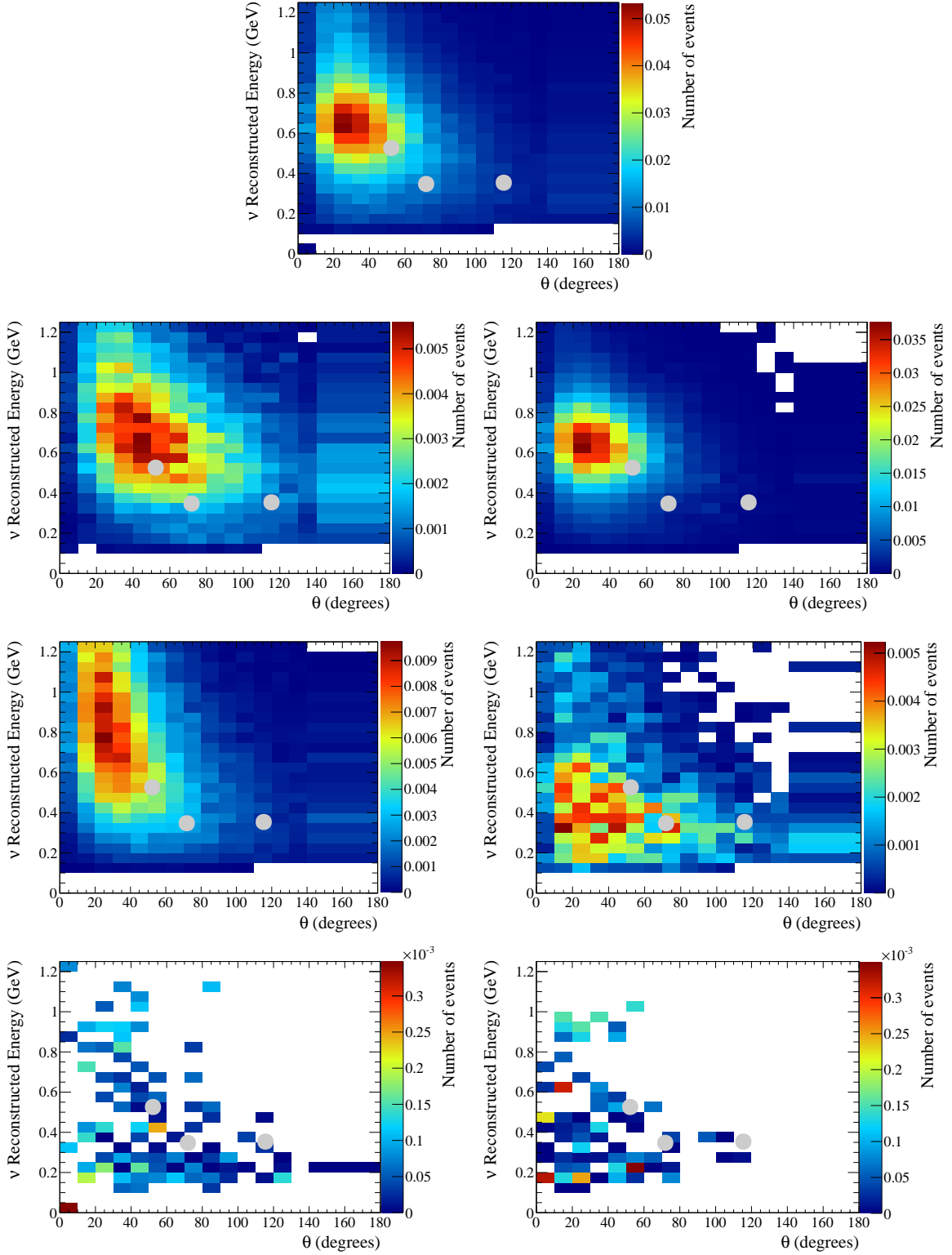


Figure E.2: Predicted spectra of electron-like events as a function of the reconstructed neutrino energy and the angle between the outgoing lepton and the neutrino direction. The distributions correspond to the collected statistics in the full run 1-6 data set for an exposure of  $4.011 \times 10^{20}$  POT in antineutrino beam mode. From top left to bottom right the following components are shown: total,  $\nu_\mu \rightarrow \nu_e$ ,  $\bar{\nu}_\mu \rightarrow \bar{\nu}_e$ ,  $\nu_e + \bar{\nu}_e$  intrinsic beam, NC,  $\nu_\mu$  intrinsic beam and  $\bar{\nu}_\mu$  intrinsic beam. The spectra were generated with the systematic parameters measured with the ND280 data shown in tab. B.2 and B.3 and the oscillation parameters shown in tab. 5.2.





# Bibliography

- [1] J. Chadwick V. Deut. Phys. Ges. 16 (1914) 383.
- [2] W. Pauli, Cambridge Monogr. Part. Phys. Nucl. Phys. Cosmol., 14, 1-22, 2000.
- [3] E. Majorana, “Theory of the Symmetry of Electrons and Positrons”, Nuovo Cim. 14 (1937) 171-184.
- [4] C. Cowan, F. Reines, F. Harrison, H. Kruse, and A. McGuire, “Detection of the free neutrino: A Confirmation”, Science 124 (1956) 103-104.
- [5] T. D. Lee and C. N. Yang, “Question of Parity Conservation in Weak Interactions”, Phys. Rev. 104, 254 (1956).
- [6] M. Goldhaber, L. Grodzins, and A. W. Sunyar, “Helicity of neutrinos”, Phys. Rev., 109(3):1015-1017, Feb 1958.
- [7] G. Danby et al., “Remarks Concerning the Recent High-Energy Neutrino Experiment”, Phys. Rev. Lett., 10:260-262, 1963.
- [8] V. N. Gribov and B. Pontecorvo, Phys. Lett. B 28, 493 (1969).
- [9] B. Pontecorvo, J. Exp. Theor. Phys. 6, 429 (1957); 7, 172 (1958); 26, 984 (1968); Z. Maki, M. Nakagawa, and S. Sakata, Prog. Theor. Phys. 28, 870 (1962).
- [10] S. Fukuda et al. (Super-Kamiokande Collaboration), “Measurement of the flux and zenith-angle distribution of upward through-going muons by super-kamiokande”, Phys. Rev. Lett. 82 2644 (1999)
- [11] K. Kodama et al. (DONUT Collaboration), Phys. Lett. B 504, 218 (2001)
- [12] K. S. Hirata et al. (KAMIOKANDE-II Collaboration), Phys. Rev. Lett. 63, 16 (1989).
- [13] A. I. Abazov et al. (SAGE Collaboration), “Search for Neutrinos from the Sun Using the Reaction  ${}^{71}\text{Ga}(\nu_e, e^-){}^{71}\text{Ge}$ ”, Phys. Rev. Lett. 67, 3332-3335 (1991)
- [14] P. Anselmann et al. (GALLEX Collaboration), “Implications of the GALLEX determination of the solar neutrino flux”, Phys.Lett. B285 (1992) 390-397
- [15] Q. R. Ahmad et al. (SNO Collaboration), “Measurement of the Rate of  $\nu_e + d \rightarrow p + p + e^-$  Interactions Produced by  ${}^8\text{B}$  Solar Neutrinos at the Sudbury Neutrino Observatory”, Phys. Rev. Lett. 87, 071301 (2001)

- [16] LEP Collaboration, G. Alexander et al., “Electroweak parameters of the  $Z^0$  resonance and the Standard Model: the LEP Collaborations”, Phys. Lett. B276 (1992) 247-253.
- [17] C. Athanassopoulos et al. (LSND Collaboration), Phys. Rev. Lett. 77, 3082 (1996) A. Aguilar et al. (LSND Collaboration), Phys. Rev. D 64, 112007 (2001)
- [18] Aguilar-Arevalo et al. (MiniBooNE Collaboration), Phys. Rev. Lett. 105, 181801 (2010).
- [19] G. Mention et al., “Reactor Antineutrino Anomaly”, Phys. Rev. D 83, 073006, arXiv:1101.2755v4 [hep-ex]
- [20] C. Giunti and M. Laveder, “Statistical significance of the gallium anomaly”, Phys. Rev. C 83, 065504 (2011)
- [21] N. Agafonova et al. [OPERA], “Discovery of tau neutrino appearance in the CNGS neutrino beam with the OPERA experiment”, Phys. Rev. Lett. 115 (2015) 121802,
- [22] F. P. An et al. [Daya Bay Collaboration], “Observation of Electron-Antineutrino Disappearance at Daya Bay”, Phys. Rev. Lett. 108, 171803 (2012)
- [23] Abe et al. (T2K Collaboration), “Observation of Electron Neutrino Appearance in a Muon Neutrino Beam”, Phys. Rev. Lett. 112, 061802 (2014)
- [24] F. Englert and R. Brout, “Broken Symmetry and the Mass of Gauge Vector Mesons”, Phys. Rev. Lett. 13, 321; Peter W. Higgs, “Broken Symmetries and the Masses of Gauge Bosons”, Phys. Rev. Lett. 13, 508; G. S. Guralnik, C. R. Hagen, and T. W. B. Kibble, “Global Conservation Laws and Massless Particles”, Phys. Rev. Lett. 13, 585
- [25] L. Landau, Nucl. Phys., 3, 127, 1957
- [26] T. D. Lee and C. N. Yang, Phys. Rev., 105, 1671, 1957
- [27] A. Salam, Nuovo Cim., 5, 299, 1957
- [28] L. Wolfenstein, “Neutrino oscillations in matter”, Phys. Rev. D 17, 2369 (1978).
- [29] S. P. Mikheev and A. Y. Smirnov, Sov. J. Nucl. Phys., 42, 913-917, 1985.
- [30] S. P. Mikheev and A. Y. Smirnov, Nuovo Cim., C9, 17-26, 1986.
- [31] M. Freund, Phys.Rev. D64, 053003 (2001), arXiv:hep-ph/0103300 [hep-ph].
- [32] M. C. Gonzalez-Garcia, M. Maltoni , J. Salvado and T. Schwetz, “Global fit to three neutrino mixing: critical look at present precision”, JHEP 12 (2012) 123, arXiv:1209.3023
- [33] P. Huber, “On the determination of anti-neutrino spectra from nuclear reactors”, arXiv:1106.0687
- [34] ALEPH, DELPHI, L3, OPAL, and SLD Collaborations, and LEP Electroweak Working Group, and SLD Electroweak Group, and SLD Heavy Flavour Group, Phys. Reports 427, 257 (2006).
- [35] J. Kopp, P.A.N. Machado, M. Maltoni and T. Schwetz, “Sterile Neutrino Oscillations: The Global Picture”, JHEP 05 (2013) 050, arXiv:1303.3011

- [36] M. Fukugita and T. Yanagida, Phys. Lett. B 174, 45 (1986).
- [37] A. D. Sakharov, Pisma Zh. Eksp. Teor. Fiz. 5 (1967) 32 [JETP Lett. 5 (1967) 24] [Sov. Phys. Usp. 34 (1991) 392] [Usp. Fiz. Nauk 161 (1991) 61].
- [38] S. Pascoli, S. T. Petkov and A. Riotto, Phys. Rev. D 75, 083511 (2007), S. Pascoli, S. T. Petkov and A. Riotto, Nucl. Phys. B 774, 1-52 (2007).
- [39] G. P. Zeller, “Low energy neutrino cross sections: Comparison of various Monte Carlo predictions to experimental data”, arXiv:hep-ex/0312061.
- [40] D. Casper, “The nuance neutrino physics simulation, and the future, Nucl. Phys. Proc. Suppl. 112 (2002) 161170”, arXiv:hep-ph/0208030.
- [41] G. P. Zeller, “Low energy neutrino cross sections from K2K, MiniBooNE, SciBooNE, and MINERvA”, J. Phys. Conf. Ser. 136 (2008) 022028.
- [42] R. A. Smit and E. J. Moniz, “Neutrino reactions on nuclear targets”, Nucl. Phys. B43 (1972).
- [43] Ankowski, A. M., and J. T. Sobczyk, “Argon spectral function and neutrino interactions”, Phys.Rev. C74, 054316 (2006)
- [44] J. Nieves, J. E. Amaro and M. Valverde, “Inclusive quasielastic charged-current neutrino-nucleus reactions”, Phys. Rev. C 70, 055503 (2004)
- [45] M. Martini, M. Ericson, G. Chanfray and J. Marteau, “Unified approach for nucleon knock-out and coherent and incoherent pion production in neutrino interactions with nuclei”, Phys. Rev. C 80, 065501 (2009)
- [46] J. Nieves, I. Ruiz Simo and M. J. Vicente Vacas, “Inclusive charged-current neutrino-nucleus reactions”, Phys. Rev. C 83, 045501 (2011)
- [47] A.Bodek and U.K.Yang, “Axial and Vector Structure Functions for Electron- and Neutrino- Nucleon Scattering”, hep-ph/1011.6592.
- [48] Borexino Collaboration, “Neutrinos from the primary proton-proton fusion process in the Sun”, Nature (28 August 2014) VOL 512, 383
- [49] R. Davis, D.S. Harmer and K.C. Hoffman, “Search for neutrinos from the sun”, Phys. Rev. Lett. 20 (1968) 1205-1209; B.T. Cleveland et al. (Homestake Collaboration), “Measurement of the solar electron neutrino flux with the Homestake chlorine detector”, Astrophys. J., 496, 505-526, 1998.
- [50] F. Kaether *et al.*, Phys. Lett. B **685**, 073006 (2010).
- [51] J. N. Abdurashitov *et al.* (SAGE collaboration), Phys. Rev. C **59**, 2246 (1999).
- [52] J. N. Abdurashitov *et al.* (SAGE collaboration), Phys. Rev. C **73**, 045805 (2006).
- [53] K. S. Hirata, T. Kajita, T. Kifune, et al., “Observation of  $^8B$  solar neutrinos in the kamiokande-II detector”, Phys. Rev. Lett. 63 (Jul, 1989) 16-19

- [54] K. S. Hirata, K. Inoue, T. Ishida, et al., “Real-time, directional measurement of  $b_8$  solar neutrinos in the kamiokande ii detector”, Phys. Rev. D 44 (Oct, 1991) 2241-2260
- [55] K. S. Hirata, K. Inoue, T. Ishida, et al., “Erratum: Real-time, directional measurement of  $^8B$  solar neutrinos in the kamiokande ii detector”, Phys. Rev. D 45 (Mar, 1992) 2170-2170
- [56] J. N. Bahcall and M. H. Pinsonneault, “Standard solar models, with and without helium diffusion, and the solar neutrino problem”, Rev. Mod. Phys. 64 (Oct, 1992) 885-926. <http://link.aps.org/doi/10.1103/RevModPhys.64.885>.
- [57] Aldo M. Serenelli, Wick C. Haxton, Carlos Pena-Garay, Solar models with accretion. I. Application to the solar abundance problem, Astrophys. J. 743, 24 (2011).
- [58] J. N. Bahcall, A. M. Serenelli, and S. Basu, Astrophys. J., 621, L85-L88, 2005, astro-ph/0412440.
- [59] Q. R. Ahmad et al. (SNO Collaboration), “Direct Evidence for Neutrino Flavor Transformation from Neutral-Current Interactions in the Sudbury Neutrino Observatory”, Phys. Rev. Lett. 89, 011301 (2002)
- [60] S. Fukuda et al. (Super-Kamiokande Collaboration), “Determination of solar neutrino oscillation parameters using 1496 days of Super-Kamiokande-I data”, Phys. Lett. B 539, 179 (2002).
- [61] A. Gando, et al. (KamLAND Collaboration), “Constraints on  $\theta_{13}$  from a three-flavor oscillation analysis of reactor antineutrinos at KamLAND”, Phys. Rev., Vol. D 83, 052002 (2011)
- [62] K. Abe et al. (T2K Collaboration), “Precise Measurement of the Neutrino Mixing Parameter  $\theta_{23}$  from Muon Neutrino Disappearance in an Off-axis Beam”, Phys. Rev. D 89, 092003 (2014)
- [63] P. Adamson et al. (MINOS Collaboration), “Combined Analysis of  $\nu_\mu$  Disappearance and  $\nu_\mu \rightarrow \nu_e$  Appearance in MINOS Using Accelerator and Atmospheric Neutrinos”, Phys. Rev. Lett. 112, 191801
- [64] Abe et al. (T2K Collaboration), “Indication of Electron Neutrino Appearance from an Accelerator-Produced Off-Axis Muon Neutrino Beam” Phys. Rev. Lett 107, 041801 (2011)
- [65] J. Beringer et al. (Particle Data Group with 2013 update), Phys. Rev. D 86, 010001 (2012)
- [66] K.A. Olive et al. (Particle Data Group 2014 with 2015 update), Chin. Phys. C, 38, 090001
- [67] Light Sterile Neutrinos: A White Paper, <http://arxiv.org/pdf/1204.5379v1.pdf>
- [68] J. Kopp et al., arXiv:1303.3011v2 [hep-ph] 30 Apr 2013.
- [69] Aguilar-Arevalo et al. (LSND Collaboration), Phys. Rev. D 64, 112007 (2001).

- [70] A. A. Aguilar-Arevalo et al. (MiniBooNE Collaboration), Phys. Rev. Lett. 110, 161801 (2013), “Improved Search for  $\bar{\nu}_\mu \rightarrow \bar{\nu}_e$  Oscillations in the MiniBooNE Experiment”
- [71] Th. A. Mueller et al., “Improved predictions of reactor antineutrino spectra”, Phys. Rev. C 83, 054615 (2011)
- [72] C. Giunti et al, “Update of Short-Baseline Electron Neutrino and Antineutrino Disappearance”, Phys. Rev. D 86, 113014 (2012)  
<http://arxiv.org/pdf/1210.5715.pdf>
- [73] A.C. Hayes, J.L. Friar, G.T. Garvey, Gerard Jungman, G. Jonkmans, “Systematic Uncertainties in the Analysis of the Reactor Neutrino Anomaly”. arXiv:1309.4146v3 [nucl-th]
- [74] Cheng, G. et al. (MiniBooNE and SciBooNE Collaborations), “Dual baseline search for muon antineutrino disappearance at  $0.1 \text{ eV}^2 < \Delta m^2 < 100 \text{ eV}^2$ ”, Phys. Rev. D 86, 052009 (2012)
- [75] J. M. Conrad et al., “Sterile Neutrino Fits to Short-Baseline Neutrino Oscillation Measurements”, arXiv:1207.4765 [hep-ex] (2012).
- [76] C. Giunti et al., “Pragmatic view of short-baseline neutrino oscillations”, Phys. Rev. D 88, 073008 (2013).
- [77] P. A. R. Ade et al. (Planck Collaboration), “Planck 2015 results. XIII. Cosmological parameters”, arXiv:1502.01589 [astro-ph.CO]
- [78] M. Wyman, D. H. Rudd, R. A. Vanderveld, and W. Hu, “Neutrinos Help Reconcile Planck Measurements with the Local Universe”, Phys. Rev. Lett. 112, 051302 (2014), arXiv:1307.7715 [astro-ph.CO].
- [79] F. P. An et al. (Daya Bay Collaboration), “Search for a Light Sterile Neutrino at Daya Bay”, Phys. Rev. Lett. 113, 141802 (2014)
- [80] A. de Gouvea, W. C. Huang and J. Jenkins, “Pseudo-Dirac Neutrinos in the New Standard Model”, Phys. Rev. D 80, 073007 (2009)
- [81] S. Dodelson and L. M. Widrow, “Sterile neutrinos as dark matter”, Phys. Rev. Lett. 72, 17 (1994), arXiv:hep-ph/9303287 [hep-ph]; A. Kusenko, “Sterile neutrinos: The dark side of the light fermions”, Phys. Rept. 481, 1 (2009), arXiv:0906.2968 [hep-ph]; T. Asaka, S. Blanchet and M. Shaposhnikov, “The  $\nu$ MSM, dark matter and neutrino masses”, Phys. Lett. B 631, 151 (2005)
- [82] A. Kusenko, F. Takahashi, and T. T. Yanagida, “Dark matter from split seesaw”, Phys. Lett. B 693, 144 (2010), arXiv:1006.1731 [hep-ph].
- [83] K. Abe et al. (T2K Collaboration), “Measurements of neutrino oscillation in appearance and disappearance channels by the T2K experiment with  $6.6 \times 10^{20}$  protons on target”, Phys. Rev. D 91, 072010 (2015)
- [84] K. Abe et al. (T2K Collaboration), “The T2K experiment”, Nucl. Instrum. Meth. A 659, 106, (2011).

- [85] D. Beavis, A. Carroll, I. Chiang et al., Physics Design Report, BNL 52459 (1995)
- [86] S. Assylbekov, et al., “The T2K ND280 off-axis pi-zero detector”, Nucl. Instrum. Meth., Vol. A686, pp. 48-63, 2012.
- [87] N. Abgrall, et al., “Time Projection Chambers for the T2K Near Detectors”, Nucl. Instrum. Meth., Vol. A637, pp. 25-46, 2011.
- [88] P.-A. Amaudruz, et al., “The T2K fine-grained detectors”, Nucl. Instrum. Meth., Vol. A696, pp. 1-31, 2012.
- [89] D. Renker, E. Lorenz, “Advances in solid state photon detectors”, Journal of Instrumentation 4 (2009) P04004.
- [90] I. Giomataris, et al., Nuclear Instruments and Methods in Physics Research A 560 (2006) 405.
- [91] D. Allan, et al., “The electromagnetic calorimeter for the T2K near detector ND280”, JINST, Vol. 8, p. P10019, 2013.
- [92] S. Aoki, et al., “The T2K Side Muon Range Detector (SMRD)”, Nucl. Instrum. Meth., Vol. A698, pp. 135-146, 2013.
- [93] Y. Fukuda, et al., “The Super-Kamiokande detector”, Nucl.Instrum.Meth., Vol. A501, pp. 418-462, 2003.
- [94] G. Battistoni, F. Cerutti, A. Fasso, A. Ferrari, S. Muraro, J. Ranft, S. Roesler, and P. R. Sala, AIP Conf. Proc. 896, 31 (2007).
- [95] A. Ferrari, P.R. Sala, A. Fasso, and J. Ranft, Report No. CERN-2005-010; Report No. SLAC-R-773; Report No. INFN-TC-05-11.
- [96] R. Brun, F. Carminati, and S. Giani, Report No. CERN- W5013.
- [97] C. Zeitnitz and T.A. Gabriel, in Proceedings of International Conference on Calorimetry in High Energy Physics (Elsevier Science B.V., Tallahassee, FL, 1993).
- [98] A. Fasso, A. Ferrari, J. Ranft, and P. R. Sala, in Proceedings of the International Conference on Calorimetry in High Energy Physics, 1994.
- [99] <http://www.staff.uni-mainz.de/zeitnitz/Gcalor/gcalor.html>
- [100] HARP Collaboration, M. G. Catanesi et al., “Measurement of the production cross-section of positive pions in p Al collisions at 12.9-GeV/c” Nucl. Phys. B732 (2006) 1-45, arXiv:hep-ex/0510039.
- [101] N. Abgrall, B. Popov and J.-M. Levy, “Predictions of neutrino fluxes for T2K: NA61 analysis and data taking strategy”, NA61/T2K Internal note 2009-01 draft 2.1 (2010).
- [102] N. Abgrall et al. (NA61/SHINE Collaboration), Phys. Rev. C 84, 034604 (2011).
- [103] N. Abgrall et al. (NA61/SHINE Collaboration), Phys. Rev. C 85, 035210 (2012).

- [104] N. Abgrall et al. (NA61/SHINE Collaboration), “Measurements of  $\pi^\pm$ ,  $K^\pm$ ,  $K_S^0$ ,  $\lambda$  and proton production in proton-carbon interactions at 31 GeV/c with the NA61/SHINE spectrometer at the CERN SPS”, accepted by EPJ C, arXiv:1510.02703[hep-ex]
- [105] T. Eichten et al., Nucl. Phys. B 44, 333 (1972).
- [106] J. V. Allaby et al., Tech. Rep. 70-12 (CERN, 1970).
- [107] R. Feynman, Phys. Rev. Lett. 23, 1415 (1969).
- [108] K. Abe et al. (T2K Collaboration), “T2K neutrino flux prediction”, Phys. Rev. D 87, 012001 (2013)
- [109] “Flux Prediction and Uncertainty Updates with NA61 2009 Thin Target Data and Negative Focussing Mode Predictions”, T2K Technical Note 217
- [110] G. Bellettini, G. Cocconi, A.N. Diddens, E. Lillethun, G. Matthiae, J. P. Scanlon, and A. M. Wetherell, Nucl. Phys. 79, 609 (1966).
- [111] M. Gazdzicki, M. Gorenstein and P. Seyboth, “Onset of deconfinement in nucleus-nucleus collisions: Review for pedestrians and experts”, Acta Phys. Pol. B 42 (2011) 307
- [112] Y. Itow et al. [T2K Collaboration], “The JHF-Kamioka neutrino project 2001”, [arXiv:hep-ex/0106019]
- [113] N. Abgrall et al. [NA61/SHINE Collaboration], “NA61/SHINE plans beyond the approved program”, CERN-SPSC-2012-022; SPSC-P-330-ADD-6.
- [114] J. Abraham et al. [Pierre Auger Collaboration], “Properties and performance of the prototype instrument for the Pierre Auger Observatory”, Nucl. Instr. Meth. A 523 (2004) 50.
- [115] T. Antoni et al. [KASCADE Collaboration], “The cosmic-ray experiment KASCADE”, Nucl. Instr. Meth. A 513 (2003) 90.
- [116] S. Afanasev et al. (NA49 Collaboration), “The NA49 large acceptance hadron detector”, Nucl. Instrum. Meth. A430 (1999) 210-244.
- [117] C. Alt et al. (NA49 Collaboration), “Inclusive production of charged pions in p p collisions at 158 GeV/c beam momentum”, Eur. Phys. J. C45 (2006) 343-381, arXiv:hep-ex/0510009.
- [118] C. Alt et al. (NA49 Collaboration), “Inclusive production of charged pions in  $\pi + C$  collisions at 158 GeV/c beam momentum”, Eur. Phys. J. C49 (2007) 897-917, arXiv:hep-ex/0606028
- [119] N. Abgrall et al. (NA61/SHINE collaboration), “NA61/SHINE facility at the CERN SPS: beams and detector system”, arXiv:1401.4699
- [120] S. Gilardoni and D. Manglunki (ed), “Fifty years of the CERN Proton Synchrotron”, CERN-2011-004.
- [121] C. Bovet, R. Maleyran, A. Placci, M. Placidi, “The Cedar (Cherenkov Differential Counters with Achromatic Ring Focus Project)”, IEEE Trans. Nucl. Sci. 25 (1978) 572.

- [122] S. Afanasiev et al., “The NA49 large acceptance hadron detector”, Nucl. Instr. and Meth. A430 (1999) 210.
- [123] D. Varga, “Study of Inclusive and Correlated Particle Production in Elementary Hadronic Interactions”, Ph.D. Thesis, Budapest, 2003  
[[http://edms.cern.ch/file/900941/1/phd\\_varga.pdf](http://edms.cern.ch/file/900941/1/phd_varga.pdf)]
- [124] N. Abgrall et al. (NA61 Collaboration), “Measurements of cross sections and charged pion spectra in proton-carbon interactions at 31 GeV/c”, Phys. Rev. C84, 034604 (2011).
- [125] N. Abgrall et al. (NA61 Collaboration), “Measurement of production properties of positively charged kaons in proton-carbon interactions at 31 GeV/c”, Phys. Rev. C85 035210 (2012).
- [126] N. Abgrall et al., “Pion emission from the T2K replica target: method, results and application”, Nucl. Instrum. Meth. A701, 99(2013).
- [127] Claudia Strabel, “Evaluation of Particle Yields in 30 GeV Proton-Carbon Inelastic Interactions for Estimating the T2K Neutrino Flux”, Ph.D. Thesis, Zurich, 2011
- [128] S. Agostinelli et al. [GEANT4 Collaboration], “GEANT4: A simulation toolkit”, Nucl. Instrum. Meth. A 506, 250 (2003).
- [129] J. Allison et al., “Geant4 developments and applications“, IEEE Transactions on Nuclear Science 53(1), 270 (2006)
- [130] Ph.D. thesis of Laura Zambelli, “Contraintes sur la prdiction des flux de neutrinos de T2K par les donnees de l’experience de hadroproduction NA61/SHINE.”
- [131] A. Schiz et al., “Hadron-nucleus elastic scattering at 70, 125, and 175 GeV/c”, Phys. Rev. D 21 3010 (1980)
- [132] A. S. Carroll et al., “Absorption cross sections of  $\pi^\pm$ ,  $K^\pm$ ,  $p$  and  $\bar{p}$  on nuclei between 60 and 280 GeV/c”, Phys. Lett. B 80 319 (1979)
- [133] S. P. Denisov et al., “Absorption cross sections for pions, kaons, protons and antiprotons on complex nuclei in the 6 to 60 GeV/c momentum range”, Nucl. Phys. B 61 62 (1973)
- [134] J. M. Paley et al., “Measurement of Charged Pion Production Yields off the NuMI Target”, Phys. Rev. D 90 032001 (2014)
- [135] B. M. Bobchenko et al., “Measurement of total inelastic cross-sections from proton interactions with nuclei in the momentum range from 5 GeV/c to 9 GeV/c and  $\pi^-$  mesons with nuclei in the momentum range from 1.75 GeV/c to 6.5 GeV/c”, Sov. J. Nucl. Phys. 30, 805 (1979)
- [136] K. Abe et al. (T2K Collaboration), “Search for Short Baseline  $\nu_e$  Disappearance with the T2K Near Detector”, Phys.Rev. D91 (2015) 051102, arXiv:1410.881
- [137] T2K Technical Note, “Study of electron neutrino disappearance with the ND280 tracker”, <http://www.t2k.org/docs/technotes/158>
- [138] T2K Technical Note, “Measurement of the electron neutrino beam component in the ND280 Tracker for 2013 analyses”, <http://www.t2k.org/docs/technotes/149>



- [139] K. Abe et al. (T2K Collaboration), “Measurement of the intrinsic electron neutrino component in the T2K neutrino beam with the ND280 detector”, Phys. Rev. D **90** 072012 (2014), arXiv:1403.3140
- [140] Y. Hayato, Phys. Proc. Supp. **B112**, 171 (2002).
- [141] K. Abe et al. (T2K Collaboration), “Evidence of electron neutrino appearance in a muon neutrino beam”, Phys. Rev. D **88**, 032002 (2013).
- [142] P. de Perio et al., “Cross section parameters for the 2012a oscillation analysis”, T2K technical note, T2K-TN-108
- [143] Melanie Day, Kevin S. McFarland, “Differences in quasielastic cross sections of muon and electron neutrinos”, Phys. Rev. D **86**, 053003 (2012)
- [144] Glen Cowan, Kyle Cranmer, Eilam Gross, Ofer Vitells, “Asymptotic formulae for likelihood-based tests of new physics”, Eur. Phys. J. C **71** 1554,2011
- [145] S. Baker and R. Cousins, Nucl. Instrum. Methods Phys. Res. **221**, 437 (1984).
- [146] G. J. Feldman and R. D. Cousins, Phys. Rev. D **57**, 3873 (1998).
- [147] R. D. Cousins and V. L. Highland, Nucl. Instrum. Methods **A320**, 331 (1992).
- [148] J. Stuart, A. Ord and S. Arnold, Kendall’s Advanced Theory of Statistics, Vol 2A (6th Ed.) (Oxford University Press, New York, 1994).
- [149] B.E. Bodmann *et al.* (KARMEN Collaboration), Phys. Lett. B **332**, 251 (1994).
- [150] B. Armbruster *et al.*, Phys. Rev. C **57**, 3414 (1998).
- [151] L. B. Auerbach *et al.* (LSND Collaboration), Phys. Rev. C **64**, 065501 (2001).
- [152] F. Kaether, W. Hampel, G. Heusser, J. Kiko, and T. Kirsten, Phys. Lett. B **685**, 47 (2010).
- [153] B. T. Cleveland *et al.* (Homestake Collaboration), Astrophys. J. **496**, 505 (1998).
- [154] J.N. Abdurashitov *et al.* (SAGE Collaboration), J. Exp. Theor. Phys. **95**, 181 (2002).
- [155] J. Hosaka *et al.* (Super-Kamkiokande Collaboration), Phys. Rev. D **73**, 112001 (2006).
- [156] J. Cravens *et al.* (Super-Kamkiokande Collaboration), Phys. Rev. D **78**, 032002 (2008).
- [157] K. Abe *et al.* (Super-Kamkiokande Collaboration), Phys.Rev. D **83**, 052010 (2011).
- [158] M. Smy (Super-Kamiokande Collaboration), in XXV International Conference on Neutrino Physics and Astrophysics, 2012 (Neutrino, Kyoto, 2012).
- [159] Q. R. Ahmad *et al.* (SNO Collaboration), Phys. Rev. Lett. **89**, 011302 (2002).
- [160] B. Aharmim *et al.* (SNO Collaboration), Phys. Rev. C **72**, 055502 (2005).
- [161] B. Aharmim *et al.* (SNO Collaboration), Phys. Rev. Lett. **101**, 111301 (2008).
- [162] G. Bellini *et al.* (Borexino Collaboration), Phys. Rev. Lett. **107**, 141302 (2011).

- [163] G. Bellini *et al.* (Borexino Collaboration), Phys. Rev. Lett. **108**, 051302 (2012).
- [164] A. Gando *et al.* (KamLAND Collaboration), Phys. Rev. D **83**, 052002 (2011).
- [165] A. Palazzo, MPLA, Vol. 28, No. 7 (2013) 1330004
- [166] “fTQun: A New Reconstruction Algorithm for Super-K”, T2K technical note, T2K-TN-146
- [167] D. Ayres *et al.* (NOvA Collaboration), “NOvA Proposal to Build a 30 Kiloton Off-Axis Detector to Study Neutrino Oscillations in the Fermilab NuMI Beamline”, arXiv:0503053v1 [hep-ex]
- [168] Jianming Bian, “First Results of  $\nu_e$  Appearance Analysis and Electron Neutrino Identification at NOvA”, arXiv:1510.05708 [hep-ex]
- [169] K. Abe *et al.* (T2K Collaboration), “Measurement of muon anti-neutrino oscillations with an accelerator-produced off-axis beam”, arXiv:1512.02495v1 [hep-ex]
- [170] “fTQun: A New Reconstruction Algorithm for Super-K”, T2K technical note, T2K-TN-146
- [171] “Cross section parameters for 2014 oscillation analysis”, T2K technical note, T2K-TN-192
- [172] “Implementation of additional NIWG cross section parameterizations for 2014 analyses”, T2K technical note, T2K-TN-193
- [173] “Tuning the NEUT resonance model”, T2K technical note, T2K-TN-197
- [174] P. Sinclair *et al.*, “Implementation of a multi-nucleon interaction model into NEUT”, T2K-TN-170, 2014.
- [175] K. Iwamoto and K.S. McFarland, “Radiative Charged Current Quasi-Elastic Scattering in T2K-SK”, T2K-TN-205, 2014
- [176] A. Redij and C. Wilkinson, “Implementation of the Random Phase Approximation model in NEUT and NIWGReWeight”, T2K-TN-207, 2014
- [177] J. Kameda, “Updated study of the systematic error in  $\nu_\mu$  disappearance analysis from Super-Kamiokande”, T2K-TN-159
- [178] J. Albert *et al.*, “Study on SK  $\nu_e$  candidates and systematic errors with T2K  $3.23 \times 10^{19}$  POT data” T2K-TN-157
- [179] J. Hignight *et al.*, “Super-Kamiokande events and data quality studies for T2K Run4” T2K-TN-148,
- [180] M. Hartz *et al.*, “Constraining the Flux and Cross Section Models with Data from the ND280 Detector for the 2014/15 Oscillation Analysis” T2K-TN-220,
- [181] Llewellyn-Smith, “Neutrino interactions at high energies”, Phys. Rep. **3C**, 261 (1972).
- [182] S.D. Biller and S.M. Oser, “Another Look at Confidence Intervals: Proposal for a More Relevant and Transparent Approach”, arXiv:1405.5010

- [183] P.S. Laplace, “Memoir on the probability of causes of events,” *Memoires de Mathematique et de Physique*, Tome Sixieme, (1774). (English translation by S. M. Stigler, *Statist. Sci.*, 1(19):364378, 1986.).
- [184] K. Abe et al., “Physics Potential of a Long Baseline Neutrino Oscillation Experiment Using J-PARC Neutrino Beam and Hyper-Kamiokande”, *PTEP*, May 2015, arXiv:1502.05199 [hep-ex].
- [185] “T2K  $4.0108 \times 10^{20}$ -POT 3-Flavour Electron-Antineutrino Appearance Analysis”, T2K technical note, T2K-TN-252
- [186] “T2K Neutrino and Anti-Neutrino 3-Flavour Joint Analysis of Run 1-6 ( $6.914 \times 10^{20}$ -POT  $\nu$   $4.0108 \times 10^{20}$ -POT  $\bar{\nu}$ ), Run 1-7 ( $7.002 \times 10^{20}$ -POT  $\nu$   $7.471 \times 10^{20}$ -POT  $\bar{\nu}$ ) and Run 1-7c ( $7.482 \times 10^{20}$ -POT  $\nu$   $7.471 \times 10^{20}$ -POT  $\bar{\nu}$ ) data sets”, T2K technical note, T2K-TN-266

# Curriculum vitae of Davide Sgalaberna

Institut für Teilchenphysik, ETH Zurich  
CH-8093 Zurich  
Switzerland

Phone: +41 76 7374788  
Work e-mail: [davide.sgalaberna@cern.ch](mailto:davide.sgalaberna@cern.ch)  
Personal e-mail: [davidesgalaberna@gmail.com](mailto:davidesgalaberna@gmail.com)

CERN 182/R-022  
CH-1211 Geneva  
Switzerland

## Personal

**Name:** Davide Sgalaberna

**Born** April 15 1986, Lugo (RA), Italy

**Citizenship:** Italian

## Education

**PhD candidate:** March 2012 -

ETH Zurich (Switzerland)

Topic of thesis: Standard and non standard neutrino oscillations with the T2K experiment

Supervisor: Prof. Dr. André Rubbia

**Master's degree in Physics:** October 2008 - October 2010 110/110 *cum laude*

University of Bologna (Italy)

Title of thesis: "Measurement of cross section of top quark production in the hadronic channel in the proton-antiproton collisions at  $\sqrt{s} = 1.96$  TeV at CDF"

Supervisor: Prof. Dr. Andrea Castro

**Summer Student:** July 2009 - September 2009

Fermi National Accelerator Laboratory (Chicago, USA)

Research activity: analysis of data obtained with the CDF experiment. Measurement of prompt central diphoton cross section, with particular emphasis to fake photon background subtraction

Supervisor: Dr. Aliaksandr Pranko (Lawrence Berkeley National Lab)

**Bachelor's degree in Physics:** September 2005 - October 2008 110/110 *cum laude*

University of Bologna (Italy)

Title of thesis: "Measurement of propagation velocity in signal cables of TOF detector of ALICE Experiment at LHC"

Supervisor: Prof. Dr. Luisa Cifarelli

## Professional experience

### T2K experiment

2012-

T2K is a long baseline neutrino oscillation experiment in Japan. Its goal is to precisely measure the parameters of the neutrino mixing matrix and search for a first hint of CP violation in the leptonic sector.

I Joined the T2K near detector electron-neutrino working group focusing on the study of systematic uncertainties related to the electron-neutrino selection at the near detector, like the muon misidentification, and I participated to the measurement of the electron-neutrino flux at the near detector. Finally I performed the search for  $\nu_e$  disappearance due to mixing with sterile neutrinos at ND280.

I worked on the first analysis of anti-neutrino data at the far detector (Super-Kamiokande),  $\bar{\nu}_\mu$  disappearance and search for standard  $\bar{\nu}_e$  appearance. I work on the full joint analysis of the  $\nu - \bar{\nu}$  data searching for CP violation in the leptonic sector.

As member of the VALOR Fitting Group, which performs data analyses in several neutrino experiments (DUNE, Hyper-Kamiokande, T2K), I work on the oscillation neutrino analyses at the T2K far detector.

### NA61/SHINE experiment

2012-

The NA61/SHINE fixed target experiment consists of a wide-acceptance hadron spectrometer at the CERN SPS. One of the goals of NA61/SHINE is to perform precise hadron production measurements in p+C interactions, in order to improve the calculations of the neutrino flux at the T2K experiment.

Hadrons produced by interactions of protons on a 2 cm Carbon target are detected and  $\pi^\pm$ ,  $K^\pm$ ,  $p$ ,  $\bar{p}$ ,  $\lambda$ ,  $K_S^0$  spectra are measured. In this context I measured the total hadronic production cross section which is needed to normalize the measured spectra as well as to give the overall neutrino flux normalization.

### CDF experiment

2010

CDF is a collider experiment of Tevatron at Fermilab that collected  $p\bar{p}$  data until 2011. At CDF the top quark was discovered. Searches for the Higgs boson as well as for beyond Standard Model physics like super-symmetric particles were performed.

During the period as summer student at Fermilab I worked on the cross section measurement of prompt di-photon production in  $p - \bar{p}$  collisions. My contribution was the study and implementation of a new method of fake photon background subtraction based on the track isolation, a variable which is particularly able to separate fake from true photons, allowing

for a drastic reduction.

The topic of my Master's thesis was the measurement of  $t\bar{t}$  production cross section in the hadronic channel from  $p - \bar{p}$  collisions with  $\sqrt{s} = 1.96$  TeV at the CDF experiment. A template method, analogue to the one used for the top quark mass measurement, has been used for the first time in CDF to measure the cross section, instead of a simple event counting. The advantage of this method was a better signal - background discrimination, since also signal and background shape informations were exploited. The measurement was performed using a maximum likelihood method, with a simultaneous calibration of the Jet Energy Scale, the largest systematic uncertainty.

## **ALICE experiment**

2008

ALICE is an experiment of LHC at CERN which aims to precisely measure signals of the quark gluon plasma at energies of a few TeV in the center of mass. I was involved in the ToF detector group. The ToF has a time resolution lower than 100 ps and it is fundamental to know with high precision the time that the electric signal takes to go from the detector to the read-out electronic. My contribution was to measure the signal propagation delay in cables, which connect the ToF detector to read-out electronics, needed for the final detector calibration. It was the topic of my Bachelor's thesis.

## **Employment**

### **Researcher in industry:**

July 2011 - February 2012

Laboratory for technology transfer (T3Lab) at the tecnopolo of the University of Bologna

Researcher in the field of smart grid: modeling of power production of photovoltaic plants. The software, developed with Matlab, provided very good forecast results of the power production useful for the detection of anomalies and failures in the system.

## **Other activities**

### **Teaching**

Teaching assistant of Physics I, Physics II and neutrino physics at ETH Zurich for seven semesters.

## **Skills**

### **Analysis**

- Extensive experience with analysis of large data samples in high energy physics
- Expert in high level statistical tools for data analysis

### **Computing**

- Programming: C, C++, LaTeX, perl, shell scripting, python
- Analysis software: ROOT, Matlab, R (basic)
- Office applications: Apple iWork and Microsoft Office
- Operating systems: Mac OS X, Linux and Windows

## Languages

- Italian: mother tongue
- English: fluent
- French: beginner

## Schools and Conferences

### Schools

- International Neutrino Summer School (St. Andrews University, Scotland, 2014)
- Introduction to MPI programming (CINECA, Italy, 2011)
- Techniques and tools for HPC scientific programming (CINECA, Italy, 2011)
- Accelerated C++ Short Course (Fermilab, USA, 2009)

### Conferences

- Swiss Physical Society (SPS) Annual Meeting 2012  
Title of poster: "Measurements of  $\pi^\pm$ ,  $K^+$ ,  $K_0$  and proton differential production cross sections and trigger cross section with NA61/SHINE for T2K"
- European Physical Society conference on High Energy Physics (EPS-HEP) 2013  
Title of poster 1: "Probing the neutrino reactor anomaly with the T2K near detector"  
Title of poster 2: "Measurement of the electron neutrino component of the T2K beam in the ND280 Tracker"
- 37th International Conference on High Energy Physics (ICHEP) 2014  
Title of poster: "Constraints on the T2K neutrino flux prediction from hadron production measurements at NA61/SHINE"
- 26th Rencontres de Blois, Particle Physics and Cosmology Title of talk: "Results of T2K"
- XXVI International Conference on Neutrino Physics and Astrophysics, Neutrino 2014 (poster)  
Title of poster: "A first search for sterile neutrinos with the T2K near detector"
- XVIth International Workshop on Neutrino Factories and Future Neutrino Facilities (NUFACT) 2014 (talk)  
Title of talk: "Hadron production measurements at the NA61/SHINE experiment for the T2K Neutrino Flux Prediction"
- Seminar at "Thursday Talks" on 2015 physics Nobel prize (ETH Zurich and University of Zurich)  
Title of talk: "Neutrino oscillations: an open window on new physics"

## Selection of publications

### Journal Articles (major contribution)

- The CDF Collaboration (T. Aaltonen et al.), "Measurement of the cross section for prompt isolated diphoton production in  $p\bar{p}$  collisions at  $\sqrt{s} = 1.96$  TeV", Phys. Rev. D 84, 052006
- The T2K Collaboration (K. Abe et al.), "Measurement of the Intrinsic Electron Neutrino Component in the T2K Neutrino Beam with the ND280 Detector", Phys.Rev. D89 (2014) 092003; arXiv:1403.2552[hep-ex]
- The T2K Collaboration (K. Abe et al.), "Search for Short Baseline  $\nu_e$  Disappearance with the T2K Near Detector", Phys.Rev. D91 (2015) 051102; arXiv:1410.8811[hep-ex]
- The NA61 Collaboration (N. Abgrall et al.), "Measurements of  $\pi^\pm$ ,  $K^\pm$ ,  $K_S^0$ ,  $\lambda$  and proton production in proton-carbon interactions at 31 GeV/c with the NA61/SHINE spectrometer at the CERN SPS", submitted to EPJ C, arXiv:1510.02703[hep-ex]
- Paper on  $\bar{\nu}_\mu$  disappearance at T2K far detector in preparation

### Internal notes

- CDF/PHYS/JET/CDFR/10009, "Measurement of the central diphoton production cross section at CDF"
- T2K-TN-149, "Measurement of the electron neutrino beam component in the ND280 Tracker for 2013 analyses"
- T2K-TN-158, "Study of electron neutrino disappearance with the ND280 tracker"
- T2K-TN-217, "Flux Prediction and Uncertainty Updates with NA61 2009 Thin Target Data and Negative Focussing Mode Predictions"
- T2K-TN-243, "T2K  $2.315 \times 10^{20}$  POT 3-Flavour Muon-Antineutrino Disappearance Analysis"
- T2K-TN-252, "T2K  $4.0108 \times 10^{20}$  POT 3-Flavour Electron-Antineutrino Appearance Analysis"

### Proceedings

- "Hadron Production measurements at the NA61/SHINE experiment for the T2K Neutrino Flux Prediction", Proceedings Of Science (NUFACT2014)051
- "Measurement of the electron neutrino component of the T2K beam in the ND280 Tracker", PoS(EPS-HEP 2013)010
- "Probing the neutrino reactor anomaly with the T2K near detector", PoS(EPS-HEP 2013)011

Last updated: July 18, 2016